Argonne
NATIONAL LABORATORY

High-Efficiency Thermal Energy Storage System for Concentrated Solar Power

Energy Systems Division

High-Efficiency Thermal Energy Storage System for Concentrated Solar Power

by
D. Singh, W. Yu, W. Zhao, T. Kim, D. M. France, and R. K. Smith
Energy Systems Division, Argonne National Laboratory

May 2017

Final Report

Project Title:	High Efficiency Thermal Energy Storage System for Concentrated Solar Power
Project Period:	10/01/12 – 9/30/15
Budget Period:	
Submission Date:	01/29/16
Recipient:	Argonne National Laboratory
Address:	9700 S. Cass Avenue
	Argonne, IL 60439
Award Number:	DE-EE0025682
Project Team:	Argonne National Laboratory Ohio Aerospace Institute University of Wisconsin - Madison
Principal Investigator:	Dileep Singh, Group Leader Thermal-Mechanical Research Energy Systems Division Phone: 630-252-5009 Fax: 630-252-2785 Email: dsingh@anl.gov
Business Contact:	Sandra Davis, Assistant Division Director Energy Systems Division Phone: 630-252-8259 Fax: 630-252-5132 Email: sdavis@anl.gov
HQ Technical Manager:	Dr. Levi Irwin
HQ Project Officer:	Christine Bing
GO Grant Specialist:	
GO Contracting Officer:	

Executive Summary

This work supports the Department of Energy's (DOE's) SunShot initiative goal to reduce the cost for solar energy electricity production to about $0.06/kWh by 2020. The goal of the proposed work was to develop and demonstrate a high-temperature and high-efficiency system for thermal energy storage (TES). Current high-temperature TES systems are based on sensible heat or latent heat of materials such as salts. However, these salts are limited in terms of their thermal performance, and thus it takes extremely long times to fully charge/discharge the storage systems with high efficiencies.

The approach used in this proof-of-concept project was to develop an efficient, high-temperature, laboratory-scale, latent heat TES system (LHTES) prototype by utilizing phase change material (PCM) in combination with new, high-conductivity graphite foams. The resulting combined system has thermal conductivities significantly greater than the salt alone. This approach permits rapid charge/discharge cycles as well as maximum utilization of the PCM volume (i.e., minimal dead zones) in the TES. The laboratory-scale prototype LHTES was built and tested with the purpose of gathering performance data (e.g., transport properties, system durability, and thermal cycling). In addition, associated technologies needed for scale-up and practical implementations were also developed. Specific tasks accomplished as part of this project were:

- o Characterization of various PCMs and down selection to best candidates
- o Thermal modeling and exergy efficiency analysis of high-conductivity graphite foam/PCM for LHTES
- o Determination of properties and characterizations of graphite foam
- o Joining process development for LHTES system integration
- o Process development for infiltration of graphite foam with PCM
- o Corrosion studies of various LHTES materials
- o Laboratory-scale test loop design and construction for prototypes
- o Fabrication of laboratory-scale prototypes
- o Charging/discharging experiments and data analysis for prototypes

Several prototypes were fabricated using $MgCl_2$ as the PCM. Silicon carbide coating of the graphite foam demonstrated mitigation of foam oxidation, while maintaining the thermal/transport properties and mechanical integrity. Infiltration of graphite foam was conducted to almost full capacity (>97%) by using molten PCM. Corrosion studies indicated that removal of moisture from the PCM and LHTES system is critical to mitigate degradation of the system component materials. A test loop system was built and tested to meet the requirements. Charging/discharging experiments were conducted in the temperature range of 700 °C-750 °C to evaluate the performance of the prototypes. Multiple thermal cycling tests showed that the prototypes were repeatable in their performance. Experimental data were compared with the simulations and agreed quite well. Based on the experiments, estimated exergetic and energetic efficiencies were >95%. The experimental data and simulations indicate that the graphite foam/PCM-based LHTES system is capable of meeting the performance targets of 8 h charging/discharging with exergy efficiency >95%. A limited durability study (250 h at 750 °C exposure) on a prototype showed minimal degradation.

Contents

1. Background

With the development of advanced concentrating solar power (CSP), there is a need for high temperature media for transporting and storing thermal energy at temperatures beyond 700⁰C [1, 2]. In particular, systems utilizing high temperature PCMs are of interest due to the efficiencies offered by storing heat based on the enthalpy of transformation. This approach allows for much greater energy storage capacity versus sensible heat alone. In addition, because of the narrow operating temperature (i.e., melt point), the system is highly proficient regarding exergy and round-trip efficiency. Stored heat will allow for continuous power generation for CSP systems (e.g., nighttime or cloudy day power production) without the need for supplementation from green-house gas-producing power plants. Expansion of such power sources will allow the U.S. to reduce its dependence on foreign sources.

For some time, LHTES systems have been studied. However, most studies have been focused on single-composition or multi-composition eutectic salts with melting temperatures <500 °C [3]. One of the main issue with the LHTES has been that, because of the low thermal transport properties of the salts, a full scale system would require unfeasible long times for charging and discharging.

Numerous approaches have been investigated to improve the thermal performance of PCMs, including (a) finned tubes, (b) heat pipes, (c) particles, and (d) metal foams. Carbon-based foams became popular for variety of engineering applications in the 1990s when a new process was developed that resulted in a graphitic phase of the foam structure with extremely high bulk thermal conductivities (~180 W/m-K) [4]. This technological advancement has led to use of the graphitic foams for thermal management, including heat sinks [4, 5], heat exchangers [6], and TES systems [7, 8].

For LHTES applications graphite foams have been primarily used with low temperature PCMs such as paraffin wax [7, 8]. Mesalhy et al. [8] conducted numerical and experimental studies to predict the thermal characteristics of a thermal protection system that consists of carbon foam matrix saturated with a PCM. Their results illustrated that the higher the porosity, the more stable the thermal performance of the matrix composite. Zhong et al. [9] used meso-phase pitch based graphite foams with different thermal properties and pore size to increase thermal diffusivity of paraffin wax, for LHTES application. They found that the thermal diffusivity of the paraffin-GF can be enhanced as much as 570 times as compared with that of pure paraffin wax. Warzoha et al. [10] investigated the effect of infiltration method on the saturation rate of paraffin PCM within graphite foam. They used two methods to infiltrate the foam: a simple submersion technique and a vacuum infiltration technique. The effect of the infiltration method on the paraffin saturation rate was found to be significant with the vacuum system yielding better results.

There are very few experimental studies about high temperature PCM with graphite foam for the LHTES system. Lafdi et al. [6] conducted an analysis of the thermal performance of graphite foams infiltrated with PCM (LiF+CaF$_2$) for space and terrestrial

energy storage systems. They found that the average value of the output power of the new energy storage system was increased significantly due to the high thermal conductivity of graphite foams. Pincemin et al. [11] developed thermal storage composites made of graphite foam and $NaNO_3$/KNO_3 eutectic for solar thermal power plants using direct solar steam generation. Their results showed that compound composites have isotropic properties and thermal conductivity enhancements.

More recently, a high temperature salt has been used in conjunction with silicon carbide foam to fabricate a TES system [12]. In this work, sodium sulfate was impregnated into the silicon carbide foam. The resulting composite thermal conductivity was found to be ~6 W/m-K, and the thermal energy storage density was 161 kJ/kg when the TES system was cycled between 800 °C and 900 °C [12]. Thermal cycling did not degrade the TES system performance.

Based on the extensive literature survey, several studies have used graphite foams in combination with low temperature PCMs for LHTES. Thermal performance advantages of low temperature PCMs based on graphite foam are quite evident. However, for elevated temperature LHTES, specifically >700 °C, limited work has been cited in the literature. This is probably due to the recent development of the graphite foam technology and the challenges associated with developing and testing with a PCM.

The goal of this proof-of-concept project is to develop an efficient, high temperature, laboratory-scale TES prototype by utilizing PCMs in combination with new, high conductivity graphite foams. This system will allow for quick, even distribution of thermal energy into the PCM, resulting in rapid charge/discharge cycles as well as full utilization of the PCM volume (i.e., minimal dead zones). The laboratory-scale TES prototypes were built and tested with the purpose of gathering performance data (e.g., transport properties, system durability, and thermal cycling) regarding a combination of PCM mixtures and foam types and densities. In addition, associated technologies needed for scale-up and practical implementation were also developed. These include the process to infiltrate the foams, coating the foams for strength and environmental (oxidation/corrosion) durability enhancements, and joining techniques for system integration. LHTES units will be built and evaluated in order to down-select and fine-tune the appropriate implementation technologies as well as to identify the optimal design concerning the specific PCM formulation and foam density.

The novelty of the proposed research is in the use of high thermal conductivity foams to significantly enhance the thermal performance of the salt-based PCM. As such, the proposed concept has not been used for a CSP TES system (>700 °C). Multiple aspects of this project are deemed decidedly innovative. This includes utilization of new, high temperature, salt based PCMs as well as the employment of graphite foams for efficient and uniform transfer of thermal energy into the PCM.

The next section summarizes the tasks performed in this project with their specific milestones as per the Statement of Project Objectives (SOPO) [13].

2. Project Tasks and Milestones

Task 1.1: Thermal energy storage device modeling and design

This task focuses on three aspects: (a) model/simulate the movement of the PCM melting front during charge/discharge cycles to establish the benefits of using the proposed foam/PCM based TES system, (b) model/simulate the melt front movement for a full-scale TES system and determine the optimum conditions that would ensure 8 hours of the charging time and 12 hours of the discharging time, and (c) design a laboratory-scale test system for gathering key properties and conduct TES system durability tests.

In-house TES modeling procedures (unique and inclusive to this team) will be used to design high-temperature, laboratory-scale TES device prototypes. The models will dictate the appropriate size and configuration of the unit based on foam (e.g., density), PCM properties, heat transfer fluid (HTF) piping size, HTF flow rates, etc. The models will also compare the thermal performance of TES systems with and without conductive foam (thermal energy capacities and reaction times), clearly showing the advantages of the proposed approach. Models will also be developed for predicting the performance of full-scale systems.

Milestone (Task 1.1): Obtain design and performance predictions of TES laboratory-scale prototype (assembly and testing to follow). Performance predictions have to meet the SunShot goals for exergetic efficiency of >0.95, as defined in the ARPA-E High Energy Advanced Thermal Storage (HEATS) Funding Opportunity Announcement (FOA) for TES operating temperatures of over 700 °C and charging/discharging times of less than 8 hours for a full-scale system.

Task 1.2: Coating of graphite foam for improving strength, oxidation resistance, and surface heat transfer characteristics

Focus will be on the application of SiC coatings of the graphite foam substrate. Two approaches will be assessed: a single step process using chemical vapor reaction and a pre-ceramic polymer solution. Mechanical and transport properties will be characterized, and relevant oxidation studies will be conducted together with assessments using optical microscopy, scanning electron microscopy/energy dispersive X-ray spectroscopy (SEM/EDS), X-ray diffraction (XRD), and transmission electron microscopy (TEM). Although the system will be designed to be isolated from oxygen (e.g., by utilizing an inert gas to back fill the closed TES system), oxidative studies will be conducted to assess the durability of the graphite foam in operating conditions.

Milestone (Task 1.2): Down select most appropriate coating approach that maintains durability as well as the foam's thermal performance. To establish durability, target mechanical properties (tensile & compressive strengths) of coated foams must be 10% more than the uncoated foams. Also must demonstrate no weight loss, within the error bars of the measurement system, of the coated foams in post-oxidation studies. If

weight changes are observed, the rate of coating oxidation will be used to model the coating lifetime.

Task 1.3: Salt-based phase change materials

The team will study and down select candidate PCM salt mixtures based on past NASA and DOE data as well as team member experience. NASA colleagues have authored reports assessing salt mixtures for high temperature energy storage for advanced solar dynamics space power aimed at optimizing melt temperatures and heat of fusion values. Furthermore, the reports studied the corrosive effects of the salt mixtures on various containment materials. Undercooling behavior of the PCM will be another property that will be established, since significant undercooling will degrade the overall efficiency of the TES system. Ideally, the candidate PCM should be compatible with the structural materials (based on past research and corrosion studies conducted during this project). Throughout the PCM experiments, sodium chloride (favorable heat of fusion) will serve as the fall back PCM for the proof-of-concept.

Milestone (Task 1.3): Down select at least two candidate PCMs based on the thermal performance data. PCM performance requirement will be dependent on the TES design and modeling outcome of Task 1.1. At the minimum, the property data requirement will be: melting point >700 °C, heat of fusion >250 J/g, and undercooling <35 °C.

Task 2.1: Joining technologies

The team will develop robust integration approaches utilizing advanced bonding techniques for thermal management systems (i.e., graphite foams to plates and pipes composed of ceramics and/or refractory alloys). The appropriate bond will offer high strength and thermal conductivity as well as resistance to oxidation and corrosive attack by the PCMs. The braze material is required to provide good wettability of the graphite foam as well as the ceramic and metallic plates/tubes. Minimization of interfacial thermal resistance will be important in the overall performance of the TES system. Experiments will be conducted to compare the heat transfer time constants at temperature for systems with brazed joints and non-bonded joints in order to ascertain the thermal advantages of a brazed system.

Milestone (Task 2.1): Define braze material and associated processing procedure (e.g., braze thickness, pressure, temperature, and time), with braze thickness being used as the guiding parameter for joint optimization, for bonding graphite foam to various materials (based on test results as well as up-scale feasibility). Appropriate joint strengths will be identified by isolation of fracture failures to the foam during plate/foam/plate or foam/tube tensile/shear tests. Joint strengths (tensile/shear modes) that are equal or greater than the inherent foam strength will be achieved.

Task 2.2: Corrosion study

One of the parameters of interest will be the corrosive effect of the salts on the container metal and the coated graphite foam. Previous studies on high-temperature

alloys have indicated that alkali based salts have minimal corrosion. In addition, silicon carbide is unaffected by the alkali salts in the expected system operating temperature range. Nevertheless, it will be prudent to conclusively establish that there is minimal or no corrosion of the container materials selected in this work.

Milestone (Task 2.2): The corrosion rate determined must be less than 30 microns/year. Projected survivability of the component over a 30-year period will be the determining factor for the container alloy selection.

Task 2.3: Process development for foam infiltration

The team will employ various approaches to infiltrate the selected foams with appropriate amounts of salt (allowing for contraction and expansion). The process will involve using vacuum infiltration along with the introduction of an inert gas (reducing oxidation risk). Stress loading of the foams will depend on the thermal expansion behaviors of the salt within the foam.

Milestone (Task 2.3): Develop process for controlled infiltration of the salt melts in the foams with greater than the minimum calculated infiltration necessary for the PCM selected. Infiltration is defined as the volume of the salt that goes in the foam divided by the total volume of the foam (value based on previous studies employing low temperature melts). Demonstrate at least 500 melt/solidification cycles showing no appreciable (<10%) degradation in structural/thermal properties of the infiltrated foam as a function of thermal cycling.

Task 2.4: Assembly of TES device prototypes and preparation laboratory for testing

The team will utilize the material level data and PCM characterization results to select the optimal material and fabrication procedures for assembling at least four TES devices (based on two graphite foam densities and two salt mixtures). Low-density graphite foams offer greater thermal capacity (greater volume of PCM) while the higher density foams provide a faster response time. Although the eventual TES system will be compatible for the $S-CO_2$ power cycle, laboratory prototypes will employ either suitable high temperature commercial HTF or *in situ* heating of the heat transfer pipe to appropriate temperatures to simulate the HTF.

Milestone (Task 2.4): Test facilities will be prepared and assembled to run elevated temperature thermal performance tests of the TES prototype. This includes high energy inputs simulating real-world conditions, pumping systems, heat exchangers to control HTF temperatures, and the necessary measurement equipment for fully characterizing the TES PCM response. Argonne environmental, health, and safety (EH&S) approval to begin testing will be completed. Leak tests will demonstrate no external system leakage.

Task 3.1: Preparation of laboratory test loop for prototype testing and test procedures

Test facilities will be prepared for elevated temperature testing (> 700 °C). This will entail procuring the flow loop equipment, assembling the loop, and completing loop check-out testing. At this point, all the necessary material data and design prints will be available for assembling multiple laboratory-scaled, high-temperature TES prototypes. Optimal graphite foam densities, coating strategies, joining methodologies, and structural materials for fabricating laboratory scaled prototypes will be defined.

Milestone (Task 3.1): Test facilities will be prepared and assembled to run elevated temperature thermal performance tests of TES prototypes. Experimental measurement variables and controls are listed in Table 2-1. This includes high temperature fluid (air) for thermal energy delivery, pumping systems, controls for HTF temperatures, and the necessary measurement equipment for fully characterizing the TES PCM response. Argonne EH&S approval to begin testing will be completed.

Table 2-1. Experiment measurement variables.

	Measurement range of set point	Verification method
Air flow	±3%	NIST traceable air flow meter
Air temperature control	±2.0 °C	Temperature will be measured at the exit of the heater using NIST traceable thermocouple (TC).
Furnace temperature control	±2% of the set temperature in the hot zone	Will be determined by measuring temperatures in the hot zone using NIST traceable TCs.

Task 3.2: Fabrication of TES prototypes

Typical dimensions of the prototype will be 4.5 in. diameter and 6 in. length. The shell of the prototype (Incoloy 800H) will enclose the infiltrated graphite foam. Six thermocouples will be used to monitor the temperature profile in the prototype to establish the movement of the melting front in 3D. It is expected that the weight of PCM ($MgCl_2$) will be 1.5-2.0 kg, and the total stored energy in the prototype will be up to 900 kJ. To investigate system parameters, various prototypes will be fabricated as illustrated in Table 2-2.

Milestone (Task 3.2): Fabrication and delivery of 2-3 prototypes of each of the 3 types of prototypes described in Table 2-2. Table 2-3 illustrates the control values to qualify the fabrication procedures for each prototype.

Table 2-2. Various types of prototypes that will be built and evaluated.

Prototype	Description	Objectives
1	• 0.5" O.D. HTF pipe • With brazing (BNi$_4$) • With SiC coating on graphite foam • Incoloy 800H	• The prototype is scaled to the real TES system in the CSP plant • Confirm the simulation model • Investigate the feasibility of the TES system for the CSP plant
2	• 0.5" O.D. HTF pipe • Without brazing • Use of Ni plated Incoloy[1] HTF pipe and container • With SiC coating on graphite foam • Incoloy 800H	• Investigate how the gap (no brazing) affects the heat transfer process • Investigate the interaction between the Ni plated Incoloy and the graphite foam-MgCl$_2$ after multiple thermal cycles • Establish whether the brazing process can be removed or not for the TES system
3[2]	• 0.5" O.D. HTF pipe • Addition of ~0.5 wt.% Mg metal/MgCl$_2$ composite • No brazing and Ni plating • With SiC coating on graphite foam	• Study whether the Mg metal additive affects the heat transfer process or not (whether the Mg metal additive alters the properties of graphite foam-MgCl$_2$) • Investigate the corrosion of MgCl$_2$ to Incoloy 800 H pipes to establish whether the Mg metal additive can prevent corrosion or not

[1] Cr inter-diffusion in Ni was estimated to be ~3-10 µm/year at 750 °C based on Chen et al. (2003) [14]. This implies Ni plating thickness should be >250 µm.
[2] Prototype 3 will depend on the outcome of the investigation at Savannah River National Laboratory (SRNL) and guidance provided by SRNL in terms of supply of the composite PCM.

Table 2-3. Control measurements for prototype fabrication consistency.

Prototype fabrication procedures	Control measurements
Machining graphite foam	Measure the dimensions of the graphite foam post machining; ±0.05" of design requirement.
SiC coating on graphite foam	Weight measurements before and after polymer derived coating process. Estimate the coating coverage (based on weight change) such that it is similar to oxidation tests (>0.02 g/m^2).
Brazing Incoloy 800H and graphite foam	Application of braze such that the resulting braze thickness >250 µm; estimated from weight of braze applied and the applied area.
Ni-plating Incoloy 800H	Ni plating thickness >250 µm; QA from plating company.
Infiltration of graphite foam	Weight measurement before and after infiltration to ensure infiltration rate >90%.
Drilling holes on the infiltrated foam for TCs	Measure the weight change before and after drilling holes on the infiltrated foam; thermocouple locations ±0.10" of design.
Welding and sealing of the prototype	Measure the weight change before and after welding process, weight change <1%. Test prototype for leakage, hold vacuum (~200 mTorr for 2 h).

Task 3.3: Performance data for TES device prototypes

The team will conduct thermal performance tests of the TES device prototypes (e.g., transport properties and cyclic behavior) to assess the influence of the PCM mixtures and their effect on structural alloys. This system-level data will be used for further design modifications and tailoring of the TES devices for future employment in CSP systems. Additional activities include comparisons to and modifications of the thermal model as well as assessment of the structural integrity of the TES devices (visual inspection to qualify the corrosion of the TES prototype).

Subtask 3.3.1: Initiate testing of TES device prototypes and analyze thermal behavior as a function of foam density and PCM selection. Collect substantial thermal performance data of unique TES device prototypes.

Milestone (Subtask 3.3.1): Demonstration of graphite foam/salt PCM TES system for 3-5 thermal cycles from a "cold" temperature of 600 °C to a "hot" temperature of 750 °C, with the data repeatability within ±10% to indicate stable system performance. For those specific time steps deemed important to understand the functionality of the prototypes, the difference tables described in Task 3.2 above will be populated with measurement data for each dependent variable.

Subtask 3.3.2: Utilize experimental data to verify model predictions (and to modify model parameters). Also employ model to assess more traditional TES approaches, thereby showing advantages of the current project. Also, use the calibrated model to predict performance of full-scale systems. Further, the exergetic efficiency of the prototypes tests will be estimated, and prediction for the full-scale system will be made.

Milestones (Subtask 3.3.2): Model verification. All diagonal cells in the difference matrix for those time steps chosen in Milestone (Subtask 3.3.1) are to demonstrate that experimental data and model predictions agree to within ±15%.

Milestone (Task 3.3): For those time steps deemed important in Milestones (Subtask 3.3.1 and Subtask 3.3.2), we will clearly present the meaningful differences in the performance of the three prototypes through a rigorous statistical analysis of the data collected on the dependent variables for each of the 3-5 repeat runs for each prototype. Differences will be reported in the conclusion table through comparison of each group of 3-5 measured values between all prototypes using the student's t-test at the 95%[1] confidence interval. For each comparison (or groups of related comparisons) that shows difference, we will formulate a hypothesis that may explain the observed difference. These hypotheses will be tested as part of Subtask 3.3.3 and Subtask 3.3.4.

Note: If there is no statistically significant difference between the measured values for each prototype at those coordinates at the 95% confidence interval, the cells will be painted "green". If there is a statistically significant difference between the measured

---

[1] The confidence interval will be finalized after few initial tests with the first prototype once some experience is gained on its performance.

values for each prototype at those coordinates at the 95% confidence interval, the cells will be painted "red".

Subtask 3.3.3: Performance testing for post long-term high temperature exposure of the TES prototype. After the performance testing per Subtask 3.3.1, selected prototypes will be transferred to a second furnace for long-term high temperature exposure such that PCM in the prototype is completely melted (~750 $^{\circ}$C). Exposure time will range up to 500 hours. After the long-term exposure process, the prototype will be put back on the test loop for performance testing as per Subtask 3.3.1. To ensure no degradation effects because of the long-term hold, the performance of the prototype will be expected to be with ±10% to the results obtained prior to the exposure testing. If deviations or degradation in the prototype performance is observed, then the prototype will be sectioned to identify the root cause and to attempt to validate the hypotheses presented in Milestone (Task 3.3).

Milestones (Subtask 3.3.3): Ensure prototype performance within ±10% of the results obtained prior to high temperature melt exposure.

Subtask 3.3.4: System improvement studies and analyses will be completed. This will entail material and system tweaking that may lead to further improvements in prototype system performance. In addition, this task will conduct post-mortem analysis of the tested prototypes to investigate any failure/degradation. We will attempt to validate the hypotheses presented in Milestone (Task 3.3). This will help in the development of a full-scale TES systems.

Milestones (Subtask 3.3.4): Provide a peer-reviewed journal publication that will serve as a roadmap for the large-scale TES systems.

Final Project Deliverables: The final deliverables include actual laboratory-scale TES device prototypes and the associated test data (data presented in report form as well as conference and journal publications). The TES device is designed for elevated temperatures (>700 $^{\circ}$C) and rapid response times (less than 8 hours for full scale system, predictions based on prototype results and model), making it appropriate for CSP applications. Cost estimations will be made for the optimized TES design and will be compared with the DOE target of $15/kW$_{th}$. Lastly, based on simulations and experimental data, the exergetic efficiency of the full-scale system will be determined to ensure it meets the target of >95% exergetic efficiency, as defined in the ARPA-E HEATS FOA.

3. Characterization of Various Phase Change Materials and Down Selection

As part of the project, effort was spent on reviewing the literature for the potential PCM materials. The PCM reviewed fell into three main categories – chlorides, carbonates, and fluorides. Criteria used for identification and down selecting the PCMs were as follows:

Physical requirements: (a) suitable phase change temperature (700 °C ~ 800 °C); (b) large volumetric heat of fusion; (c) temperature cycling stability, (d) little or no super-cooling; and (e) good thermal conductivity.

Property requirements with respect to storage: (a) low vapor pressure; (b) small volume change; (c) wetting properties of the PCM with graphite; (d) chemical stability/corrosion of the PCM with other structural materials; and (e) safety constraints (non-toxic, non-flammable materials).

Economic requirements: (a) low price and (b) capability of PCM to be recycled for environmental and economic reasons.

Literature search was conducted to identify the potential high-temperature PCMs. In particular, chlorides, carbonates, fluorides, and their mixtures were identified. In general, fluoride-based PCMs have high heat of fusion, but are also costly as compared to the chlorides and carbonates.

An extensive characterization effort was undertaken to determine the various properties of the selected PCMs. The PCMs used for the characterizations were from commercial sources using a differential scanning calorimeter (TA Instruments, Model Q600) and are presented in Table 3-1. For the most part, the experimentally measured values in Table 3-1 are in good agreement with the literature values. For the case of lithium carbonate, there is a large discrepancy between the literature heat of fusion and the measured values. The difference is because of the high volatility of the salt at the temperature range tested, which leads to significant changes in the weight and causes large error (scatter) in the measurements.

Based on the results presented in Table 3-1, $MgCl_2$ appears to be an excellent candidate for the prototype test system. This conclusion was reached because of its melting temperature range, high volumetric heat of fusion, and small under-cooling. Although, among the other chlorides, magnesium chloride has somewhat higher volatility, this is not expected to be an issue since the proposed LHTES system is closed and sealed. Carbonates were not considered because of their lower heat of fusion. As a backup, sodium chloride was selected.

Another key aspect in the selection of the PCM was the ability to infiltrate the PCM into the graphite foam. Since the approach to infiltrate the PCM was spontaneous or pressure induced, several factors were considered. As per Darcy's law, the infiltration process is governed by several parameters, including foam pore size and pore

distribution, dynamic viscosity of the fluid, wettability of PCM on graphite, depth of infiltration, etc. In this regard, an infiltration model for metal infiltration in porous ceramics, developed by Mortensen's group [15], was used. As per the model, the contact angle between graphite and PCM is a key parameter that determines the infiltration energy. A literature review revealed that most chloride salts do not wet (contact angle >90°) graphite [16]. However, chlorides with large cations apparently do have better wettability. Coating of graphite with carbides improved wetting and infiltration [17]. In this regard, coating of graphite with a ceramic such as silicon carbide (SiC) on the graphite foam was considered to promote complete infiltration with a chloride PCM. It should be noted that spontaneous infiltration of a sulfate PCM into porous SiC has been demonstrated [12]. Further, the SiC coating is expected to mitigate oxidation of graphite and provide structural integrity.

PCM selection and evaluation activity fulfilled the milestone 1.3: "*Selection of two PCM salts with melting points > 700 °C, heat of fusion > 250 J/g, and undercooling <35 °C"*.

Table 3-1. Selected PCMs for characterizations.

PCM	Measured Melting Point: T_m (°C)	Literature Melting Point: T_m (°C)	Measured Heat of Fusion (MJ/m³)	Literature Heat of Fusion (MJ/m³)	Measured Heat of Fusion (kJ/kg)	Literature Heat of Fusion (kJ/kg)	Measured Under Cooling (°C)
$MgCl_2$	710.5 (±0.1)	714	733.7 (±10.2)	758	437.3 (±6.1)	452	10.6 (±0.4)
NaCl	798.0 (±0.2)	800	675.1 (±3.4)	766	433.7 (±2.2)	492	13.3 (±0.3)
KCl	767.1 (±0.1)	771	516.5 (±4.6)	539	338.1 (±3.0)	353	9.9 (±0.2)
$CaCl_2$	753.7 (±3.4)	782	533.8 (±4.0)	478	256.6 (±1.9)	230	87.6 (±3.4)
Li_2CO_3	716.6 (±7.2)	723	674.4 (±193.9)	1109.48	368.3 (±105.9)	606	22.0 (±4.7)
Na_2CO_3-K_2CO_3 (56:44 mol%)	699.1 (±2.4)	710	294.6 (±14.9)	321.80	149.8 (±7.6)	164	7.4 (±2.0)
Na_2CO_3-K_2CO_3 (85:15 mol%)	789-731	790-737	340.8 (±57.4)	500.89	172.8 (±29.1)	254	11.9 (±1.9)

4. Thermal Modeling/Simulation of High Conductivity Graphite Foams/PCM for LHTES System

A significant portion of the project effort was spent on thermal modeling of the proposed LHTES. Both 1-D and 3-D models were formulated to predict the performance of the full-scale LHTES system. Parametric studies were conducted to evaluate the effects of different system variables on the LHTES performance. Finally, exergetic efficiency analysis was carried out to understand the implications of graphite foam additions to the PCM.

A mathematical analysis was conducted for an LHTES system having a 50 MWe CSP plant with 12-hour storage. The storage tank contains a PCM and vertical oriented pipes carrying a pumped liquid to add and remove heat. The number of pipes was determined to charge or discharge the storage tank in eight-hour time. Then the system was reconfigured with the PCM stored in the connected cells of a thermally conducting graphite foam, and the number of pipes was recalculated for this efficient case.

4.1. 1-D Modeling for 8-h charge/discharge

Transient conduction heat transfer was considered to discharge the LHTES tank for a CSP plant. A simple construction for the LHTES tank was considered with HTF pipes running vertically, with the remaining volume being either PCM or PCM infiltrated foam (Figure 4-1a). It was assumed that the PCM in the storage tank was all liquid at its solidification/melting temperature; when cooler HTF started flowing through the pipes, heat was removed and the PCM solidified. The thickness of the solidified PCM layer around the pipes increases with the time to a maximum at the end of eight hours. It is desirable to know the solidified PCM thickness at the end of this 8-h discharging time in order to determine the pipe spacing and number of pipes in the storage tank.

In this study, the semi-analytical solution [18] was adopted to solve the CSP discharge problem (Figure 4-1b). Solidification of the foam/PCM composite around the tube at the center position of PCM/tube system is a 1-D problem along the radial direction in the cylindrical coordinate system. Details of the assumptions and analysis have been published in a journal paper (T. Kim, D. France, W. Yu, and D. Singh, "Heat Transfer in a Latent Heat Thermal Energy Storage System Using Graphite Foam for Concentrated Solar Power," Solar Energy 103 (2014) 438-447).

The ordinary differential equation for the location of the solid-liquid interface is obtained from the governing equation and boundary conditions:

$$\frac{dS}{dF_0} = \frac{\sqrt{1 + 2\theta_0 Ste} - 1}{S \ln\left(\dfrac{S}{R_0}\right)} \quad \text{(W/m-K)} \quad (T \text{ in K}) \tag{4-1}$$
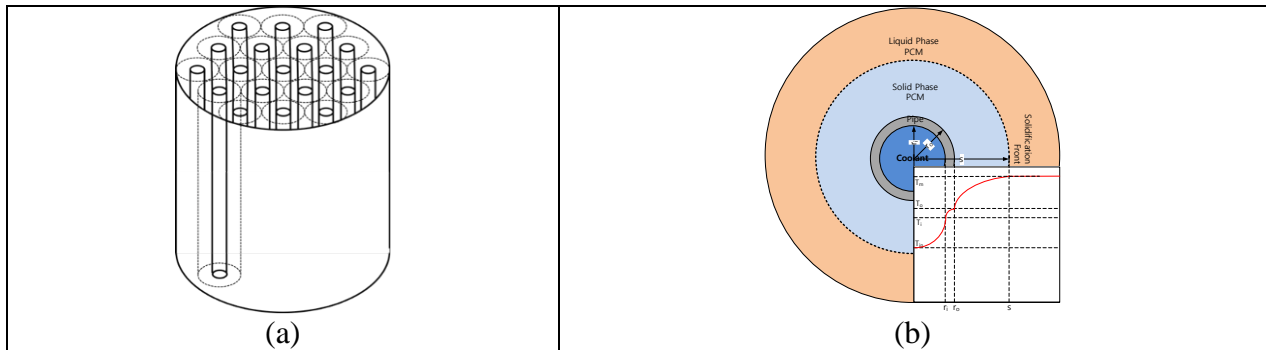
Figure 4-1. Schematic of (a) pipe arrangement in LHTES and (b) PCM solidification during discharge cycle.

where S is the dimensionless radius of the liquid-solid interface, F_0 is the dimensionless time, θ_0 is the dimensionless outer surface temperature of the pipe, R_0 is the dimensionless outer radius of the pipe, and Ste is the Stefan number.

The method described above was applied to the discharge transient for an LHTES system, which has a capacity of 12 equivalent full load hours and a charging/discharging time less than 8 hours for a 50 MWe CSP plant with operating temperature between 700 ˚C and 800 ˚C. The objective was to determine the amount of the PCM solidified during an 8-hour transient. The effects of the pipe outer diameter, pipe thickness, type of HTF, HTF velocity, thermal conductivity, and type of salt were evaluated. All parameters of the LHTES for analysis are summarized in the Table 4-1.

4.2. Benefits of using graphite foams (parametric study)

4.2.1. Effective thermal conductivity
The effect of the $MgCl_2$/graphite foam thermal conductivity is presented in Figure 4-2 as a function of the time at a HTF velocity of 0.5 m/s. The solidification thickness increased by the addition of the graphite foam. This result indicates that the heat transfer between the PCM and the HTF can be enhanced dramatically by using the graphite foam as the heat transferring media. The beneficial effect of the graphite foam was put into the perspective of the number of pipes in the LHTES tank. It was shown that the number of pipes could be reduced by 85~97% by introducing the graphite foam (Figure 4-3). Further, the cross-sectional radius of the LHTES tank without graphite foam is much higher than that with graphite foams (Figure 4-4). This increase in radius of the tank can cause a significant increase in tank material cost. In other words, the utilization of the graphite foam can reduce the capital cost of LHTES.

4.2.2. Heat transfer fluid velocity
The HTF velocity effect on the solidification front for $MgCl_2$/graphite foam with FLiNaK HTF was considered for three turbulent flows, and the results are given in Figures 4-5 and 4-6.

Table 4-1. Parameters of LHTES system for analysis.

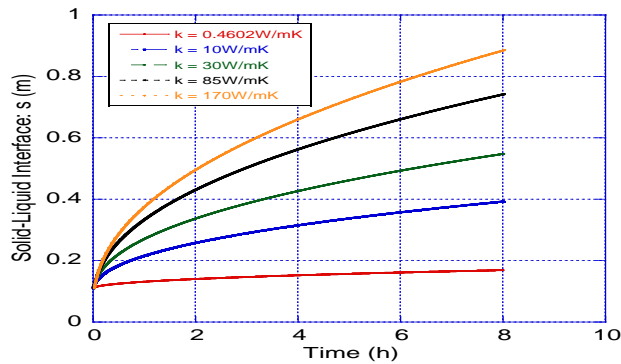| Latent Heat Thermal Energy Storage System			
Foam + PCM	Salt	MgCl$_2$, NaCl, KCl, CaCl$_2$, Li$_2$CO$_3$, Na$_2$CO$_3$-K$_2$CO$_3$(56-44), NaF-CaF$_2$-MgF$_2$(65-22-13), KF-NaF(60-40)	
	Foam	Graphite Foam	SiC Foam
	Effective Thermal Conductivity	10 W/m-K (95% Porosity), 30 W/m-K (90% Porosity), 85 W/m-K (80% Porosity), 170 W/m-K (70% Porosity)	3 W/m-K (90% Porosity), 7.5 W/m-K (85% Porosity), 15 W/m-K (70% Porosity)
HTF	Type	FLiNaK, Sodium, Lead	
	Flow Velocity	0.1 m/s, 0.5 m/s, 1 m/s	
Pipe	Material	Inconel 617	
	Outer Diameter	2", 4", 8", 12", 16"	
	Thickness	Sch5, Sch10, Sch20, Sch40	

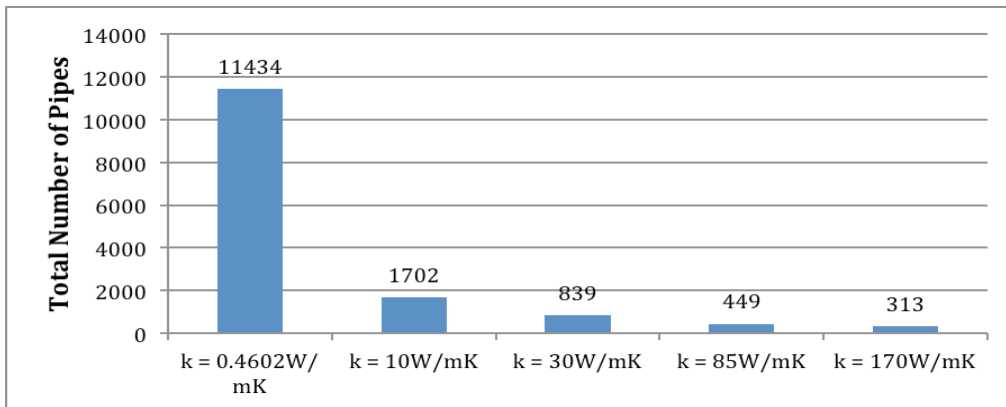Figure 4-2. Solidification front versus time at v = 0.5 m/s, OD = 8", and thickness = Sch10.

Figure 4-3. Total numbers of pipes for values of thermal conductivities (k) at v = 0.5 m/s, OD = 8", and thickness = Sch10.
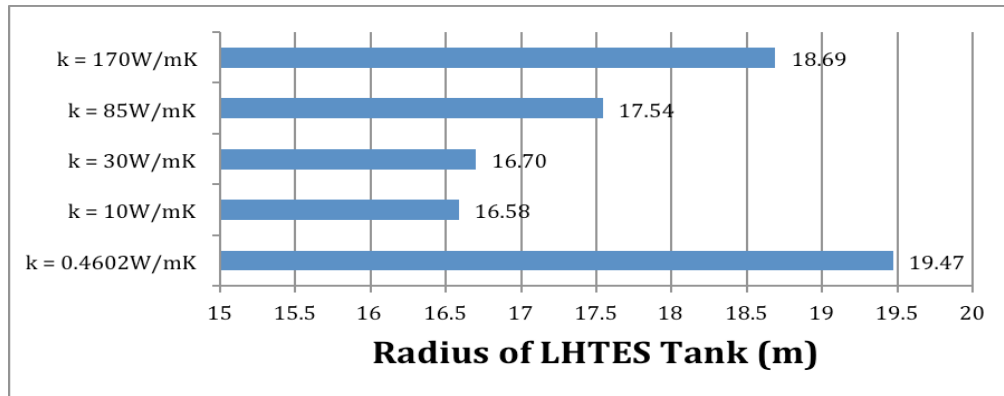
Figure 4-4. Radius of LHTES Tank for different k at v = 0.5 m/s, OD = 8",
and thickness = Sch10.

For the $MgCl_2$ without graphite foam with thermal conductivity of 0.46 W/m-K, in Figure 4-5 indicates that the solidification front radii after 8 hours are less than 0.2 m for all three turbulent velocities. There is essentially no effect of HTF velocity on the solidification front for the PCM without foam. In this case, the PCM is the major resistance to heat transfer, and decreasing the HTF resistance (by increasing its velocity/Reynolds number) has little effect on the solidification during the discharge process.

The effect of HTF velocity on the solidification front was considered for a $MgCl_2$/graphite foam combination with an effective thermal conductivity of 30 W/m-K. In this case, Figure 4-6 indicates that the solidification thickness increased 17% by increasing the velocity from 0.1 m/s to 0.5 m/s and increased 3% by increasing the velocity from 0.5 m/s to 1 m/s. The thermal resistance of the PCM with foam is sensitive to HTF velocity because the resistance to heat transfer of the PCM/foam is much lower than that without foam and the same order as the HTF resistance.
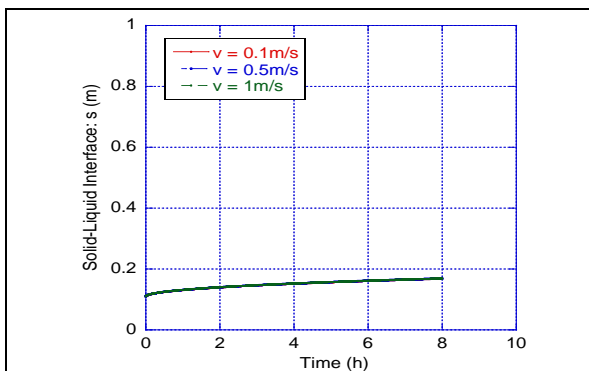
| Figure 4-5. Solidification front versus time for PCM alone at k = 0.46 W/m-K, OD = 8", and thickness = Sch10. | Figure 4-6. Solidification front versus time for PCM/foam at k = 30 W/m-K, OD = 8", and thickness = Sch10. |

4.2.3. Effect of pipe outer diameter

The outer diameter effect on the solidification front for $MgCl_2$/graphite foam with FLiNaK is analyzed by plotting solidification front radius (s) versus the time for different outer

diameters of the pipe (Figure 4-7). The solidification fronts increased with increasing outer diameter of the pipe. It is seen in Figure 4-8 that the number of pipes decreased with increasing the outer diameter of the pipe. However, the total mass flow rate of the HTF, which is related to the pumping power, increased with increasing outer diameter of the pipe. Therefore, the pipe outer diameter should be determined by considering both the number of pipes and the mass flow rate of the HTF. To that end, the mass flow rate can be minimized while keeping the HTF in turbulent flow with a "reasonable" number of pipes in the LHTES tank, by selecting a pipe diameter of ~2 in. and a HTF velocity of approximately 0.1 m/s. Also, a foam/PCM thermal conductivity of 25-30 W/m-K appears to be near optimum for graphite foams. These parameters were used in the exergy analysis presented later.
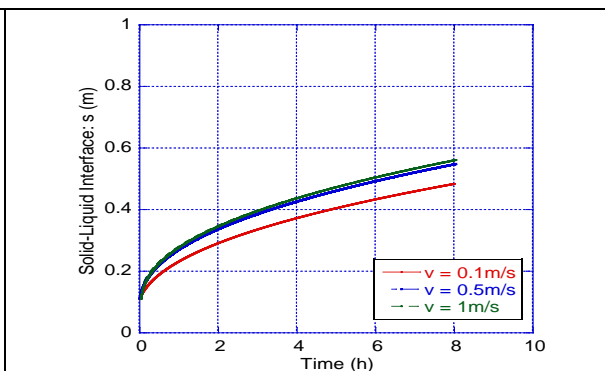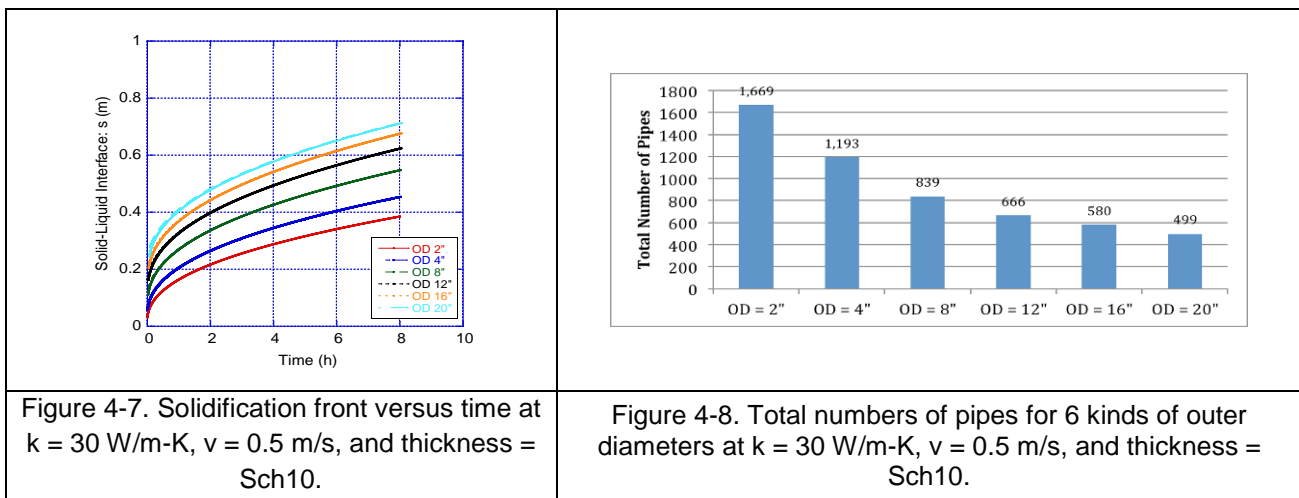

| Figure 4-7. Solidification front versus time at k = 30 W/m-K, v = 0.5 m/s, and thickness = Sch10. | Figure 4-8. Total numbers of pipes for 6 kinds of outer diameters at k = 30 W/m-K, v = 0.5 m/s, and thickness = Sch10. |

4.2.4. Effect of candidate PCM salts on LHTES performance

The solidification front radii of the FLiNaK HTF with various salts are shown in Figure 4-9. The effective PCM/graphite foam thermal conductivity was assumed to be 30 W/m-K for all salts because the effective thermal conductivity of the graphite foam infiltrated with a salt is an unknown parameter, and it is dominated by the thermal conductivity and the porosity of the foam. The solidification front radii of the chloride salts are higher than those of the fluoride salts. Calcium chloride salt has highest value of the solidification front radii among the chloride salts. The sodium-potassium carbonate has higher value for the solidification front radii than lithium carbonate.
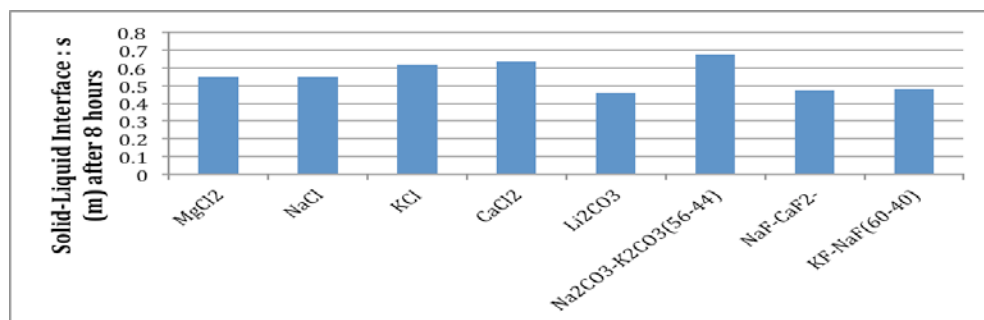
Figure 4-9. The solidification fronts for various salts at k = 30 W/m-K, v = 0.5 m/s, OD = 8", and thickness = Sch10.

To select the salt for the LHTES, not only the solidification front but also the total size of the tank that is related to the heat of fusion and the density of salt need to be considered. The total numbers of pipes for various salts are shown in Figure 4-10. The PCM are listed from the minimum number of pipes of them as follows:

$KF-NaF$ (60-40) < $NaF-CaF_2-MgF_2$ (65-23-13) < Li_2CO_3 < $MgCl_2$ < $NaCl$ < KCl < $CaCl_2$ < $Na_2CO_3-K_2CO_3$ (56-44)

Total cross-sectional radii of the PCM/graphite foam and radii of the TES tank for various salts are shown in Figure 4-11. The salts are listed from the minimum cross-sectional radius of LHTES tank, as follows:

Li_2CO_3 < $KF-NaF$ (60-40) < $NaF-CaF_2-MgF_2$ (65-23-13) < $MgCl_2$ < $NaCl$ < KCl < $CaCl_2$ < $Na_2CO_3-K_2CO_3$ (56-44)
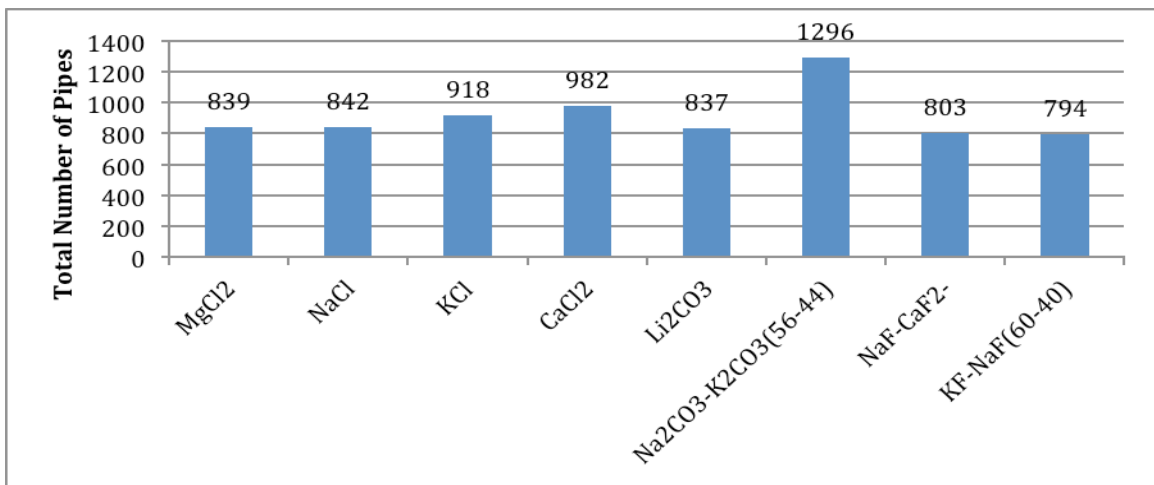

Figure 4-10. Required numbers of pipes for various salts at k = 30 W/m-K, v = 0.5 m/s, OD = 8", and thickness = Sch10.

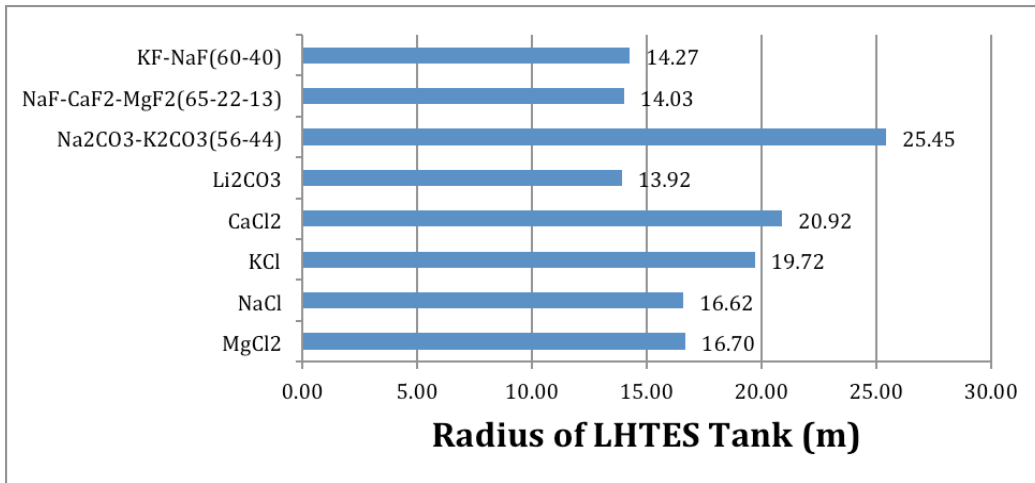Figure 4-11. Radius of LHTES tank for different salts at k = 30 W/m-K, v = 0.5 m/s, OD = 8", and thickness = Sch10.

4.2.5. Benefits of using SiC foams

The beneficial effect of utilization of graphite foam was analyzed in the previous sections. It was shown that the total required number of pipes could be reduced by 85~97% by introducing graphite foam. Same analyses were conducted for utilization of SiC foam. This was done since SiC is an inherently more stable high temperature material. The effect of $MgCl_2$/SiC foam thermal conductivity is presented in Figure 4-12 as movement of the solidification front versus the time for the velocity of 0.5 m/s. The solidification thickness increased by over a factor of 4.2 as the effective thermal conductivity increased from 0.46 W/m-K to 7.5 W/m-K by addition of the 85% porosity SiC foam. The beneficial effect of the SiC foam was put into the total required number of pipes in the LHTES tank. It was shown that the number of pipes could be reduced by 68~89% by introducing the SiC foam (Figure 4-13). The beneficial effect of SiC foam on the total required number of pipes is lower than that of the graphite foam. However, it is still quite significant compared to the case without any foam.
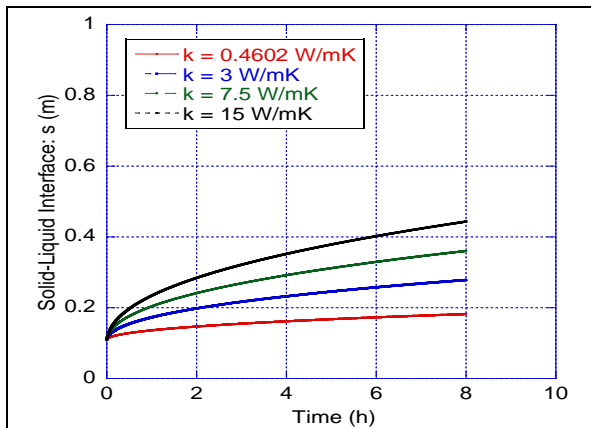

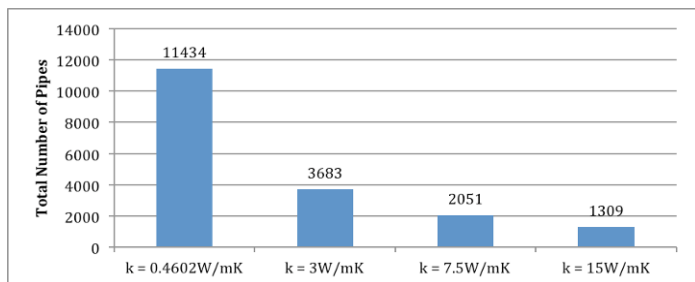Figure 4-12. Solidification front versus time at v = 0.5 m/s, OD = 8", and thickness = Sch10.

Figure 4-13. Total numbers of pipes for 4 kinds of thermal conductivities at v = 0.5 m/s, OD = 8", and thickness = Sch10.

4.3. Simulation of graphite foams/PCM for thermal energy storage

In this section, we present the results of heat transfer analysis using commercial software, COMSOL [19]. The objectives of this analysis were to (a) verify the 1-D semi-analytical analysis presented above [18] and (b) conduct 2-D analysis of the proposed graphite foam/PCM LHTES system to establish the melt front along the radial and axial directions of HTF pipes. The heat transfer analysis aimed to establish the thermal performance of the LHTES system relative to the performance targets.

4.3.1. 1-D heat transfer simulations

A semi-infinite domain of the PCM with an 8-in. diameter HTF pipe vertically passing through the foam/PCM as shown in Figure 4-14. Magnesium chloride ($MgCl_2$) was used as PCM. Since the thermal conductivity of $MgCl_2$ is very low, we filled $MgCl_2$ into graphite foam to improve the thermal performance of the PCM. Thus, the thermal conductivity of graphite foam-$MgCl_2$ composition increased as illustrated in Table 4-2. The HTF was liquid LiF-NaF-KF (46.5-11.5-42 mol %) (FLiNaK). Inconel alloy 617 was applied to the HTF pipe. The properties of these materials are listed in Table 4-2.

Table 4-2 Properties of PCM, HTF, and fluid pipe.

	Density (kg/m^3)	Thermal conductivity (W/m·K)	Heat capacity (J/kg·K)	Latent heat of fusion (kJ/kg)	Dynamic viscosity (Pa·s)
Graphite foam-$MgCl_2$ composite	1580[a]	25[c]	967.4	407.6[e]	
Liquid FLiNaK[b]	2018.9	0.92	2011.6	---	0.0029
Inconel alloy 617	8360[d]	24.2 [d]	419 [d]	---	---

[a]B. Poling, et al (2008); [b]C. Forsberg (2007); [c] D. Yang & H. Wang (2012); [d]G. Janz (1967); [e]Special Metals Corp.
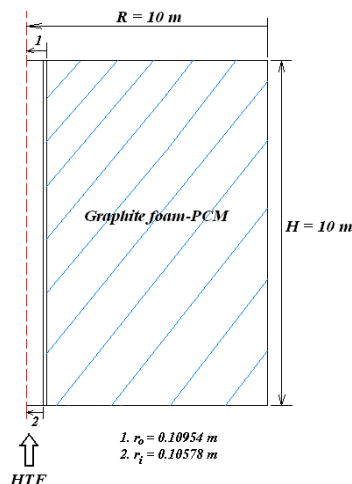

Figure 4-14. Schematic of the embedded pipe in foam/PCM system used for analysis.

Before the simulations, convergence studies of the numerical simulation were conducted. Since the simulation is for a semi-infinite domain of graphite/PCM, we used a large radius of the graphite/PCM to indicate the infinite domain [20, 21]. We compared

the results with 2-, 5-, 10-, and 20-m radii of PCM. The comparison results are shown in Figures 4-15 and 4-16 The HTF temperature was maintained at 850 °C while the flow velocity was 0.5 m/s. The melting point of $MgCl_2$ was 714 °C, and the initial temperature of PCM was taken as 714 °C. Analysis was conducted for the charging process for 8 hours to study the liquid interface movement and the temperature profiles in PCM during the 8-h energy storage process.
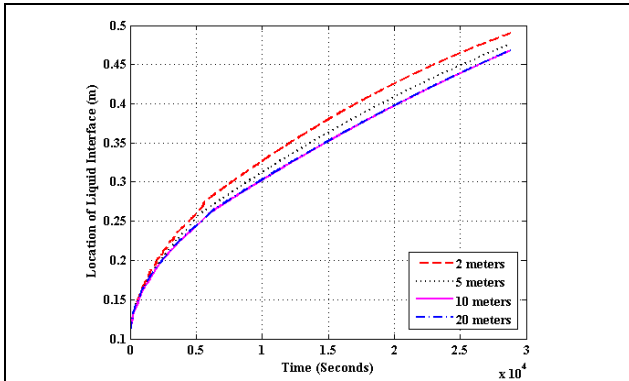
Figure 4-15. Interface movement during melting process.	Figure 4-16. Temperature profiles at various locations.
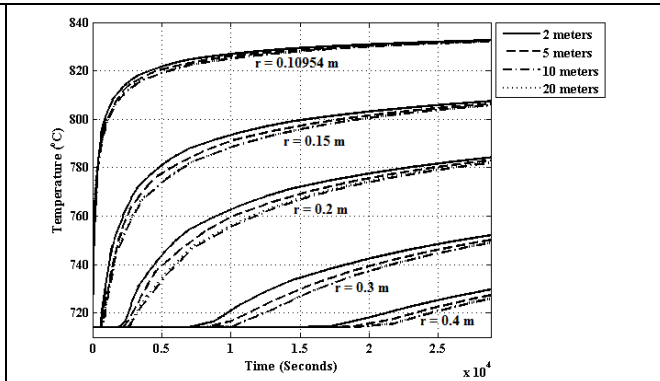
4.3.2. 1-D heat transfer simulations

One-dimensional simulations were conducted with various HTF temperatures for the graphite foam-$MgCl_2$ composite. The HTF flow velocity was 0.5 m/s. The HTF temperature was 850 °C for the model. The initial temperature of the PCM was 714 °C. The charging process was for 8 hours. The COMSOL simulation results were compared with 1-D semi-infinite analytical model calculation. Predictions agree quite well, as evidenced in the following graphs. Figures 4-17 to 4-19 display the liquid interface movement and temperature profiles in the foam/PCM. Further, Table 4-3 illustrates the location of liquid interface in foam/PCM after 8-h charging for various HTF temperatures. The results of the two methods agree quite well. The agreement between the two methods at lower HTF temperatures is better than at higher HTF temperatures.

Table 4-3. Location of liquid interface in PCM after 8-h charging.

	HTF Temp. 800 °C	HTF Temp. 850 °C	HTF Temp. 900 °C
COMSOL, 1-D numerical simulation	0.422 m	0.468 m	0.507 m
1-D semi-infinite analytical model	0.413 m	0.477 m	0.527 m
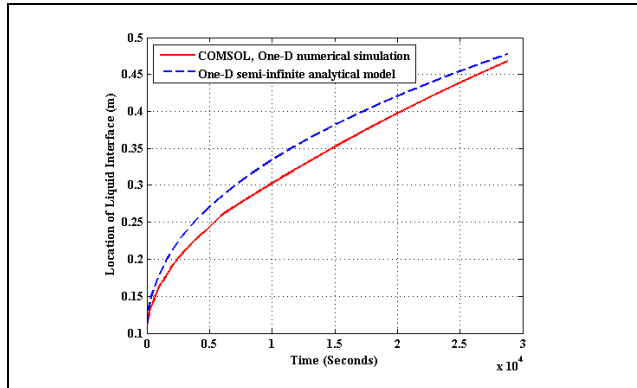
Figure 4-17. Interface movement during melting process as predicted by 1-D simulations and analytical solution.
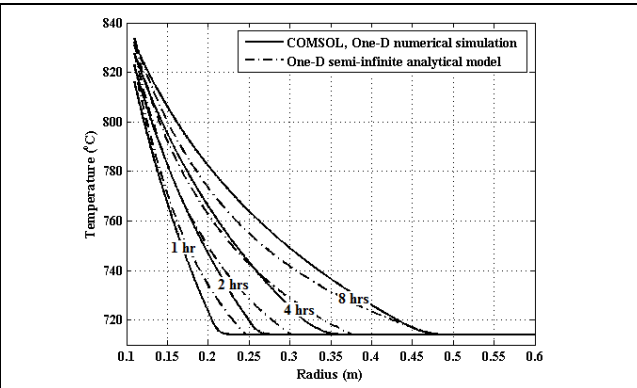
Figure 4-18. Temperature distributions at various locations with times during melting process obtained from COMSOL simulations and analytical solution.
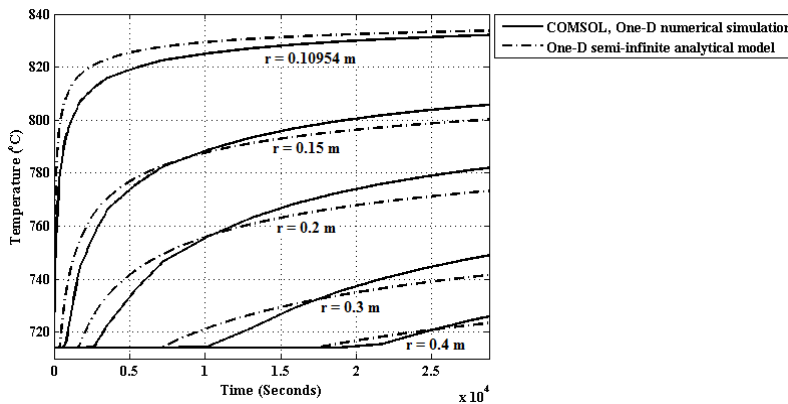
Figure 4-19. Temperature profiles at various locations.

4.4. 2-D heat transfer simulations

An 8-in. diameter HTF pipe for the LHTES was considered for 2-D modeling. The HTF flow velocity inside the pipe was 0.5 m/s. The HTF inlet temperature was maintained at 850 °C while the initial PCM temperature was 714 °C. Front movement and temperature profiles were evaluated over eight hours for the charging process. Figure 4-20 shows the location of the liquid/solid interface in the foam/PCM during the charging process. As compared to the 1-D analysis, the 2-D simulations indicated the faster movement of the interface (Table 4-4). Therefore, more PCM was melted after eight-hour energy storage process based on the 2-D numerical simulation.

Figure 4-21 displays the temperature variations in the PCM. The temperature profiles for 2-D simulations are also higher than the results from 1-D analysis. Thus, the 1-D simulation is conservative compared to the 2-D results. The interface movement and temperature profile plots of the two-dimensional simulations are at the 5 m height of the PCM (the total height of PCM is 10 m).

Figure 4-22 shows the 2-D liquid/solid interface movement inside the foam/PCM for the charging process. Since the HTF inlet and outlet temperatures do not vary significantly for the flow velocity of 0.5 m/s in an 8-in. diameter pipe, there is no significant difference for the interface locations between the top and the bottom of the tank.

Figure 4-20. Comparison of the melt interface movement in foam/PCM as predicted from simulations and analysis.

Table 4-4. Location of liquid interface in foam/PCM after 8-hour charging process.

	HTF Temp. 850 ˚C
COMSOL, 1-D numerical simulation	0.468 m
COMSOL, 2-D numerical simulation	0.581 m
1-D semi-infinite analytical model	0.477 m

Figure 4-21. Temperature profiles at various locations.
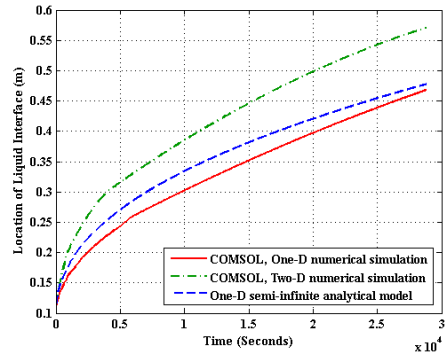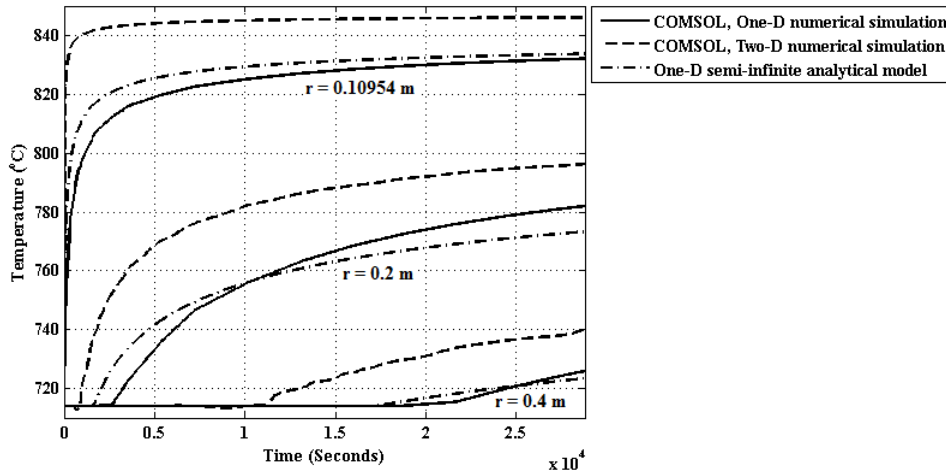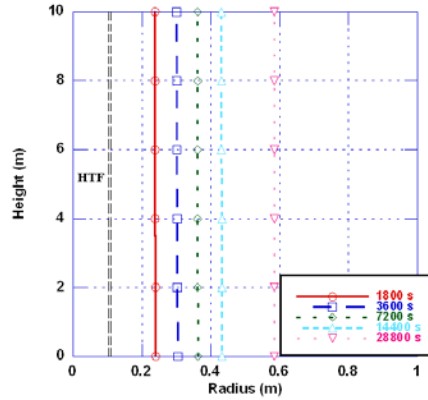
Figure 4-22. 2-D interface movement in foam/PCM of LHTES (HTF inlet from bottom).

In summary, although there are some differences between the 2-D and 1-D simulation results, the latter gives the estimated results of the thermal performance in the PCM storage system. Based on the 2-D heat transfer analysis, the 1-D simulation results are conservative. The actual PCM storage system would have better thermal performance in terms of charging/discharging than predicted by 1-D analysis.

4.5. 2-D heat transfer simulations incorporating anisotropy and temperature effects

In general, graphite foam has anisotropic thermal properties. Thermal conductivity is highest in the foam "rise" direction as compared to the other two orthogonal directions. In the plane perpendicular to rise direction, thermal conductivity is isotropic. Therefore, it is prudent to orient the foam/PCM in the LHTES in such a way that the highest thermal conductivity direction is in the radial direction of the pipe. Thus, the thermal conductivities of the graphite foam-MgCl$_2$ composition in the cross section of the PCM domain, as a function of temperature, can be given as [22]:

$$k_{comp\_Y} = 58.5 - 0.0313 \times T \text{ (W/m-K)} \ (T \text{ in K})$$ (4-2)

$$k_{comp\_X} = k_{comp\_Y} / 2 \text{ (W/m-K)}$$ (4-3)

Equations (4.2) and (4.3) are applicable for both solid- and liquid-state PCM. The thermal conductivity in the x-direction is half of the value of the y-direction. The specific heat of the PCM also varies with temperature, as follows:

$$c_{p\_composite\_solid} = 650.24 + 0.5317T - 1.3444 \times 10^{-4} T^2 \text{ (J/kg-K)} \ (T \text{ in K})$$ (4-4)

$$c_{p\_composite\_liquid} = 752.5 + 0.389T - 1.3444 \times 10^{-1} T^2 \text{ (J/kg-K)} \ (T \text{ in K})$$ (4-5)

The density of the PCM was assumed to be constant, 1580 kg/m^3, during the energy storage process, and the latent heat of the graphite foam-MgCl$_2$ composition was

407.6 kJ/kg. The initial PCM temperature was also at 714 °C. The diameter of the HTF pipe was 8 in. The HTF temperature was maintained at 850 °C, and the flow velocity at 0.5 m/s.

The 2-D heat transfer simulation results in the cross section of the PCM domain are presented in Figure 4-23. The melt front boundary after the 8-h energy storage process is skewed. Since the thermal conductivity in the *y*-direction is larger than that in the *x*-direction, the liquid/solid interface moves faster in the y-direction. After the eight-hour charging process, the interface in the *y*-direction moved to about 0.6 m, while the interface in the *x*-direction moved to approximately 0.5 m. Figure 4-24 shows the corresponding temperature profile in the foam/PCM after the eight-hour energy storage process. From the temperature contour, the temperature also spreads further in the *y*-direction because of the higher effective thermal conductivity in the *y*-direction.
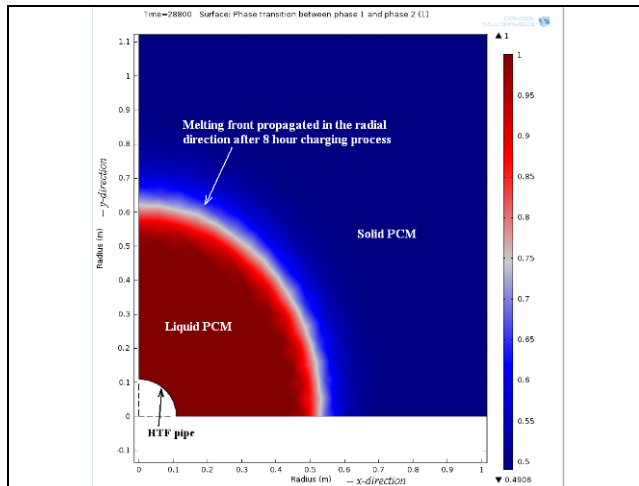
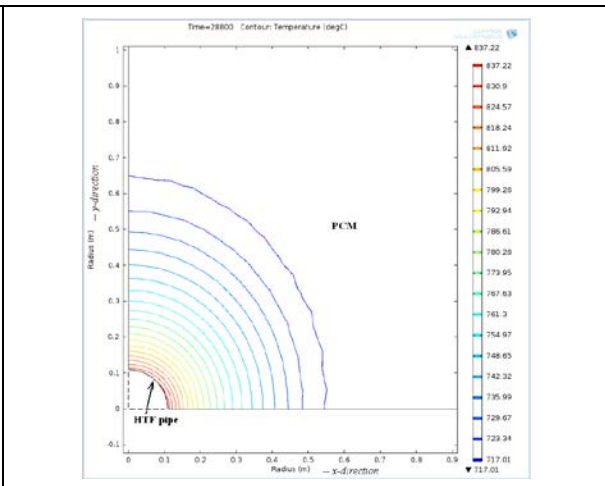|	
Figure 4-23. Location of melting front in PCM after 8-h charging process.	Figure 4-24. Temperature contour in foam/PCM after 8-h charging process.

5. LHTES System Efficiency

Exergy can be used to define the useful energy obtainable in a thermal system, and exergy analysis can help the performance assessment and optimization of such a system. Performance of the proposed LHTES system can be optimized by increasing its exergy efficiency [23].

The LHTES system configuration used for analysis is sketched in Figure 5-1. The foam/PCM is contained in a large tank through which HTF flows through vertical pipes. One such pipe, in the central region of the tank, is shown in Figure 5-1. Heat transfer fluid flows from the bottom to the top, and the height of the HTF pipe is assumed as 10 meters. The outer boundary of the thermal system is assumed to be well insulated. The outer diameter of the HTF pipe is 0.060 m (2.375 in.), and the thickness of the pipe is 2.77 mm. The pipe is made of Inconel alloy 617.
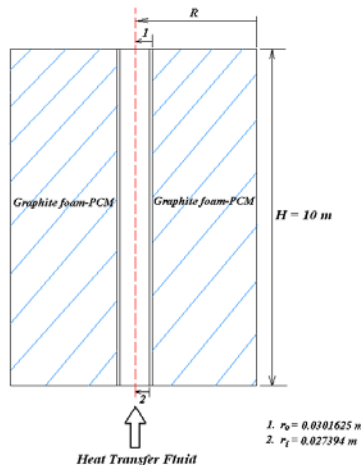
Figure 5-1. Graphite foam/PCM LHTES system

In the present analysis, currently available materials were chosen for the PCM and HTF. Magnesium chloride ($MgCl_2$) was used as the PCM, and liquid LiF-NaF-KF (46.5-11.5-42 mol.%) (FLiNaK) was used for the HTF. Properties of the graphite foam-$MgCl_2$ composition, FLiNaK, as well as the HTF pipe are given later in Table 5-2.

5.1. Exergy analysis

In this study, three methods were used to determine the exergy efficiency of the latent heat storage system. Equations to calculate the exergy efficiency are given as follows: [20-27]. Note that the nomenclature used in this section is listed at the end of Section 3.

5.1.1. Overall exergy efficiency

The symbol $\psi_{overall}$ is the overall exergy efficiency of the storage system [23-26], including the efficiency of both the charging process and the discharging process, which is defined by Eq. (5.3). The overall exergy efficiency involves the exergy input/output of both the HTF and PCMs. T_a is the environment temperature, which was taken as 20 °C, and T_m is the melting point of the PCM, which is 714 °C for $MgCl_2$. $T_{HTF,out}$ is the outlet

temperature of the HTF, which varies with the time during the charging/discharging process. In order to reduce the complexity of the calculation model, this study used the average outlet HTF temperature for charging and discharging processes. Furthermore, $T_{PCM,init}$, the initial temperature of PCM before the charging process, was taken as 550 °C. $T_{PCM,char}$ is the final temperature of PCM after the charging process while $T_{PCM,dis}$ is the final temperature of PCM after the discharging process. Since $T_{PCM,char}$ and $T_{PCM,dis}$ vary in the radial direction in the PCM, the average temperatures in the radial direction were also used in this study. Under these parametric conditions, the commercial computer code COMSOL was used to determine the values of $T_{HTF,out}$, $T_{PCM,char}$, and $T_{PCM,dis}$ for the exergy calculations.

$$\psi_{char} = Ex_{PCM\_stored} \big/ Ex_{HTF\_char} \tag{5-1}$$

$$\psi_{dis} = Ex_{HTF\_dis} \big/ Ex_{PCM\_supplied} \tag{5-2}$$

$$\psi_{overall} = \psi_{char}\psi_{dis} \tag{5-3}$$

where

$$Ex_{PCM\_stored} = Mi_{sl}\left(1 - \frac{T_a}{T_m}\right) + Mc_{PCM,s}\left[(T_m - T_{PCM,init}) - T_a \ln\left(\frac{T_m}{T_{PCM,init}}\right)\right]$$
$$+ Mc_{PCM,l}\left[(T_{PCM,char} - T_m) - T_a \ln\left(\frac{T_{PCM,char}}{T_m}\right)\right] \tag{5-4}$$

$$Ex_{PCM\_supplied} = Mi_{sl}\left(1 - \frac{T_a}{T_m}\right) + Mc_{PCM,s}\left[(T_m - T_{PCM,dis}) - T_a \ln\left(\frac{T_m}{T_{PCM,dis}}\right)\right]$$
$$+ Mc_{PCM,l}\left[(T_{PCM,char} - T_m) - T_a \ln\left(\frac{T_{PCM,char}}{T_m}\right)\right] \tag{5-5}$$

$$Ex_{PCM\_char} = \rho_{HTF} A V c_{HTF}[(T_{HTF,in} - T_{HTF,out}) - T_a \ln(T_{HTF,in}/T_{HTF,out})]t \tag{5-6}$$

$$Ex_{PCM\_dis} = \rho_{HTF} A V c_{HTF}[(T_{HTF,out} - T_{HTF,in}) - T_a \ln(T_{HTF,out}/T_{HTF,in})]t \tag{5-7}$$

5.1.2. Round-trip efficiency
The symbol ψ_{round} is the round-trip efficiency [23,24,26], which is determined from the ratio of the discharging HTF recovered exergy and the charging HTF supplied exergy.

$$\psi_{round} = Ex_{HTF\_dis} \big/ Ex_{HTF\_char} \tag{5-8}$$

5.1.3. Round-trip exergetic efficiency
Equation (3.9) is the round-trip exergetic efficiency, ε [27], defined by the ARPA-E proposal [27]. This round-trip exergetic efficiency is based on the temperature

differences and ratios of HTF inlet and outlet temperatures during the charging and discharging processes.

$$\varepsilon = \frac{\Delta G_{dis}}{\Delta G_{char}} = \frac{\left\{c_{HTF}\left[(T_{HTF,out} - T_{HTF,in}) - T_a \ln\left(\frac{T_{HTF,out}}{T_{HTF,in}}\right)\right]\right\}_{dis}}{\left\{c_{HTF}\left[(T_{HTF,in} - T_{HTF,out}) - T_a \ln\left(\frac{T_{HTF,in}}{T_{HTF,out}}\right)\right]\right\}_{char}} \tag{5-9}$$

Equations (5-3), (5-8), and (5-9) were used to calculate the exergy efficiency of the latent heat storage system. The system is the PCM/graphite foam tank and the HTF in vertical pipes described above. The results of the analyses are presented later.

5.2. Exergy calculation procedure

To conserve pumping power in the CSP electric plant, the HTF flow was restricted to the low end of the turbulent range. For the charging process, the HTF velocity was set to 0.15 m/s. The inlet HTF temperature during the charging process was set to 800 °C or 850 °C in the various calculations. The operation time for charging was 8 h, and the radius of the PCM, R, was determined at the end of that time. After an 8 hours charging, all of the PCM is melted.

The discharging process occurs over a 12-h period. During the discharge, the HTF flow rate and inlet temperatures during charging/discharging were adjusted such that the liquid remained turbulent, and the total energy stored in PCMs during the previous charging process was retrieved. The outlet temperatures were determined from COMSOL 2-D simulation.

5.3. LHTES system efficiency with single PCM and cascading PCMs

Table 5-1 gives the results of the exergy efficiency calculations for different situations utilizing one or two PCMs. As a compromise between low pumping power and low capital cost, the HTF pipes were taken at a nominal diameter of 2 in. The charging HTF inlet temperature was set at 850 °C for Case 1 to Case 3 and 800 °C for Case 4. In all four cases, the total amount of energy stored in the PCMs was similar. For the cascading systems of Cases 2-4, it was assumed that half of the volume of the system is filled with $MgCl_2$, and the other half of the volume is filled with a different PCM. The exergy efficiencies from the three calculations discussed previously are presented in Table 5-1 for each of these four cases.

Case 1 is a single PCM storage system. The fluid velocity for the discharging process is 0.1 m/s based on 8 hour charging and 12 hour discharging. The round-trip exergetic efficiency, ε, is approximately 97%, as given in Table 5-1, and the three efficiency calculations produced similar results within 1%. This efficiency level for the $MgCl_2$ based

latent heat storage system under the conditions for Case 1 is quite high, above the target value of 95% for LHTES systems.

Table 5-1. Exergy analysis results.

	Overall exergy efficiency, $\psi_{overall}$	Round-trip efficiency, ψ_{round}	Round-trip exergetic efficiency, ε (defined by the ARPA-E proposal)
Case 1 PCM: $MgCl_2$ 8-h charging, inlet temp. 850 °C, average outlet temp. 781.1 °C, V_{HTF_char} = 0.15 m/s 12-h discharging, inlet temp. 536 °C, average outlet temp. 611.0 °C, V_{HTF_dis} = 0.1 m/s	98.1 %	97.4 %	97.4 %
Case 2 Cascading PCMs: NaCl and $MgCl_2$ 8-h charging, inlet temp. 850 °C, average outlet temp. 788.9 °C, V_{HTF_char} = 0.15 m/s 12-h discharging, inlet temp. 539 °C, average outlet temp. 603.7 °C, V_{HTF_dis} = 0.1 m/s	93.9 %	94.5 %	94.5 %
Case 3 Cascading PCMs: NaCl and $MgCl_2$ 8-h charging, inlet temp. 850 °C, average outlet temp. 788.9 °C, V_{HTF_char} = 0.15 m/s 12-h discharging, inlet temp. 537 °C average outlet temp. 604.2 °C, V_{HTF_dis} = 0.095 m/s	92.2 %	93.2 %	98.1 %
Case 4 Cascading PCMs: $MgCl_2$ and LiCl 8-h charging, inlet temp. 800 °C average outlet temp. 733.2 °C, V_{HTF_char} = 0.15 m/s 12-h discharging, inlet temp. 472 °C, average outlet temp. 545.0 °C, V_{HTF_dis} = 0.1 m/s	90.2 %	95.1 %	95.1 %

Cases 2 to 4 are for cascading PCMs with higher and lower melting temperatures than $MgCl_2$. Cases 2-3 are for the cascading PCMs using NaCl and $MgCl_2$, where the melting point of NaCl is 800 °C, which is higher than that of $MgCl_2$. (In Case 4, the second PCM has a lower melting point than $MgCl_2$.) The properties of NaCl used in the exergy calculations are given in Table 5-2. The system operating condition for Case 2 are the same as that for Case 1. According to the calculations, the exergy efficiency is very high for the NaCl and $MgCl_2$ cascading system, though it is slightly lower than the single $MgCl_2$ PCM system. This slight reduction may be due to the higher melting point of NaCl or the fact that it does not completely melt during the charging process. Controlling the amount of PCM material could mitigate the latter effect.

For Case 3, the discharging HTF velocity was reduced from 0.1 m/s to 0.095 m/s to decrease the mass flow rate while maintaining turbulent flow.   The lower fluid velocity caused a larger temperature difference between the inlet and the outlet of the HTF. Consequently, the round-trip exergetic efficiency was improved for the lower discharging fluid velocity of Case 3.

Case 4 is similar to Case 2, but uses LiCl (with a melt temperature of 610 °C) instead of NaCl (with a melt temperature of 800 °C). In this case, the HTF inlet temperature was adjusted to maintain the total heat storage similar to Cases 1-3. Properties of the graphite foam-LiCl composition are given in Table 5-2, and the exergy efficiency results of Table 5-1 are still very high with the round-trip exergetic efficiency of the system at approximately 95%.

Table 5-2. Properties of graphite foam-NaCl and graphite foam-LiCl compositions.

	Density (kg/m^3)	Thermal conductivity (W/m-K)	Solid heat capacity (J/kg-K)	Liquid heat capacity (J/kg-K)	Latent heat of fusion (kJ/kg)
Graphite foam-NaCl composite	2160[a]	25	931[d]	1200[c]	432[c]
Graphite foam-LiCl composite	2068[e]	25	1132[d]	1545[c]	427[c]

[a]B. E. Poling et al. (2008); [b]B. Zalba, et al. (2003); [c]G. Janz (1979); [d]M. Chase (1998); [e]J. Dean, et al. (1999).

5.4. Optimum operating conditions for high exergy efficiency

The results given in Table 5-1 show high exergy efficiencies for all three methods used and all four parametric cases studied. The exergy efficiencies were almost all above the CSP plant LHTES target of 95%. The efficiency was high for LHTES systems with and without cascading. Other parameters were changed when cascading was introduced, and an actual plant situation offers the ability to optimize these parameters. However, when entire plant analyses are performed, it would be desirable to alter some of the parameters used in this study. In such a circumstance, one should recognize the parameters most important to achieving high exergy efficiency in the LHTES system.

The results presented in this study show that a lower HTF velocity can help to increase the temperature difference between inlet and outlet HTF, thus increasing the exergy efficiency of the storage system. Nevertheless, a low HTF velocity will slow the energy storage/retrieval process inside the PCM. The current Reynolds number in the HTF pipe is between 3000 and 4000, just above the minimum Reynolds number for turbulent flow. Care must be taken not to reduce the HTF velocity below the threshold for turbulent flow. Furthermore, using cascading PCMs can also help to keep the storage system at high exergy efficiency. However, proper PCMs and quantities should be chosen for the storage system to ensure that the different melting point PCMs completely melt during the charging process. To facilitate this condition, the difference of the melting points among cascading PCMs should not be large. Finally, the exergy efficiency of an LHTES system is quite sensitive to the HTF temperature difference between the inlet and the outlet of the system. Smaller temperature differences are desirable for the charging process compared to the discharging process. Smaller temperature differences

between the HTF inlet temperature and the melting point of PCMs are also beneficial but not to the same extent.

In summary, thermal analysis and modeling of a full-scale LHTES system based on the graphite foam/PCM composite can fulfill the SunShot's performance targets. This task fulfilled Milestone 1.1.

Nomenclature used for this section

A	Cross section area of heat transfer fluid pipe (m^2)
c_{HTF}	Heat capacity of heat transfer fluid (J/kg·K)
$c_{pcm,l}$	Heat capacity of liquid state PCM (J/kg·K)
$c_{pcm,s}$	Heat capacity of solid state PCM (J/kg·K)
Ex_{HTF_char}	Exergy supplied from HTF during charging process (J)
Ex_{HTF_dis}	Exergy retrieved of HTF during discharging process (J)
Ex_{PCM_stored}	Exergy stored in PCM during charging process (J)
$Ex_{PCM\_supplied}$	Exergy supplied by PCM during discharging process (J)
G	Gibbs free energy (J)
H	Height of the heat transfer fluid pipe (m)
i_{sl}	Latent heat of fusion of PCM (J/kg)
M	Mass of PCM (kg)
R	Radius of PCM (m)
r_i	Inner radius of the heat transfer fluid pipe (m)
r_o	Outer radius of the heat transfer fluid pipe (m)
T_a	Environment temperature (K)
$T_{HTF,in}$	Heat transfer fluid inlet temperature (K)
$T_{HTF,out}$	Heat transfer fluid outlet temperature (K)
T_m	Melting point of PCM (K)
$T_{PCM,char}$	Final temperature of PCM after charging process (K)
$T_{PCM,dis}$	Final temperature of PCM after discharging process (K)
$T_{PCM,init}$	Initial temperature of PCM before charging process (K)
t	Time (Seconds)
V	Flow velocity (m/s)
V_{HTF_char}	HTF velocity during charging process (m/s)
V_{HTF_dis}	HTF velocity during discharging process (m/s)

Subscripts

$char$	Charging process
dis	Discharging process

Greek symbols

ε	Round-trip exergetic efficiency (Defined by the ARPA-E Proposal)
ρ_{HTF}	Density of HTF (kg/m^3)
ψ_{char}	Exergy efficiency for charging process
ψ_{dis}	Exergy efficiency for discharging process
$\psi_{overall}$	Overall exergy efficiency
ψ_{round}	Round-trip efficiency

6. Graphite Foam: Properties and Characterizations

Graphite foams at various densities are now manufactured in bulk by several companies, such as POCO Graphite and Graftech. For the present investigation, graphite foams were obtained from Graftech. Three sets of graphite foams have been investigated with nominal densities of ~ 0.1, 0.2, and 0.4 g/cc. In general, the density variations from sample to sample could be ±10%. Hence, from hereon, these foams will be referred to as low density (LD), medium density (MD), and high density (HD). Nominal properties of the three foam densities are listed in Table 6-1. Figure 6-1 shows a typical bulk and a high magnification image of a MD foam.

Foam Type	Foam Density (g/cc)	Solid Volume Fraction (%VF)	Pores/in. (PPI)	Windows/in. (WPI)	Bulk Thermal Conductivity, x-y plane (W/m-K)	Bulk Thermal Conductivity, z direction (W/m-K)
low	0.10-0.15	~6	24-41	~26-37	~25	~50
medium	0.20-0.25	~11	30-40	~23-31	~40	~80
high	0.45-0.55	~22	19-33	~8-20	~60	~120

Table 6-1. Properties of graphite foams with varying densities [22].
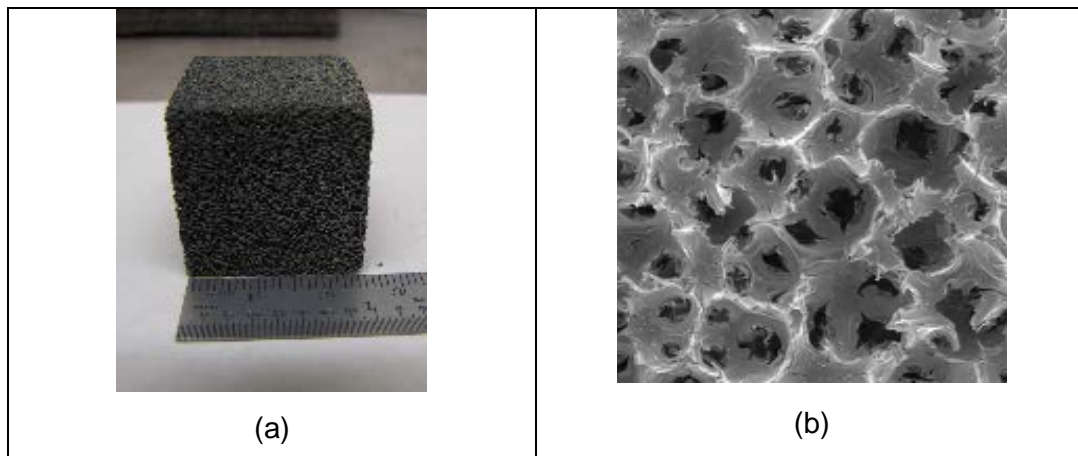

Figure 6-1. (a) Bulk sample of 0.2 g/cc density and (b) microstructure of the 0.2 g/cc density foam (mag. 20X).

6.1. Coating of graphite foam

The key reasons of coating the graphite foams are four-fold: (a) protect the graphite from oxidation and improve environmental durability, (b) improve mechanical reliability, (c) enhance the wettability of the graphite foam for PCM infiltration, and (d) enhance bonding and integration capability. In the proposed LHTES system, graphite will not be exposed to oxygen since the system will be purged out and back filled with an inert gas.

Nevertheless, since the LHTES system will be operating at temperatures >700 °C, oxidation could be an issue if there is any residual oxygen in the system.

In this project, two types of coating approaches were utilized for coating of foams: (a) chemical vapor reaction (CVR) and (b) pre-ceramic polymer-based coatings. Down selection of the coating process will be made based on the coating properties, performance, scalability, and cost.

6.1.1. Chemical vapor reaction

The SiO vapor phase infiltration/reaction approach was used to form thin SiC coatings on graphite foams. For the production of SiO gas, commercially available Patinal® SiO pellets were used. These pellets have congruent vaporization, and by optimizing infiltration temperature and time, one can control the extent of infiltration. The reaction of the foam with the SiO vapor forms SiC. Process optimization studies were carried out earlier at 1300-1500 °C for various infiltration/reaction times.

Figure 6-2(a) shows the schematic of the test set-up. Measured amounts of SiO pellets were confined in a graphite fixture placed within a graphite crucible with a lid. The foam specimen/preform was placed on top of the fixture so that the infiltration can occur in the axial direction. The processing condition of 1450 $^{\circ}$C for 30 min was used for coating. Typical foam sizes for these experiments were 1 x 1 x 1 in. and 1 x ½ x ½ in. Figure 6-2(b) is a photograph of coated foam pieces. Coated samples were analyzed by SEM/EDS. Furthermore, XRD was performed to verify the phases present in all of the coated samples.
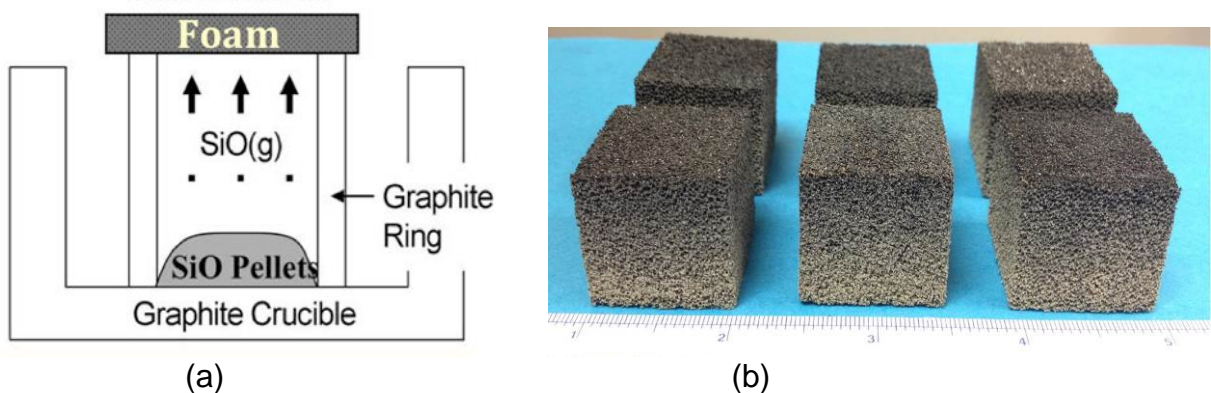

Figure 6-2. (a) Schematic of foam coating set-up and (b) photograph of various foams coated using CVR process.

The SEM micrographs of CVR SiC-coated specimens of varying density are given in Figure 6-3(a-c). These micrographs show that the original microstructure of the porous foam is retained after the coating.

X-ray diffraction analysis of as-received and CVR coated foams was also carried out to identify different phases and crystallinity. Data were gathered on a D8 Advance diffractometer using Cu-Kα radiation. Figure 6-4(a) shows the XRD scans of foam samples of different densities (low, medium, and high) with the graphite (002) peaks truncated. These patterns show good crystallinity, indicating excellent conversion of

carbonaceous materials to graphitic structure. Figure 6-4(b) shows the graphite (100) peak, indicating the strong preferreed orientation of the graphite phase in all the samples.

X-ray diffraction analysis of CVR SiC-coated foams was also carried out to identify the phases. Figures 6-5(a,b) show the diffraction patterns of coated foam samples. Figure 6-5a shows the graphite phase where (002) peaks have been truncated.
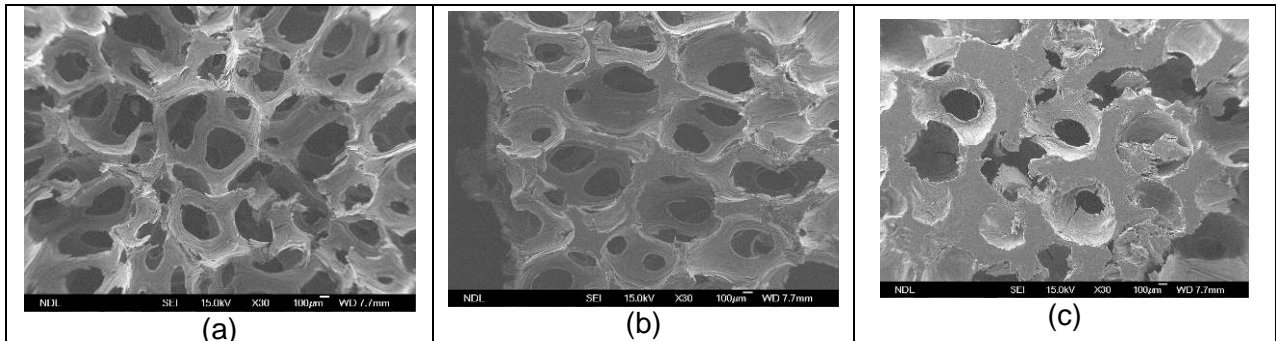

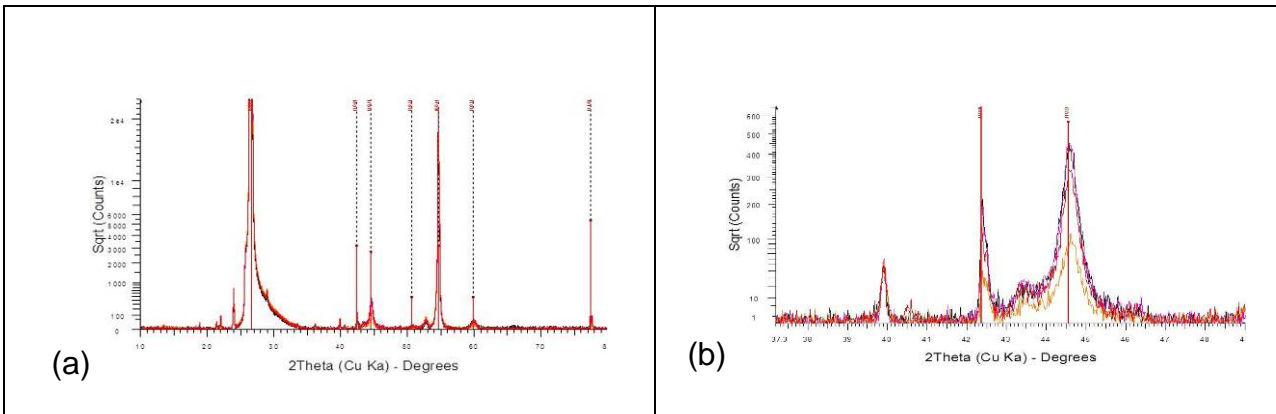Figure 6-3. SEM analysis of coated foams samples of (a) low, (b) medium, and (c) high densities.

Figure 6-4. (a): XRD scans of foam samples of different densities graphite (002) peak truncated and (b) XRD pattern showing graphite (100) peak indicating the strong preferred orientation in all samples.

---- Low density
---- Medium density
---- High density

The SiC-3C peaks in coated samples are shown in Figure 6-5(b) for all SiC peaks; the order of peak intensity is low density > medium density > high density. Because this order is consistent across all peaks, preferred orientation is ruled out, and the differences can be attributed to the amount of graphite converted to SiC, relative to the other samples.

Figure 6-6 shows the SEM image of uniform SiC coating on the graphite foam ligaments, as confirmed by the line scan across the foam ligament. The silicon peaks observed in the analysis coincide with the coating regions (bright) on the SEM image.

A number of LD, MD, and HD samples (1 x1 x 1 in.) were coated for the mechanical property studies and the preliminary test results are discussed below. In addition, 1 x 0.5 x 0.5 in. samples were coated for the oxidation studies.
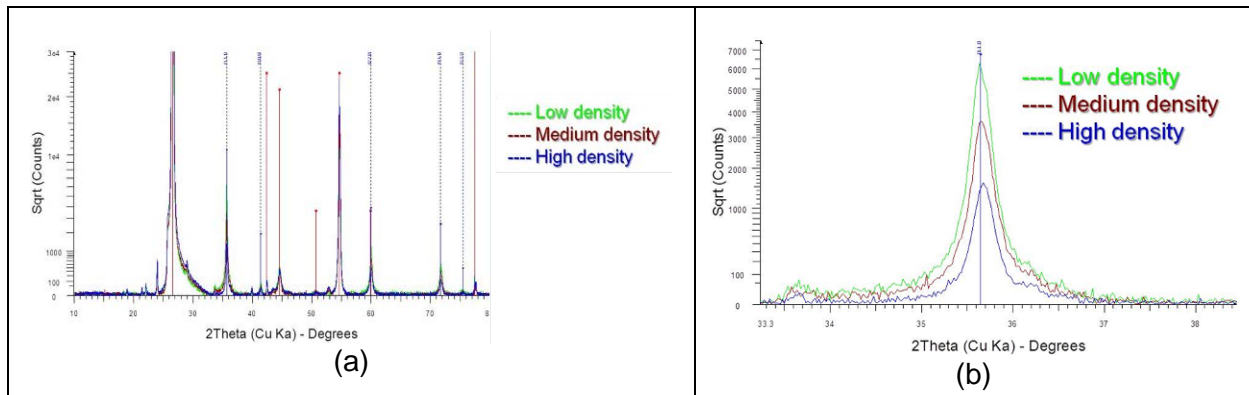

Figure 6-5. (a) XRD scans of CVR SiC-coated foam samples of different densities graphite (002) peak truncated and (b) XRD pattern showing SiC-3C (111) peak.
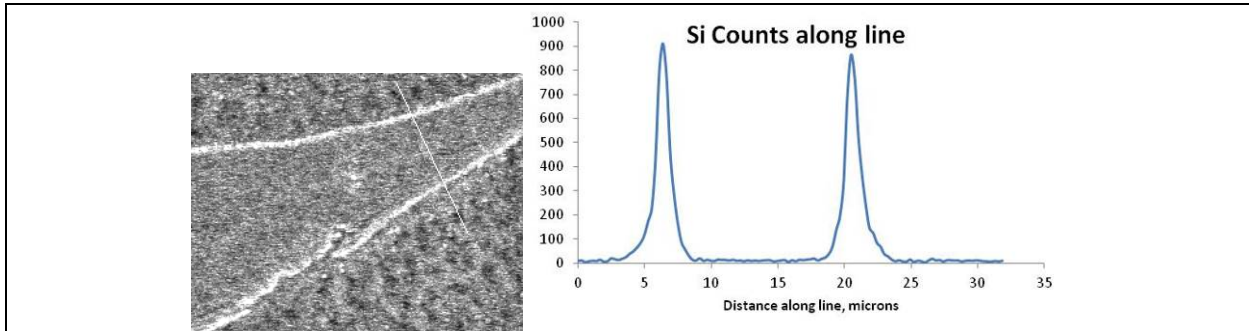

Figure 6-6. Scanning electron microscope image showing the SiC coating on the graphite ligaments (confirmed by electron dispersive analysis).

6.1.2. Pre-ceramic polymer derived SiC coating (PDC-SiC coating)
The PDC SiC process was initiated by dissolving polycarbosilane (PCS) polymer in high pressure liquid chromatography (HPLC) grade toluene in order to make a clear solution. The graphite foam specimens were dipped in the solution and then cured at 100 °C for 1 hour and then at 150 °C for 1 hour. After the appropriate number of dip/cure steps, the specimens were pyrolyzed at 1000 °C in argon. Specimen weight gains, at most 10%, were minimized by appropriately adjusting the concentration of the PCS in the toluene. A concern arose with the quality and thoroughness of the PDC SiC coating when using only a one-dip process, as was the case for the earliest specimens. Hence, all specimens have used multiple dip/cure steps prior to the final pyrolysis to assure maximum and complete coverage of graphite ligaments.

6.2. Mechanical properties

The compressive tests were based on the ASTM C1674 standard. Key points of the standard include a specimen size with at least 10 pores per side and a load rate that allows the maximum stress to be reached between 30 and 50 seconds. All measurements were made along the "with rise" direction. Tests were conducted on an Instron machine with a laser-equipped strain monitoring system.

Compressive data for graphite foams (with varying densities) coated by CVR or PDC process are presented in Table 6-2. For the MD foam, a sizable increase in strength was observed for both coating processes. For a typical LHTES system, there are pressure loads in the form of normal compressive forces: hence, the importance and dominance of the compressive strength. Table 6-3 shows the tensile strengths for the PDC-coated graphite foam as a function of foam density.

Table 6-2 Compressive strengths of coated- and CVR-coated foam samples.

Foam Type	Coating	Avg. Density (g/cc)	Ave. Compressive Strength [kPa (psi)]	Percent Change
Low Density	None	0.11	93.9 (13.6)	
Low Density	CVR SiC	0.10	122 (17.7)	29.9
Medium Density	None	0.23	291 (42.3)	
Medium Density	CVR SiC	0.23	514 (74.5)	76.2
Medium Density	PDC SiC	0.25	419 (60.8)	44.0
High Density	None	0.45	1282 (186)	
High Density	CVR SiC	0.37	1420 (206)	11.0
High Density	PDC SiC	0.45	1409 (204)	10.0

* Density and strength averages exclude the outlier point with 0.6 g/cm^3 density.

Table 6-3. Uncoated and PDC SiC-coated with-rise (WR) tensile strengths of PDC-coated foam.

Foam Type	Coating	Ave. Density (g/cm^3)	Ave. Tensile Strength [kPa (psi)]	Percent Change
Low Density	None	0.11	193 (28.1)	
Medium Density	None	0.22	844(122)	
Medium Density	PDC SiC	0.29	1209 (175)	43
High Density	None	0.43	2009 (291)	
High Density	PDC SiC	0.45	2950 (428)	47

Through mechanical characterization testing of the uncoated foams and the various coated foams (CVR SiC, single or multi-dipped PDC SIC), it was shown that the mechanical properties were enhanced for all of the SiC\-coated foams. In particular, a 44% increase in compressive strength and a 43% increase in tensile strength were demonstrated by the medium density (~0.22 g/cm^3), 3-dip (the favored number of dip/cure cycles), PDC SiC-coated foams as compared to the uncoated foam values. The results appeased the >10% compressive strength improvement, as well as offering increased tensile strength as a bonus. Note that for a typical TES system, there are pressure loads in the form of normal compressive forces, hence, the importance and dominance of the compressive strength. The coating is meant to provide multiple functions including oxidation and corrosion resistance in case of unexpected exposure to oxygen.

6.3. Thermal diffusivity and conductivity

The transport behavior was assessed via thermal diffusivity experiments followed by the calculation of the thermal conductivity for uncoated and SiC-coated graphite foams. The focus of the measurements was on medium and high density foams. A schematic of the set-up is shown in Figure 6-7. A commercial pulse thermography system was used during the two-sided tests where heat was applied on one side using photographic flash lamps, and the temperature rise was measured on the back side using an infrared camera. The diffusivity is calculated using the Parker equation, defined in Figure 6-7, where α is the thermal diffusivity, a is the sample thickness in the direction of heat flow, and t_{50} is the half life to achieve the maximum back-side temperature. The thermal conductivity is obtained by multiplying the diffusivity by the density, ρ, and constant pressure specific heat, c_p. An in-house program was written to calculate the diffusivity for each pixel of the observed specimen, thus providing a 2D image of diffusivity.

Pulsed Thermography Setup

Parker expression: $\alpha = 0.139 a^2/t_{50}$ $k = \alpha \rho c_p$

C_p (graphite) = 710, C_p (SiC) = 750 J/KgK

(a)   (b)
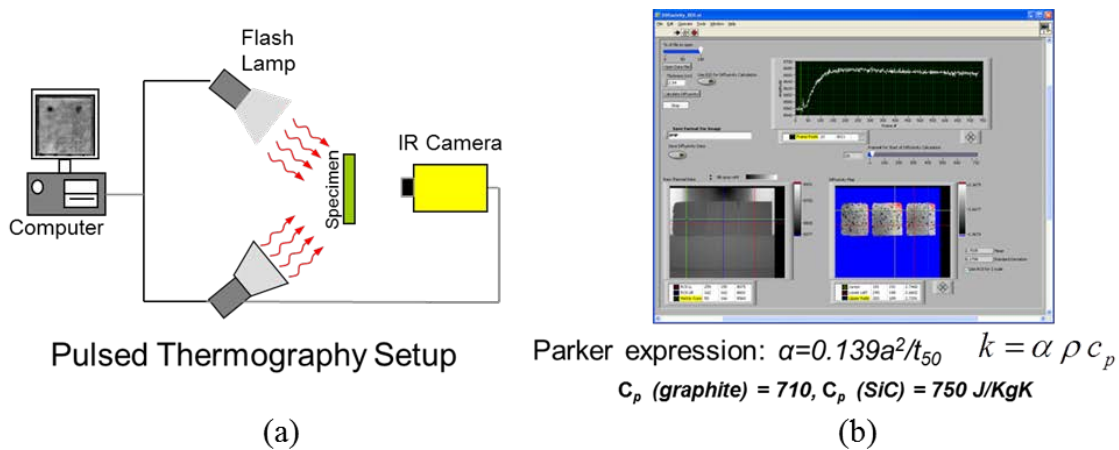
Figure 6-7. (a) Set-up for thermal diffusivity experiments and (b) image of in-house software for calculating diffusivity.

The room temperature data in Table 6-4 indicate essentially no change in thermal diffusivity values or in the associated calculated conductivities (less than 2 percent, within the statistical noise) as a result of the CVR SiC coating for the medium density foam. The high density foams showed a small drop in the diffusivity and conductivity values of 7.5%, which is still reasonable. For each density, measurements were made before and after using the same specimens (14 specimens for the medium density and 16 for the high density). Because the CVR is a conversion process, there was negligible change in the density values. For PDC-coated samples the conductivity showed a larger decrease of 10-15%. However, the change in thermal diffusivities was much lower (<8%). Note that the conductivity calculation, which is the product of diffusivity, density, and specific heat simply exaggerates the density influence; hence, the comparison of the thermal diffusivities is the fairer comparison (again, showing a minimal loss due to the PDC SiC coating).

In summary, minimal (e.g., at the high density) to no difference (e.g., at the medium density) was observed in the thermal properties between uncoated and coated samples measured in the WR direction.

Table 6-4 Thermal diffusivity and conductivity data for uncoated and SiC-coated medium and high density foams in WR direction.

Foam Type	Coating	Ave. Density (g/cm^3) (stnd dev)	Thermal Diffusivity (cm^2/sec) (stnd dev)	% Change Diff.	Conductivity (w/m-K) (stnd dev)	% Change Cond.
Medium Density	None	0.25 (0.0046)	2.76 (0.137)		48.2 (2.48)	
Medium Density	CVR SiC	0.25 (0.0042)	2.63 (0.156)	-4.7	47.4 (2.71)	-1.6

|						
Medium Density	PDC SiC	0.227 (NA)	2.70 (NA)	-2.2	43.3 (NA)	-10
High Density	None	0.46 (0.008)	3.81 (0.235)		126 (8.07)	
High Density	CVR SiC	0.47 (0.005)	3.60 (0.190)	-5.5	121 (6.20)	-4.0
High Density	PDC SiC	0.43 (NA)	3.51 (NA)	-7.8	107 (NA)	-15

* Used C_p=0.710 J/g-K in Parker equation since mass fraction of SiC is assumed to be extremely low.

6.4. Flow/pressure drop measurements

Due to the lack of pressure drop data for this porous graphite, room temperature flow tests were conducted using water as the medium to serve as a preliminary assessment (coincidentally, many salts have similar viscosities at high temperatures). A flow facility was assembled, and tests were run and completed for three densities of the uncoated foams. The cylinder foam samples, 2.5 cm dia. x 10 cm length (1 in. x 4 in.), were held in steel tubes with 5 pressure measurement ports while water was pumped using a 1-horsepower DC variable speed motor. Figure 6-8(a) shows an image of the flow facility set-up while Figure 6-8(b) displays the plots of pressure drop versus flow velocity. The curves behave as expected, with the pressure drop being largest for the HD material. Note that previous experience with Ni- and Cu-coated foams showed minimum to no changes in the pressure drop behavior as a result of the thin coatings.

(a)
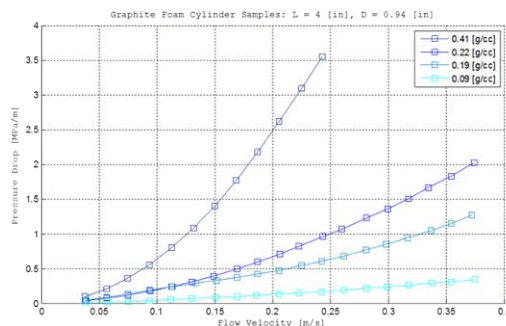
(b)

Figure 6-8. (a) Water flow test set-up and (b) pressure drop curves displayed as pressure drop versus flow velocity for multiple densities of uncoated foam.

Similar to CVR coatings, the multiple dip PDC SiC coating did not negatively influence the pressure drop behavior, as witnessed by the test data for 1 dip, 2 dip, and 3 dip PDC SiC-coated specimens. The pressure drop versus flow velocity data were in line with the uncoated specimens, and were simply a function of the overall foam densities rather than the particular coating process. A similar result was obtained for PDC-coated samples.

Based on the results of various characterizations on the CVR- and PDC-coated graphite foams, the PDC SiC coating procedure was chosen over the earlier chemical vapor reaction (CVR) approach due to its being more suitable for scale-up. To scale up the CVR process, optimization of various operating parameters regarding the high temperature furnace is required and may prove to be overly difficult for utility size foam pieces. On the other hand, the solution-based PDC coating process is not expected to have major size limitations and can prove to be quite cost effective and easy to scale up without the need for major capital investments.

6.5. Oxidation studies on graphite foams

Graphite foams have poor oxidation resistance at high temperatures in an oxidizing atmosphere. Enhancement methods for oxidation resistance of graphite materials have been extensively studied. Ceramic coatings are commonly employed to protect graphite materials from oxidation [28-30]. Although several coating systems have been developed, SiC is considered to be among the best due to its good mechanical properties, low density, excellent physical-chemical compatibility with graphite, and excellent oxidation resistance below 1800 °C [31].

The oxidation resistance of uncoated graphite foams and SiC-coated graphite foams was investigated by measuring weight changes (resolution of ±0.005 mg) as a function of the exposure time at elevated temperatures. Sample sizes were 1 x 0.5 x 0.5 in. Tests were conducted under two conditions: flowing argon in a furnace and static argon furnace. The flowing argon test was conducted in a tube furnace [Figure 6-9(a)] that had end caps through which argon gas flowed in. The system was not hermetically sealed. For the static argon test, prior to heating, the test chamber [Figure 6-9(b)] was evacuated to either 2 mTorr using a diffusion pump or 20 mTorr using a roughing pump and was back-filled with argon gas. In an actual system, static argon atmosphere is expected, whereas the flowing argon experiment is overly aggressive. After the experiments, weight loss rate (%/h) and lifetime (time to reach 90% of initial weight) were calculated and reported. The assumption is that the weight loss rate remains same for the entire lifetime.
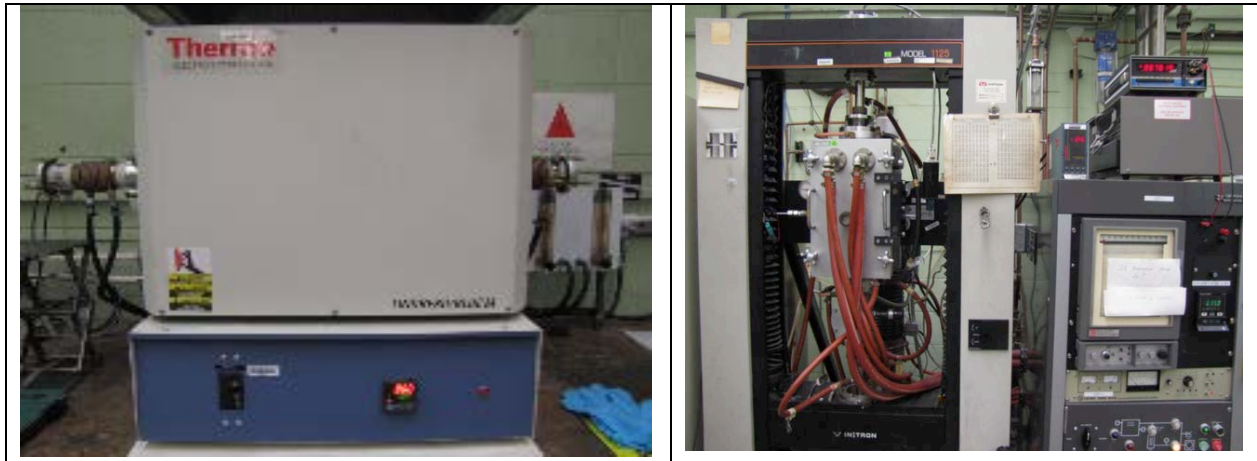
Figure 6-9. Oxidation tests in (a) tube furnace in flowing Ar and (b) static Ar atmosphere.

6.5.1. Flowing argon oxidation experiments

The weight changes of 0.11, 0.23, 0.73 g/cm^3 graphite foams with and without CVR SiC coating were measured at 700, 800, and 900 °C for 500 hours by using a flowing argon furnace. For medium density foams, samples from two different CVR coating runs were evaluated.

Figure 6-10 shows the weight loss (%) for the various samples at the three test temperatures. Three measurements were made, and average values are reported. Standard deviations are within the data symbol. The samples were oxidized and became progressively more so at higher temperatures, which is expected. The reason for the oxidation in the flowing argon atmosphere is significant leakage of air (oxygen) into the system. Based on the weight loss measurement, the lifetimes of the samples to reach 10% weight reduction were calculated and listed in Table 6-5. Results show that the CVR SiC coating does not prevent oxidation of graphite foam under flowing argon atmosphere.
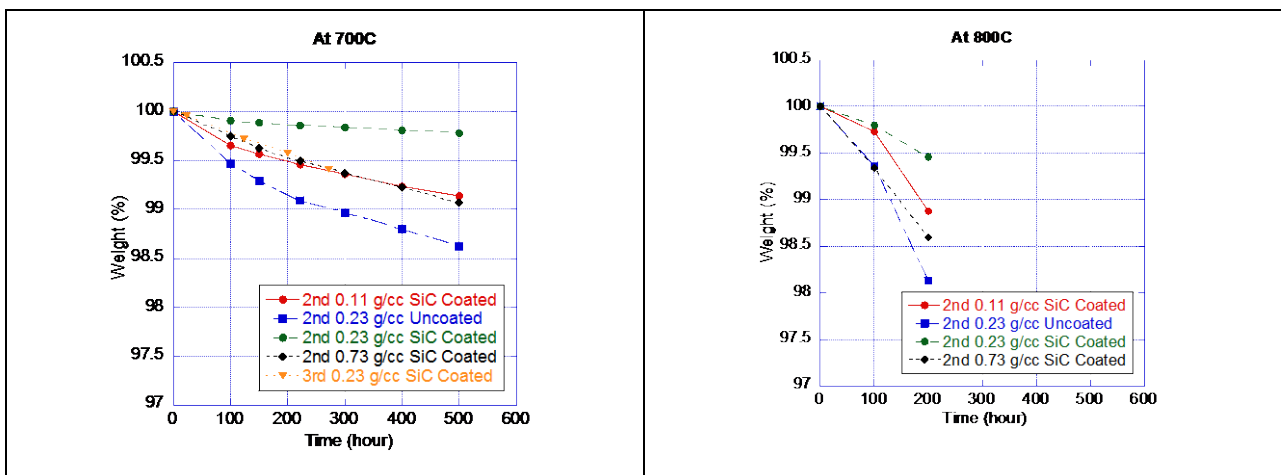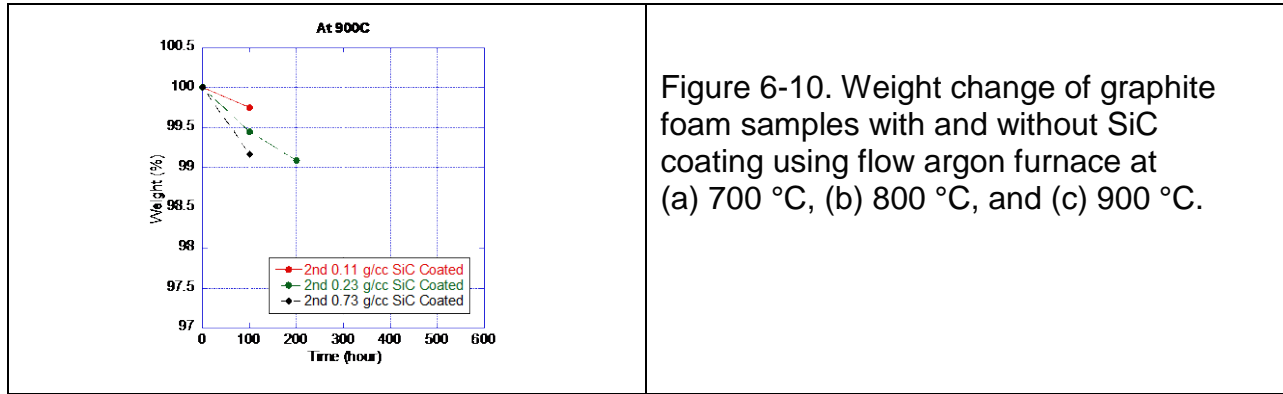
Figure 6-10. Weight change of graphite foam samples with and without SiC coating using flow argon furnace at (a) 700 °C, (b) 800 °C, and (c) 900 °C.

6.5.2. Static argon oxidation experiments

As for the case of flowing argon, similar experiments were conducted for the static argon atmosphere. Figure 6-11 shows the weight loss measurements for the various samples tested at temperatures as high as 910 °C. It should be noted that the LHTES system being designed is not expected to operate >800 °C. Table 6-6 lists the weight loss rates and the projected lifetimes. Clearly, for static argon condition with a low partial pressure of argon, there is significantly less weight loss. The projected lifetimes were >25 years for the coated samples. However, the baseline uncoated foam samples still show oxidation, and their lifetimes are significantly lower. These data confirm the utility of CVR-SiC coating in oxidation prevention.

It should be noted that the 0.11 g/cc coated sample does show oxidation. It is believed that during coating, not all the surface was coated for the low density samples. Although, based on previous analysis and data, we do not expect to use the low density foam, it will be critical to optimize the coating process to ensure full coverage of the graphite foam with SiC.

Table 6-5 Weight loss rate (%/h) and lifetime (years) of graphite foams in flowing argon

Temperature (°C)	Samples	Exposure Time (h)	Average Loss Rate (%/h)	Life Time (yr)
700	2nd 0.11g/cc SiC Coated	500	0.00173	0.66
	2nd 0.23g/cc Uncoated		0.00275	0.42
	2nd 0.23g/cc SiC Coated		0.00043	2.65
	2nd 0.73g/cc SiC Coated		0.00186	0.61
	3rd 0.23g/cc SiC Coated		0.00215	0.53
800	2nd 0.11g/cc SiC Coated	200	0.00561	0.20
	2nd 0.23g/cc Uncoated		0.00936	0.12
	2nd 0.23g/cc SiC Coated		0.00271	0.42
	2nd 0.73g/cc SiC Coated		0.00703	0.16
900	2nd 0.11g/cc SiC Coated	100	0.00247	0.46
	2nd 0.23g/cc SiC Coated		0.00545	0.21
	2nd 0.73g/cc SiC Coated		0.00833	0.14

Finally, experiments were also conducted for the static argon case, where the initial vacuum was quite low (~20 mTorr) prior to back filling the chamber with argon. Figure 6-12 shows the weight loss data on the various samples. Again, the uncoated foam shows the most loss in weight over the 100-h test period. The low density foam also shows oxidation, and the reason for that has been discussed above. The medium and high density foams do not show any appreciable oxidation. Based on the oxidation rates, the lifetimes of the foams are estimated in a simplistic manner and presented in Table 6-7.

Figure 6-11. (a-c) Weight change of graphite foams with and without CVR SiC coating using static argon atmosphere.
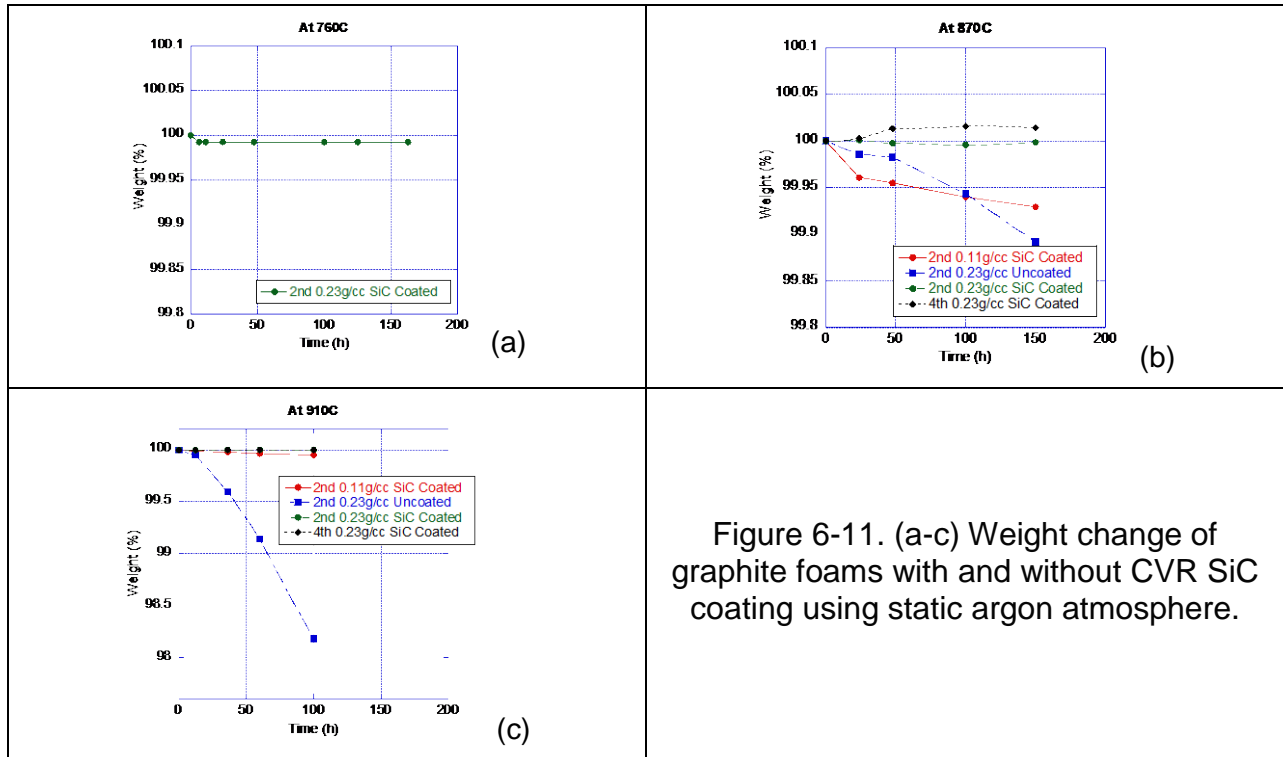
Table 6-6 Weight loss rate (%/h) and lifetime of graphite foams under static argon condition.

Temperature (°C)	Samples	Exposure Time (h)	Average Loss Rate (%/h)	Life Time (yr)
760	2nd 0.23 g/cc CVR-SiC Coated	163	0.000046	25
870	2nd 0.23 g/cc Uncoated	150	0.000724	1.6
	2nd 0.23 g/cc CVR-SiC Coated		0.000012	>25
	2nd 0.11 g/cc CVR-SiC Coated		0.000471	2.42
	4th 0.23 g/cc CVR-SiC Coated		-0.000160	>25
910	2nd 0.23 g/cc Uncoated	100	0.018222	0.06
	2nd 0.23 g/cc CVR-SiC Coated		0.000010	>25
	2nd 0.11 g/cc CVR-SiC Coated		0.000495	2.30
	4th 0.23 g/cc CVR-SiC Coated		0.000048	~24
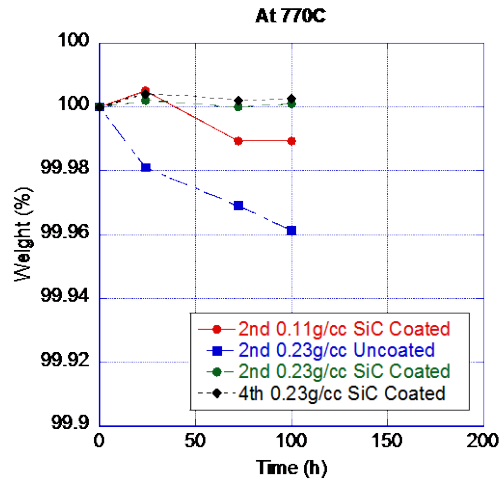
Figure 6-12. Weight change of graphite foams with and without CVR-SiC coating under low vacuum using static argon vacuum furnace.

Table 6-7. The weight loss rate (%/h) and lifetime of graphite foams under low vacuum condition.

Temperature (°C)	Samples	Exposure Time (h)	Average Loss Rate (%/h)	Life Time (yr)
770	2nd 0.23 g/cc Uncoated	100	0.000388	2.95
	2nd 0.23 g/cc CVR-SiC Coated		-0.000011	>25
	2nd 0.11 g/cc CVR-SiC Coated		0.000106	10.75
	4th 0.23 g/cc CVR-SiC Coated		-0.000025	>25

The oxidation rates for the various PDC-coated samples are extremely small, as shown in Figures 6-13 and 6-14. The oxidation rates decreased with time. Clearly, tests done over 500 h cannot be used to predict the graphite lifetime over 25 years; however, the results do show confidence in the survivability of the coated graphite foams from oxidation attack.

Figure 6-13. Oxidation rate as a function of time for SiC-coated graphite foam samples tested at 900 °C.	Figure 6-14. Oxidation rate as a function of time for SiC-coated graphite foam samples (0.44 g/cc) tested at 900 °C.
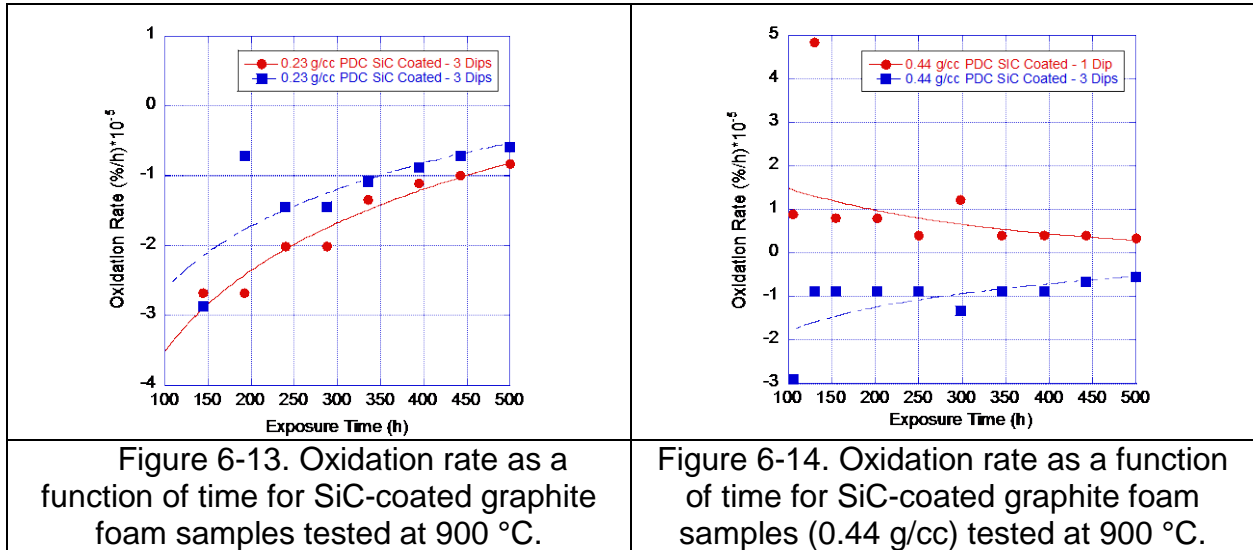
In summary, development of the SiC coating process and its application on graphite foam demonstrated enhancement in the foam structural integrity and improved oxidation resistance without adversely affecting the thermal and flow properties of the graphite foam. The SiC process development work met the deliverables of Milestone 1.2.

7. Joining Process Development for LHTES System Integration

Brazing/joining is important to integrate the graphite foam to the HTF pipes to maintain thermal connectivity. In this portion of the project, coated and uncoated medium density graphite foams were vacuum brazed to Incoloy 800H using mainly BNi-4 nickel-based braze alloy. BNi-4 is a commercially available braze alloy (Ni-3.5Si-1.85B) with solidus and liquids temperatures of 982 °C and 1066 °C, respectively. Braze powders were utilized during the joining procedures. The reason for selecting BNi-4 braze was that it does not have any chromium. The presence of chromium makes the material highly susceptible to corrosion in alkali salt PCMs at elevated temperatures.

7.1. Microstructural characterization

As a first step, Incoloy 800H (also commercially known as Ferrochronin 800 and Nicrofer 3220) plates (30.5 cm x 30.5 cm x 0.318 cm: 12 x 12 x 0.125 in.) were machined into 2.54 cm x 1.27 cm (1 x 0.5 in.) size pieces for microstructural investigation of brazed joints. All the Incoloy 800H materials were ultrasonically cleaned in acetone for 15 min prior to brazing. Vacuum brazing was done following the procedure described in the previous report. Briefly, braze powders were mixed with glycerin to make a thick paste with dough-like consistency, and the paste was applied using a spatula to the metallic and foam surfaces to be joined. A normal load of 0.30-0.40 N was applied to the assembly. The assembly was heated in an atmosphere-controlled furnace to the brazing temperature (1070 °C) under vacuum (10^{-6}-10^{-5} torr), isothermally held for 5 minutes at the brazing temperature, and then slowly cooled to room temperature. After the brazing runs, samples were visually examined; then mounted in epoxy, ground, and polished on a Buehler automatic polishing machine using the standard procedure; and then examined using optical microscopy (Olympus DP 71 system) and scanning electron microscopy (SEM) on a JSM 840A unit coupled with energy dispersive spectroscopy (EDS) for elemental analysis. The hardness measurements on brazed joints were made with a Knoop micro-indenter on a Struers Duramin A-300 machine under a load of 200 g and loading time of 10 seconds.

Figure 7-1 shows the SEM images of the joints made using BNi-4 and medium density foam (i.e., 0.22 g/cm^3). There was evidence of good braze infiltration in the medium density foam. However, there was no evidence of major reaction and secondary phase formation, unlike in the BNi-5 system (briefly discussed later). Note that the BNi-4 system also provides flexibility in terms of the brazing time, and the temperature can be varied as well. The infiltration of porous carbon (30% porosity) by Ni-Si alloys has been reported in earlier studies [32]. Braze infiltration is beneficial to mechanical keying and adhesion strength as well as to thermal conduction. For comparison, high density POCO foam was also brazed by the same procedure. Figure 7-2 shows low- and high-magnification SEM views of a POCO/Incoloy 800H joint made using BNi-4 braze alloy. The high-magnification SEM images and the EDS composition maps are at the marked locations in Figure 7-2. Figures 7-1 and 7-2 indicate no evidence of significant chemical reaction between BNi-4 and carbon.

Eustathopoulos and co-workers [33, 34] have shown that at temperatures in the 1100-1300 °C range in Ni-Si alloys with less than 36% Si, no reaction between Si and C occurs. The only interaction is a very limited dissolution of carbon in molten Ni-Si alloy. At Si contents in excess of 36%, Si in Ni-Si alloys reacts with C to form SiC in a manner similar to the pure silicon-carbon system. The braze alloy BNi-4 composition (in weight percent) is: 94.65Ni-3.5Si-1.85B. This converts in atom percent to: 85Ni-6.2Si-8.8B. The very low Si content of BNi-4 suggests no SiC formation during brazing. This is actually confirmed from the SEM and EDS observations shown in Figure 7-2, where no reaction layer formed at the interface (in comparison to BNi-5 which contains chromium). It is also important to note that partial wetting could be caused by the dissolution without a reaction layer formation. This could be the reason for the relatively good contact between the carbon foam and BNi-4 in Figures 7-1 and 7-2. Studies [35] have shown that even pure nickel wets and forms a low (<90°) contact angle with carbon simply because carbon dissolution lowers the surface tension of Ni, even though no chemical reaction-induced wetting occurs.

Figure 7 -1. SEM images
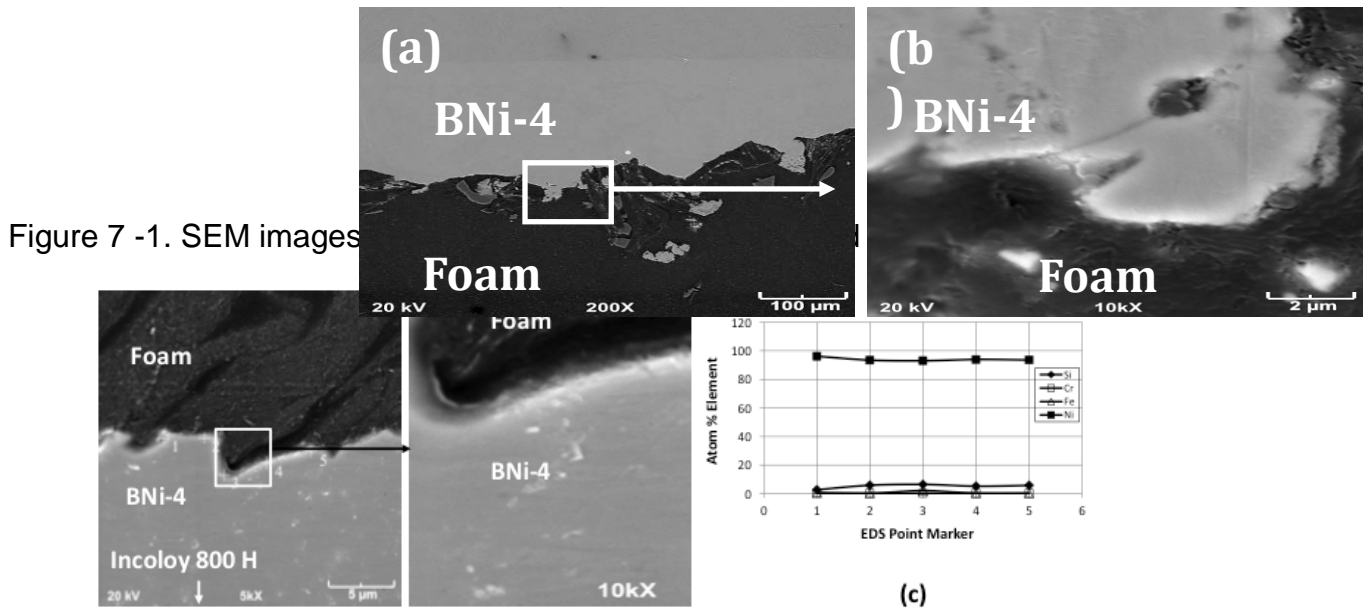
Figure 7-2. SEM micrographs of a POCO foam/Incoloy 800H joint using BNi-4 braze alloy.

In addition to the BNi-4 braze alloy, BNi-5 braze was used to create some joints with 0.22 g/cm^3 medium density foam and Incoloy 800H. The objective was mainly to investigate the microstructure and composition of the interface. Figure 7-3 shows the low- and high-magnification SEM images of a BNi-5 joint. There is clear evidence of reaction phase formation with a reaction layer thickness of about 3-5 μm. The EDS scans at point markers shown in the high-magnification view of the interface reveal that the reaction layer is rich in Cr, with roughly 60-90% Cr residing at the interface. This is a strong indication of a chromium carbide forming reaction, which is known from the literature studies to promote wetting and bonding between carbon and Ni-base alloys. The braze alloy has wet and infiltrated the foam to a distance of about 2 mm in 5 minutes of brazing time. Note that the brazing temperature used for BNi-5 was

1150 °C in comparison to that of BNi-4, which was brazed at 1070 °C. The temperature difference also plays a role in the reactivity of the constituents. Further runs are planned with BNi-4 braze alloy at 1130 °C to evaluate the influence of braze temperature on reactivity with the foam.
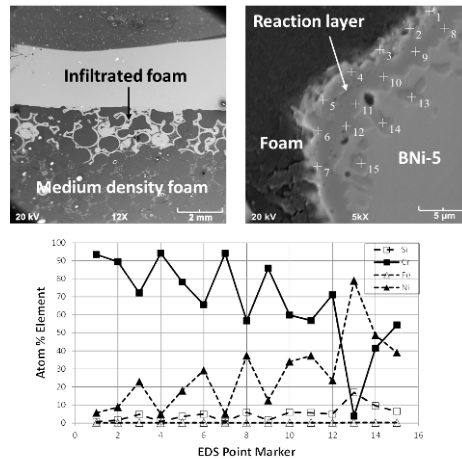
Figure 7-3. SEM images of a foam/Incoloy 800H joint made using BNi-5 braze and medium density coated foam.

Figure 7-4 shows photomicrographs of brazed joints and Knoop micro-indentation marks in foam/Incoloy 800H joints made using medium density foam and BNi-4 braze alloy. Also shown are the corresponding hardness profiles for the joints and also for a medium density coated foam joint made using BNi-5. As seen in Figure 7-5, the joint made using BNi-5 has substantially higher hardness in the vicinity of the bonded region. This is due to the presence of Cr in BNi-5 and formation of a hard chromium carbide reaction layer at the interface. Further out from the bonded region and into the Inconel 800H substrate, the hardness drops to about 180-200 HK, a value that agrees well with the data provided by the braze supplier. The photomicrographs shown in Figure 7-5 reveal that Knoop indentation hardness can accurately reveal the presence of hard and soft phases in the joint region.
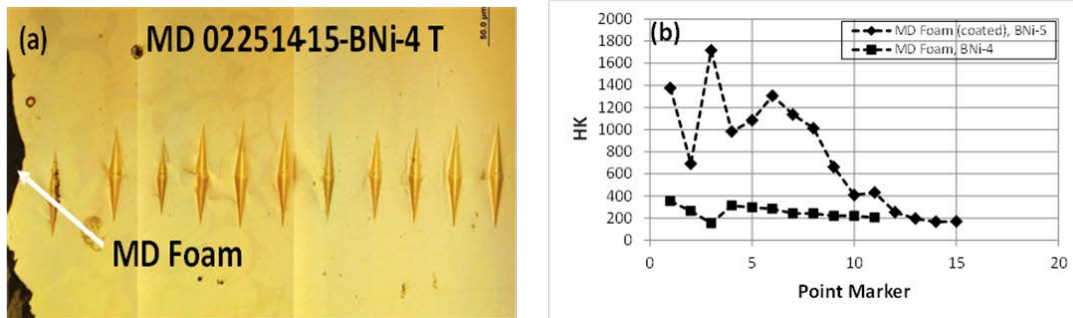
Figure 7-4. (a) Photomicrograph showing Knoop hardness distribution in a foam/Incoloy 800H joint made using medium density foam and BNi-4 braze alloy, and (b) Knoop hardness distribution in medium density foam joints made using BNi-4 and BNi-5.
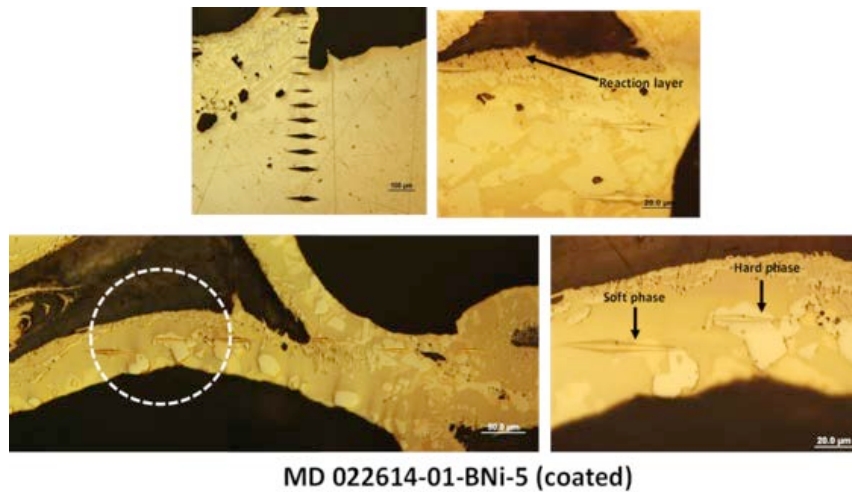
Figure 7-5. Photomicrographs showing Knoop indentation marks at various locations of an infiltrated medium density coated foam/Incoloy 800H joint made using BNi-5 braze alloy. The indentation marks reveal hard and soft phases in the joint.

Joints made using PDC SiC-coated and uncoated medium density foam and Incoloy 800H with BNi-4 braze alloy are shown in Figure 7-6. Also, shown is the hardness distribution in the joints as a function of the distance from the bonded region. There is no significant difference in the hardness profiles; the relatively large initial difference is due to the different phases encountered by the indenter in its path in the two joints (the point markers 1, 2, 3, etc., do not represent exactly the same location in the two types of joints). Therefore, thin PDC SiC coating does not appear to affect the hardness distribution in the joint.
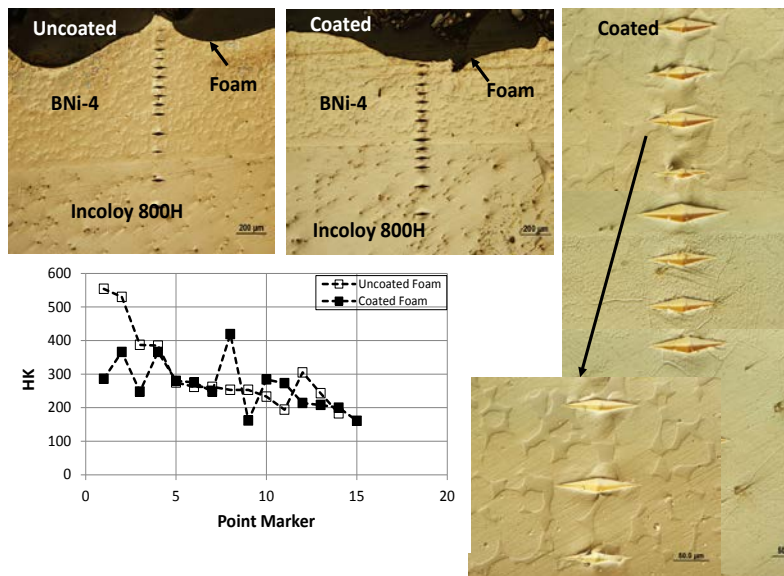
Figure 7-6. Photomicrographs showing Knoop indentation marks at various locations of PDC-coated and uncoated medium density foam/Incoloy 800H joint made using BNi-4 braze alloy. Also shown is the hardness distribution in the joints as a function of the distance from the bonded region.

A few joints were made to reinforce the BNi-4 braze using fine SiC powders (β-phase, HSC grade 400) to realize the benefit of reduced thermal expansion and residual stress without compromising the thermal conductivity of the joint. Joints were made using the following weight percentages of SiC powders in BNi-4: 10, 20, 30, 40 and 50%. Joints with 40 and 50% SiC did not bond due presumably to an insufficient quantity of the braze and an overly large percentage of SiC. (Because of its lower density than BNi-4, the SiC volume fractions would be very large.) Figure 7-7 shows joint microstructures of medium density foam/Incoloy 800H joints made using BNi-4 braze alloy containing 10 and 30 wt % SiC powders. Also shown is the hardness distribution in joints made using 10, 20, and 30% SiC powders. As is evident from Figure 7-7 the joints containing SiC powders had consistently much higher hardness than the unreinforced joints depicted in the other figures. As before, the very large abrupt increase in the hardness value for the 20% SiC joint is because the Knoop hardness values are sensitive to the actual path of the indenter. Thus, indentation marks made on dispersed SiC particles will abruptly raise the hardness by many fold. The SiC is well dispersed in the bonded region; however, in the 30% SiC sample, there is evidence of somewhat greater porosity than the 10 and 20% samples. An important note to make when brazing a foam is that any penetration of the braze material into the pores allows for an extraordinarily large surface contact area by the very nature of the foam (much larger than simply the contact area of the cross sections). This equates to excellent thermal transfer between the materials being joined. Also, as mentioned earlier, the mechanical strength is reasonable due to the keying action, even when reactions are lacking (see later mechanical tests section).
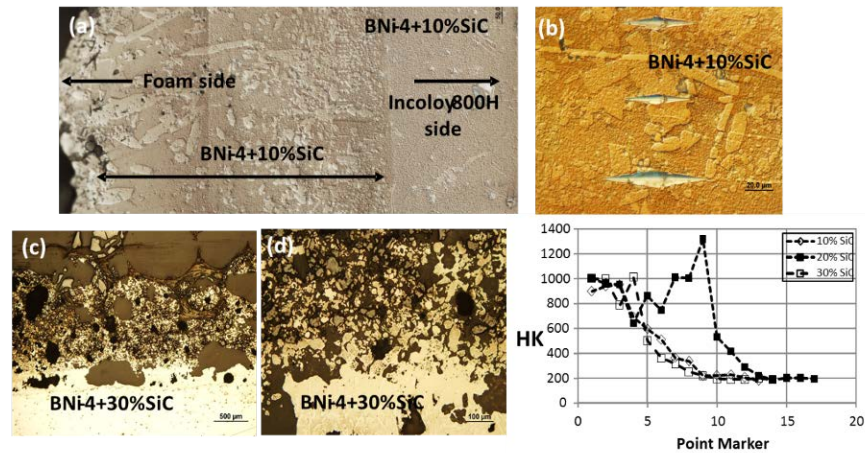
Figure 7-7. Photomicrographs showing medium density foam/Incoloy 800H joint made using BNi-4 braze alloy containing (a, b) 10 wt % SiC powders and (c, d) 30 wt % SiC powders. Beta-SiC (grade 400, HSC) was used to reinforce the BNi-4 braze alloy. Also shown is the hardness distribution in joints made using 10, 20, and 30% SiC powders.

7.2. Quality assessment of bonded specimens

To assess the quality and thermal transfer characteristics of BNi-4 brazed joints, one-sided pulsed thermography tests were conducted on the plate/foam sandwich specimens that were used for the tensile tests. The 0.22 g/cm^3 foam pieces with a cross section of 12 x 12 mm and length of 25 mm, were brazed on both ends to 25-mm square Incoloy 800H plates (3-mm thickness). The pulse thermography nondestructive evaluation (NDE) is based on introducing a pulse of thermal energy on a given surface of a specimen and viewing the time-based thermal response as the heat conducts into the material. The thermal energy is introduced via photographic flash lamps, and a 2-D image is monitored using an infrared camera focused on the same side.

All the joints, including the tops and bottoms of each tensile specimen, were inspected. Select thermal images are shown in Figure 7-8. In addition, the temperature (non-dimensional camera units) versus time behavior is plotted at multiple points, identified by the colored crosses. By viewing the derivative images, sharper contrast can be obtained because the derivative values mark when a point starts to deviate from the ideal cool-down curve after heat is deposited on the surface. It is seen that the cool down curves for the black and yellow crosses (in the upper right corner of the first two specimens, i.e., no foam, only the plate) plateau earlier, indicating that the thermal pulses have reached the back surface of the plates. The points identified by the green and blue crosses continue to cool since the well-bonded foams allow for continued transport of the thermal energy (until the back surfaces of the foams are reached at a later time). Based on this approach, no apparent/major anomalies, which may inhibit thermal conductivity, were seen in any of the tensile specimens.
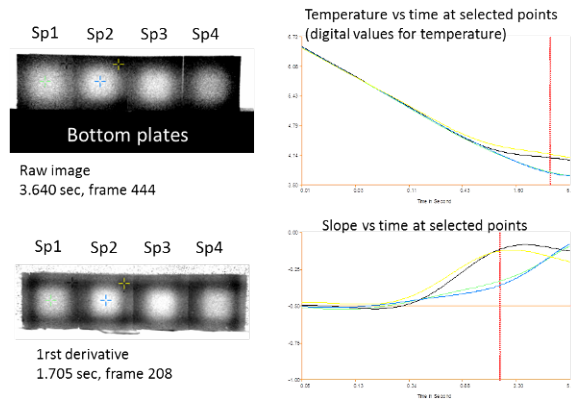
Figure 7-8. Original and first derivative pulsed thermography images of select specimens (1 through 4) with good bond (25 mm square, 3mm thick Incoloy 800H plate brazed to 12 x12 mm cross section with 25.4 mm length of foam).

7.3. Mechanical tests results of BNi-4 sandwich specimens

During this reporting period tensile tests were conducted to assess the strength of the plate/foam/plate sandwich specimens. The foam/metal joints were mechanically stressed at room temperature using an electromechanical universal testing machine. The dimensions of the plates and PDC SiC-coated foam piece are given in the above thermal inspection section. The sandwich specimens were adhered to aluminum test tabs using two-part epoxy. Figure 7-9 shows multiple views of a tabbed specimen as well as failure images to be discussed next. An alignment rig was used to ensure that the tabs and specimen remained in position while the 2-part epoxy cured.

During test set-up, the tabbed specimen was carefully inserted into a top steel sleeve within the test system's load train, and then lowered into the bottom sleeve. Pins were then used to secure the sample in place. To eliminate any alignment concerns, two universal joints were used in the fixture; one above and one below the sample. This way, if the specimen ends were not cut perfectly perpendicular, or if the sample did manage to shift during the epoxy cure time, then uniaxial loading would still be maintained. Samples were loaded in crosshead control, at a rate of 0.64 mm/min. Further details are given in references [36] and [37]. Lastly, as a side activity, a single CCD camera together with open source software was used as a tool to obtain 2D displacement maps of select specimens during testing.

The average, room-temperature tensile strength of the sandwich specimens was 551 ± 38 kPa. For comparison, the un-brazed coated medium density foam has a strength of about 844 ± 122 kPa. These sandwich strengths were comparable to the sandwich strengths of references [36] and [37], where a more ductile and active silver-based Cusil-ABA braze was employed. The fracture always occurred in the foam, although near the edge of the braze zone, as seen in Figure 7-9. Because of the location of the fractures (i.e., adjacent to the braze), there is a concern regarding specimen design and possible alignment issues. Although this specimen design was utilized in earlier studies [36, 37], it is not a standardized procedure. Hence, strength tests are continuing with a new specimen design (a larger 25.4-mm^2 cross section versus the old 12.7-mm^2 one)

aimed at reducing possible alignment and handling issues. It should be reiterated that within the actual TES system, the foams will be subjected to minimal loading, mainly in the form of compressive stresses. Therefore, the strengths obtained for the braze sandwich specimens should be more than adequate for TES applications.
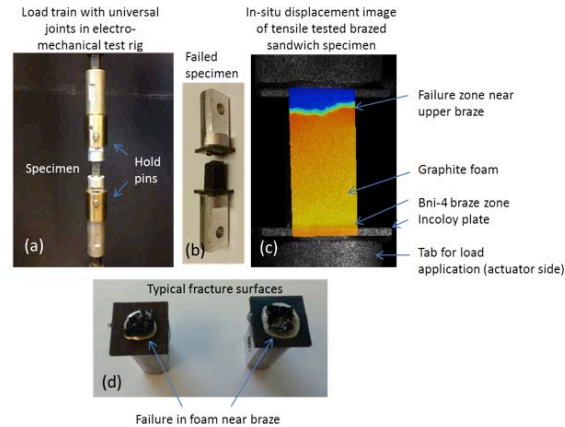

Figure 7-9. Images of (a) tensile set-up and load train within uniaxial electromechanical test rig, (b) typical failed specimen, (c) load direction displacement map using newly developed digital image correlation system (relative displacements), and (d) typical failure surfaces adjacent to braze. Note that the sandwich specimens were epoxied to the aluminum tabs prior to testing.

7.4. Thermal cycling of brazed graphite foam/Incoloy 800H joints

The bonding quality between the Incoloy-800H (structure material) and graphite foam is an important parameter in heat transfer of LHTES systems. The thermal diffusivities of Incoloy-800H with graphite foam before brazing, after brazing, and after a thermal cycling test were measured.

The effective thermal diffusivity of a two-layer system can be calculated by the following equation by Lucio et al. (1995) [38]:

$$\alpha = \frac{1}{\frac{x^2}{\alpha_1} + \frac{(1-x)^2}{\alpha_2} + x(1-x)\left(\frac{y}{\alpha_1} + \frac{1}{y\alpha_2}\right)} \qquad (7\text{-}1)$$

where x is the thickness fraction of material 1 in the composite sample, and y is the ratio of thermal conductivity of material 1 to material 2. It is assumed that there is no gap resistance between the two materials.

The calculated thermal diffusivity of Incoloy-800H with graphite foam composite is 17.14 mm^2/s at room temperature. This value is very close to the measured value of Incoloy-800H with graphite foam composite after brazing. This result confirmed that the bonding between the Incoloy-800H and the graphite foam is almost perfect.

Thermal diffusivity of Incoloy-800H with graphite foam before and after the thermal cycling test (100 cycles) was almost the same at all test temperatures, as shown in Figure 7-10. This result indicate that the bonding between the Incoloy-800H and the graphite foam is not degraded by the thermal cycling between 650 ˚C and 750 ˚C for at least 100 cycles.
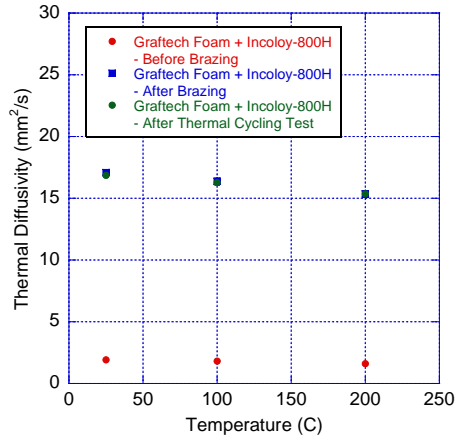
Figure 7-10. Thermal diffusivities of Incoloy-800H with graphite foam before brazing, after brazing, and after a thermal cycling test (100 cycles).

In summary, procedures for brazing of graphite foam to Incoloy 800H were developed, and data for assessing the joints were produced. The joints were shown to provide good thermal contact and adequate mechanical strength. The failure of brazed samples occurring within the foam suggests that the braze strength is equal or greater than that of the graphite foam. Further, high temperature thermal cycling did not degrade the joints. The tasks described here completed Milestone 2.1.

8. Infiltration of Graphite Foam with Phase Change Material

8.1. Infiltration process

One of the key tasks for this project is to infiltrate the selected PCM into the graphite foam in a controlled manner. A vacuum infiltration method was used in collaboration with a commercial vendor. As shown in Figure 8-1, the porous preform is put under a vacuum and preheated to temperatures >800 °C. In a separate chamber the PCM ($MgCl_2$) is melted. Subsequently, the PCM melt is allowed to flow into the porous graphite foam.
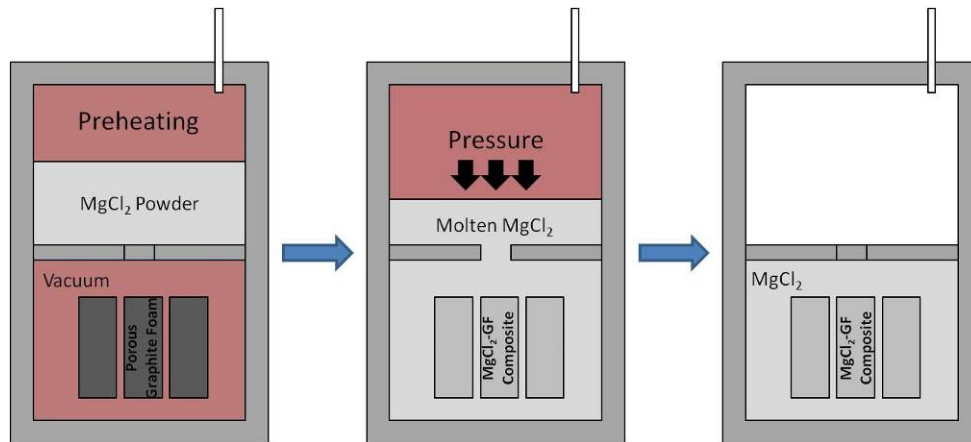
Figure 8-1. Schematic of vacuum infiltration.

Two types of commercial graphite foams were infiltrated. Properties of graphite foams and $MgCl_2$ are summarized in Table 8-1. Figure 8-2 shows the infiltrated samples of the two graphite foams. From visual observations, infiltration appeared to be uniform in both the samples.

Table 8-1. Properties of graphite foam and $MgCl_2$

	Density (g/cm³)	Porosity (%)	Dimension (in.)	Thermal Conductivity (W/m-K)*	
				Out of Plane	In Plane
POCO HTC Foam	0.9	57.95	3x6x3/4	245	70
Graftech Foam	0.22	90	3x6x3/4	50	25
$MgCl_2$	2.32 (solid at 25˚C) 1.68 (liquid at 714˚C)			0.46	

 *As reported in the literature.

Prior to infiltration testing, each foam sample was weighted using a Mettler Toledo's scale with an accuracy of ±0.01 g. After infiltration testing, the graphite foam with solidified $MgCl_2$ mass was then weighed using the same digital scale. The mass of solid $MgCl_2$ contained within the foam corresponds to the increase in sample mass, as follows:
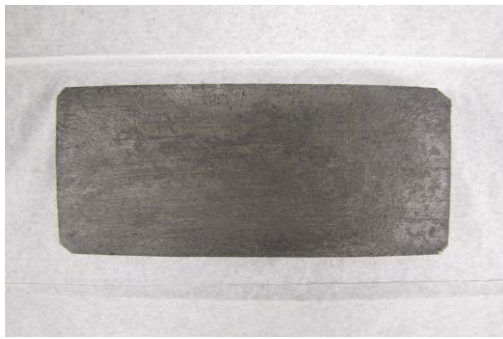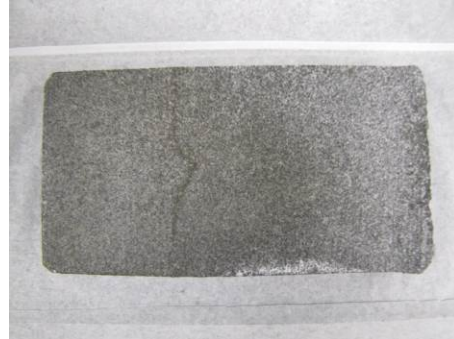
POCO HTC Foam   Graftech Foam

Figure 8-2. POCO HTC graphite foam (high density) and Graftech graphite foam
(medium density) after infiltration.

$$m_{\text{MgCl}_2} = m_{\text{final sample}} - m_{\text{initial sample}} \qquad\qquad (8\text{-}1)$$

Warzoha et al. [10] defined the infiltration rate (or saturation rate) as follows:

$$\text{infiltration Rate} = \frac{V_{PCM}}{\varphi_{foam} V_{foam}} \qquad\qquad (8\text{-}2)$$

where V is volume, and φ is porosity.

The mass changes and infiltration rates for all samples are summarized in Tables 8-2
and 8-3. From the tables, it can be inferred that when the PCM is in liquid state, the
infiltration is quite high: ~98% of the total open porosity. This is important since it
indicates that PCM can be infiltrated to the full volumetric capacity.

Table 8-2. Infiltration rate of graphite foams with $MgCl_2$ using solid density of $MgCl_2$.

		Mass Initial (g)	Mass Final (g)	Mass of MgCl$_2$ (g)	Volume of Solid MgCl$_2$ (cm^3)	Infiltration Rate
1	POCO HTC Foam	199.10	410.66	211.56	91.188	0.711
2	POCO HTC Foam	199.10	386	186.90	80.56	0.63
3	Graftech Foam	48.67	377.72	329.05	141.83	0.71

Table 8-3. Infiltration rate of graphite foams with $MgCl_2$ using liquid density of $MgCl_2$.

		Mass Initial (g)	Mass Final (g)	Mass of MgCl$_2$ (g)	Volume of Liquid MgCl$_2$ (cm^3)	Infiltration Rate
1	POCO HTC Foam	199.10	410.66	211.56	126.08	0.98
2	POCO HTC Foam	199.10	386	186.90	111.39	0.87
3	Graftech Foam	48.67	377.72	329.05	196.11	0.99

8.2. Characterization of graphite foam infiltrated with MgCl₂

8.2.1. Microstructural analysis

Figure 8-3 shows the SEM micrographs of PCM infiltrated in Graftech foam. Also, shown are the energy dispersive X-ray (EDX) analysis that is consistent with the $MgCl_2$/graphite system. Further, EDX mapping was conducted to ensure no interaction of the PCM with the graphite foam. Figure 8-4 shows the EDX mapping for C, Mg, and Cl in the selected area. As expected, Mg and Cl are restricted to the PCM region. There is some evidence of $MgCl_2$ in the graphite region, but the SEM micrograph appears to indicate the presence of surface residue, probably a result of sample preparation.
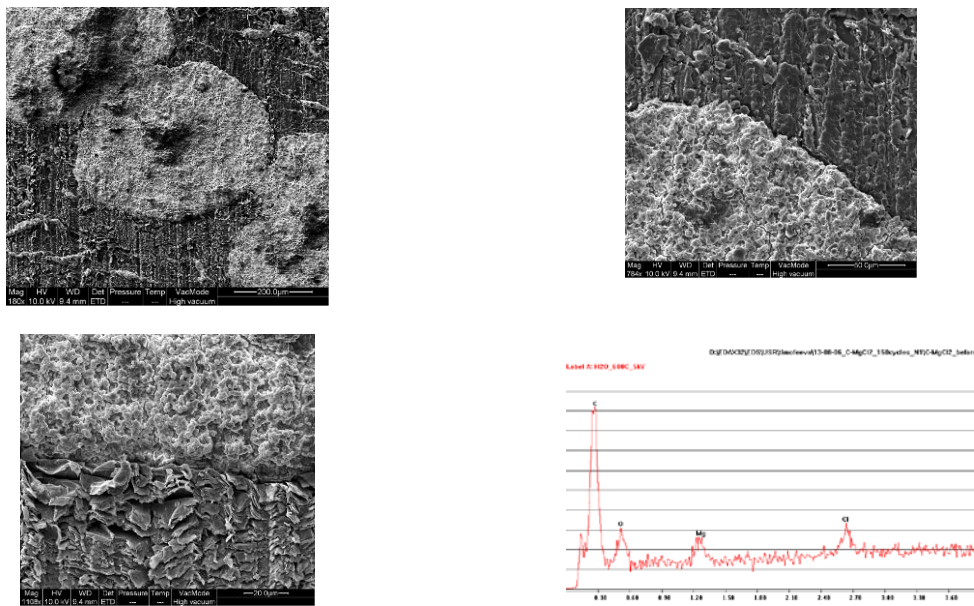
Figure 8-3. SEM images and EDX analysis of POCO-HTC foam infiltrated with $MgCl_2$.

8.2.2. TGA-DSC analysis

Thermal gravimetric analysis-differential scanning calorimetry (TGA-DSC) using SDT-Q600 of TA Instruments was conducted for both POCO-HTC foam infiltrated with $MgCl_2$ and Graftech foam infiltrated with $MgCl_2$ to investigate the heat of fusion of the infiltrated foam.

8.2.2.1. POCO-HTC foam infiltrated with MgCl₂

The heat flow and weight change of the high density POCO-HTC foam infiltrated with $MgCl_2$ for 100 cycles of melting and freezing are shown in Figure 8-5. The heat of fusion of the POCO-HTC foam infiltrated with $MgCl_2$ was from 225.2 kJ/kg to 238.5 kJ/kg for all cycles. Except the heat of fusion of the 1st cycle, it was from 234.9 kJ/kg to 238.5 kJ/kg.
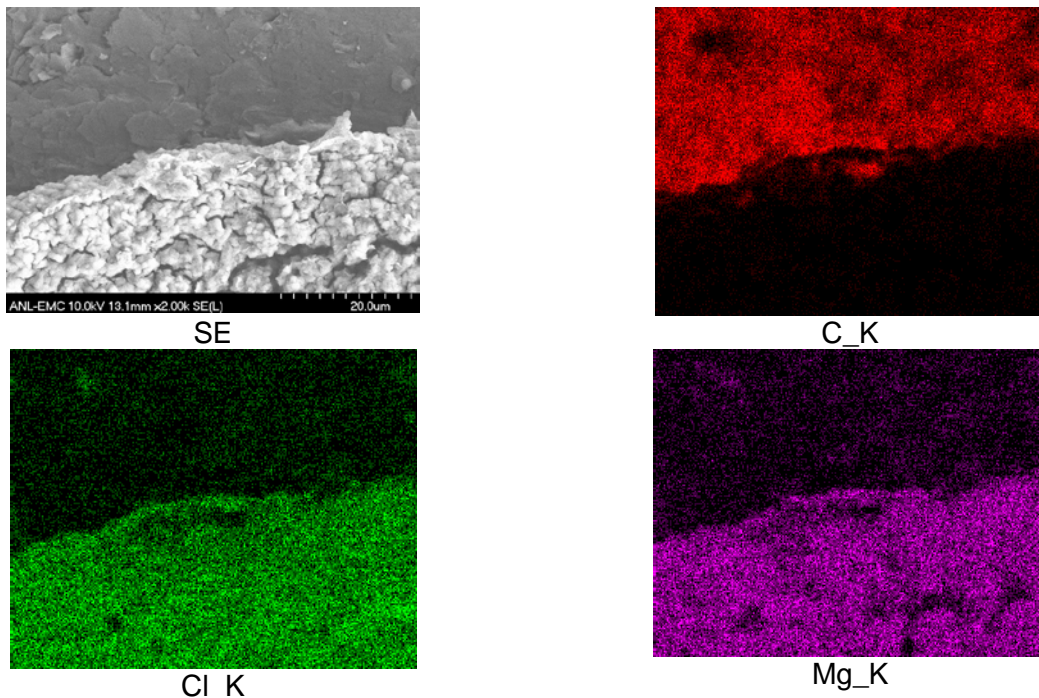
Figure 8-4. SEM image and EDX-map analysis of Graftech foam infiltrated with $MgCl_2$.

Mass ratio of $MgCl_2$ in the $MgCl_2$/POCO-HTC foam composite was calculated by the ratio of measured heat of fusion of $MgCl_2$/POCO-HTC foam composite and baseline $MgCl_2$. The mass ratio of the $MgCl_2$ in the $MgCl_2$/POCO-HTC foam composite ranged from 49.8% to 52.78% as a function of thermal cycling. The values obtained are quite close to 53.71%, as determined from weight measurements during infiltration. These two values are close.

The curves of heat flow for 100 cycles were found to be very repeatable (Figure 8-5a). This result indicated that $MgCl_2$/POCO-HTC foam composite could continuously charge and discharge thermal energy. As shown in Figure 8-5b, there is weight loss as a function of thermal cycling (3% over 100 cycles). Initial weight loss was high, and then it plateaued (<0.5%). Since the tests were done in flowing nitrogen, weight loss could be due to graphite oxidation and/or vaporization of $MgCl_2$. It should be noted that the graphite foam will be coated by SiC, and the atmosphere will be controlled with inert gas in the actual LHTES system. Furthermore, the LHTES tank will be sealed to avoid loss of $MgCl_2$. Therefore, in the actual LHTES system, no weight loss of the $MgCl_2$/graphite foam composite is expected.

8.2.2.2. Graftech foam infiltrated with $MgCl_2$
The heat flow and weight change of the Graftech foam (medium density) infiltrated with $MgCl_2$ for 100 cycles of melting and freezing are shown in Figure 8-6. The heat of fusion of the Graftech foam infiltrated with $MgCl_2$ was from 353.6 kJ/kg to 379.6 kJ/kg for all cycles. These values are consistent with those determined from the infiltrate rate. The weight loss rate was higher for Graftech foam as compared to the POCO foam samples. This could be due to a higher fraction of $MgCl_2$ in the system.
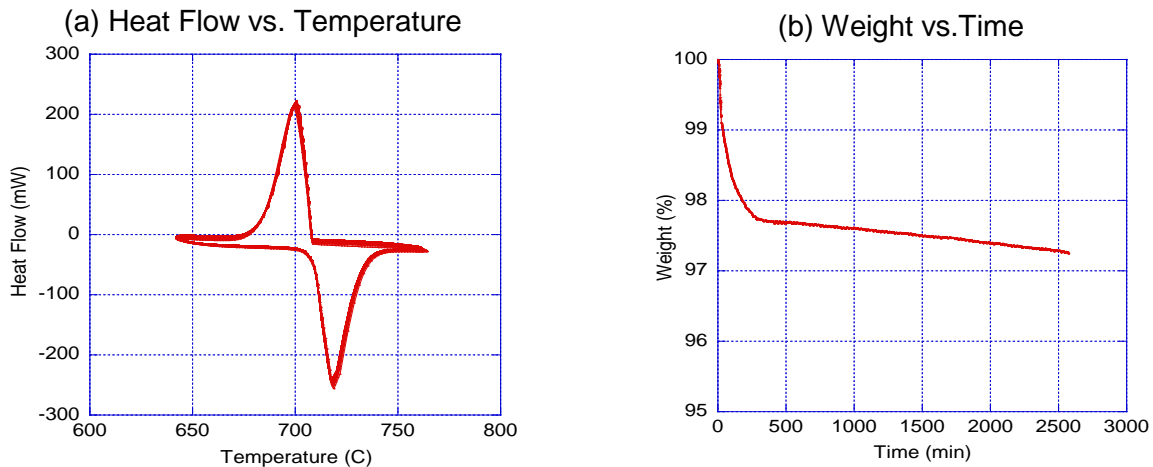
Figure 8-5. TGA-DSC analysis for POCO-HTC graphite foam infiltrated with $MgCl_2$.
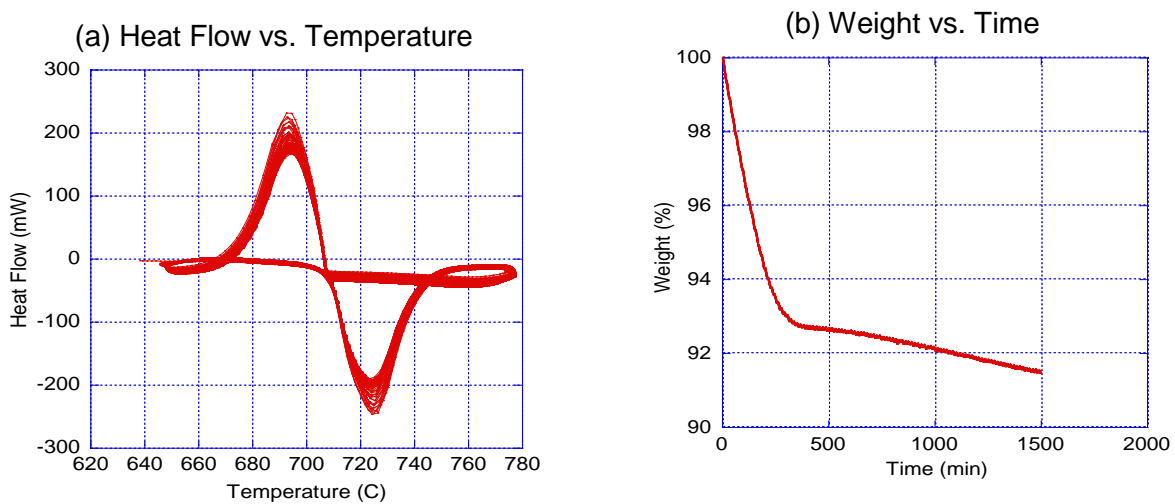
Figure 8-6. TGA and DSC analysis for Graftech graphite foam infiltrated with $MgCl_2$.

8.2.3. Thermal diffusivity and thermal conductivity

Thermal diffusivities and thermal conductivities of the two types of graphite foams with and without $MgCl_2$ in the Z- and XY-directions were investigated. The DXF-900 system (TA Instruments) was used. The thermal diffusivities of graphite foams without $MgCl_2$ were measured with increasing temperature up to 800 °C, while the thermal diffusivities of graphite foams infiltrated with $MgCl_2$ were measured up to 600 °C due to the melting point of $MgCl_2$ (714 °C).

In heat transfer analysis, thermal diffusivity is the thermal conductivity divided by the density and specific heat capacity at the constant pressure. It has SI unit of m²/s. The formula is as follows:

$$\alpha = \frac{k}{\rho c_p}$$

(8-3)

where α is thermal diffusivity, k is thermal conductivity, ρ is density, and c_p is specific heat capacity. Therefore, thermal conductivity can be calculated by the following:

$$k = \alpha \rho c_p \qquad\qquad\qquad (8\text{-}4)$$

The densities and the specific heat capacities for all samples were determined by the rule of mixtures. It was assumed that pores of graphite foam without $MgCl_2$ were completely filled with nitrogen, and that pores of graphite foam with $MgCl_2$ were completely filled with $MgCl_2$.

Thermal diffusivities of POCO-HTC foams with and without $MgCl_2$ in the Z- and XY-directions are plotted in Figure 8-7 as a function of temperature. For all samples, the thermal diffusivities decreased with increasing temperature. The thermal diffusivities of POCO-HTC foam with $MgCl_2$ are lower than those of POCO-HTC foam without $MgCl_2$ for both the Z-direction and XY-direction.

Thermal conductivities of POCO-HTC foams with and without $MgCl_2$ in the Z- and XY-directions are plotted in Figure 8-8 as a function of temperature. The thermal conductivities of POCO-HTC foam with $MgCl_2$ were higher than those of POCO-HTC foam without $MgCl_2$ for the Z- and XY-directions, as expected. At room temperature, thermal conductivities of POCO-HTC foams with and without $MgCl_2$ in the Z-direction are 270 and 232 W/m-K, respectively. Similarly, the conductivities in the XY-directions with and without $MgCl_2$ were 119.2 W/ and 92.8 W/m-K, respectively. Note that the manufacturer-provided values for the POCO graphite foam in the Z- and XY-directions are 245 and 70 W/m-K, respectively.

The thermal diffusivities of Graftech foams with and without $MgCl_2$ in the Z- and XY-directions are plotted in Figure 8-9 as a function of temperature. The thermal diffusivities of Graftech foam with $MgCl_2$ were lower than those of Graftech foam without $MgCl_2$ for the Z- and XY-directions. The corresponding thermal conductivities of Graftech foams with and without $MgCl_2$ in the Z- and XY-directions are plotted in Figure 8-10. Unlike the POCO-HTC foam case, the thermal conductivities of Graftech foam with $MgCl_2$ were lower than those of the Graftech foam without $MgCl_2$ for the Z- and XY-directions. One possible reason for this behavior could be moisture absorption by $MgCl_2$ to form a hydrated $MgCl_2*6H_2O$. If the properties of $MgCl_2*6H_2O$ are used for the calculation, the thermal conductivity of Graftech foam with $MgCl_2$ in the Z-direction at room temperature would be 43.8 W/m-K, which is slightly higher than that of Graftech foam without $MgCl_2$ in the Z-direction. XRD confirmed that chloride is hydrated. The reason for this phenomenon is apparent: Graftech foam is due higher porosity and, consequently, large fraction of PCM as compared to graphite foam in the system.
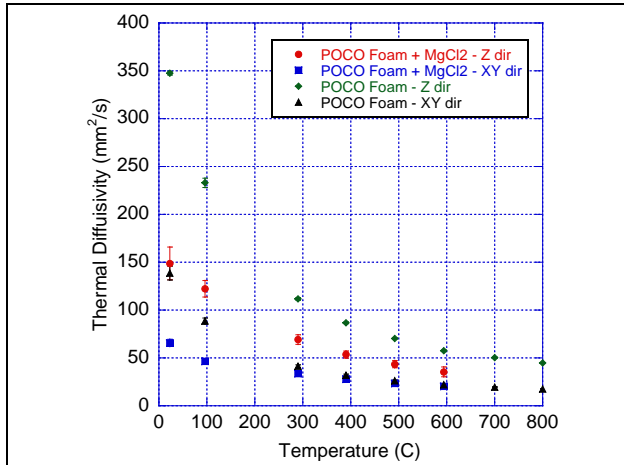
Figure 8-7. The thermal diffusivities of POCO-HTC foam with and without MgCl$_2$ in Z- and XY-directions. (Note: error bars within symbol size not shown.)
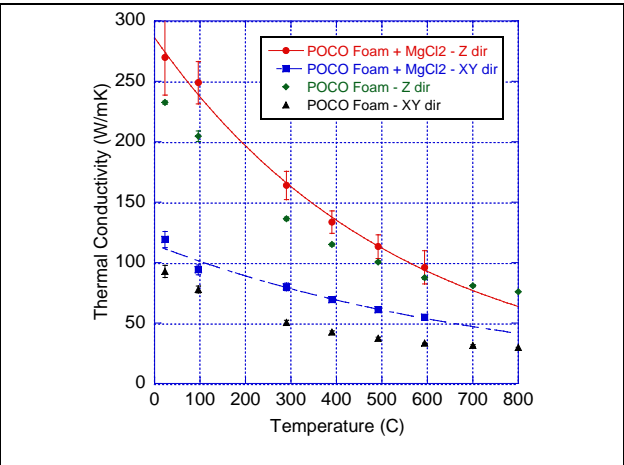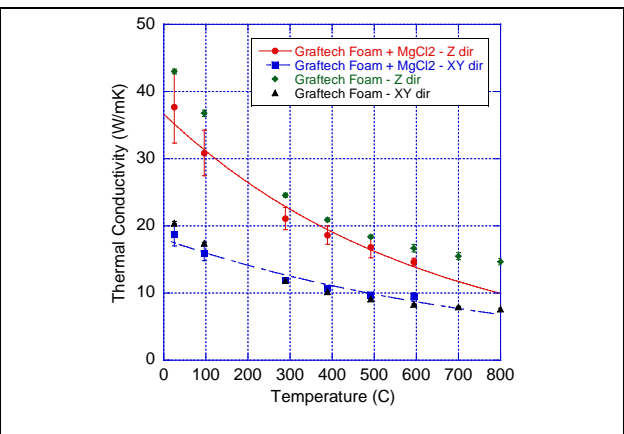

Figure 8-8. The thermal conductivities of POCO-HTC foam with and without MgCl$_2$ in Z- and XY-directions. (Note: error bars within symbol size not shown.)
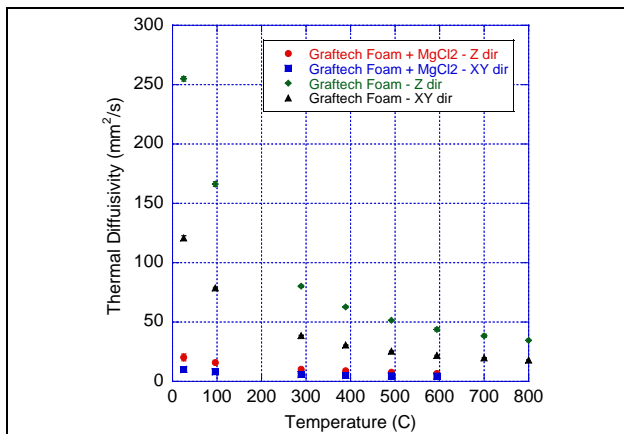
Figure 8-9. The thermal diffusivities of Graftech foam with and without MgCl$_2$ in Z- and XY-directions. (Note: error bars within symbol size not shown.)

Figure 8-10. The thermal conductivities of Graftech foam with and without MgCl$_2$ in Z- and XY-directions. (Note: error bars within symbol size not shown.)

8.2.4. Effects of thermal cycling on PCM/graphite

The purpose of this effort was to establish the interactions between the MgCl$_2$ and graphite foam as the composite is cycled between 650 °C and 750 °C. This work addresses one of the key risks: if the graphite foam degrades over time, the performance benefits would be lost. To address this, several capsules were fabricated in which the infiltrated graphite foam was placed. The sealed capsules were then cycled for 100, 200, and 500 h. Subsequently, the capsules were cut open for microstructural examination as well as thermal conductivity measurements. The thermal conductivity was measured because it would clearly establish the degradation of the graphite foam. Further, this activity helped in applying the joining processes to joining the graphite foam to structural alloys and joining of alloys to itself.

8.2.4.1. Joining experiment with un-infiltrated graphite foams, Incoloy-800H, and BNi-4 braze

The purpose of these experiments was to demonstrate the joining of the graphite foam to the alloy components in the LHTES system being developed. Brazing alloy BNi-4 (no chromium) was used to join the various components, as shown in the schematic of Figure 8-11. Braze was applied to the top and bottom Incoloy of 800-H plates and graphite foam. Brazing was done in a vacuum furnace at 1090 °C.

After joining, the sample was cut in half vertically by using a dry-cut-off machine. The cross-sectional view of the sample is given in Figure 8-12. The assembled sample using BNi-4 showed clean and solid bonding. This result indicated that BNi-4 can be utilized for joining of the graphite foam and Incoloy-800H. The joint between the Incoloy and graphite foam was analyzed by SEM/EDX. The SEM image showed a layer of BNi-4 between the graphite foam and Incoloy-800H, and some of the pores of the graphite foam were filled with braze (Figure 8-13). The EDX analysis confirmed this result. Figure 8-14 shows no chromium peak in the spectrum of BNi-4 layer, but a chromium peak in the spectrum of Incoloy-800H (this alloy has chromium in its composition) .
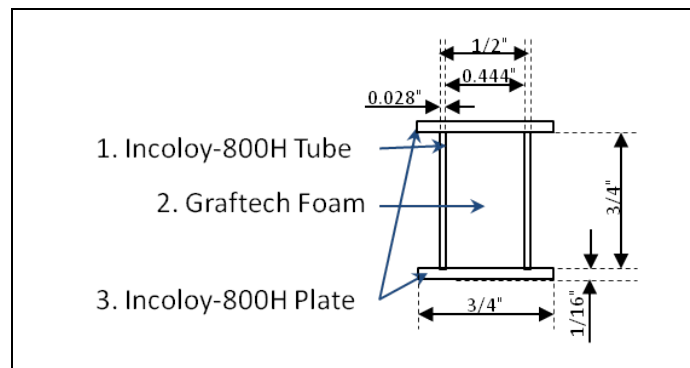
Figure 8-11. Engineering drawing of assembled sample without $MgCl_2$ using BNi-4.
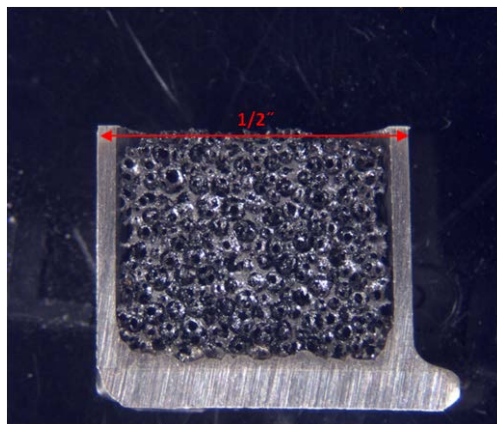
Figure 8-12. Cross-sectional view of the sample after brazing using BNi-4.
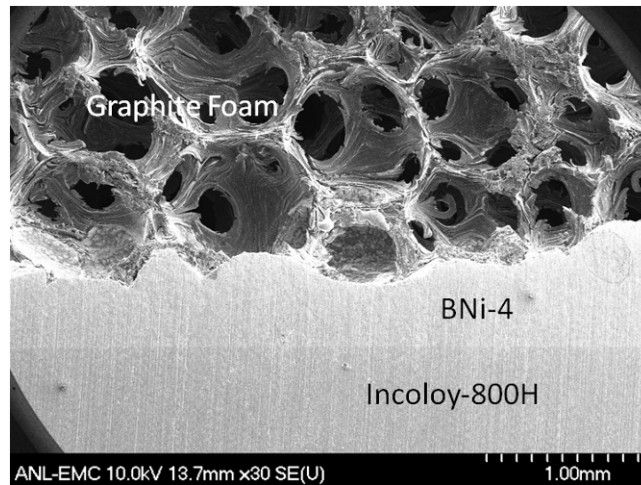
Figure 8-13. SEM image of the joint section.
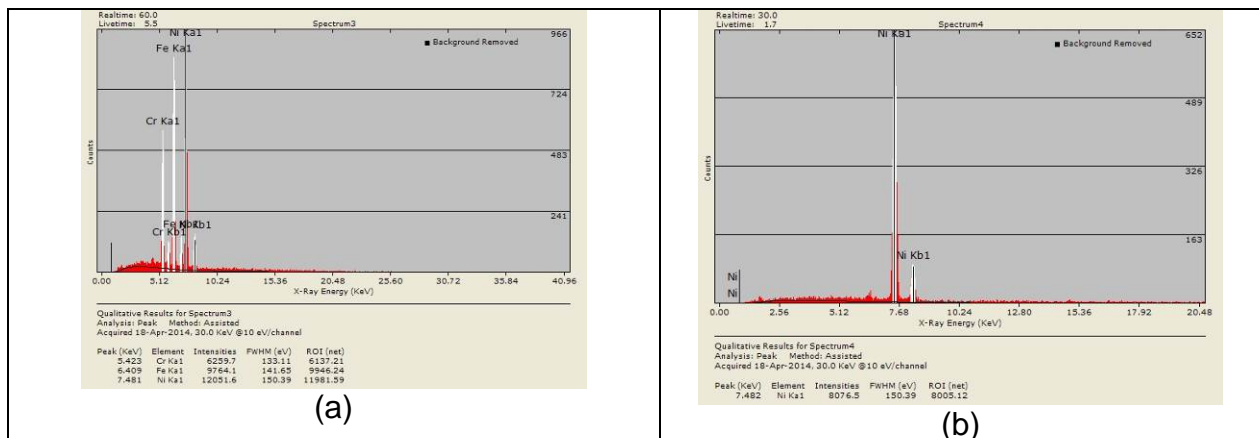
Figure 8-14. EDS analysis of the joining section: (a) Incoloy-800H and (b) BNi-4.

8.2.4.2 Joining experiment with graphite foams infiltrated with MgCl₂, Incoloy-800H, and BNi-4

Small prototype samples with $MgCl_2$ were assembled using Incoloy-800H as a container material and POCO-HTC and Graftech foams infiltrated with $MgCl_2$, BNi-4 as a brazing material tobraze the foam to container, . A schematic of samples is shown in Figure 8-15. The first step is brazing the bottom joining section of the Incoloy-800 tube, graphite foam without $MgCl_2$, and Incoloy-800H sheet using BNi-4. The second step is electron beam welding (EBW) for the top joining section of the Incoloy-800 tube and Incoloy-800H plate. Before conducting the EBW, the inside of the containers was filled with the $MgCl_2$/graphite foam composite, and then additional $MgCl_2$ for filling the empty pores was put on the top of the composite, as shown in Figure 8-15. The EBW was used for joining the top plate to avoid loss of $MgCl_2$ during brazing and contamination of the brazing furnace. Figure 8-16 shows the fabricated samples.
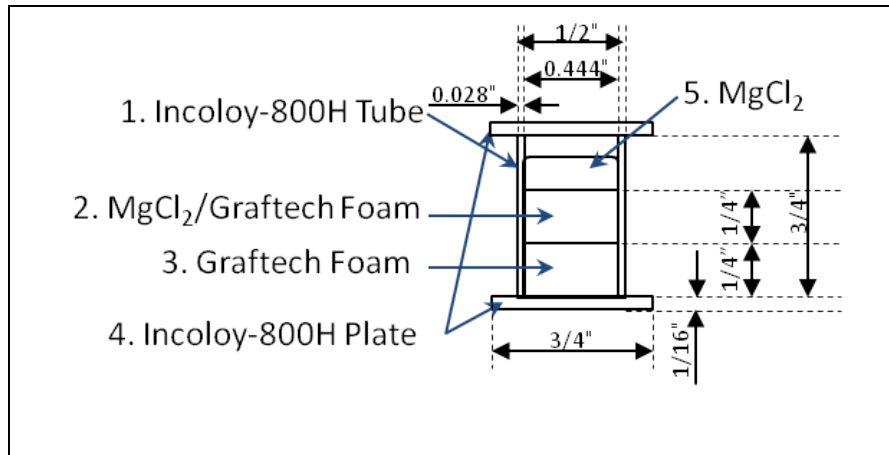
Figure 8-15. Schematic of assembled samples with MgCl$_2$ using BNi-4.

| Sample #1 | Sample #2 | Sample #3 | Sample #4 |
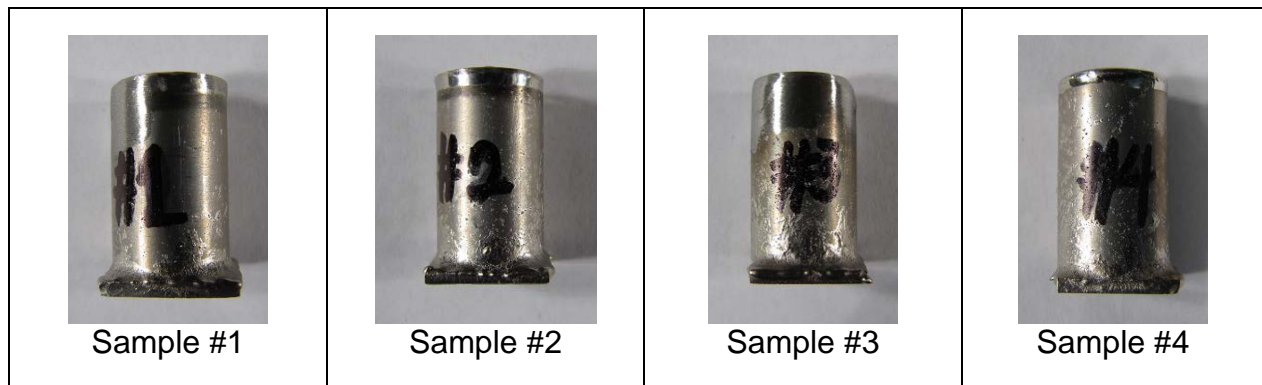
Figure 8-16. Assembled samples with graphite foam infiltrated with MgCl$_2$ using BNi-4.

8.2.4.3. Thermal cycling experiments of small prototype samples

Thermal cycling tests were conducted by heating the samples to 750°C and holding it at that temperature for 8 hours. Subsequently, the samples were cooled from 750 °C to 650 °C and held at 650 °C for 10 minutes. Then it was heated up to 750 °C and held for 8 hours. This was repeated 10-50 times to simulate melting/freezing with the cumulative hold time at 750 °C of 100, 200, and 500, respectively. After the cycling test, the samples were cut for examination. Sample #1, which was held at 750 °C for 100 hours, was cut in half vertically, while the other samples were cut horizontally (along the cylinder diameter). The cross sectional views for all samples are shown in Figure 8-17.
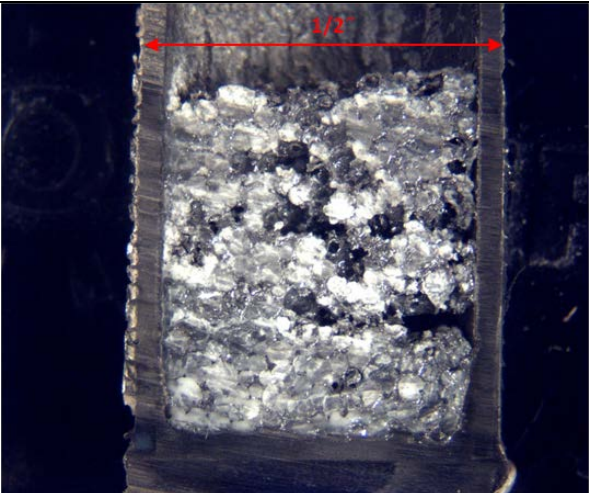
In case of the sample #1, MgCl$_2$ flowed to the pores of the bottom piece and filled the pores. Portion of the empty pores decreased because of additional MgCl$_2$. However, there were still some unfilled porosity at the center of the foam. It is expected that there will be some unfilled porosity since the difference in the density of MgCl$_2$ between liquid and solid phases was 30%. No significant degradation of the Graftech foam and Incoloy-800H was observed. The bonding between the Graftech foam and Incoloy-800H was not degraded as well. The pores near the bottom joining section were filled with BNi-4.

Samples #2, #3, and #4 were cut horizontally to get samples for thermal diffusivity measurements. The cross-sectional views (top view) showed that most of pores were filled with $MgCl_2$ after 100, 200, and 500 hours hold at 750 °C.

The morphology of the graphite foam, $MgCl_2$, and boundary between the graphite foam and $MgCl_2$ was investigated by SEM (Figures 8-18 and 8-19). The image on the left corresponds to before the thermal cycling test, and that on the right is after 500-hour hold at 750 °C. There was no obvious difference between before and after the thermal cycling test. $MgCl_2$ salt was contained in the pores in circular shape. Graphite ligaments were not damaged and maintained even after the 500-hour test. Note that the graphite foams were uncoated for these tests.

The thermal diffusivities and thermal conductivities of $MgCl_2$/Graftech foam composites before and after the thermal cycling test were investigated to verify that the thermal performance of the $MgCl_2$/Graftech foam composites did not degrade after the thermal cycling/exposure tests. The thermal conductivities of the $MgCl_2$/Graftech foam in the Z-direction before and after the thermal cycling tests are plotted in Figure 8-20 as a function of the temperature. The thermal conductivities of the $MgCl_2$/Graftech foam at room temperature before the test, post-100-hour, post-200-hour, and post-500-hour testing were 37.7 ± 5.4, 40.2 ± 0.7, 38.4 ± 1.2, and 40.1 ± 1.4 W/m-K, respectively. Similarly, at elevated temperatures, the thermal conductivities are quite similar, confirming that at least 500-hour exposure of uncoated graphite foam to molten $MgCl_2$ does not affect the foam.

The results from the infiltration studies, joining of infiltrated foam to Incoloy 800H, and thermal cycling evaluations demonstrated at least 500 melt/solidification cycles, showing no appreciable (<10%) degradation in structural/thermal properties of the infiltrated foam as a function of thermal cycling. This fulfills Milestone 2.3.

Sample #1	Total accumulated time at 750 °C: 100 hours	
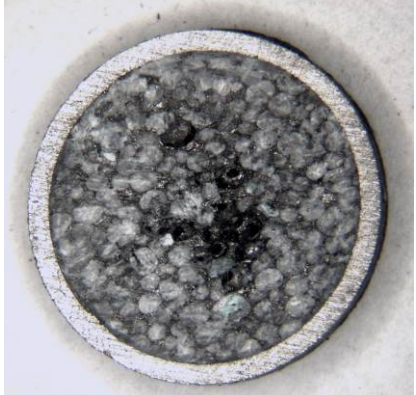
Sample #2	Total accumulated time at 750 ˚C: 100 hours	
Sample #3	Total accumulated time at 750 ˚C : 200 hours	
Sample #4	Total accumulated time at 750 ˚C: 500 hours	

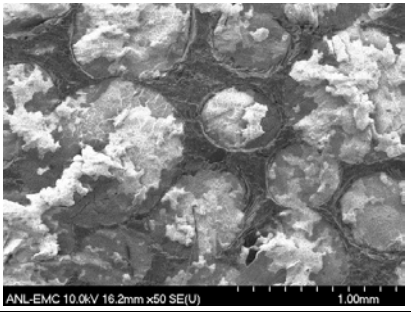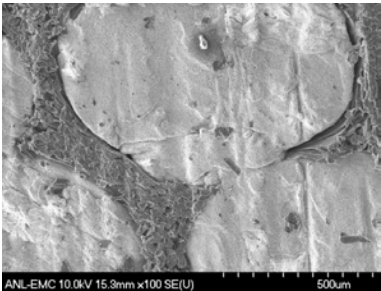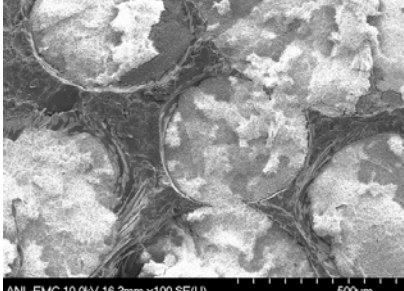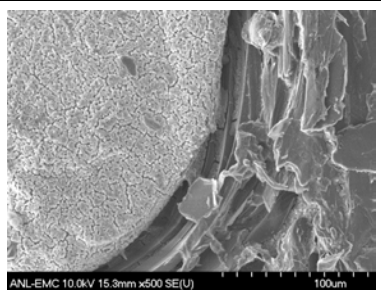Figure 8-17. Cross-sectional views of the small prototype samples using BNi-4.
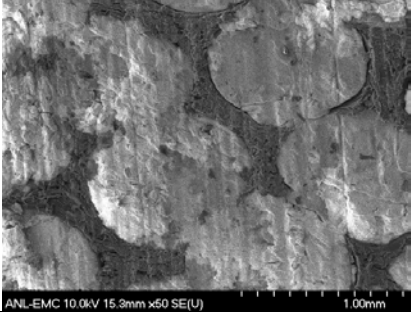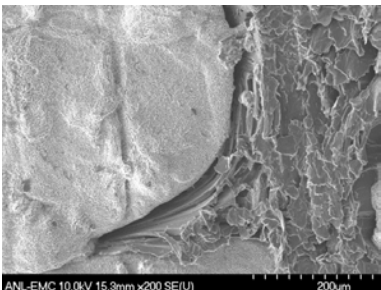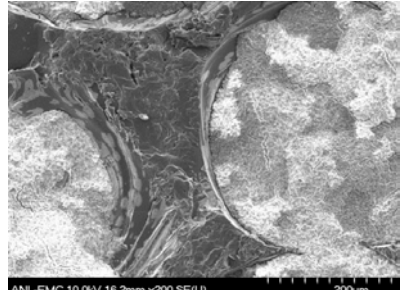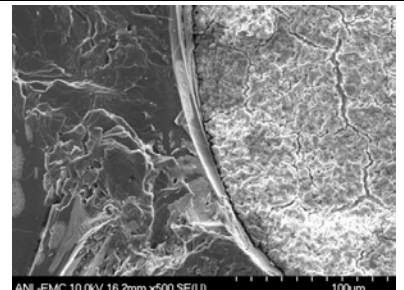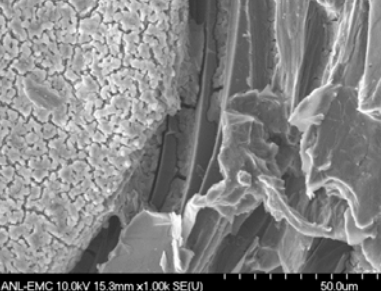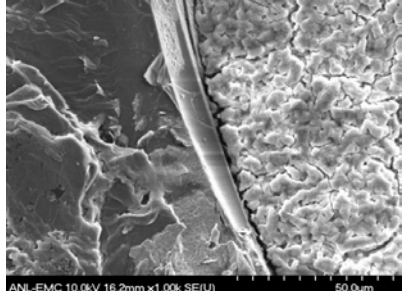
	Before the thermal cycle test	After the thermal cycle test – 100 hours at 750 ˚C (Sample #2)
x50		
x100		
x200		
x500		
x1000		

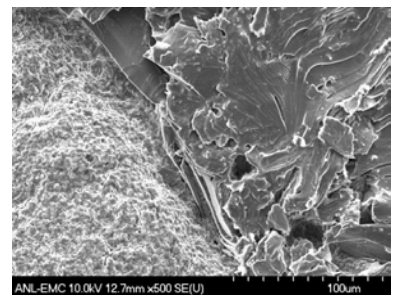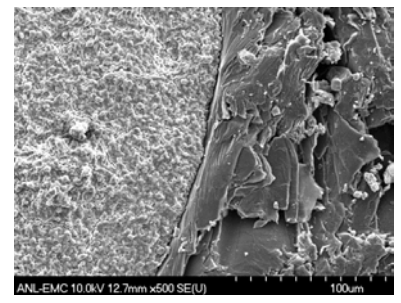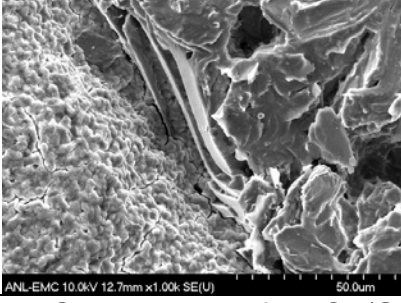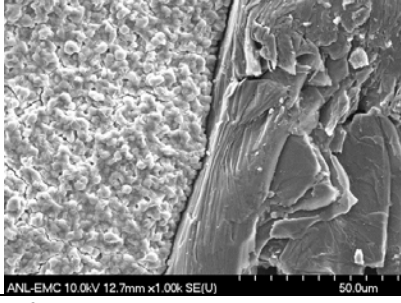Figure 8-18. SEM images of MgCl$_2$/GF before and after the thermal cycling test.
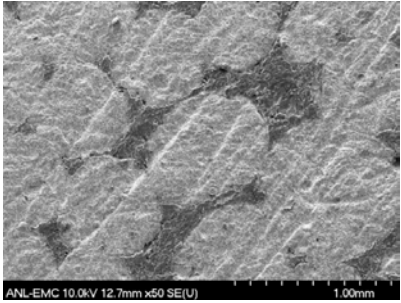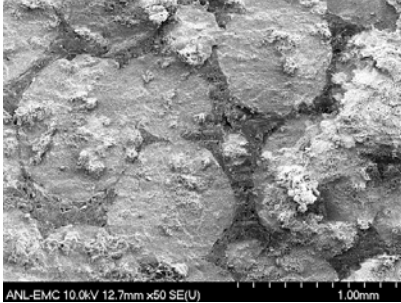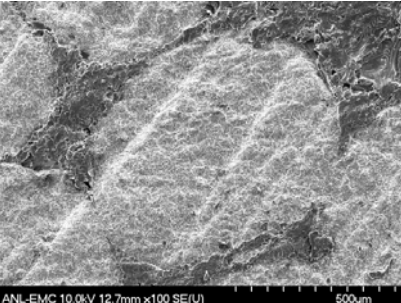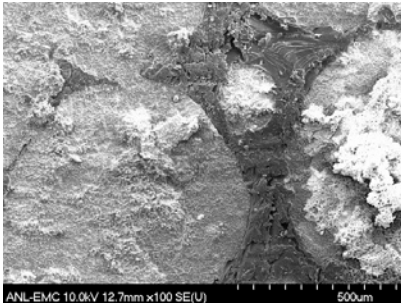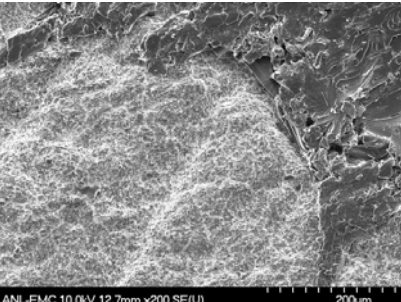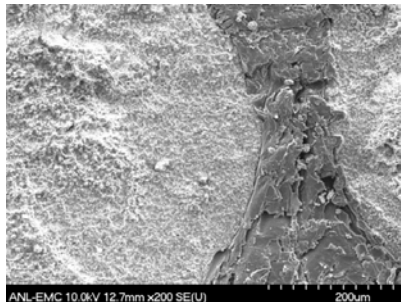
	After the thermal cycle test – 200 hours at 750 ˚C (Sample #3)	After the thermal cycle test – 500 hours at 750 ˚C (Sample #4)
x50		
x100		
x200		
x500		
x1000		

Figure 8-19. SEM images of MgCl₂/Graftech foam after the thermal cycling test.
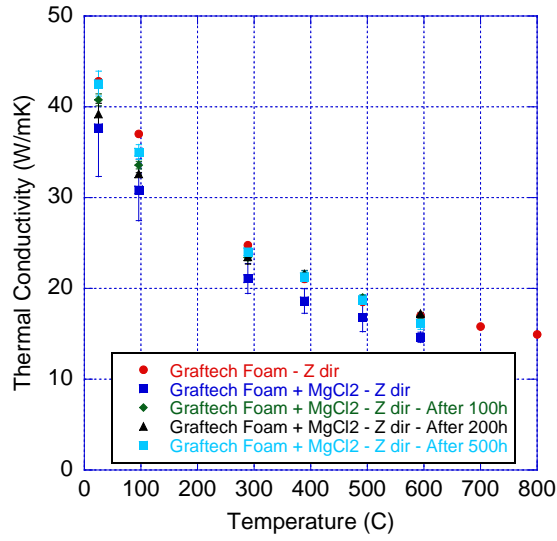
Figure 8-20. Thermal conductivities of MgCl$_2$/Graftech foam before and after the thermal cycling test. (Note: error bars within symbol size are not shown.)

9. Corrosion Studies of TES System Materials

Since the corrosive attack by chloride PCMs is well documented, it was important investigate the effects of the $MgCl_2$ PCM on the various LHTES system components (metal alloys, braze, and graphite foam) and develop appropriate approaches to mitigate corrosion. A strategy to conduct corrosion tests was developed. In particular, emphasis was to identify the key components of the proposed TES system that will be susceptible to corrosion under actual service conditions. Subsequently, experiments to mimic the real conditions/chemistries were conducted. In this regard, four specific experiments have been identified:

1. SiC-coated graphite foam with $MgCl_2$: Coated graphite foam will be in intimate contact with molten $MgCl_2$. Thus, it is critical to establish the corrosion rates for evaluating the long-term survivability of the foam.
2. Structural alloy with $MgCl_2$: This study was to establish the interaction of tank containment/piping alloy with the salt.
3. SiC-coated graphite + alloy with $MgCl_2$: This experiment was to study corrosion of both coated SiC graphite and Incoloy 800h when present simultaneously. This will help in establishing the corrosion behavior under complex chemistries.
4. SiC-coated graphite + alloy + braze with $MgCl_2$: The purpose of this experiment was to include the braze material in the mix. Braze material identified was BNi_4 which does not have any chromium. The rationale for this experiment was to recreate a realistic corrosion environment.

Corrosion tests of several candidate materials were performed in molten $MgCl_2$ salt at 750 ^{o}C (3 6ºC higher than its melting point of 714 ^{o}C) for exposure times ranging from 100 to 500 hours at the test temperature. The materials tested included: graphite foam coated with SiC (3-dips), [graphite foam coated with SiC (1-dip), Alloy 800H, BNi-coated 800H, SiC-coated graphite foam with BNi braze spot, uncoated graphite foam, and Ni-200 (commercially pure Ni). The samples of SiC-coated graphite foams (1-dip and 3-dips), uncoated graphite foams, and SiC-coated graphite foams with BNi-braze spot were tested in the as-received conditions. The 800H coupons and pure nickel were prepared by final grinding step with 1200-grit silicon-carbide paper, followed by ultrasonic cleaning in ethanol and deionized water. All the test materials (except the pure nickel) as well as the $MgCl_2$ salt were provided by ANL. Table 9-1 summarizes the test matrix used in this study.

Corrosion tests 1 to 7 were performed in a glovebox back filled with inert argon gas. A cylindrical resistance furnace with a 4-in. inner diameter was used to heat the salt for the tests. Figure 9-1 shows the experimental systems used for these tests. The crucibles for these tests were prepared by welding a Ni 200 disk to a Ni 200 pipe (1.66-in. OD x 1.38-in. ID x 6-in. high). After welding, the crucibles were cleaned with dilute 10% HNO_3 solution to remove any nickel oxide formed on the inner surface during welding and then were cleaned with ethanol. The central rod and wires for holding the test coupons were also made of Ni 200. The crucible size used in tests 1 to 7 was 1.38-in. ID, 1.66-in. OD, and 6-in. long. The size of the 800H coupons was 0.5-in. x 1-in.

x 1/16-in., and the graphite foam coupon size was 0.5 x 1 x1/8 in. Two 1/16-in. diameter holes were drilled in each test coupon for securing the coupons to the central rod. Figure 9-2 shows photographs of the glove-box and the furnace inside the glove-box during corrosion tests.

After Test 1, it was concluded that a significant amount of moisture may have been present in the MgCl$_2$ salt; therefore, the as-received MgCl$_2$ salt powder was heated at 300 °C for 12 h and subsequently at 600 °C for 12 h to eliminate this moisture. Even with these preheating treatments, some moisture could not be fully removed from the salt. This moisture was released when the MgCl$_2$ salt was melted and reacted with Cl$^-$ to form the corrosive HCl gas. Furthermore, in Tests 1 to 7, because the top of the nickel crucible was covered, the HCl gas was retained in the capsule and may have strongly affected the corrosion of materials.

In light of the problems associated with HCl gas, a new experimental system was used in Test 8 that was specifically designed to remove the water and HCl gas with flowing argon. An inner nickel crucible (3-in. ID and 3.5-in. OD and 3.5-in. long) with samples and as-received MgCl$_2$ was sealed in an outer 316 stainless steel container by welding, and high purity argon gas was passed through this system to remove the HCl formed during melting of MgCl$_2$ salt as well as provide an inert environment for the corrosion tests. Figure 9-3 shows the inner nickel crucible with samples inside, welding of the outside 316 stainless steel container, and welded 316 stainless steel container with an inner nickel crucible with test samples and salt powder. The argon gas coming out of the corrosion system was introduced into a glass beaker filled with water that was used for pH measurements. The pH measurements were performed to demonstrate the formation of HCl. Figure 9-4a schematically shows the experimental system used for Test 8. The 316 stainless steel container was heated in a resistance box furnace. The system for Test 8 is shown in Figure 9-4b.

After Test 8, the 316 stainless steel container was cut with a band saw, and the inner nickel crucible was removed. The samples were weighed before and after corrosion tests with a Sartarious CPA26P weighing balance with 1-µg accuracy to determine weight changes as a metric for corrosion. Pre- and post-test samples were also evaluated with SEM in conjunction with EDS capabilities to evaluate the mechanisms and depth of attack. Most samples were tested in triplicate.

Table 9-1. Test matrix used for studying corrosion of structural material in $MgCl_2$ salt[*]

Test #	Materials	Duration	Crucible	Salt
Test 1a	800H , 3 coupons	100 h	Ni-200	As received salt
Test 1b	SiC-coated graphite foams (3-dip), 3 coupons	100 h	Ni-200	As received salt
Test 2a	800H, 3 coupons	200 h	Ni-200	300C/12hr treated salt
Test 2b	SiC-coated graphite foams (3 dip), 3 coupons	500 h	Ni-200	300C/12hr treated salt
Test 3	SiC-coated graphite foams (1 dip), 3 coupons	100 h	Ni-200	As received salt
Test 4a	1-dip SiC-coated graphite foam with BNi braze, 3 coupons	200 h	Ni-200	600C/12hr treated salt
Test 4b	3-dip SiC-coated graphite foam with BNi braze, 3 coupons	200 h	Ni-200	600C/12hr treated salt
Test 5a	Uncoated graphite foam, 3 coupons	100 h	Ni-200	600C/12hr treated salt
Test 5b	BNi-coated 800H, 3 coupons	100 h	Ni-200	600C/12hr treated salt
Test 6a Test 6b	BNi/800H, 1coupon + SiC-coated graphite foam 2 coupons	100 h	Ni-200	600C/12hr treated salt
Test 6c	BNi-coated 800H, 3 coupons	200 h	Ni-200	600C/12hr treated salt
Test 7a[**] Test 7b[**]	SiC-coated graphite 1 pc + BNi-coated 800H, 2 pcs	100 h	Ni-200	600C/12hr treated salt
Test 7c[**]	BNi-coated 800H, 3 coupons	500 h	Ni-200	600C/12hr treated salt
Test 8[***]	SiC-coated graphite Uncoated graphite Pure Ni BNi-coated 800H	100 h	Ni-200	As received salt (labelled anhydrous), moisture was removed by flowing argon gas

[*] Tests 1 to 7 were performed in glove box with argon gas back-fill.

** In Tests 7a and 7b, some metallic parts of the vacuum pump for glove box were corroded (most likely by the HCl). Due to corrosion of pump components by HCl, some air may have been introduced into the glove box and resulted in a relatively higher oxygen partial pressure as compared to other tests.

*** Test 8 was performed in a box furnace with flowing high purity argon gas to purge the HCl formed in heating of the salt as well as to provide an inert atmosphere for corrosion test.
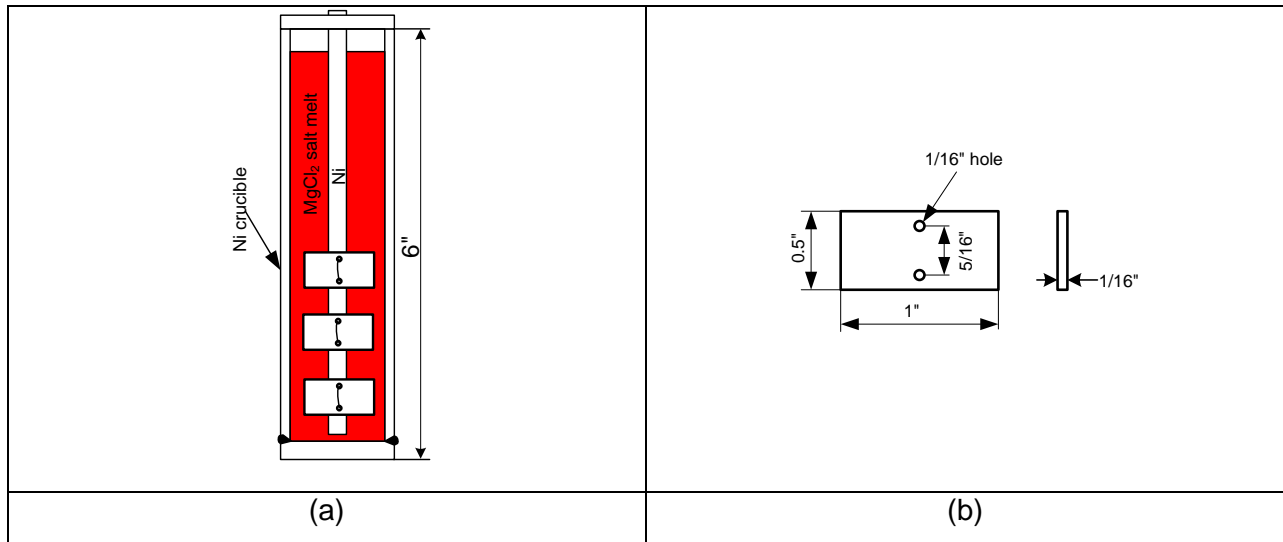
Figure 9-1. (a) Schematic illustration of the static corrosion test showing the nickel crucible, test coupons, and salt levels, and (b) dimensions of corrosion test coupons.
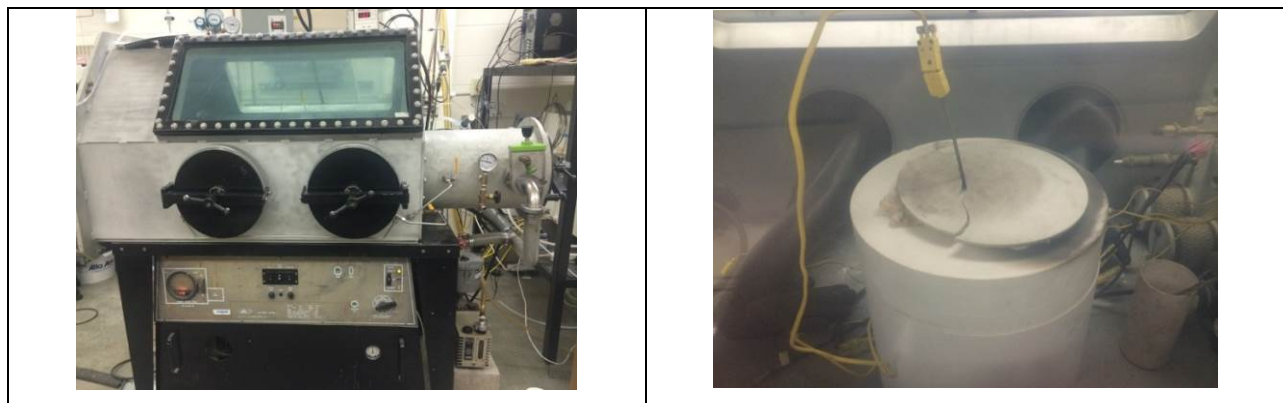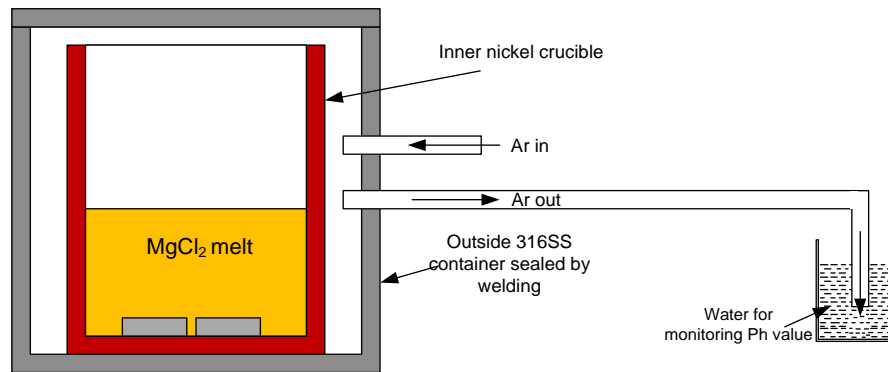

Figure 9-2. Glove-box for the corrosion tests and the furnace inside the glove-box during corrosion test.

Figure 9-3. The inner nickel crucible with samples inside (left), and welded 316 stainless steel container with an inner nickel crucible filled with samples and salt powder (right).

(a)

(b)

Figure 9-4. (a) Schematic of experimental set-up for Test 8. The pH value of the exiting Ar gas was monitored to verify the HCl formation during heating and melting of MgCl$_2$ salt as well as during corrosion test. (b) Photograph of the experimental system used in Test 8.

9.1. Corrosion of 800H and SiC-coated graphite foams (3-dip) in as-received MgCl$_2$ salt

In Test 1a, the average weight loss for the 800H samples was 37.7 ± 3.0 mg/cm^2. The attack depth (including attack along grain boundary) was 265 ± 13 µm based on measurement of the cross-sectional SEM images (Figure 9-5). The average yearly corrosion rate as extrapolated from these preliminary measurements is 23.2±1.1 mm/year, which is extremely high. However, in the first several hundreds of hours, the corrosion of materials in molten salt is mainly driven by impurities, and the corrosion rate is significantly higher. Therefore, the estimate of annual corrosion rate based on the first 100 h may be overestimated. In this test, it was found that the as-received MgCl$_2$ salt contained moisture, which may have greatly accelerated corrosion. Figure 9-5 shows the SEM images of the surface and cross sections of the 800H after corrosion tests. Severe corrosion appears to have occurred in alloy 800H with a porous layer of about 100 µm forming at the surface. In the porous layer, the Cr content was strongly depleted based on SEM-EDS measurements. Below the porous layer, the corrosion preferentially propagated along the grain boundaries. The high corrosion rate

of alloy 800H in pure nickel crucible may be also be attributable to the galvanic corrosion mechanism because dissimilar metals (800H and Ni) were in contact via $MgCl_2$ melt. To avoid these galvanic effects, the tests samples and crucible material should be made of the same material. Nevertheless, it is speculated that the moisture has a profound influence on corrosion.
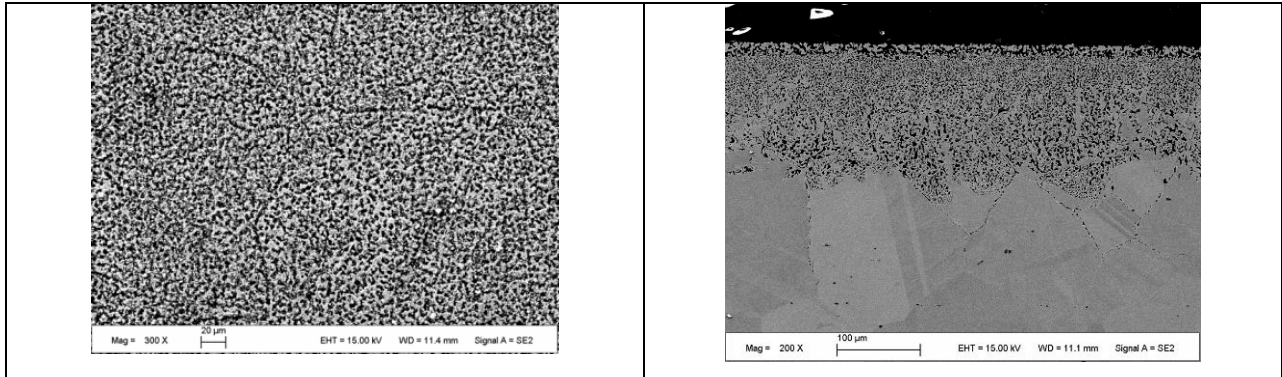

Figure 9-5. SEM images of the surface (left) and cross section (right) of alloy 800H tested as-received in Test 1.

There was a slight weight gain of 6.53 ± 0.94 mg/cm^2 for SiC-coated graphite foam samples. No visible corrosion of the sample surface was observed under SEM (Figures 9-6 to 9-8).
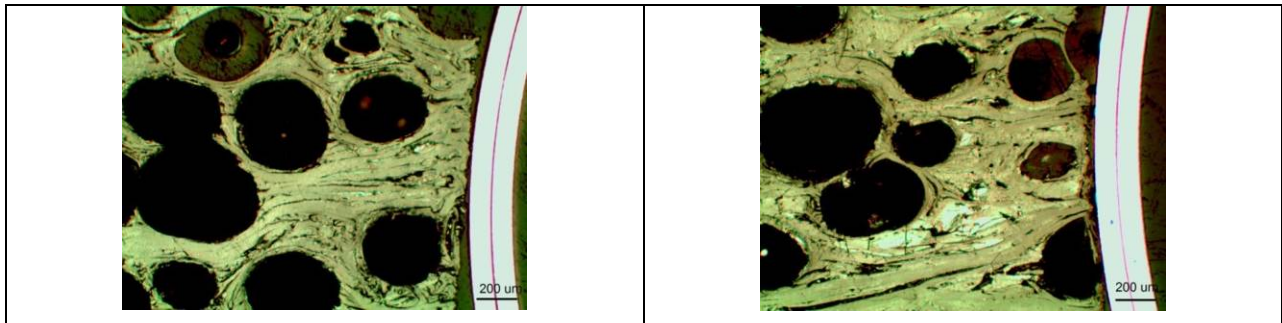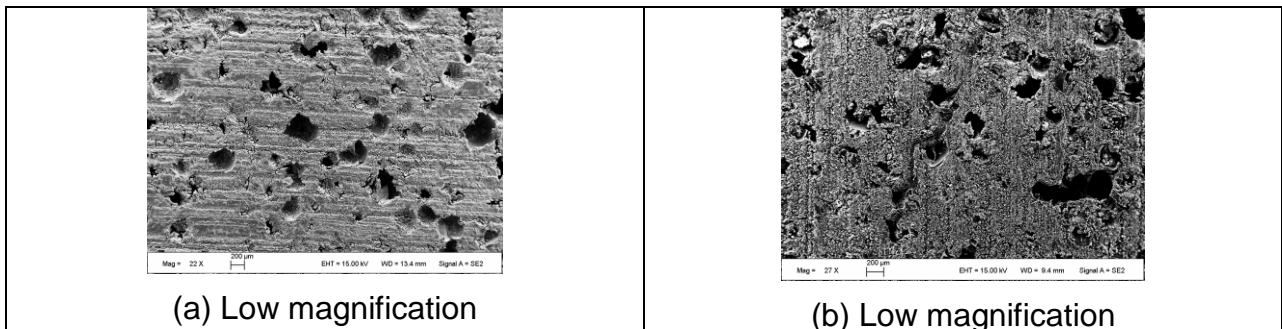

Figure 9-6. Optical images of the cross sections of the SiC-coated graphite foam sample before and after corrosion test. No damage of the graphite foam was observed, and there is no visible difference in the near surface areas in the cross sections before and after corrosion. This shows the 3-dip SiC-coated graphite foam is resistant to corrosion in $MgCl_2$ salt melt despite the presence of moisture.

| (a) Low magnification | (b) Low magnification |

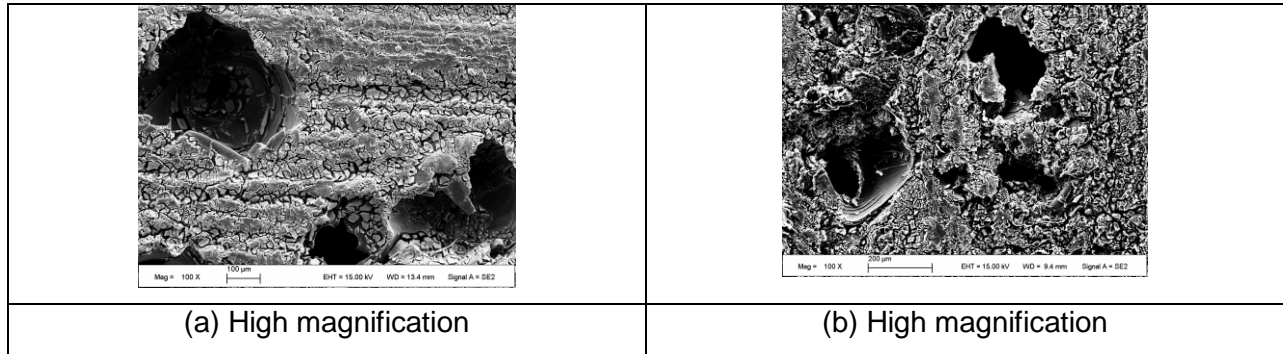|	
(a) High magnification	(b) High magnification

Figure 9-7. SEM images of surfaces of 3-dip SiC-coated graphite foam samples (a) before corrosion and (b) after Test 1.
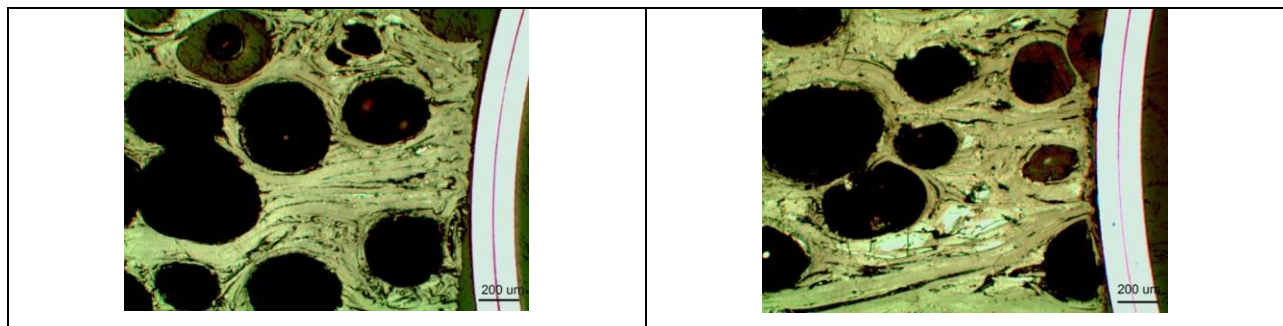

Figure 9-8. Optical images of cross section of 3-dip SiC-coated graphite foam samples before (left) and after (right) corrosion. No significant difference in cross section of graphite foam was observed after Test 1.

9.2. Corrosion of 800H and 3-dip SiC-coated graphite foam in preheated MgCl$_2$

In this test, alloy 800H samples were exposed to the salt melt, which was prepared by pre-heating the as-received salt at 300ºC for 12 hours. An average weight loss of 50.3 ± 2.6 mg/cm^2 was observed, and the corrosion attack depth was 417 ± 26 µm. This translates to an average yearly corrosion rate of 18.3 ± 1.1 mm/year. As compared to Test 1a (750ºC/100 h in as-received salt), the average corrosion rate is lower, but it is still very high. While these numbers are unrealistic, the results show that salt preheating does reduce the corrosion of alloy 8000H. Figure 9-9 shows the SEM images of the surface and cross section of 800H after corrosion tests in Test 2a. The microstructure at the surface of 800H in Test 2a is similar to that in Test 1a, with a severely corroded porous layer and grain boundary attack below the top porous layer.

The average weight gain of the 3-dip SiC-coated graphite foams was 5.6 ± 1.0 mg/cm^2. Figure 9-10 shows the SEM image of the 3-dip SiC-coated graphite foam sample from Test 2b. Almost no corrosion was observed. This figure shows that 3-dip SiC coated graphite foam is quite resistant to corrosion in molten MgCl$_2$ salt at 750 ºC despite the presence of moisture.
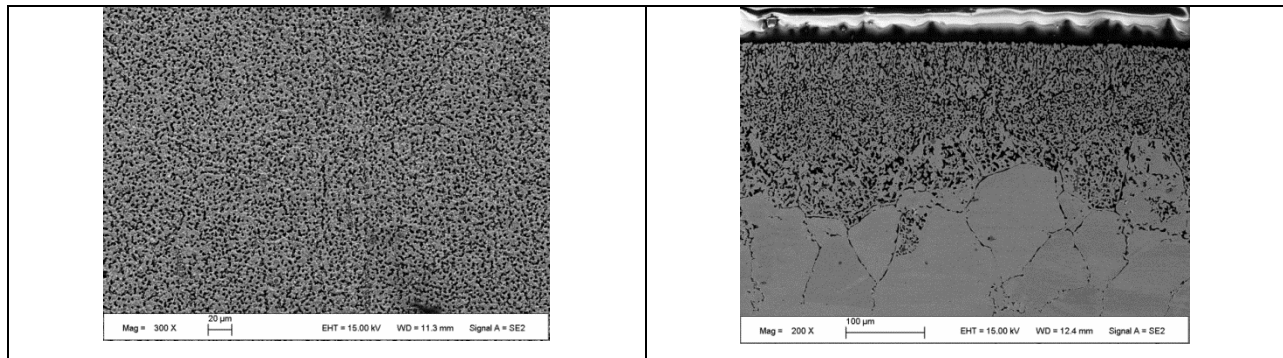
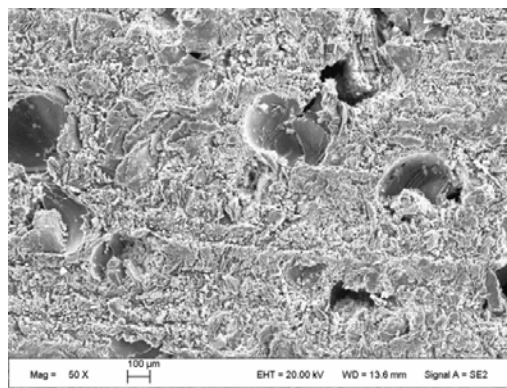Figure 9-9. SEM plan view (left) and cross-sectional (right) images of alloy 800H samples after Test 2.

Figure 9-10. SEM surface image of 3-dip SiC-coated graphite foam after Test 2. Very little corrosion was observed.

9.3. Corrosion of 1-dip SiC-coated graphite foam in as-received MgCl$_2$

The average weight gain of the 1-dip SiC-coated graphite foams per unit area is 0.37 ± 0.11 mg/cm^2. From a comparison of surface SEM images before and after corrosion (Figure 9-11), no significant corrosion was observed. The composition of the surface measured by EDS (shown in Figure 9-11) consists mainly of carbon (~97 wt.%).
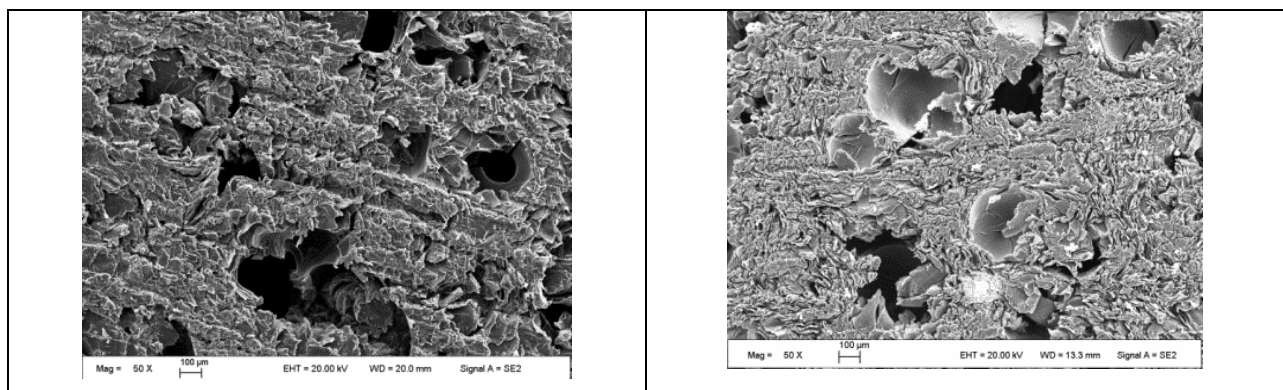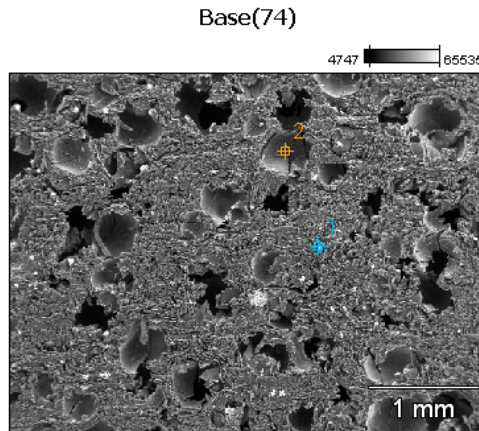

Figure 9-11. SEM surface image of 1-dip SiC-coated graphite foam samples from Test 3: before (left) and after (right) corrosion tests.

Base(74)

	C-K	Si-K	Fe-K	Ni-K
Base(74)_pt1	97.18	0.17	2.20	0.45
Base(74)_pt2	96.76	0.36	2.88	0.00

Figure 9-12. The composition of the 1-dip SiC-coated graphite foam after Test 3.

## 9.4. Corrosion of SiC-coated graphite foam samples with BNi-4 braze spot in preheated salt

Figure 9-13 shows digital photographs of SiC-coated graphite foam samples (1 dip and 3 dip) with BNi-4 braze spot before and after Test 4. It can be seen from the pictures that corrosion occurred in the BNi-4 braze spot.

The weight gain in the 1-dip SiC-coated graphite foam samples was 6.3 ± 0.2 mg/cm^2. No damage of graphite foam was observed in the cross-sectional SEM images (Figure 9-14b). Figure 9-15 shows the SEM images of the BNi-4 braze on the 1-dip SiC-coated graphite foam, and here some corrosion appears to have occurred. Since the surface of the BNi-4 braze is not polished, it is difficult to evaluate the severity of the corrosion based on the images. From the digital images as shown in Figure 9-13, some corrosion occurred in the BNi-4 braze. Some Ni-rich grains were noted to be deposited on the surface of the samples (Figure 9-16).

The weight gain of the 3-dip SiC-coated graphite foams was 8.0 ± 2.0 mg/cm^2 with some variations stemming from corrosion of BNi-4 braze, which may have different surface areas. The surface microstructure (Figure 9-17) of the samples was similar to that of 1-dip ones, with nickel-rich phases deposited on the surface (Figure 9-18). No damage of graphite foam was observed from the cross-sectional SEM image.

(a)
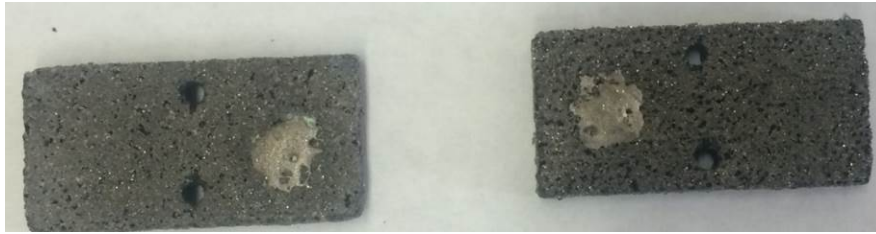
(b)

Figure 9-13. Digital pictures of SiC-coated graphite foams (1dip, left, and 3-dip, right) with BNi-4 braze spot: (a) before and (b) after Test 4.
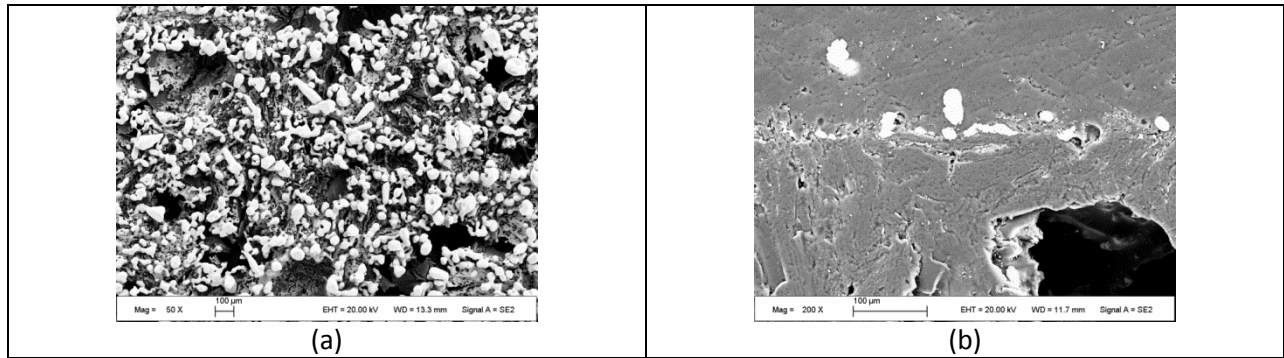

Figure 9-14. SEM images of surface (a) and cross section (b) of 1-dip SiC-coated graphite foam after Test 4.
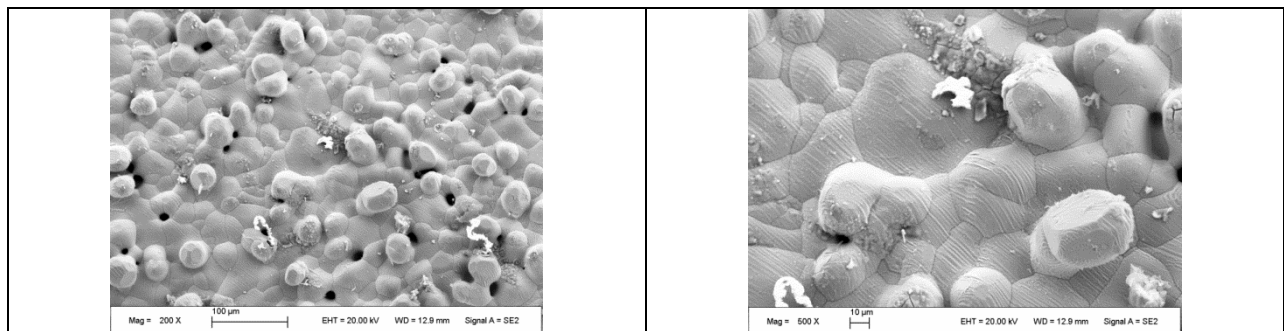

Figure 9-15. SEM images of the BNi braze on the 1-dip SiC-coated graphite foam after Test 4.
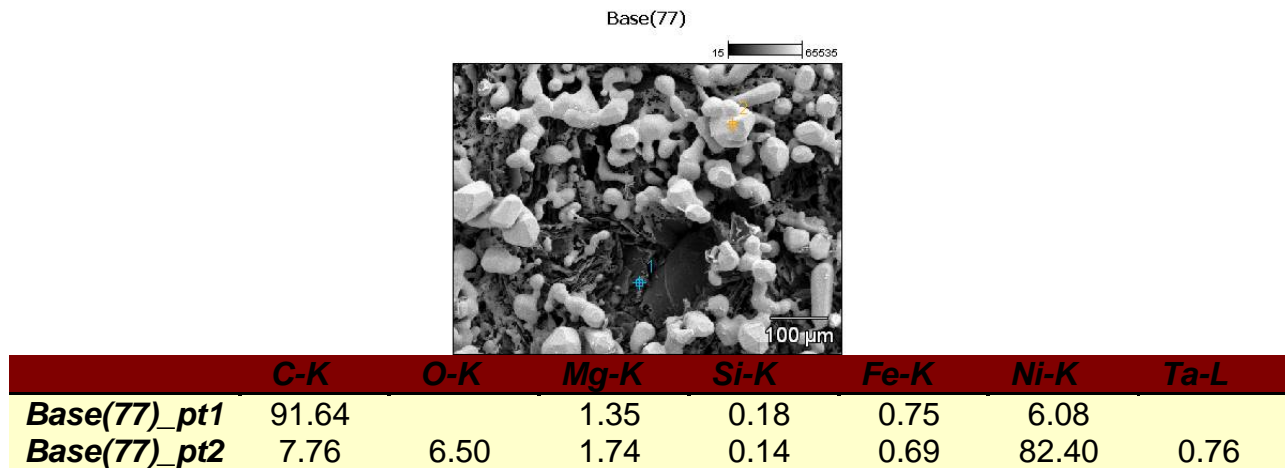
Base(77)

	C-K	O-K	Mg-K	Si-K	Fe-K	Ni-K	Ta-L
Base(77)_pt1	91.64		1.35	0.18	0.75	6.08	
Base(77)_pt2	7.76	6.50	1.74	0.14	0.69	82.40	0.76

Figure 9-16. The composition at two spots of 1-dip SiC-coated graphite foam samples after Test 4 measured by SEM-EDS.

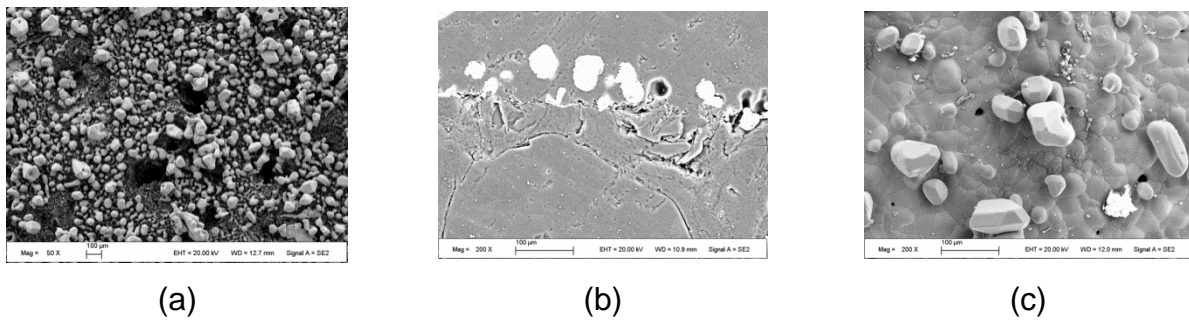| (a)	(b)	(c)

Figure 9-17. SEM images of (a) surface of 3-dip SiC-coated graphite foam, (b) cross section of 3-dip SiC-coated graphite foam, and (c) surface of BNi-4 braze spot of 3-dip SiC-coated graphite foam after Test 4.

Base(80)

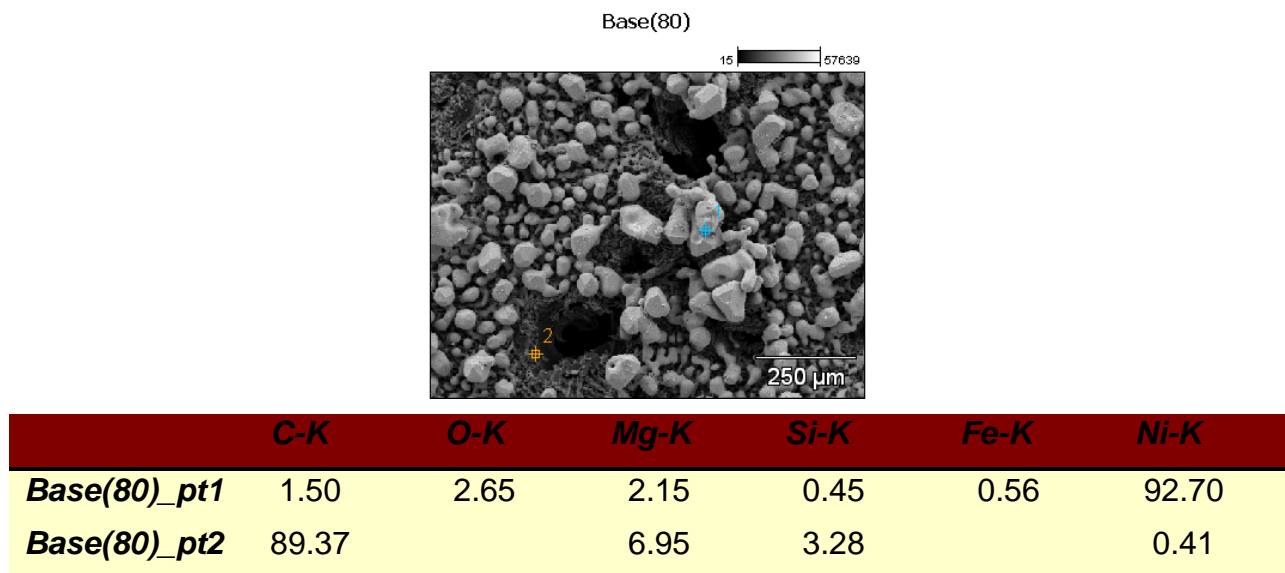|	C-K	O-K	Mg-K	Si-K	Fe-K	Ni-K
Base(80)_pt1	1.50	2.65	2.15	0.45	0.56	92.70
Base(80)_pt2	89.37		6.95	3.28		0.41

Figure 9-18. Compositional analysis at two spots of 3-dip SiC-coated graphite foam samples after Test 4 as measured by SEM-EDS.

9.5. Corrosion of uncoated graphite foam and BNi-4-coated 800H in preheated salt

Figure 9-19 shows a photograph of the uncoated graphite after Test 5a (BNi-4-coated 800H samples are also shown but this will be discussed in the next section). After the samples were cleaned in deionized water and dried in vacuum, the average weight gain of the graphite foam samples was measured to be 9.3 ± 2.2 mg/cm^2. Figure 9-20 shows the difference in surface appearance of the uncoated graphite foam before and after the corrosion tests. The original black surface of the graphite foam turns to light gray after the corrosion test, and there appears to be formation of white crystals on the surface. Figure 9-21 shows the EDS mapping of the surface (Figure 9-22 shows the SEM) and indicates the deposits to be composed of MgO and Ni-rich phases. Although the MgCl$_2$ was treated at 600 ^{o}C for 12 hours, some chemically bonded water in the salt still could be removed.

Figure 9-19. Photographs of uncoated graphite foam and BNi-4-coated 800H immediately after Test 5.
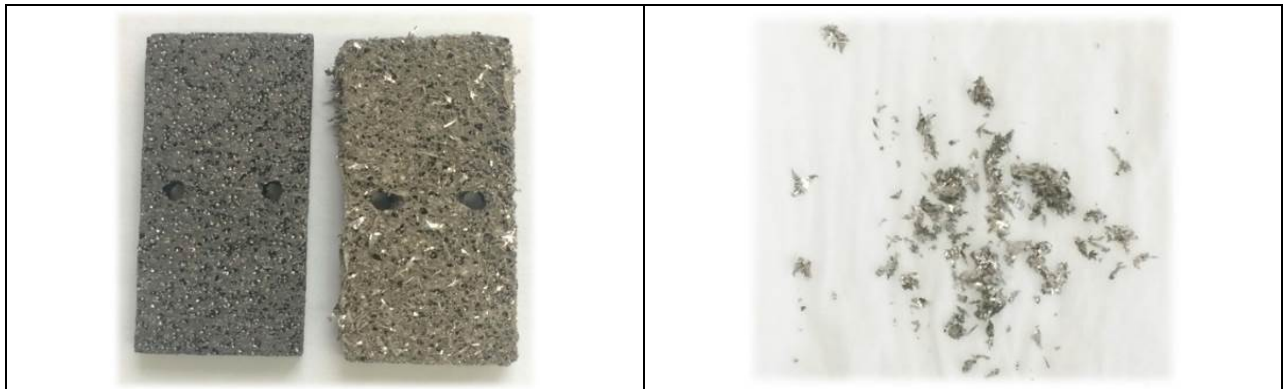

Figure 9-20. Surface condition of uncoated graphite foam samples before (left) and after (middle) Test 5. The photograph on the right shows images of crystals collected from the surface of the graphite foam.
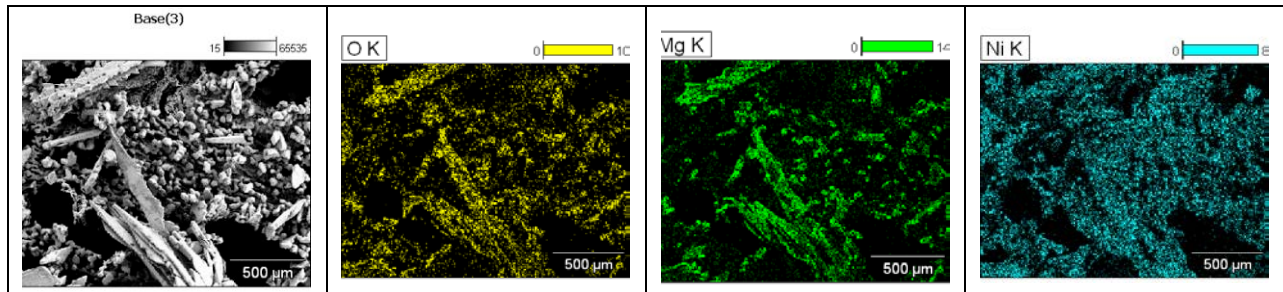
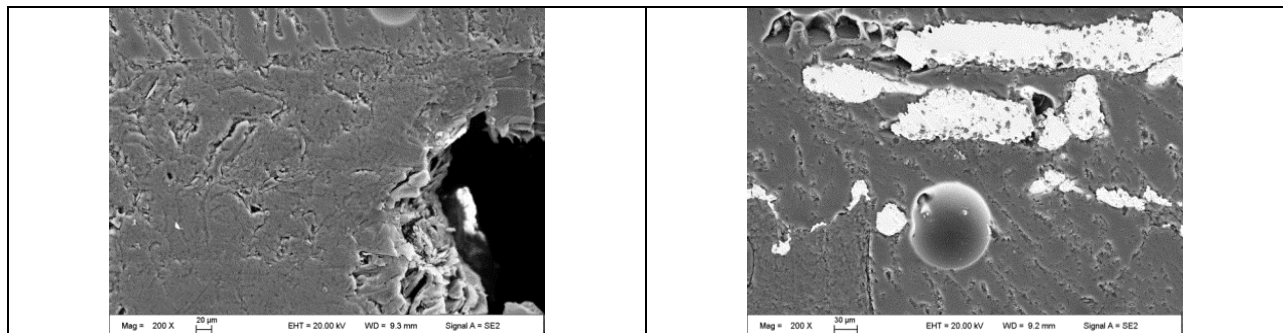Figure 9-21. EDS mapping of the surface of uncoated graphite foam after Test 5.

Figure 9-22. SEM of cross-sectional images of uncoated GF tested after Test 5.

The average weight gain of the BNi-4-coated 800H samples was 2.74 ± 0.64 mg/cm^2. This slight weight gain is mainly attributed to the net effect from two phenomena: (1) the corrosion of the BNi-4 coating, which resulted in slight weight loss, and (2) the deposition of MgO on the sample surface. Figure 9-23 shows the SEM image of the surface of the samples before and after corrosion. No significant corrosion was observed on the surface after the test, and particles were deposited on the surface. The EDS mapping analysis (Figure 9-24) showed these particles to be MgO. Figure 9-25 shows SEM images of the cross section of the BNi-4-coated 800H before and after corrosion and indicates the corrosion of the BNi-4 coating to be negligible.
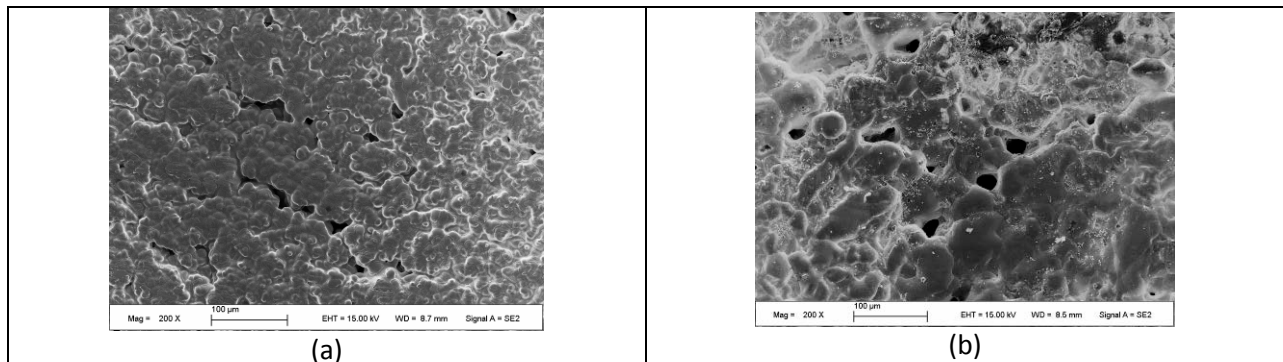

(a)
(b)
Figure 9-23. SEM images of the surface of the BNi-coated 800H: (a) before and (b) after corrosion in Test 5.

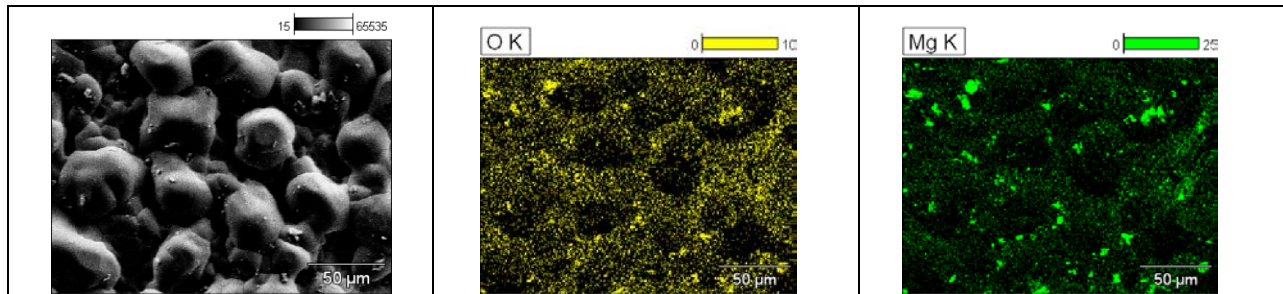Figure 9-24. EDS mapping of the surface of BNi-coated 800H after Test 5, indicating the deposited particles to be MgO.
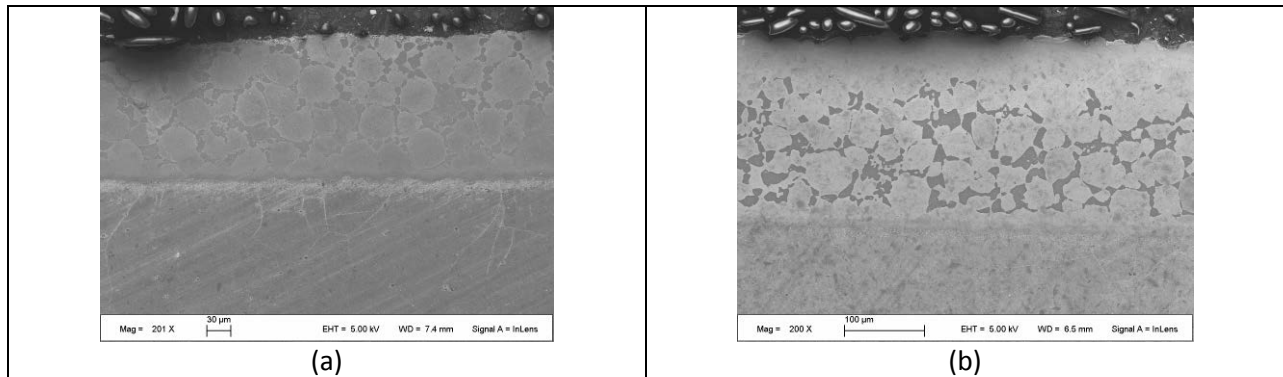

(a)   (b)

Figure 9-25. SEM cross-sectional images of the cross section of BNi-coated 800H: (a) before (b) after Test 5b.

9.6. Corrosion of BNi4-coated graphite foam and mixed BNi4-coated 800H with SiC-coated graphite foams in preheated salt

In Test 6a, the BNi-800H and SiC-coated graphite foam were exposed to the $MgCl_2$ salt melt simultaneously. A weight loss of 3.2 mg/cm^2 was observed in the BNi-coated 800H sample, indicating slight corrosion for this sample. Figure 9-26a shows SEM images of the surface after corrosion, in which some grain boundary corrosion is evident at the surface. Second phase particles (Figure 9-26b) were also observed to be deposited on the surface, which EDS analysis indicated to be MgO and nickel-rich phase. Additionally, as shown in Figure 9-27 cracks were observed in the coatings in the region near the holes used for mounting the sample to the Ni central rod. Comparing these results to those observed where only BNi-4-coated 800H samples were used in the tests, the SiC-coated graphite foam samples may have accelerated the corrosion. Figures 9-28 and 9-29 show the cross-sectional SEM images of BNi-4-coated 800H exposed simultaneously with 3-dip SiC-coated graphite foams. Note that coating thickness was not the same on both sides. Figure 9-30 shows the SEM/EDS analysis of the composition of the BNi-4-coated 800H samples after the corrosion tests. Silicon was preferentially depleted in the near-surface region due to corrosion.

(a)   (b)
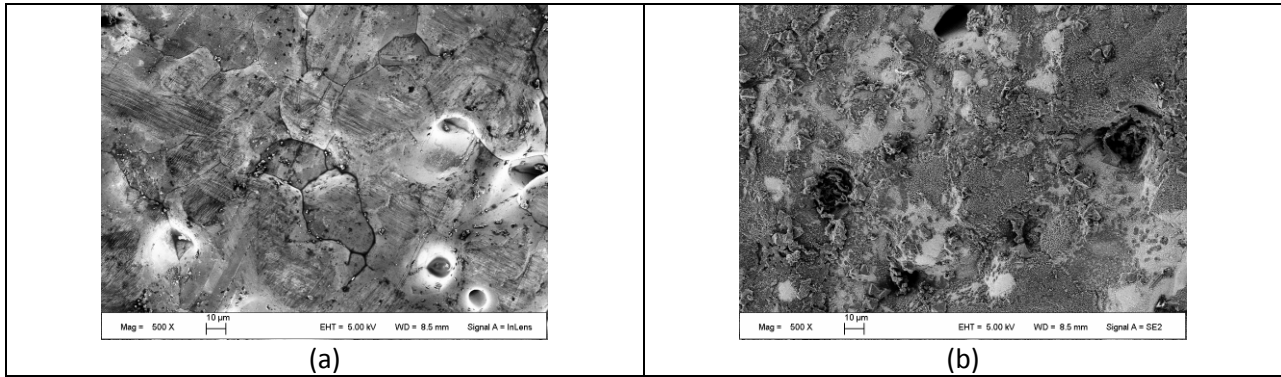
Figure 9-26. SEM images of the surface of BNi-coated 800H samples after being exposed together with 3-dip SiC-coated graphite foam in Test 6.

Figure 9-27. SEM images showing cracks on the surface of BNi-4-coated 800H samples in the vicinity of holes where the samples were fixed to the Ni central rod after Test 6a.

(a)   (b)
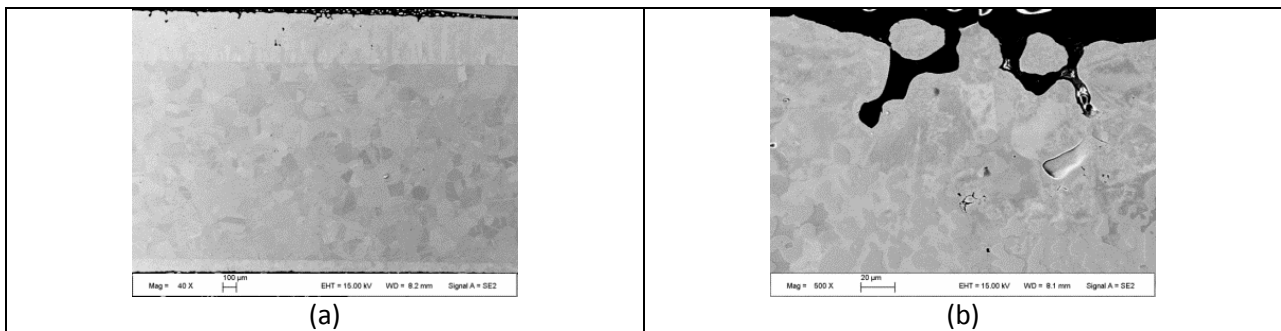
Figure 9-28. Cross-sectional SEM images of BNi-coated 800H exposed to $MgCl_2$ together with SiC-coated graphite after Test 6: (a) low magnification and (b) high magnification.
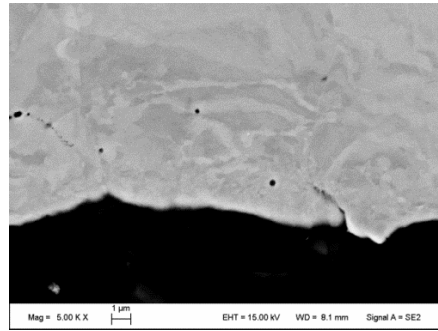
Figure 9-29. SEM image showing possible crack nucleation BNi coating.
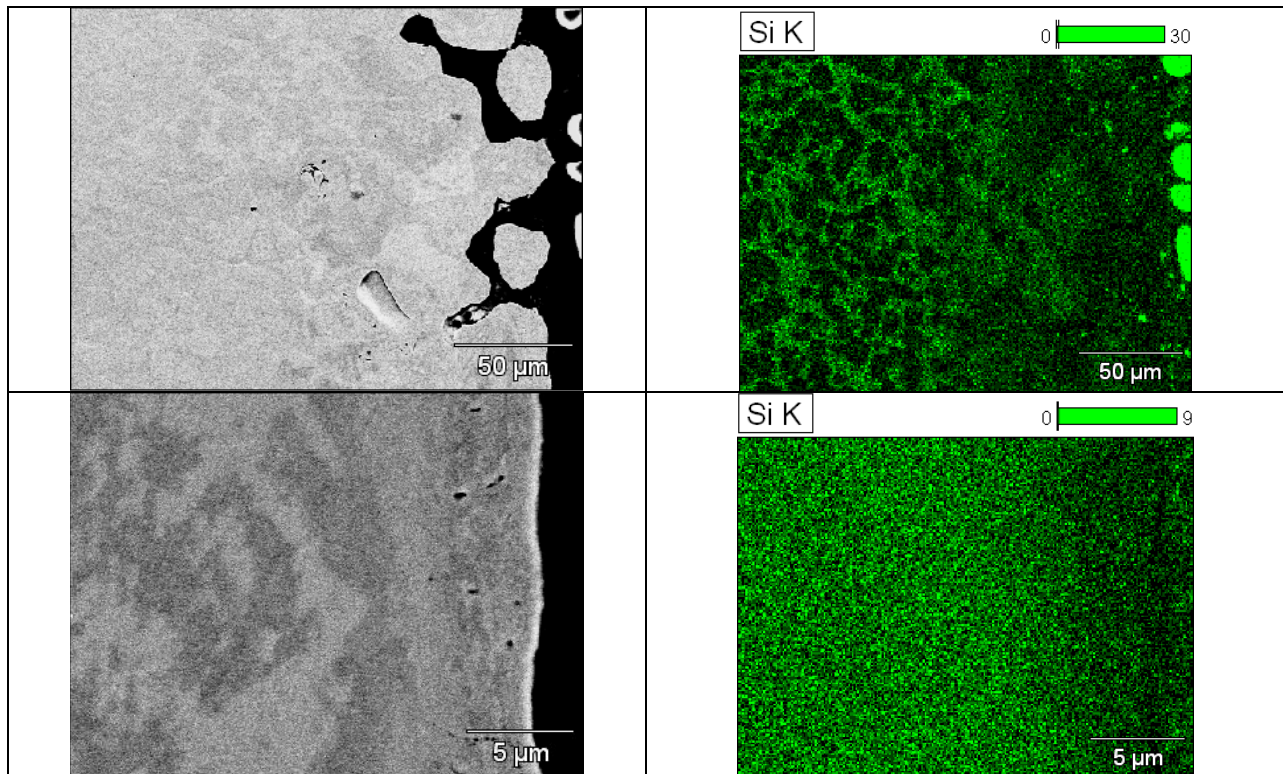
Figure 9-30. Si content in top layer of BNi-coated 800H after Test 6a. The value decreased from 7.5 wt% in the coating matrix to 2.5 wt% near the coating surface.

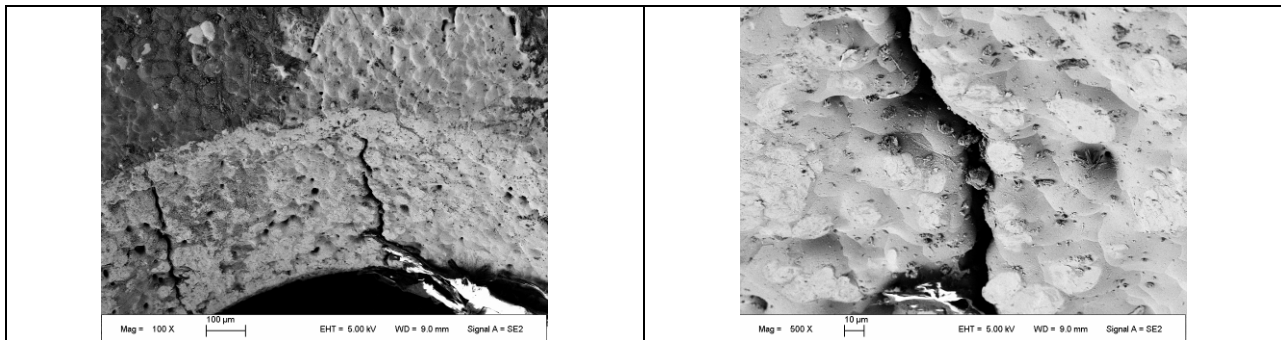The average weight change of the 3-dip SiC-coated graphite foams after Test 6b was 6.7 ± 0.58 mg/cm^2. Figure 9-31 shows the SEM images of the surface of 3-dip SiC-coated graphite foam simultaneously exposed with BNi-coated 800H. Again, particulate deposition is observed, and these phases were analyzed to be MgO and Ni-rich phase (Figures 9-32 and 9-33). Figure 9-34 shows the cross-sectional SEM images of 3-dip SiC-coated graphite foam samples. Some white phases were deposited on the surface and identified to be Ni-rich phase, containing almost 85 wt% Ni as shown in Figure 9-35. No damage or significant corrosion occurred to the 3-dip SiC coated graphite foam.
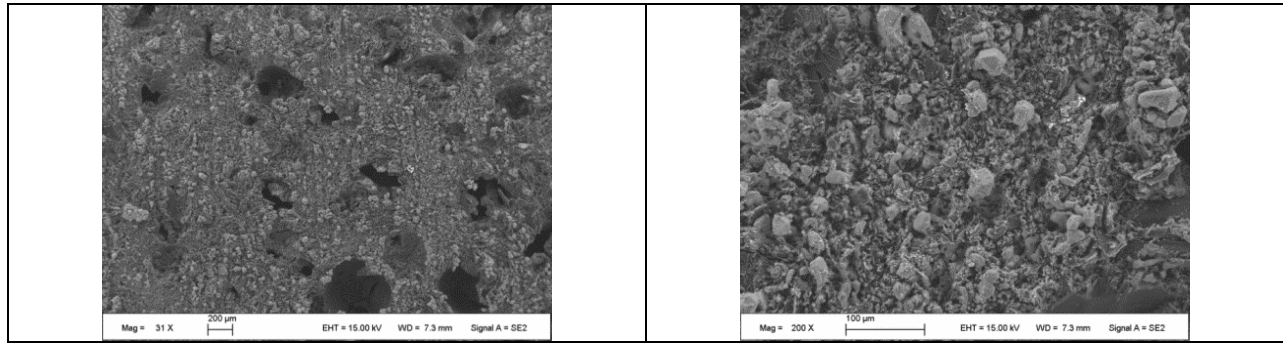
Figure 9-31. SEM images of the surface of 3-dip SiC-coated graphite foam after simultaneous exposure with BNi-coated 800H in Test 6b.

Base(33)
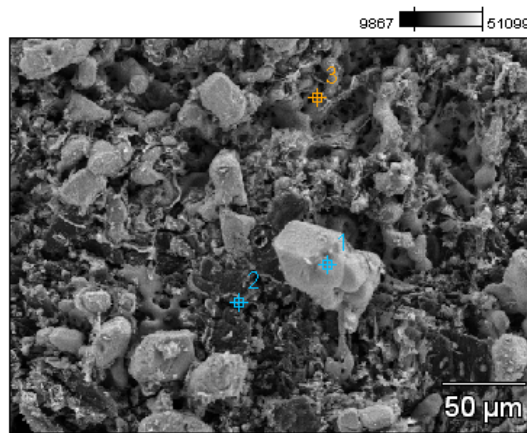
weight%	C-K	O-K	Mg-K	Al-K	Si-K	Cl-K	Cr-K	Ni-K
Point 1	14.49	5.45	1.61	0.19	0.03		0.00	78.23
Point 2	44.80	16.80	3.09		0.29	0.28	0.00	34.75

Figure 9-32. The composition of particulate phases deposited on the surface of 3-dip SiC-coated graphite foam sample in Test 6b.
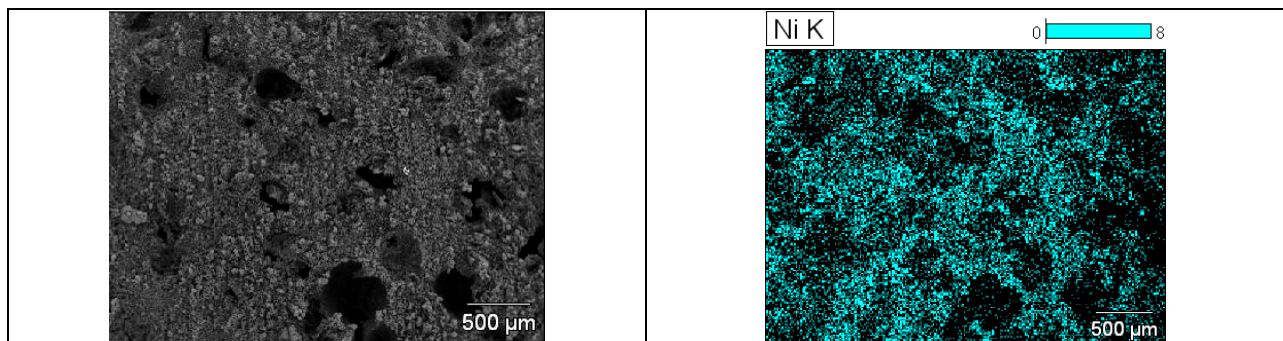
Figure 9-33. EDS mapping of the surface of 3-dip SiC-coated graphite foam in Test 6b. Ni-rich phases are found on the surface.
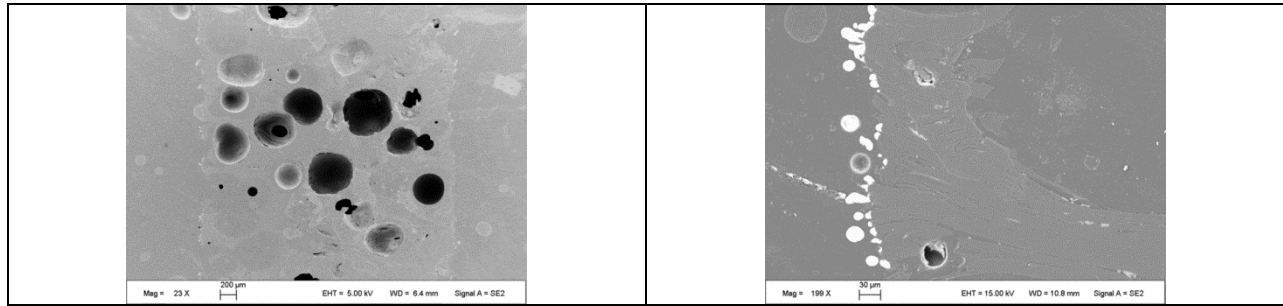
Figure 9-34. SEM cross-sectional images of 3-dip SiC-coated graphite foam sample in Test 6: low magnification image of the entire sample thickness (left) and high magnification image of the phases deposited on the surface (right).

Base(41)
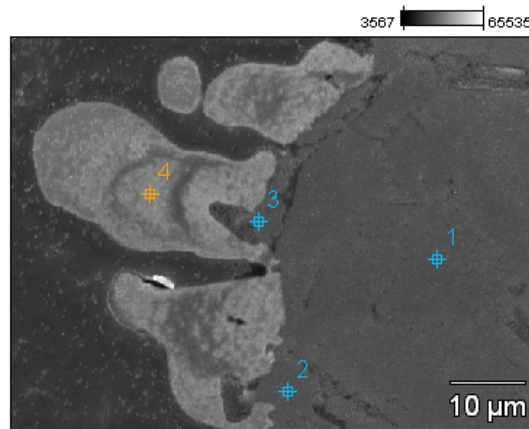
	C-K	O-K	Mg-K	Si-K	Cr-K	Ni-K	Nb-L	Au-M
Base(41)_pt1	89.29		0.04	0.03	0.00	0.94		9.70
Base(41)_pt2	87.84		0.03	1.08	0.07	0.91		10.07
Base(41)_pt3	84.24		0.03	2.52	0.01	1.53		11.67
Base(41)_pt4	0.00	3.28	0.09	2.75	0.12	84.78	8.98	

Figure 9-35. SEM/EDS mapping and point analysis of the composition of the cross section of 3-dip SiC-coated graphite foam sample in Test 6b.

Figure 9-36 shows photographs of three BNi-4-coated 800H samples after exposure for 200 h. The weight change exhibited by the three samples was dramatically different. The left sample in Figure 9-36 shows a 106-mg weight loss, while the right sample shows a 40-mg weight gain, and the middle shows a 4-mg weight loss. The significant scatter in weight change for the three coupons is attributed to the damage (as shown in Figures 9-37 and 9-38) of the coating near the holes made for mounting for corrosion testing. The weight change data are, therefore, irrelevant because of the spallation of the coating and deemed as being an inappropriate metric for evaluating corrosion of these samples.

Figure 9-39 shows the SEM images of the surface of the sample after Test 6c. The corrosion on the surface looks slight, if any, and again some oxides were deposited on

the surface, which may have contributed to the weight gain observed in some samples. Figure 9-40 shows the SEM images of the cross-sectional image of the sample after test 6, which also indicates low corrosion. Again, these cross-sectional images indicate corrosion to be very slight, and the SEM-EDS analysis shown in Figure 9-41 indicates slight depletion of Si in the near surface regions of the coating.

Figure 9-36. Photographs of three BNi-4-coated 800H samples after Test 6c.
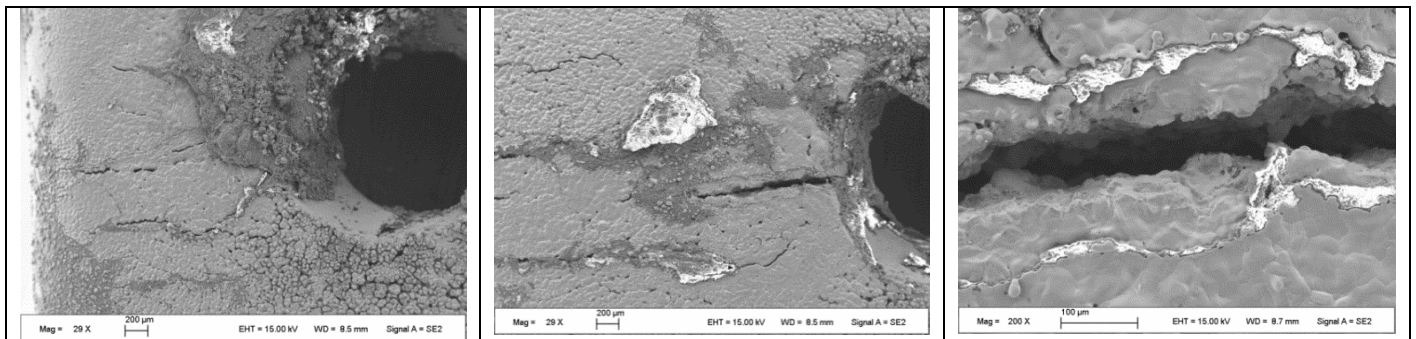

Figure 9-37. SEM images of the surface of BNi-coated 800H samples showing spallation of the coating in the vicinity of the holes used for fixing the samples to the central rod.
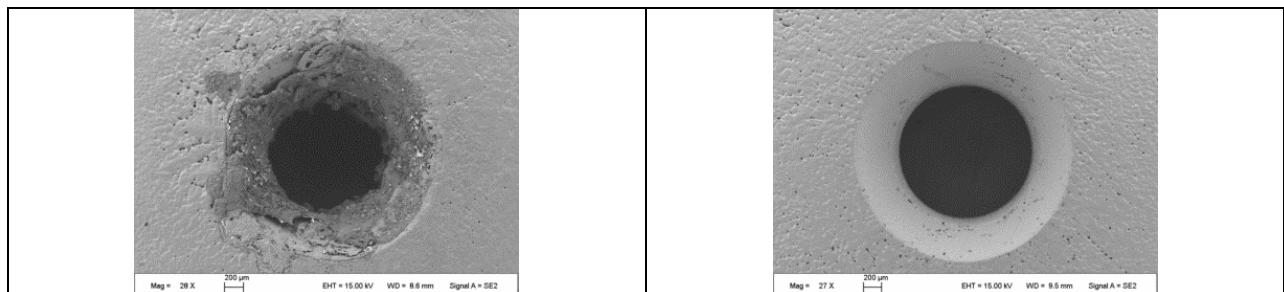
Figure 9-38. SEM images of BNi-coated 800H samples in the vicinity of the holes after Test 6c.
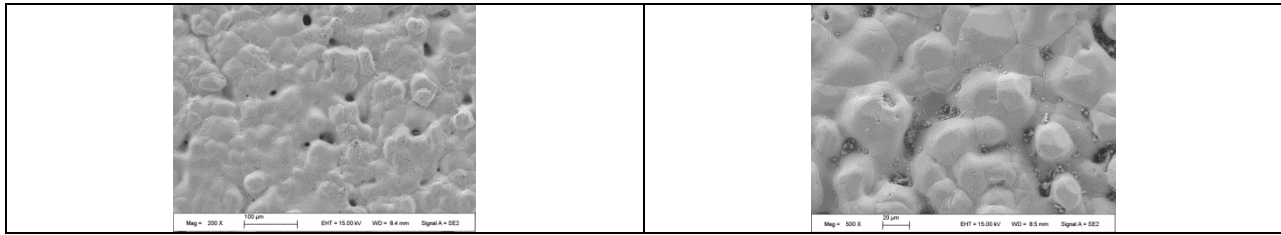
Figure 9-39. SEM images of the surface of BNi-coated 800H sample after Test 6c.
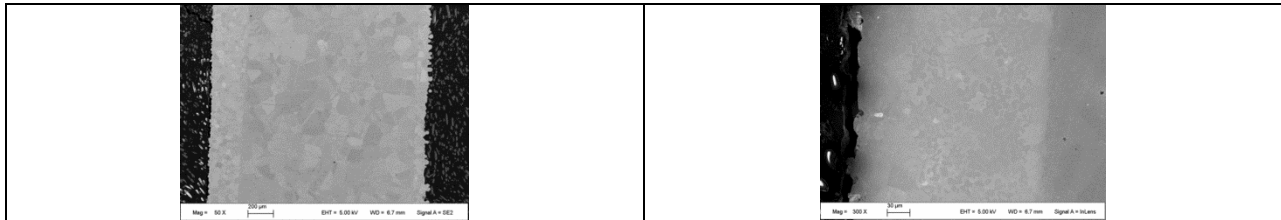
Figure 9-40. Cross-sectional SEM images of BNi-coated 800H sample after Test 6.
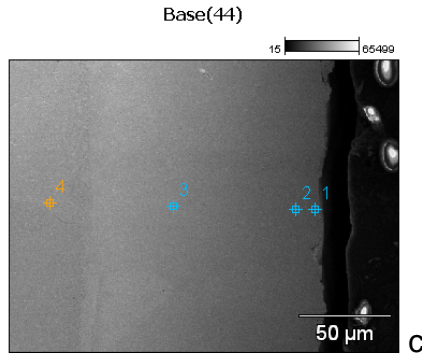
	C-K	O-K	Mg-K	Al-K	Si-K	Ti-K	Cr-K	Fe-K	Ni-K	Ta-L
Base(44)_pt1	0.11	0.57	0.00		2.37		0.22		95.86	0.86
Base(44)_pt2	1.21	0.44	0.00		5.11		0.07	0.59	92.57	
Base(44)_pt3	1.69	0.22	0.00		5.08		0.29		92.73	
Base(44)_pt4	1.88	1.46	0.10	0.87	0.51	0.41	22.17	45.45	27.15	

Figure 9-41. SEM/EDS analysis of the composition of the BNi-4-coated 800H after Test 6c.

9.7. Corrosion of mixed BNi-coated 800H with 3-dip SiC-coated graphite foam and BNi-coated 800H in preheated MgCl$_2$

This test involved ingress of oxygen into the glove box due to corrosion of pump system components resulting from Tests 1-6. Figure 9-42 shows photographs of the samples after Test 7a. The color of the SiC-coated graphite foam changed from black to gray, and the weight gain was 38 mg/cm^2. The SEM imaging of the surface of this sample showed extensive particulate deposition (Figure 9-43). The SEM/EDS analysis (Figures 9-44 and 9-45) showed the surface deposits to be mainly Ni-rich phase, MgO, and some residual MgCl$_2$. Figure 9-46 shows the SEM image of the cross section of the

sample after Test 7. Nickel-rich phases were observed on the surface, but the surface of the 3-dip SiC-coated graphite foam appears intact after corrosion tests.

Figure 9-42. Photographs of 3-dip SiC-coated graphite foam (1 coupon, left) and BNi-coated 800H (2 coupons, middle and right) after Test 7.
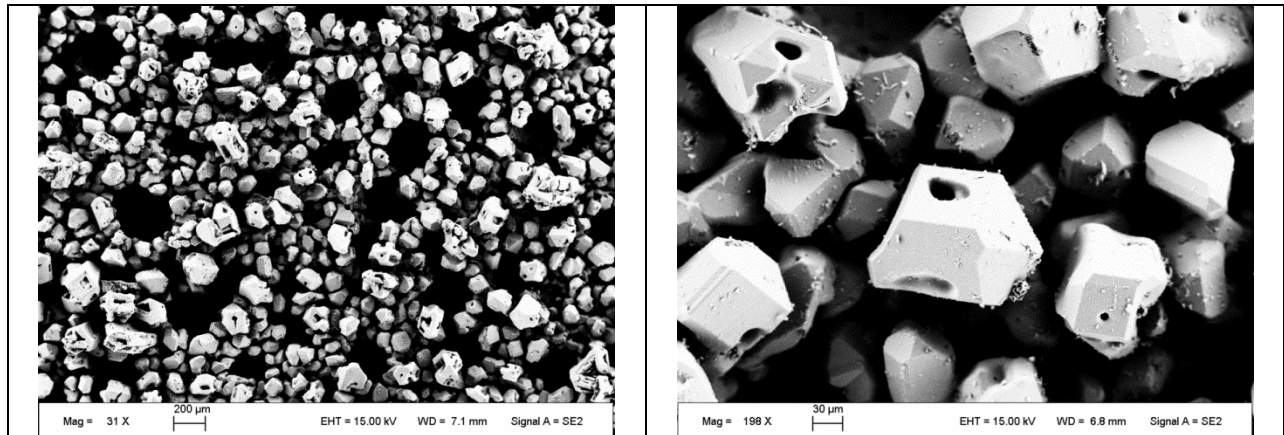
Figure 9-43. SEM images of the surface of 3-dip SiC-coated GF sample after Test 7.
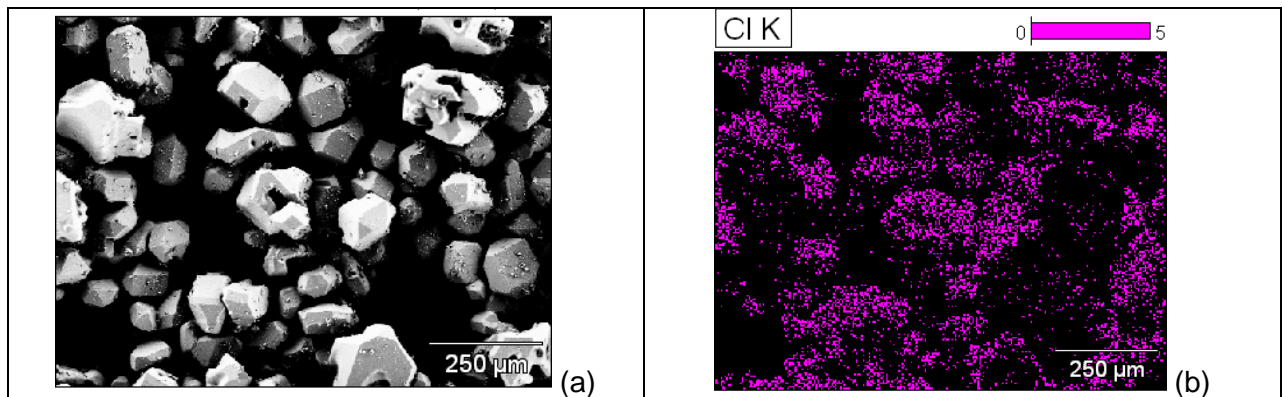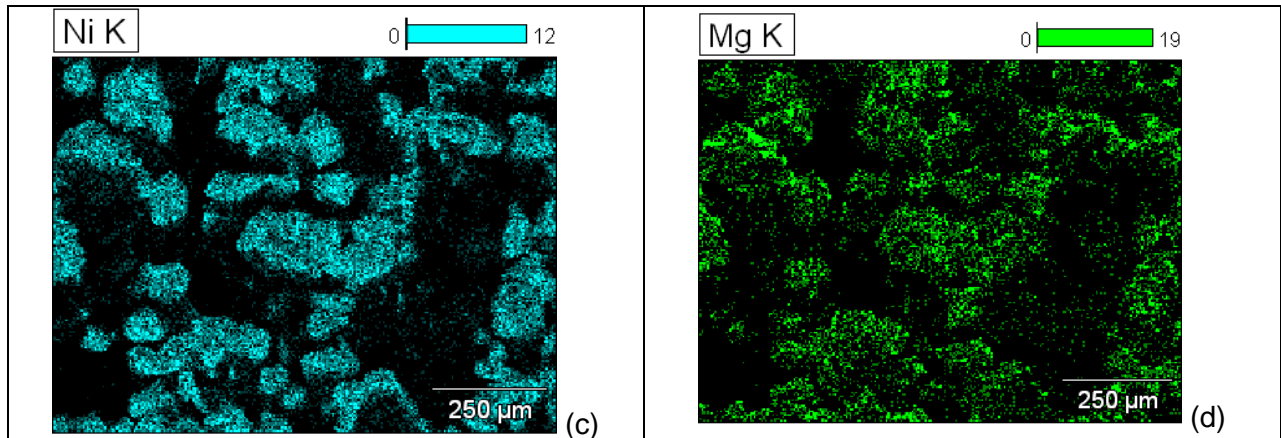
Figure 9-44 (a-d). SEM/EDS mapping of the surface of 3-dip SiC-coated GF samples after Test 7 showing Ni-phase MgO deposits, and $MgCl_2$ residue on the surface.

	C-K	O-K	Mg-K	Si-K	Cr-K	Fe-K	Ni-K
Base(141)_pt1	0.00	5.37		0.10	0.09	0.00	94.44
Base(141)_pt2	0.00	7.06	2.96	0.18	0.00	0.32	89.48
Base(141)_pt3	0.00	2.99		0.21	0.05	0.44	96.31
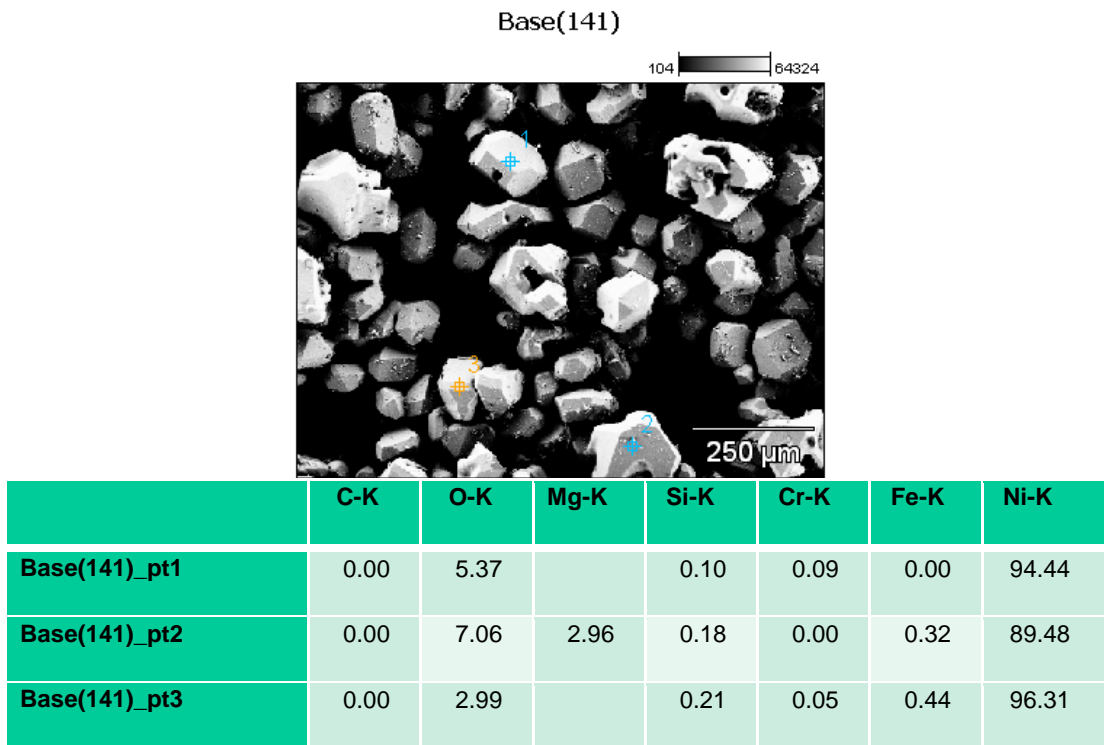
Figure 9-45. Composition the surface deposits on 3-dip SiC-coated GF samples as evaluated by SEM/EDS analysis.
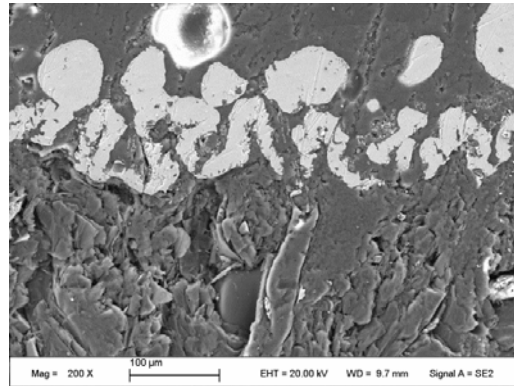
Figure 9-46. SEM cross-sectional image 3-dip SiC-coated GF samples after Test 7 showing Ni-rich phases on the surface while the sample surface was largely intact.

As shown in Figure 9-47, the samples of BNi-coated 800H showed some cracking and damage on the edges during the corrosion test. The average weight loss of the samples from Test 7 was 1.6 mg/cm^2. Because of the damage in the coating, some underlying alloy 800H alloy may have been exposed to the molten salt, which may have resulted in this weight loss. The actual corrosion rate, therefore, may be lower. Figure 9-47 shows the SEM images of the sample after corrosion testing. There is evidence of slight corrosion and grain boundary attack. Some MgO oxides were also identified on the surface by SEM/EDS mapping as shown in Figure 9-48. Figure 9-49 shows the SEM image after corrosion. From this SEM image, the corrosion of the BNi-coated 800H sample appears to be very slight, if any.
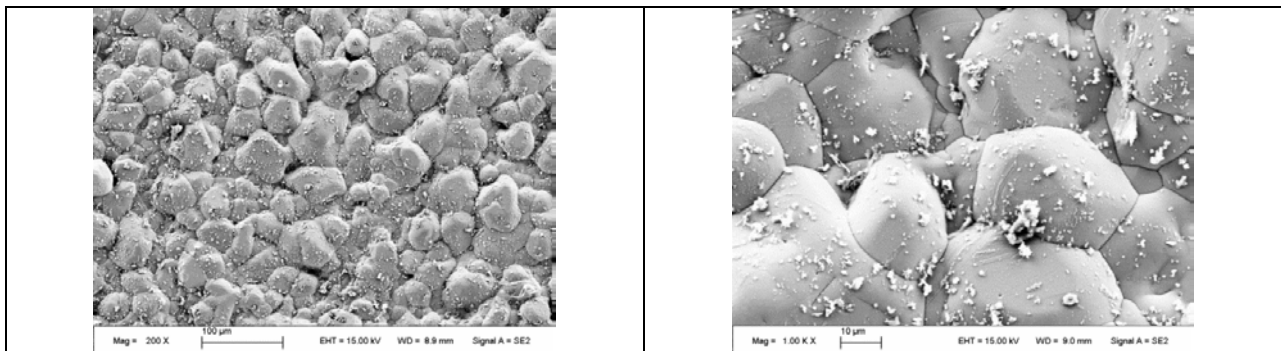
Figure 9-47. SEM surface images of the surface of BNi-coated 800H after Test 7.
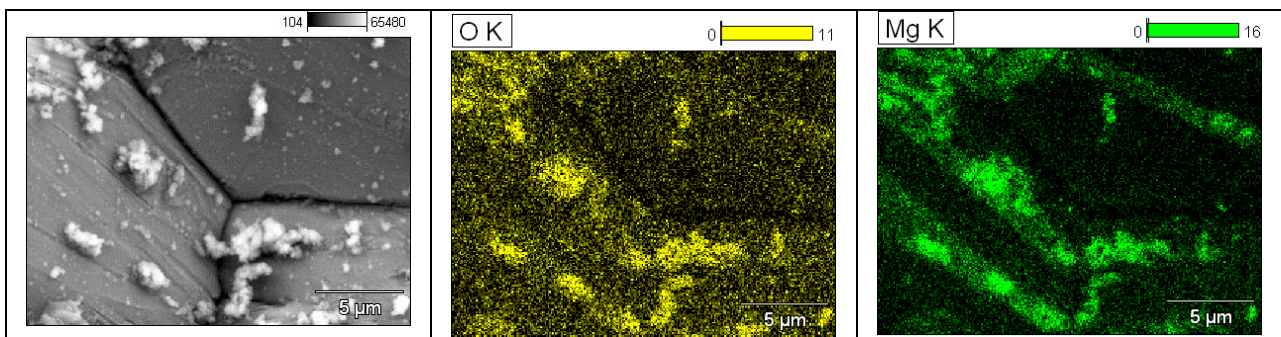
Figure 9-48. SEM/EDS X-ray mapping of the surface of BNi-coated 800H after Test 7 showing MgO particles deposited on the surface.
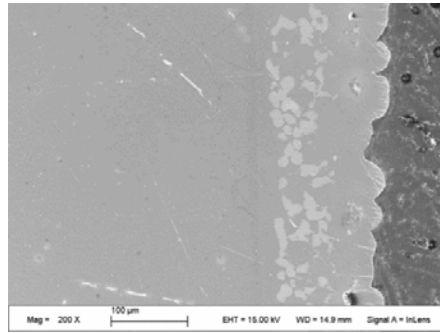
Figure 9-49. SEM cross-sectional image of BNi-coated 800H after Test 7 showing very little corrosion damage.

In Test 7c, the average weight change of BNi4-coated 800H after exposure for 500 h was a significant -36 ± 12 mg/cm^2. Figures 9-50 and 9-51 show the surface and cross-sectional SEM images of this sample, respectively. The grain-boundary corrosion attack depth was about 10 µm.
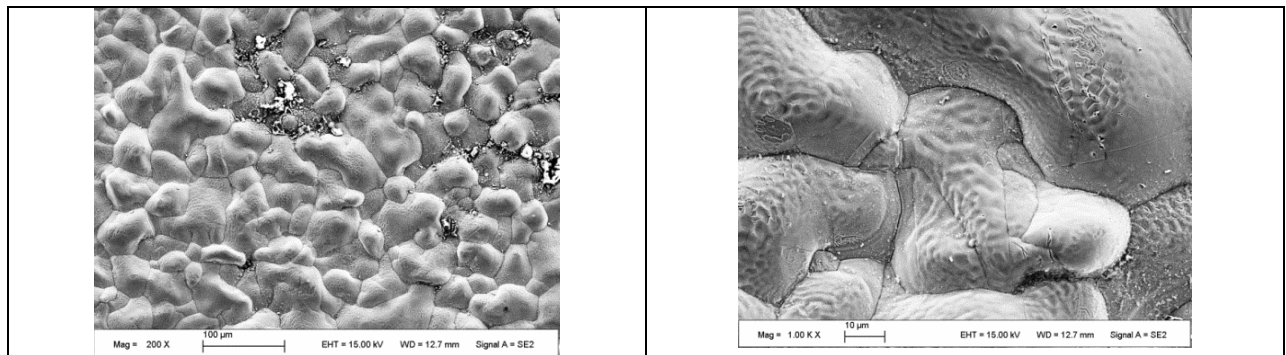
Figure 9-50. SEM plan view surface images of BNi-coated 800H samples after Test 7.
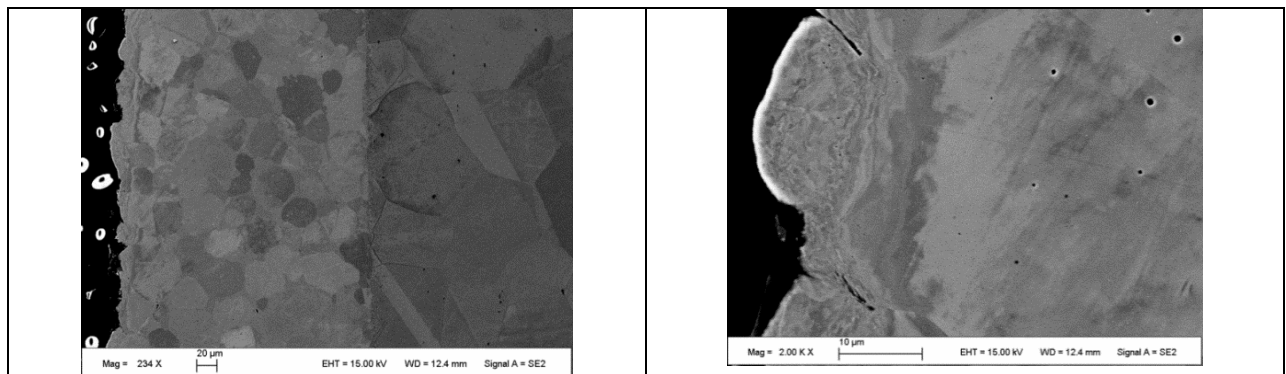
Figure 9-51. Cross-sectional SEM images of BNi-coated 800H samples after Test 7.

9.8. Corrosion of mixed samples (SiC-coated graphite foam, uncoated graphite, pure Ni, and BNi-coated 800H) in MgCl$_2$ salt

In Tests 1-7, it was clear that considerable moisture was present, including for experiments conducted with salt that was preheated at 600 ^{o}C for 12 hr. This moisture

resulted in the formation of corrosive HCl, which accelerated corrosion of materials tested and resulted in large scatter in results.

For Test 8, anhydrous $MgCl_2$ was procured, and flowing Ar gas was used to purge any HCl gas formed during the melting of the salt and during corrosion testing. Furthermore (as shown in Figure 9-52), in Test 8 the exiting HCl gas was channeled into a beaker containing water, and the pH value of the water was measured. When the temperature of the salt reached 175℃, the pH value of the water was 4.5, which indicated that HCl had already formed at this temperature. When the salt temperature was increased to 400℃, acid fog formed above the water in the beaker, indicating formation of considerable HCl at 400℃. After holding at 400 ℃ for 3 hours, the temperature of the salt was increased to 650℃, and this again led to HCl fog formation above the water level.   This salt fog formation subsided slowly after 2 hours of holding at 650℃. Increasing the temperature to 750 ℃ again led to strong HCl fog formation above the water surface. Figure 9-52 shows a picture of the HCl-fog formation over the water surface.   It is clear that complete expulsion of water from the salt is required prior to corrosion test; alternatively, some type of a purification treatment has to be employed. Figure 9-53 shows photographs of crucibles used in Tests 1 to 7 and Test 8, which show a significant difference.   In crucibles used in Tests 1-7 the greenish color represents the formation of a metal chloride as a result of the evolution of HCl. Post Test 8, the salt re-solidified in the crucible appeared very clean and dense, unlike in the previous tests. It also took much longer to dissolve the salt using in the deionized water as compared to Tests 1 to 7.

Figure 9-52. HCl fog formed above the water surface in the beaker. Detailed information on the experimental setup is shown in Figure 9-4.

Figure 9-53. Photographs of the crucibles after corrosion tests: (a) Two nickel crucible used in Test 1 to 7 and (b) nickel crucible used in Test 8 where anhydrous salt coupled with argon sparging was used.

The weight change of pure nickel (Ni-200) sample was -0.09 mg/cm^2, indicating very little corrosion. Figure 9-54 shows photographs of samples from Test 8 before and after corrosion. It appears the pure nickel (first sample from left) is brighter after the corrosion test. Generally, a thin NiO always formed on the surface of pure Ni, and this NiO was presumably fluxed away in the molten MgCl$_2$, making the pure nickel appear brighter. Figure 9-55 shows the SEM surface images of pure nickel before and after corrosion. Although some grain boundary attack occurs, corrosion is very slight. Again, in Test 8, the effects of HCl formation were minimal (lasting for several hours) as compared to Tests 1 to 7, where the crucible was covered, and the HCl was retained inside and stayed for the entire corrosion process.
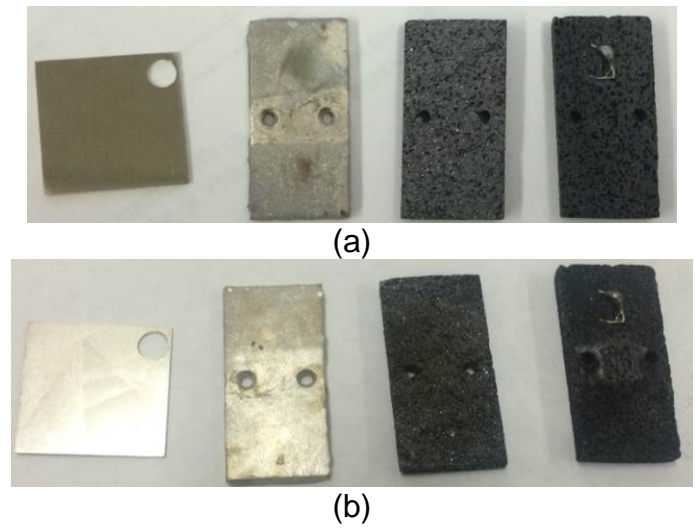
Figure 9-54. Photographs of samples after Test 8: (a) before and (b) after corrosion tests. From left to right, pure nickel, BNi-coated 800H, uncoated graphite foam, and 3-dip SiC-coated GF with BNi braze.
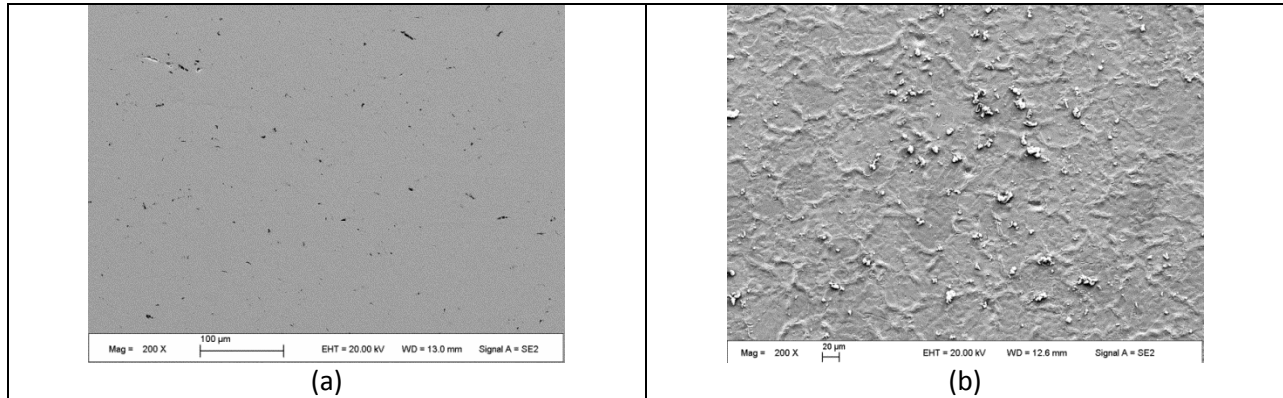
Figure 9-55. SEM image of surface of pure nickel (a) before and (b) after Test 8.

The weight change for the BNi-coated 800H sample was -0.28 mg/cm^2, which is quite low. However, slight corrosion was observed by SEM on the surface, as shown in Figure 9-56, but the corrosion attack was more severe than that of pure nickel samples.
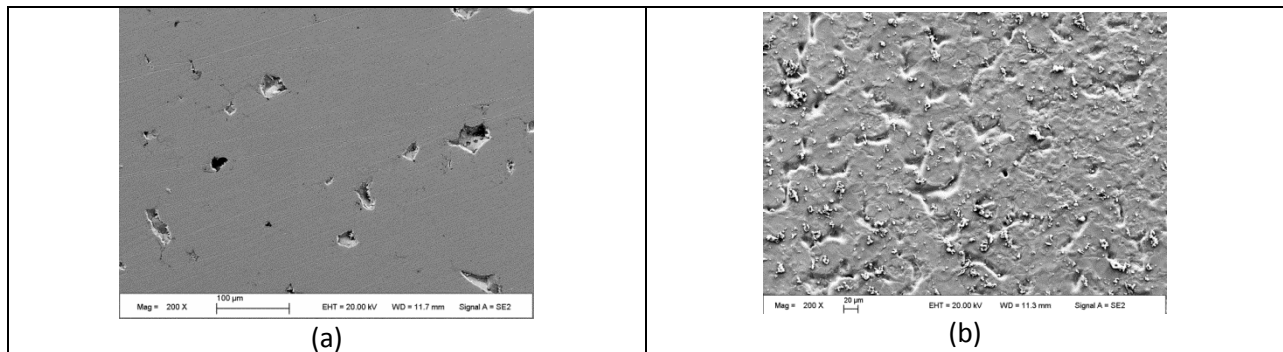
Figure 9-56. SEM surface images of BNi-coated 800H (a) before (b) after Test 8.

The weight gain for the uncoated graphite foam was 0.39 mg/cm^2, some of which could be attibuted to the deposition of oxides and Ni on the surface. Figure 9-57 shows the SEM images of uncoated graphite foam before and after Test 8. No corrosion of the uncoated graphite foam was observed. But a small amount of MgO and Ni-rich phases were detected by SEM/EDS of the surface of the sample.
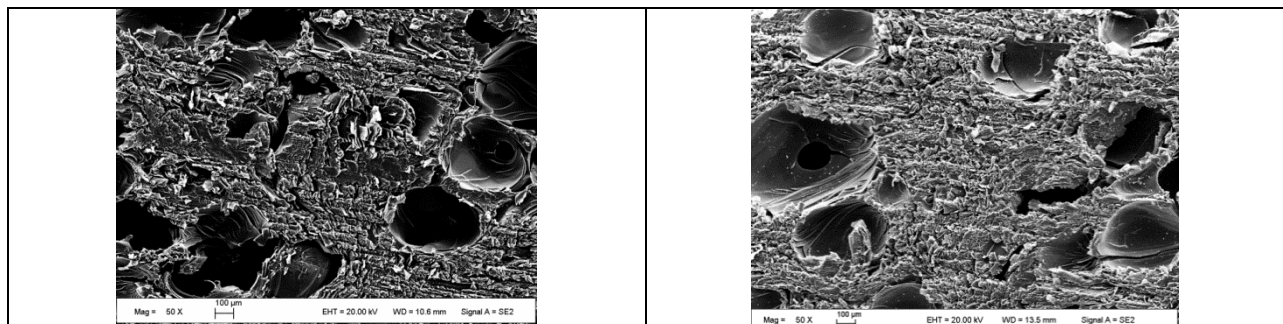
Figure 9-57. SEM surface images of uncoated GFs (a) before and (b) after Test 8.

The weight gain SiC-coated graphite foam was 1.6 mg/cm^2. Figure 7-58 shows the SEM images of the this sample with BNi braze spot before and after Test 8. No corrosion was observed on the surface of the SiC-coated graphite foam.
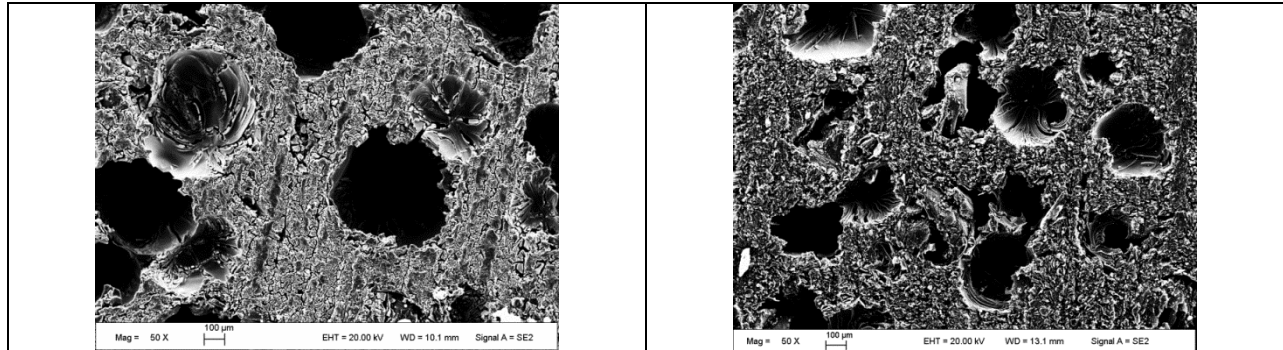
Figure 9-58. SEM images of 3-dip SiC-coated GFs (a) before and (b) after Test 8.

9.9. Comparison of various test results

Figure 9-59 lists the weight change of all the graphite foam materials after corrosion in the various tests performed in this study. In all the corrosion tests, there was weight gain after corrosion. The actual value of weight gain was dependent on the deposition of MgO and other deposits, such as Ni-rich phases. In Test 7a, significantly higher weight gain was observed as compared to other tests. This may be partly due to the ingress of a small amount of air into the glove box, because after Tests 1 to 6 some of the metallic parts of the pumping system for the glove box may have been corroded by the HCl formed during heating, melting, and corrosion tests. Based on the weight gain data and the microstructural analysis of the different graphite foams, we concluded that 3-dip SiC-coated graphite foams have good corrosion resistance in MgCl$_2$. Even under the strong effect of corrosive HCl formed in the corrosion tests, no significant corrosion was observed. No significant difference between 1-dip and 3-dip SiC-coated graphite foams was observed. From Test 8, it can be tentatively concluded that uncoated graphite foam is compatible with other materials. Whether the uncoated graphite foam has accelerating effects on the corrosion of structural materials is not clear and warrants further study.
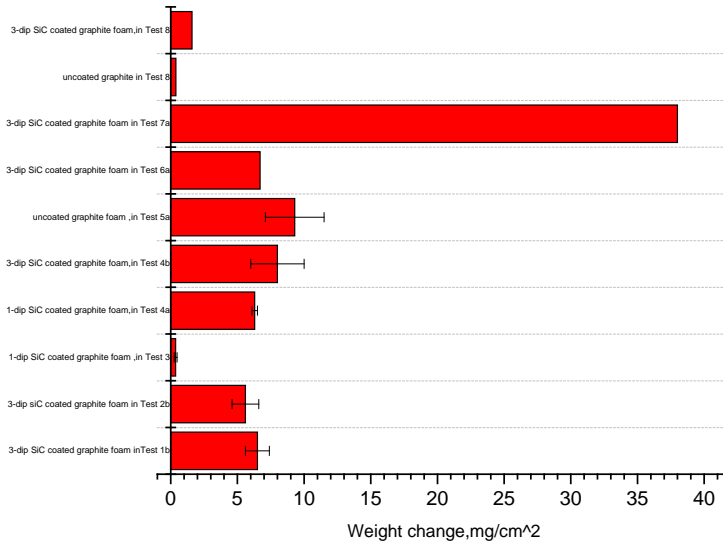
Figure 9-59. Weight change of graphite foam and SiC-coated graphite foam samples in various tests.

Figure 9-60 compares the weight change data of alloy 800H exposed for 100 h (in Test 1a) and 200 h (in Test 2a).The longer exposure time (200 h) did not increase the weight loss significantly. But in both tests, 800H had significantly higher corrosion rate, and it should be protected before being considered as a structural material in molten $MgCl_2$ salt.
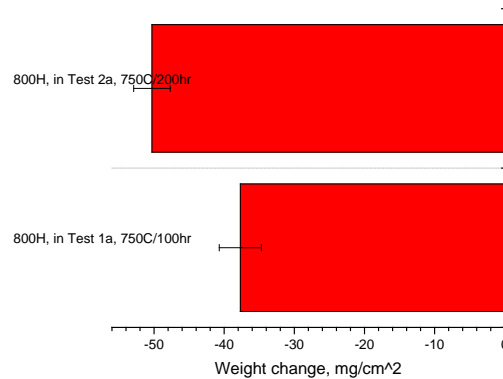
Figure 9-60. Weight change of alloy 800H in Tests 1a and 2a.

Figure 9-61 shows the weight change data of various metallic materials, including 800H, BNi-coated 800H, and pure Ni. In Test 7, some air may be introduced into the glove box, and the increase in the oxygen partial pressure may have resulted in a significantly higher weight loss of BNi-4-coated 800H in $MgCl_2$ for 500 hr. A duplicate experiment may be needed to verify the long-term corrosion for exposure to $MgCl_2$ salt. The weight gain of BNi-4-coated 800H in Test 5b is attributed to some deposits on the sample

surface. As compared to 800H, the corrosion of BNi-4-coated 800H is much lower. Almost no corrosion was observed in pure nickel. The BNi-4-coating is more susceptible to corrosion than pure nickel, and Si in the BNi coating preferentially depleted at the surface. But from the weight change data and microstructure study of the BNi4-coated 800H in different tests, we tentatively concluded that the BNi coating is corrosion resistant in $MgCl_2$. If the $MgCl_2$ is purified and the oxygen and chlorine potential of test atmosphere is well controlled, even lower corrosion rate can be expected for BNi-coated 800H.
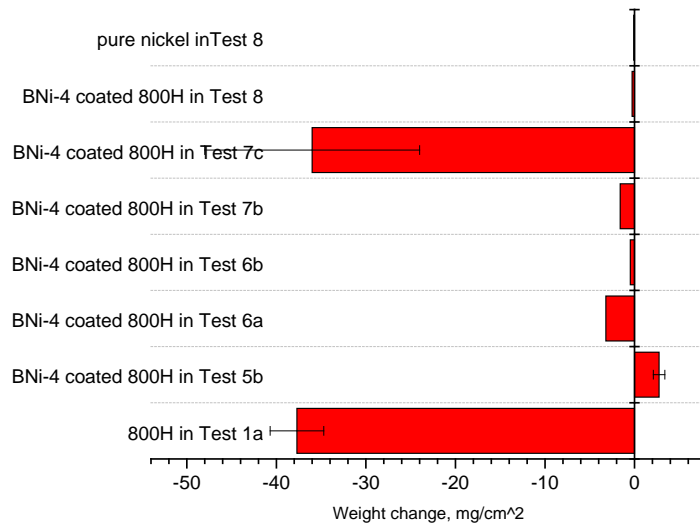
Figure 7-61. Weight change of various metallic materials 800H, BNi-coated 800H, and pure nickel in various tests

This corrosion study completed Milestone 2.2. Principal conclusions are as follows:

1. The corrosion rate of 800H in molten $MgCl_2$ is quite high due to depletion of Cr; the galvanic corrosion between 800H and Ni in the molten salt may also be a factor in the high corrosion of alloy 800H.
2. SiC-coated graphite foam is very corrosion resistant even in the $MgCl_2$ melt, as evidenced by low corrosion in moisture-ridden as-received $MgCl_2$; no significant difference was observed between 1-dip and 3-dip samples.
3. Moisture in the $MgCl_2$ can significantly affect the corrosion. Pre-heating $MgCl_2$ at 300 °C and 600 °C for 12 hours was not sufficient to eliminate this moisture. Moisture greatly accelerates corrosion due to the formation of HCl. This was verified by using anhydrous salt and Ar sparging to remove HCl from the system, where significantly lower corrosion was observed.
4. BNi-4-coated 800H is corrosion resistant in $MgCl_2$ salt in the Ni crucible, and it is generally concluded that this coating can provide good protection; however, some depletion of Si was observed in the near-surface regions of this coating.
5. Using anhydrous salt and Ar flow to eliminate moisture (Test 8) mitigates the corrosion of materials, including uncoated graphite foam.

10. Laboratory-Scale Experiment Design and Modeling

As discussed in the previous sections, detailed modeling and simulations were carried out to analyze the foam/PCM-based LHTES system in charging/discharging modes. Such studies provide insights to the performance of the LHTES system. However, several assumptions go into the simulations, such as the thermal interfacial resistances, material properties, and PCM infiltration rate. Therefore, it is necessary to validate the simulations by experiments. In this regard, the lab-scale test loop system was designed and built to evaluate the performance of prototypes.

From such testing key information could be generated in the following areas: the liquid-solid interface (the melting front for the charging process) progress as a function of the time, the temperature at a specific location as a function of time, and the temperature space distribution inside the composite of the graphite foam and the PCM. Further interpreted results for the effects of the material property on the charging/discharging cycle can be achieved through analyzing and comparing the predictions from the numerical simulations and the experimental data from tests under various conditions of thermal cycling of the PCM. It is expected that the experimental data from the lab-scale experiment, together with the predictions from the numerical simulations, will provide information for predicting the performance of full-scale LHTES systems.

10.1. Objectives of the lab-scale charging/discharging experiment

The objectives of lab-scale LHTES prototype charging/discharging experiments were to:

1) compare experiment measurements with simulation results to verify the simulation model and the properties of graphite foam-$MgCl_2$ combination (thermal diffusivity, latent heat of fusion, etc.),
2) investigate both charging and discharging processes to study the melting and solidification in the PCM,
3) repeat heating-cooling thermal cycles to determine the thermal cycling effects on the LHTES system, and
4) verify the feasibility of the LHTES system meeting the SunShot's performance targets.

10.2. Lab-scale prototype LHTES and test loop facility

10.2.1. Lab-scale prototype LHTES
A schematic of the prototype is displayed in Figure 10-1. Incoloy 800H was used for fabricating the prototype container and the heat transfer fluid (HTF) pipe. A graphite foam-$MgCl_2$ composite was used as the storage medium. The size of the whole prototype was 4.5 in. diameter and 6 in. height. The dimension of the inside graphite foam-$MgCl_2$ combination is around 3.83 in. diameter and 5 in. height. There is 1 in. void head-space above the storage medium inside the prototype container to allow the thermal expansion of $MgCl_2$ and the welding of the container cap. The outer diameter of the inside HTF tube is around 0.5 in. with a tube wall thickness of 0.028 in. There were

six thermocouples inserted in the graphite foam-PCM combination to measure the temperatures at various locations. Figure 10-2 shows the distribution of the thermocouples in the storage medium. A standard half-inch tube goes through the center of the prototype container working as the HTF tube. The procedure to fabricate the prototype is described in Table 10-1 in detail. After the fabrication of the prototype, it was assembled into the experimental loop facility for the charging/discharging experiments.
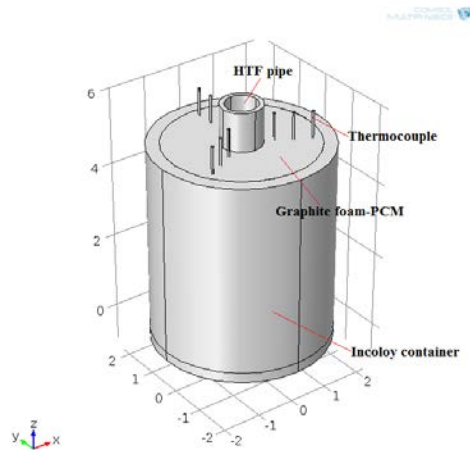
Figure 10-1. Overall view of the lab-scale LHTES prototype (inches).
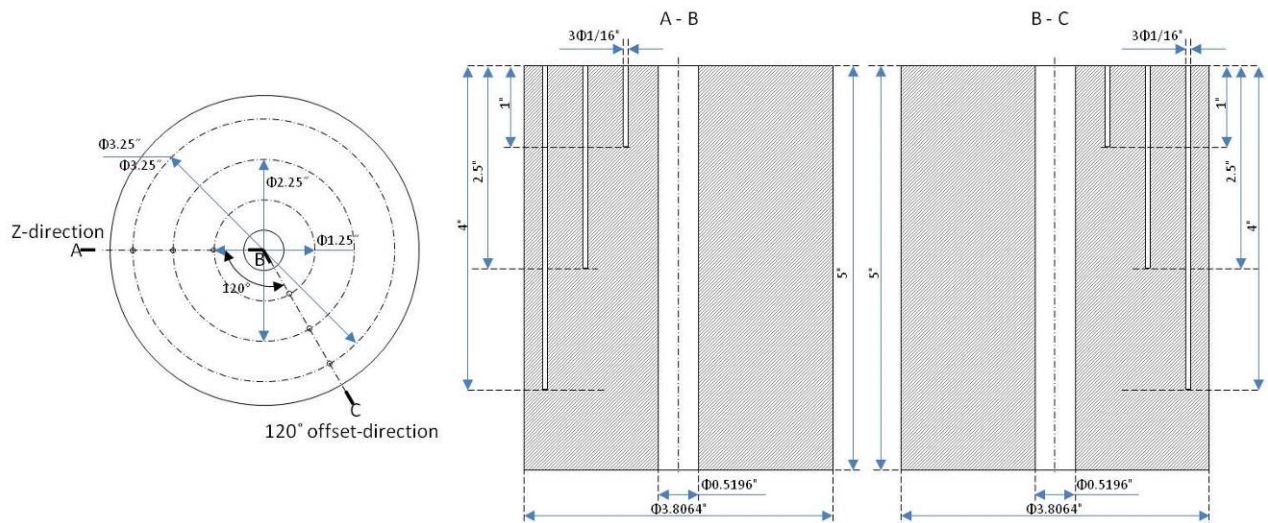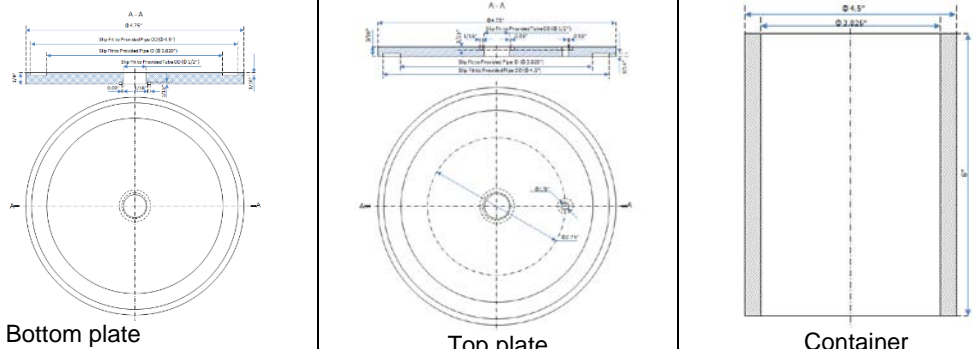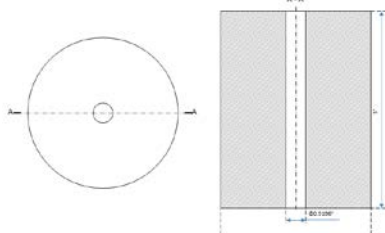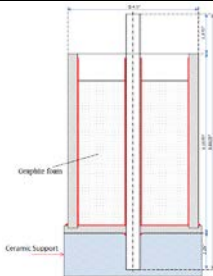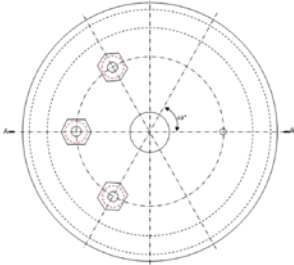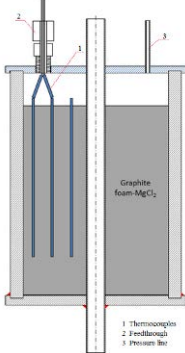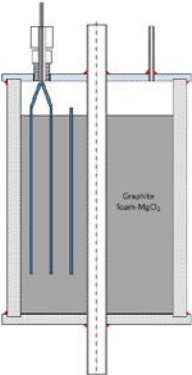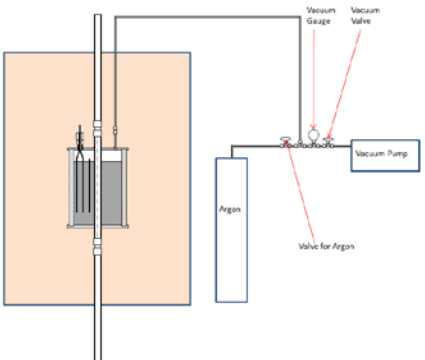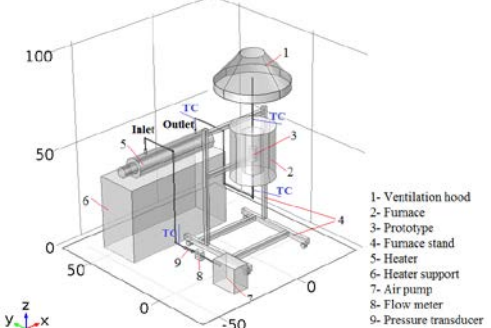
Figure 10-2. Distribution of the thermocouples in the storage medium (inches).

Table 10-1. Sequence of steps for prototype build.

Steps #	Procedure
1	Machine the parts: Bottom plate · Top plate · Container
2	Clean all parts ---
3	Weld bottom plate to the container and HTF tube
4	Machine the graphite foam to fit them into the container as fabricated in Step 3
5	Add SiC coating to the graphite foam ---
6	Brazing process: Braze the graphite foam to the bottom plate, the center tube, and the container wall

7	Infiltration process: Infiltrate molten MgCl₂ into graphite foam to form graphite foam-MgCl₂ combination	---
8	Install feedthroughs on top plates	
9	Install thermocouples in the prototype	
10	Perform second welding to attach top plate to container and HTF	

| 11 | Install vacuum/gas purging system | |
| 12 | Assemble the prototype on the experimental loop | |

10.2.2. Experimental loop facility

The experimental system is an open loop as shown in Figure 10-3. Air was used as the HTF in the system for charging and discharging. The system mainly consists of an air flow pump, a flow meter, a heater, air flow and temperature interlocks for protecting the heater from overheating, a furnace, the LHTES prototype with an inside HTF pipe, thermocouples inside the graphite foam-PCM combination and at the inlet/outlet of the HTF pipe, and the data acquisition system (DAS) to record the measurements of the thermocouples and to store the data in the computer. The air-flow pump sends air at a certain air flow rate to the system. The air flows through the heater in which it is heated from room temperature to a certain higher temperature as the inlet temperature of the LHTES system. The high-temperature air flows through the prototype to melt/solidify the PCM during charging/discharging processes. The outlet air then goes outside the building in this open loop system. Figure 10-4 shows the front and back views of the test loop facility. Details of the various components are indicated in Figure 10-4 along with individual descriptions.
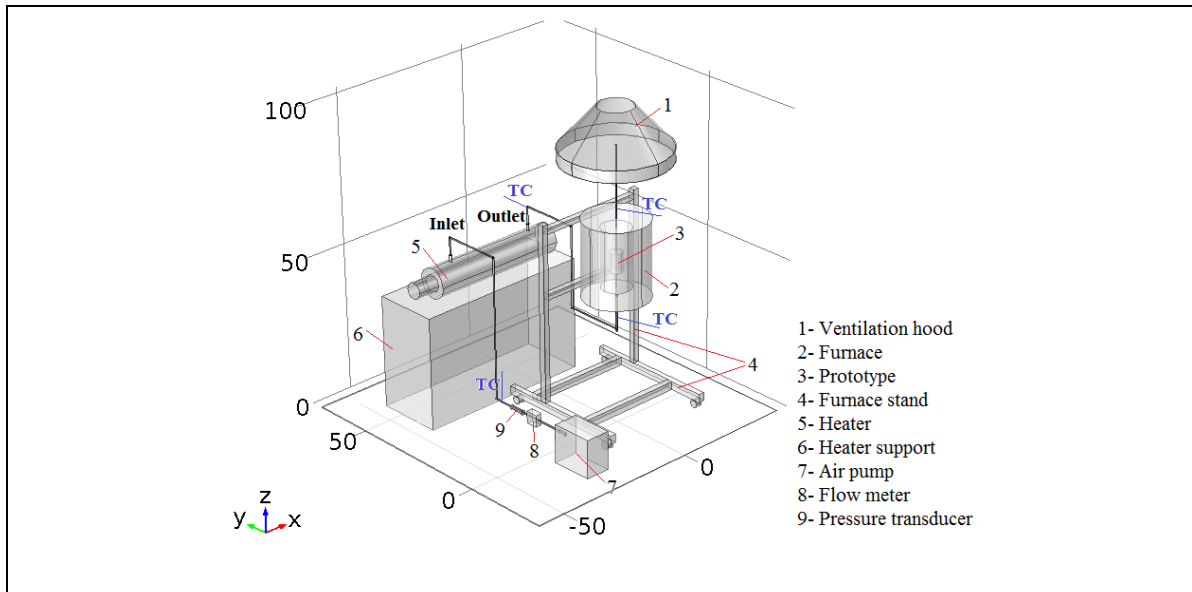
Figure 10-3. Schematic diagram of lab-scale prototype testing loop.
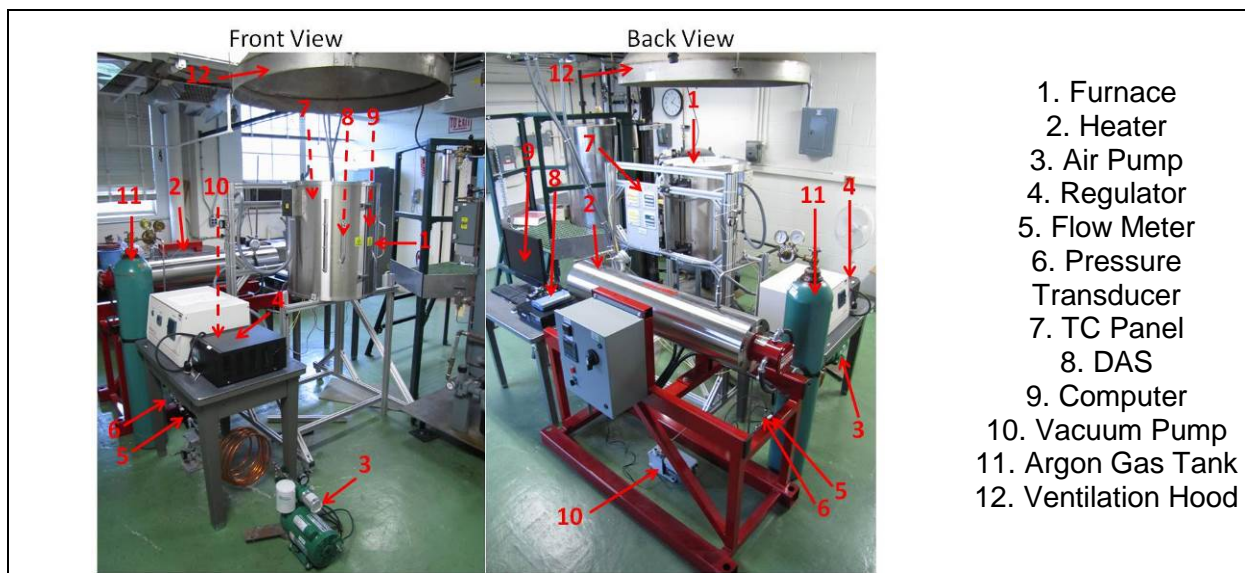
Figure 10-4. Pictures of components of lab-scale prototype test loop.

10.3. Sealing experiments

The prototype will be evacuated to a predetermined vacuum level to avoid any pressure buildup during the heating process. To maintain the vacuum inside the prototype, the sealants for the thermocouple have to be functional.

The thermocouple feedthroughs have threads that require a high temperature sealant. Deacon-8875 sealant has been identified for this purpose. It is a thermal reactive paste sealing compound that can be used up to 982 °C. Prior to assembly of the lab-scale LHTES prototype, a small prototype sample was prepared and tested to verify the

sealing of the vacuum inside the sample using sealant. The experimental set-up is shown in Figure 10-5. Instead of installing the feedthrough on the top plate of the small prototype, a Swagelok fitting was used for this experiment. The sealant was applied on the thread of the Swagelok fitting and cured to obtain a vacuum tight sealing. After the curing, the small prototype was connected to a vacuum pump to evacuate the inside of the container, as shown in Figure 10-6. Between the small prototype container and the vacuum pump, a pressure gauge and a needle valve were installed.
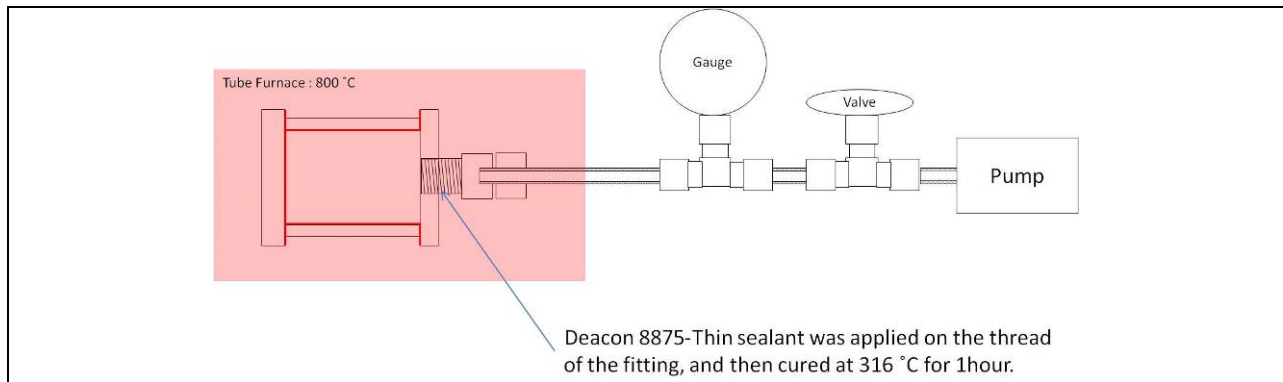
Figure 10-5. A schematic of the sealing experimental system.
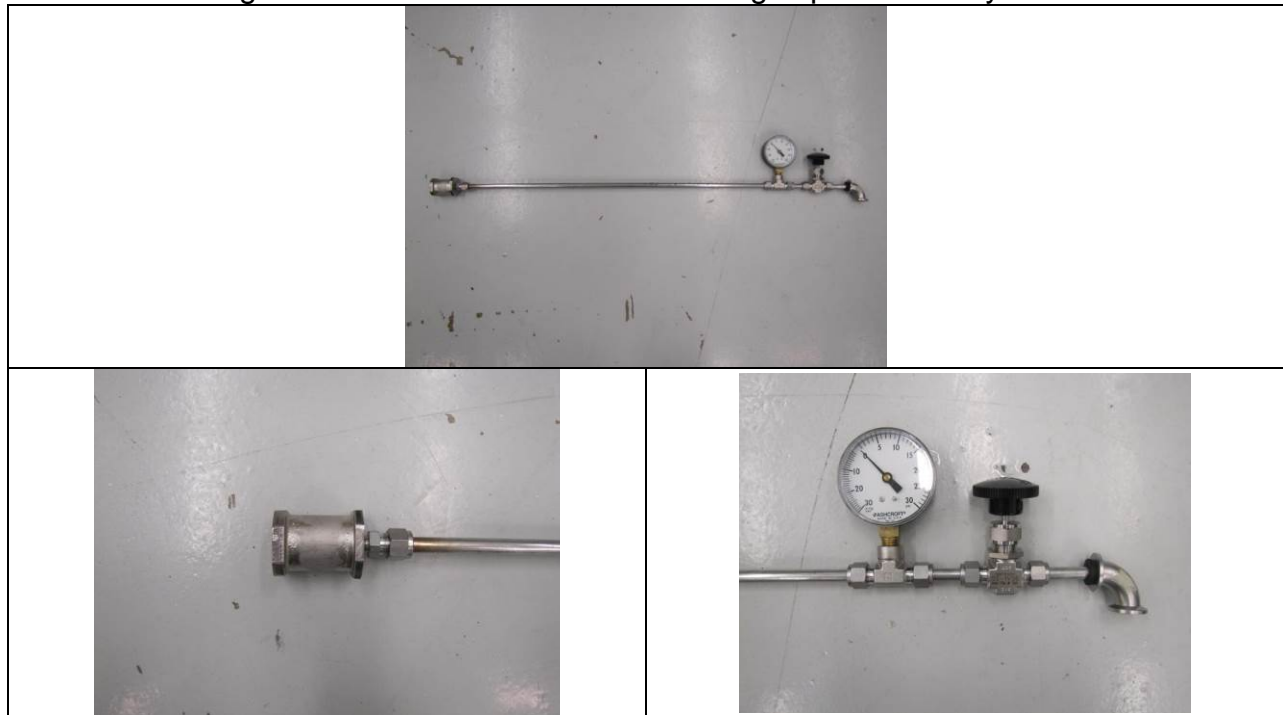
Figure 10-6. Photographs of the sealing experimental system.

Several attempts were made to evaluate and optimize the performance of the sealing approach, sealant application, and testing conditions. The first sealing experiments with Deacon 8875-Thin using small prototype samples with $MgCl_2$ were conducted to investigate whether the tight sealing can be maintained in the presence of the $MgCl_2$. A powder of $MgCl_2$ (1.5 g) was fused in the small prototype sample before the curing process of the sealant. After fusing of $MgCl_2$, the Deacon 8875-Thin was applied on the

thread of the fitting and cured at 316 °C for 1 hour to produce a good seal. After curing, the small prototype sample was connected to a vacuum pump to evacuate the inside of the container. Between the small prototype and the vacuum pump, a pressure gauge and a needle valve were installed. The sealing experimental procedure was as follows:

a) Heat the sample from room temperature to 750 °C over the course of 12 hours (ramp rate: 1 °C/min).
b) During the heating process, evacuate the sample when the inside pressure increases to remove the moisture inside the sample.
c) Hold the sample at 750 °C for 12 hours.
d) Cool the sample from 750 °C to 600 °C over the course of 12 hours (ramp rate: 0.2 °C/min).
e) Hold the sample at 600 °C for 12 hours.
f) Heat the sample from 600 °C to 750 °C over the course of 12 hours (ramp rate: 0.2 °C/min).
g) Repeat steps c-f three more times.

The heating/cooling rate decreased from 2 °C/min to 0.2 °C/min to simulate the lab-scale LHTES prototype experiment, and this change allows the sealant to release the thermal stress.

A small prototype sample with $MgCl_2$ was prepared as before and tested. The pressure change during the first heating process is shown in Figure 10-7(a). The pressure increased after 400 °C due to release of moisture from salt PCM. To remove the moisture, the sample was evacuated at 500 °C and 600 °C. After the heating process, the sample was cycled between 600 °C and 750 °C four times. The pressure and temperature change during the cycles is shown in Figure 10-7(b). The pressure increased from 2 psi to 2.9 psi during the first cooling process even though the cooling rate decreased to 0.2 °C/min. It continued to increase at 600 °C for 12 hours, and this indicated that the vacuum seal was broken. The rate of pressure increase slowed at the end of the next heating procedure. The pressure was maintained at 6.1 psi for several hours at 750 °C and decreased to 5.2 psi. This indicated that the vacuum tight seal recovered during the heating process. A similar pattern was repeated for the next several heating/cooling cycles.

Figure 10-7. The pressure change inside the sample with $MgCl_2$ and Deacon 8875-Thin during (a) the revised heating process (b) the cycles between 600 °C and 750 °C.

To improve sealing, the sealant was changed from Deacon 8875-Thin to Deacon 8875. The curing temperature for the Deacon 8875 is 270 °C. The experiment was repeated as described above. The pressure change inside the sample during the first heating process is shown in Figure 10-8(a). The sample was evacuated gradually at 300 °C, 400 °C, 500 °C, 600 °C, and 700 °C to minimize the effect of moisture on the sealant. After the heating process, the sample was cycled between 600 °C and 750 °C four times. The pressure and temperature change during the cycles is shown in Figure 10-8(b). The pressure increased from 2.9 psi to 3.9 psi during the first cooling process, and it decreased from 3.9 psi to 2.5 psi during the next heating cycle. It decreased from 2.5 psi to 2.2 psi during the second cooling cycle. This indicated that the seal was not broken during the second cooling cycle. After the first cooling cycle, the pressure continued to decrease from 3.9 psi to 1.2 psi until the end of the experiment. These results show that the vacuum tight sealing achieved by Deacon 8875 can withstand the cycling between 600 °C and 750 °C in the presence of the $MgCl_2$.
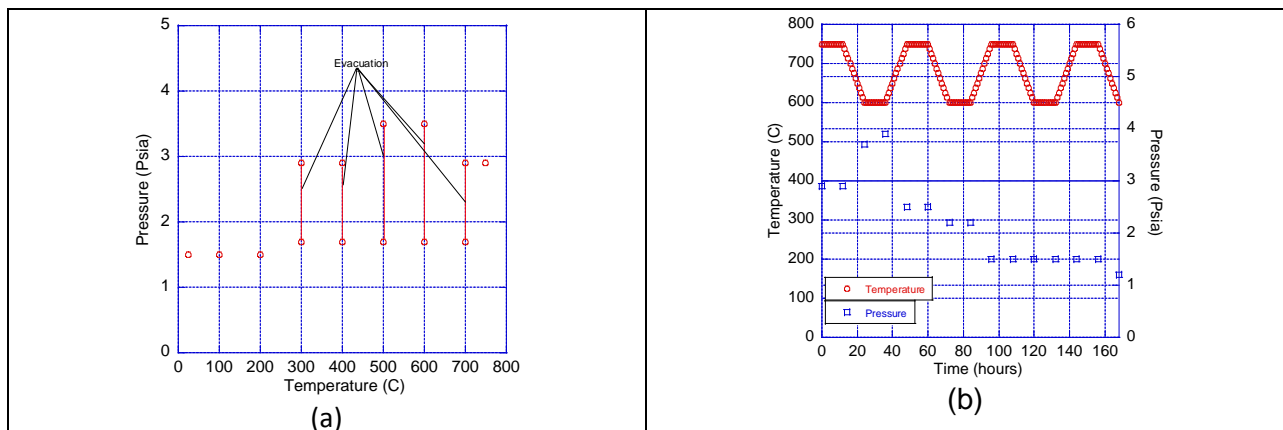
Figure 10-8. The pressure change inside the sample with $MgCl_2$ and Deacon 8875 during (a) the first heating process and (b) the cycles between 600 °C and 750 °C.

Next, another small prototype sample with increased amount of $MgCl_2$ (5 g) was prepared and tested to investigate the effect of the amount of $MgCl_2$ on the vacuum

tight sealing. The pressure change inside the sample during the first heating process is shown in Figure 10-9(a). The sample was evacuated gradually at 300 °C, 400 °C, 500 °C, 600 °C, and 700 °C to minimize the effect of moisture on the sealant. After the first heating, the sample was cycled between 600 °C and 750 °C five times. The pressure and temperature change during the cycles is shown in Figure 10-9(b). The pressure decreased from 2.5 psi to 2 psi during the first cooling process, unlike from the previous experiment. It continued to decrease from 2.5 psi to 0.5 psi until the end of the experiment. The effect of the amount $MgCl_2$ on the vacuum tight sealing was negligible. These results confirm that the vacuum tight sealing achieved by Deacon 8875 can be maintained throughout the experiment under the presence of the $MgCl_2$. In other words, these results indicate that the sealant Deacon 8875 should be adequate in maintaining the desired atmosphere at 750 °C in the actual LHTES prototype as well.

In conclusion, the sealant Deacon 8875 is applicable to seal the thread and keep the pressure level at 0.5-3.0 psi in the vessel when molten $MgCl_2$ is present. Therefore, it will be used to seal the feedthrough on the prototype cap to maintain the pressure levels around 14 psi (1-2 psi at room temperature) in the graphite foam-$MgCl_2$ prototype at elevated temperatures. These results were presented to ANL's project safety review committee and it helped in obtaining environment, safety, and health (ES&H) approval of the experimental safety plan.
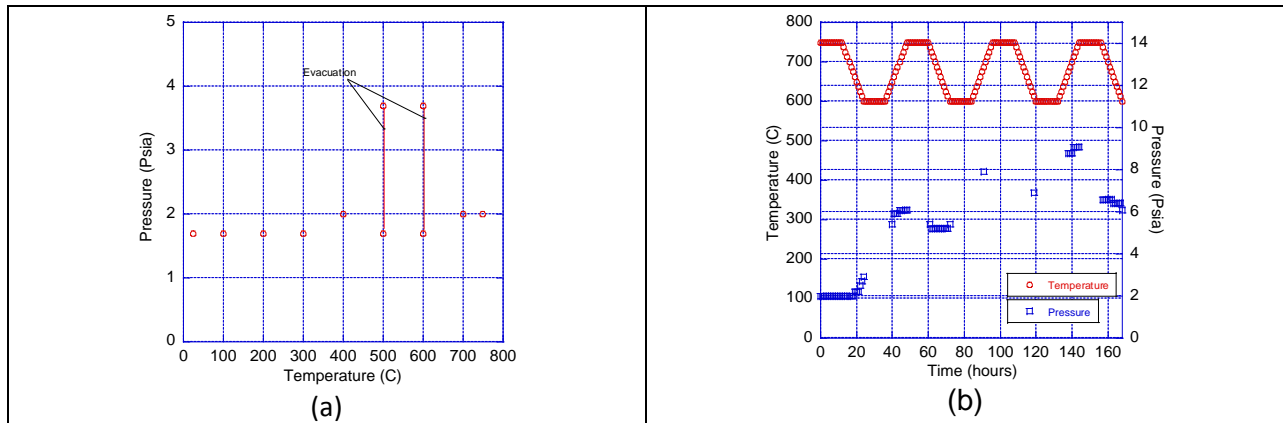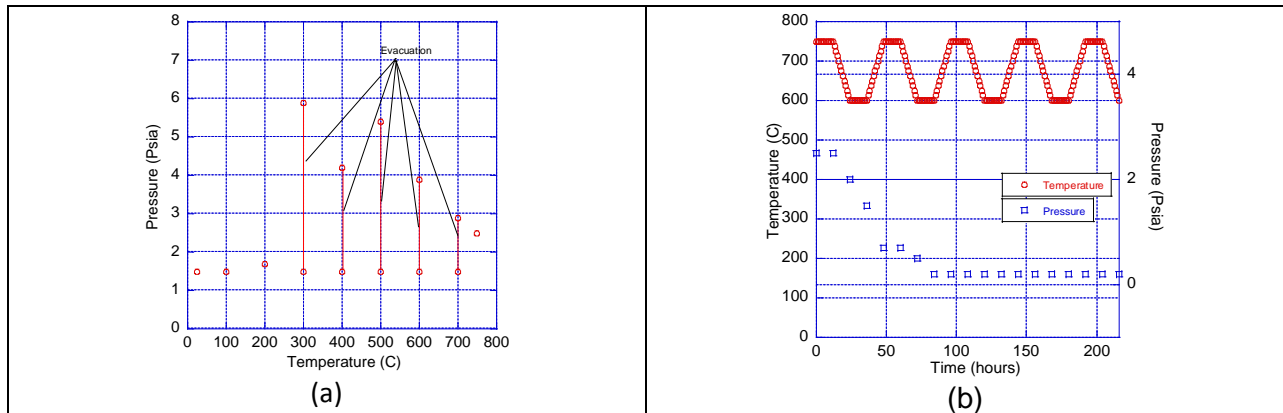

Figure 10-9. The pressure change inside the sample with $MgCl_2$ and Deacon 8875 during (a) the first heating process and (b) the cycles between 600 °C and 750 °C.

10.4. Pressure monitoring experiments
Prior to the charging/discharging experiments with the lab-scale prototypes, any moisture/impurities from the prototypes are completely removed by using the furnace and the vacuum pump, and the lab-scale prototypes are flushed by ultra-high purity argon gas. This step will mitigate corrosion from PCM in the prototypes and control the pressure in the prototypes at elevated temperatures.

The vacuum and argon gas line were installed in the prototype test loop as shown in Figure 10-10. Before the moisture removing and argon gas flushing for the prototype, a small prototype sample with 25 g of $MgCl_2$ was tested with the vacuum and argon gas line as shown in Figures 10-10 and 10-11 to verify that it worked correctly.

The small prototype sample container was brazed using BNi-4, and $MgCl_2$ was fused and put into the small prototype sample. Then, the fitting was installed on the small prototype sample and cured with Deacon-8875 (sealing material) per the procedure developed and described earlier. After the small prototype sample was prepared, it was connected to the vacuum and argon gas line of the testing loop for removal of moisture and back filling of argon gas. The procedure for the moisture removal and back filling of argon gas was as follows:

a) Evacuate the sample inside using a vacuum pump to 1 psi.
b) Heat the sample up to 700 ˚C and evacuate the sample when the inside pressure increases.
c) Repeat the evacuation process at 700 ˚C until the inside pressure does not increase to remove all the moisture inside the sample.
d) Cool the sample to room temperature.
e) Back fill the container with argon gas at room temperature.
f) Evacuate the sample to 1 psi at room temperature.
g) Repeat steps e and f to further remove the impurity in the small prototype sample.
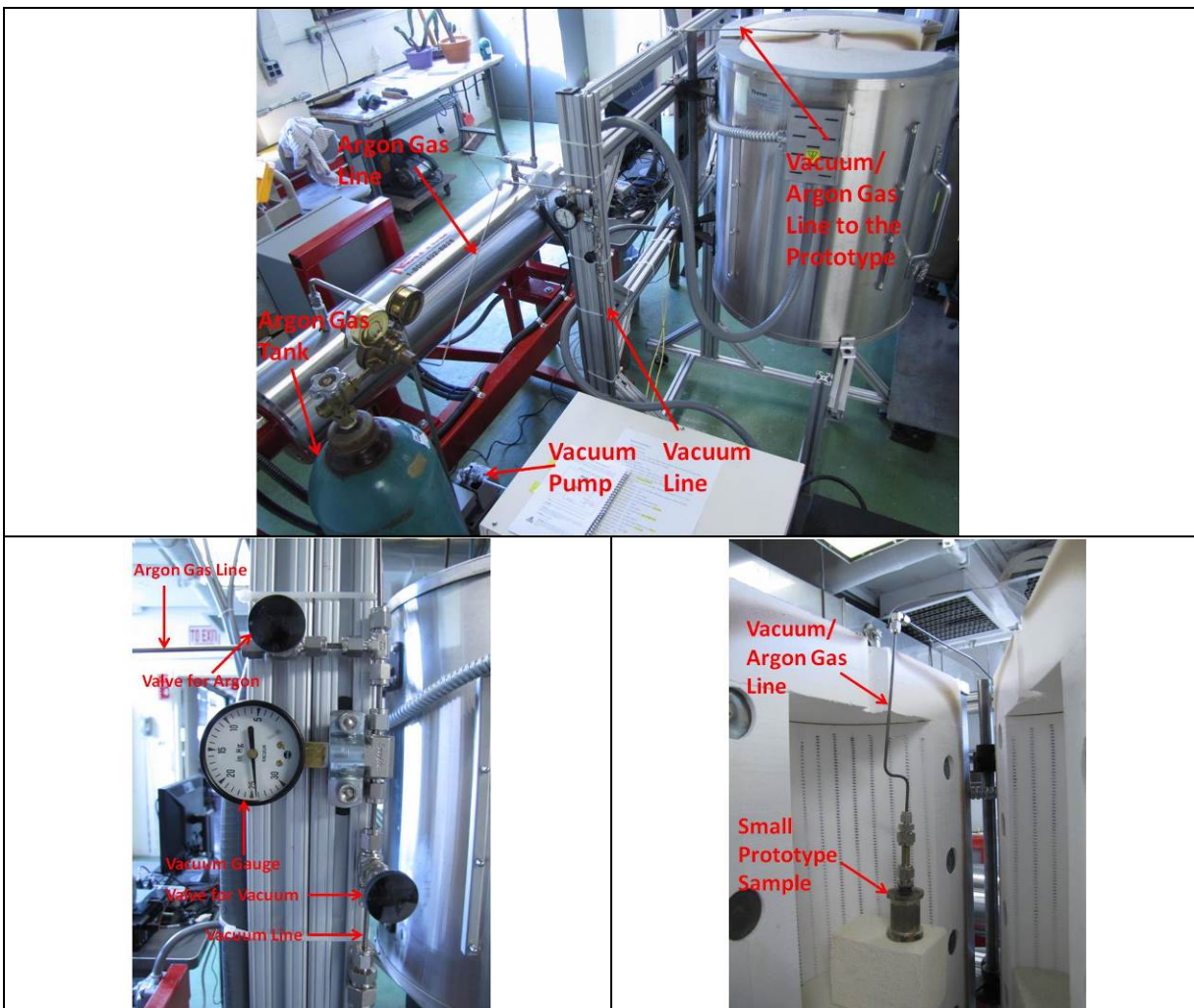
Figure 10-10. Vacuum and argon gas line on the test loop.
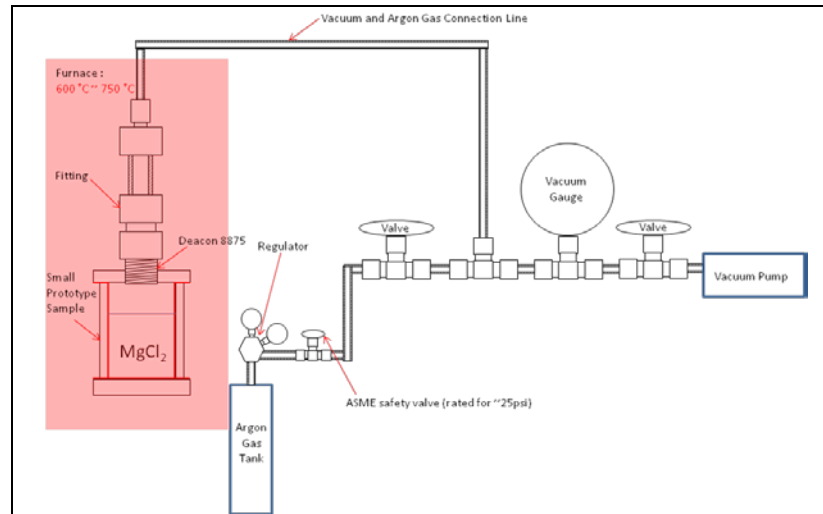
Figure 10-11. Schematic diagram of the pressure monitoring experiment.

   h) After the moisture removal and back filling of argon gas, the pressure monitoring
      experiments were conducted with the small prototype samples.

The pressure monitoring experimental procedure was as follows:

   a) Heat the sample to 750 ˚C over the course of 12 hours.
   b) Hold the sample at 750 ˚C for 12 hours.
   c) Cool the sample to 600 ˚C over the course of 12 hours.
   d) Hold the sample at 600 ˚C for 12 hours.
   e) Repeat steps a to d.
   f) Monitor the inside pressure of the prototype sample using the vacuum gauge
      during the cycles.

Three pressure monitoring tests were conducted with the small prototype samples, and
the experimental conditions of each test are summarized below:

Test 1
   ➢ Amount of $MgCl_2$: 15 g
   ➢ Initial Pressure at Room Temperature: 1 psia
   ➢ Highest Pressure during the Test: 1.5 psia

Test 2
   ➢ Amount of $MgCl_2$: 25 g
   ➢ Initial Pressure at Room Temperature: 1 psia
   ➢ Highest Pressure during the Test: 1.2 psia

Test 3
   ➢ Amount of $MgCl_2$: 25 g
   ➢ Initial Pressure at Room Temperature: 6.9 psia

➢ Highest Pressure during the Test: 11.1 psia

Test 1 was conducted by using the small prototype with 15 g of $MgCl_2$. The pressure change inside the small prototype sample during the heating process is shown in Figure 10-12(a). The sample was evacuated gradually during the heating process to minimize the effect of moisture on the sealant. The pressure increase during the heating process was higher than that seen in the sealing experiments in earlier. That was because the amount of $MgCl_2$ in the small prototype increased from 2 g to 15 g. After the moisture removal and argon back filling, the small prototype sample was cycled between 600 °C and 750 °C five times. The pressure and temperature change during the cycles is shown in Figure 10-12(b). The pressure decreased from 1.5 psi to 1 psi during the first cycle. It continued to decrease from 1 psi to 0.5 psi until the end of the experiment. These results showed that the vacuum-tight sealing achieved by Deacon 8875 can be maintained throughout the experiment under the presence of the $MgCl_2$ in the test loop. The pressure inside a small prototype sample was kept below the 1.5 psi, and there was no abnormal pressure build-up throughout the test.

Then, Test 2 was conducted using the small prototype with 25 g of $MgCl_2$ to simulate the pressure behavior in the lab-scale prototype. The pressure change inside the small prototype sample during the heating process is shown in Figure 10-13(a). The pressure increase during the heating process was higher than that seen in Test 1 because the amount of $MgCl_2$ in the small prototype increased from 15 g to 25 g. After the moisture removal and argon back filling, the small prototype sample was cycled between 600 °C and 750 °C three times. The pressure and temperature change during the cycles is shown in Figure 10-13(b). The pressure decreased from 1.2 psi to 1 psi during the first cycle. It continued to decrease from 1 psi to 0.7 psi until the end of the experiment. These results confirm again that the vacuum tight sealing can be maintained throughout the experiment. The pressure of the inside small prototype sample was kept below the 1.2 psi, and there was no abnormal pressure build-up throughout the test.

Finally, Test 3 was conducted using the small prototype with 25 g of $MgCl_2$ and 6.9 psi initial pressure to investigate the worst pressure build-up in the lab-scale prototype during the charging/discharging experiment. The pressure and temperature change during the cycle is shown in Figure 10-14. The pressure increased from 6.9 psi to 11 psi during the heating process. Then, it decreased from 11 psi to 6.9 psi during the cooling process. The pressure of the inside small prototype sample was kept under the vacuum throughout the test. The final pressure and the initial pressure were the same at 6.9 psi. These results showed that the vacuum tight sealing achieved by Deacon 8875 survived under the higher level of the pressure.
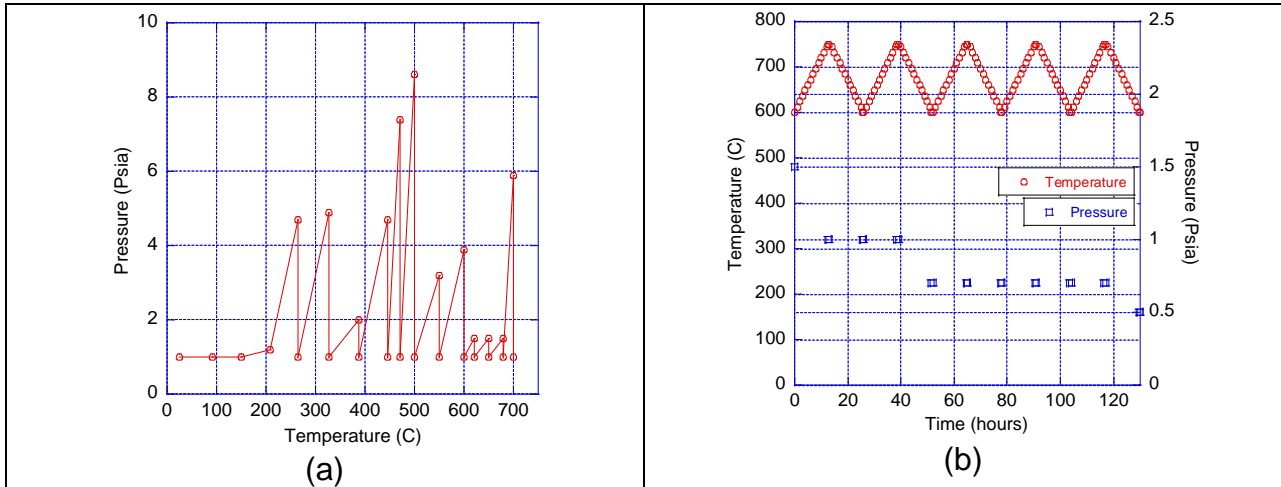
Figure 10-12. (a) Pressure change during the heating process and (b) pressure and temperature change during the cycles using the small prototype with 15 g of $MgCl_2$.
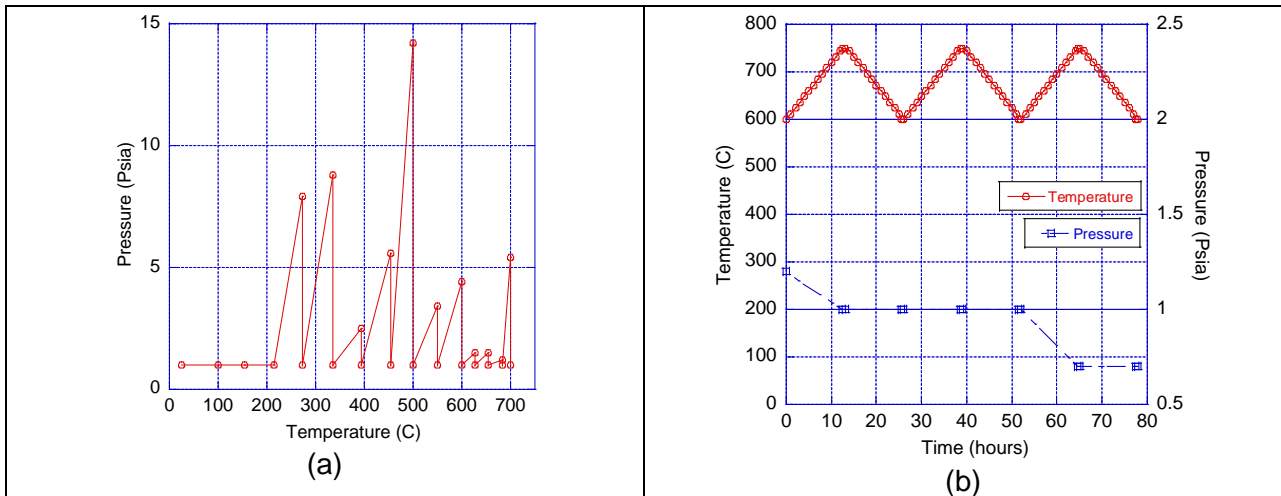
Figure 10-13. (a) Pressure change during the heating process and (b) pressure and temperature change during the cycles using the small prototype with 25 g of $MgCl_2$.
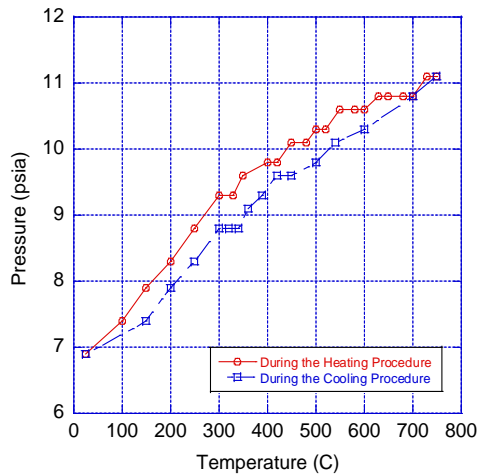
Figure 10-14. The pressure and temperature change with 6.9 psi initial pressure.

10.5. Thermocouple reliability

Type S thermocouples (Pt/Pt-10%Rh) will be used for temperature monitoring during the charging/discharging process. However, the stability and the reliability of the thermocouples in $MgCl_2$ environments are not known. Hence, objective of the work was to ensure Type S thermocouples will function during the entire prototype experiment, including after the long-term (500 h) exposure tests.

To evaluate the thermocouple performance a test cell was constructed as shown in Figure 10-15. $MgCl_2$ powders were loaded inside of a ceramic crucible. Then, a type S thermocouple with ceramic sheath was inserted into the $MgCl_2$ powders through a ceramic cap. After the installation of the type S thermocouple, the entire assembly was sealed by using a ceramic adhesive that is cured at 93°C for 2 hours.
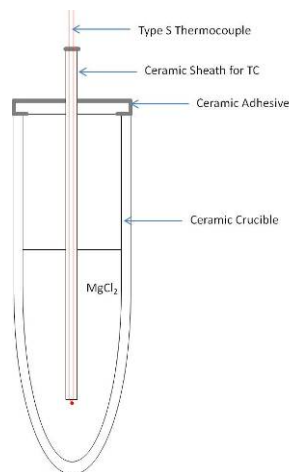
Figure 10-15. A schematic of the small prototype sample with type S thermocouple.

After curing, the test cell was heated up to 750 °C to melt all the $MgCl_2$ powder in the crucible. Thereafter, temperature of the sample was maintained at 750 °C for 400 hours. During this time, the thermocouple measured the temperature of molten $MgCl_2$. The measured temperature is shown in Figure 10-16. First 150 h data were lost due to the error of data acquisition system. The range of measured temperature was 747-753 °C. These results showed that the type S thermocouple will be feasible for temperature monitoring in molten $MgCl_2$ environment over the time expanse of interest.
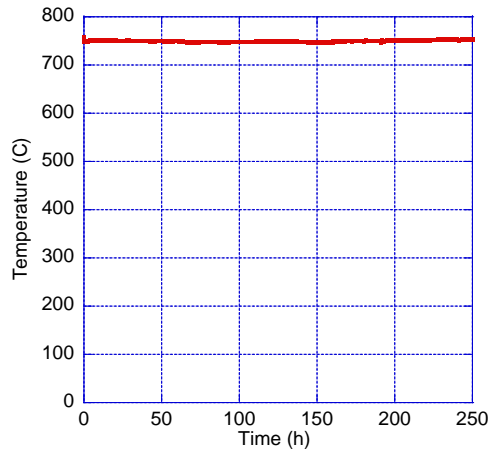
Figure 10-16. Temperature measurement by the type S thermocouple.

Figure 10-17 shows the test cell before and after the experiment. There was no significant change observed in the test cell. To ensure that the salt did not leak out, the cell was sliced open and salt was recovered. The recovered salt (Figure 10-18) was about 0.35 g, as compared to the 0.45 g that was initially placed. This discrepancy in weight could be because the salt fuses to the ceramic, and it is difficult to scrape away the entire amount. Nevertheless, the experiment confirmed the feasibility of using the type S thermocouples for the prototype testing.

| (a) Before the experiment | (b) After the 400 h experiment |
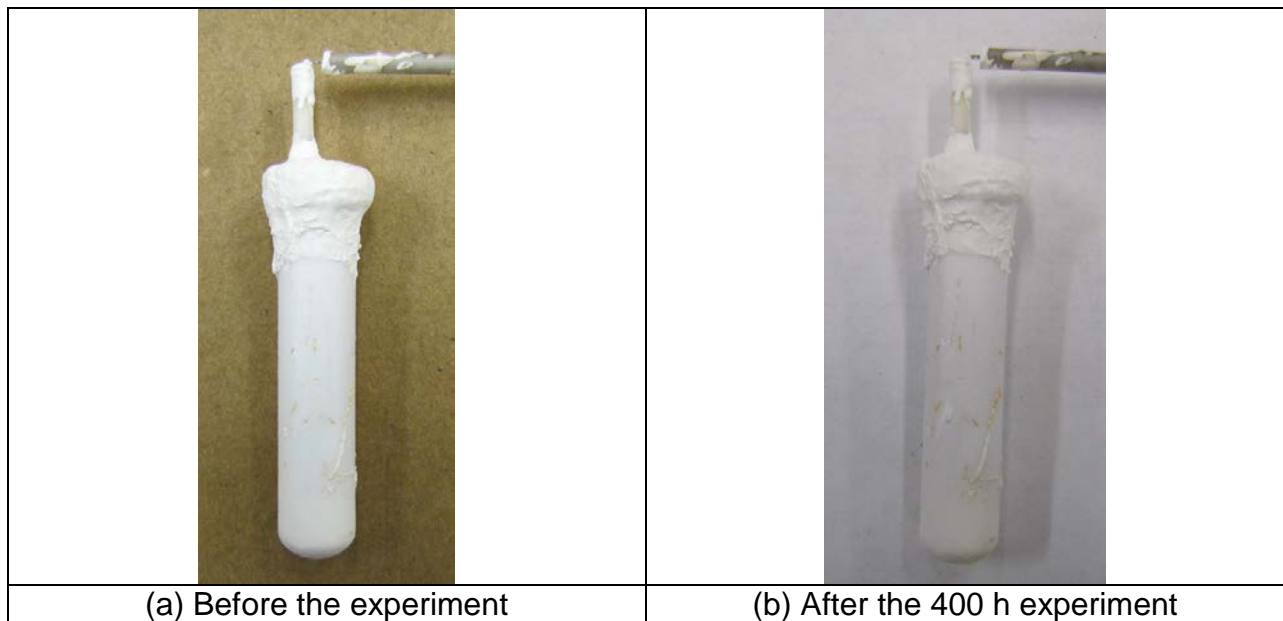
Figure 10-17. The small prototype sample (a) before and (b) after the experiment.
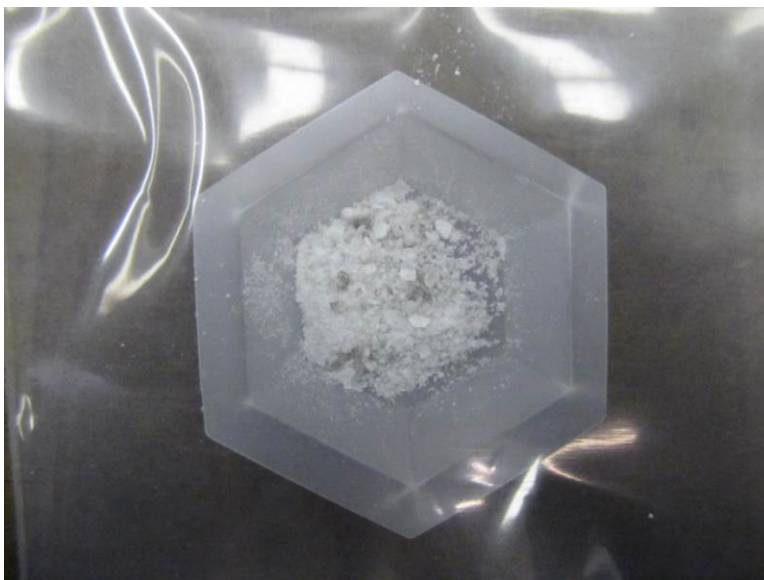
Figure 10-18. Scraped out MgCl₂ from the crucible after the experiment.

10.6. Thermocouple calibrations

Type S thermocouples (TC 1-22) (platinum TCs) were fabricated for measuring the temperatures at various locations in the prototype. The reason we are using Type S TCs is because Type K TCs react with salt, whereas Type S TCs do not. These TCs will be inserted into the infiltrated foam at different depths and radius to measure temperatures at various locations in the prototype. The measurements of the TCs will provide information on the melting/solidification front movements, as a function of time, in the prototype during the charging/discharging tests.

Before using the TCs to measure the temperatures in the prototype in the experiments, the Type S TCs were calibrated with a NIST TC to determine the measurement accuracies and the offsets of the measurements compared to the NIST TC at elevated temperatures.

In this regard, Type S thermocouples were placed with the standard NIST Type K thermocouple in the tube furnace. The Type S thermocouple measurement tip was placed very close to the NIST TC tip to ensure that the two TCs were measuring the same temperature in the furnace. The voltage reading from the NIST thermocouple was recorded, and the reference junction of the NIST TC was placed in the ice-water mixture (0 °C). Then, Type S TCs to be used in the prototype testing were calibrated against the NIST thermocouple. Because the prototype operating temperature will be between 600 °C and 800 °C, the calibration temperature was at around 750 °C. Measurements were recorded after stabilization of the furnace at the set temperature for 30 minutes.

In conclusion, the TCs meet the measurement accuracy of Type S thermocouples as defined in the SOPO [13], and are capable of measuring the temperatures in the prototype at elevated temperatures in the PCM environment during the

charging/discharging processes. The measurement offsets of each TC from the NIST thermocouple were considered in the prototype experiments and subsequent analysis.

10.7. Air flow rate and temperature measurements in the test loop

Two major measurement variables in the prototype test loop are the air flow rate and the air temperature control at the exit of the heater. The air flow rates and the temperatures at different locations in the test loop were measured under elevated heater exit temperature. The objectives of the tests were to investigate the stabilities of the air flow rates and temperatures in the test loop at room and elevated temperatures. Note that air is being used as the HTF for charging/discharging the LHTES prototype.

The air flow rates were measured by a NIST-traceable flow meter. It is connected in the test loop after the air pump as shown in Figure 10-19(a). The air pump supplies continuous air flow for the prototype test loop during the experiments. It is connected to a voltage regulator output to provide a stable flow rate in the test loop. The voltage regulator output is stabilized at 120 V ± 3%. The flow rates in the loop can be adjusted by an in-line valve and a bypass valve (Figure 10-19(a)).

Three Type K TCs were used to measure the air flow temperatures at various locations in the loop. One TC was installed before the heater inlet (TC_Heater inlet). Another TC was installed at the heater outlet (TC_Heater outlet) to ensure that the heater can provide a stable air temperature at the exit of the heater, and consequently, to the prototype to conduct the charging and discharging experiments. The third TC was installed right above the furnace (TC_Above furnace) (the location of the prototype inlet) and under the ventilation hood (for safety purposes), as shown in Figure 10-19(d), to study the temperature drop of the air from the heater outlet to the furnace (prototype inlet).

The first test was to evaluate the stability of the air flow rate in the test loop at room temperature. Various flow rates were tested, i.e., 4 cfm (113 L/min), 5 cfm (142 L/min), and 6 cfm (170 L/min). These flow rates were chosen based on typical HTF flow rates used in our simulations. The flow rate was adjusted to around the target value through the two valves shown in Figure 10-19(a) and held at that value for one hour to obtain measurements under steady state conditions.

Figure 10-20 shows the flow rate readings recorded from the flow meter. The average flow rates and the standard deviations during the measurements are displayed in Table 10-2. The flow rates were quite stable in the test loop at room temperature. The flow rate measurements were within ±0.5% of the average values, as illustrated in Table 10-2, meeting the flow rate measurement requirement (±3% of the set point) stated in the SOPO [13].
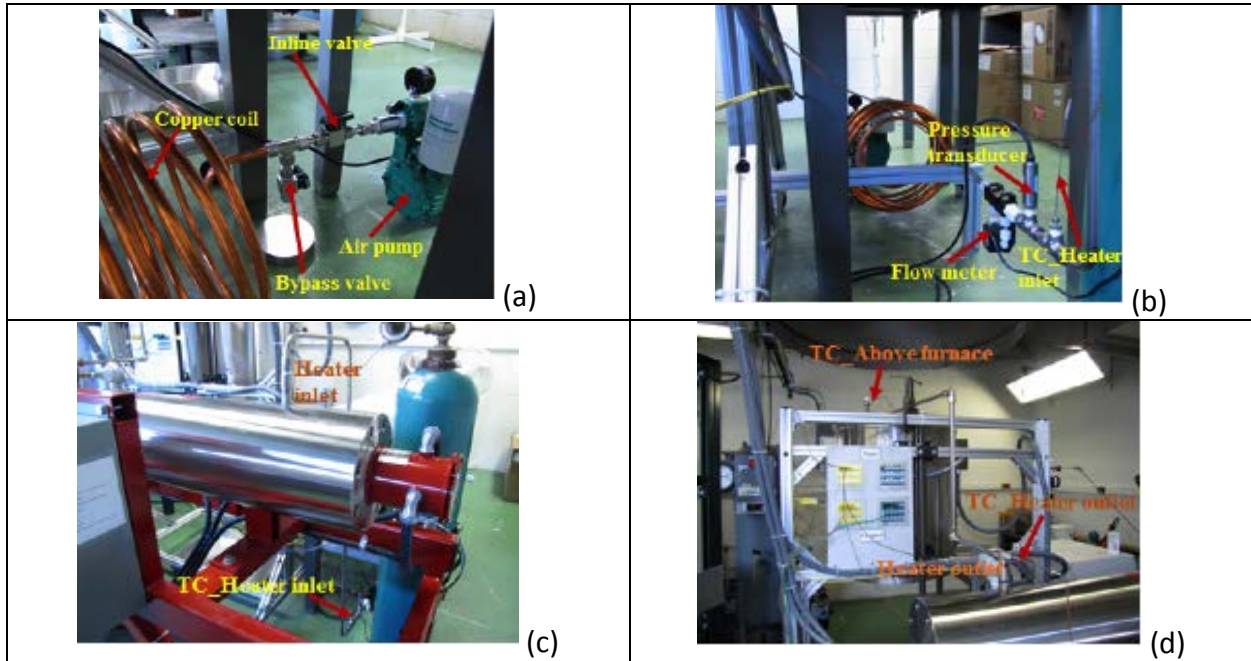
Figure 10-19. Test loop assembly showing air pump, heater, and data acquisition board.
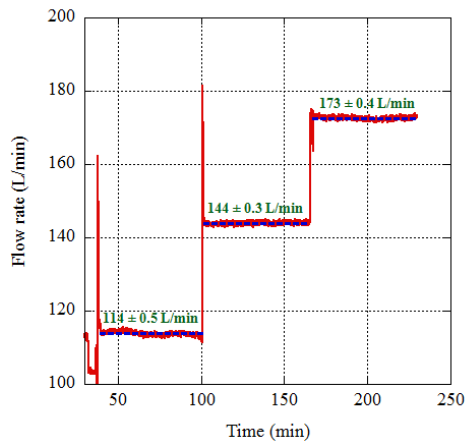
Figure 10-20. Flow rate data during preliminary testing.

Table 10-2. Air-flow rate measurements at room temperature.

Target flow rate	4 cfm (113 L/min)	5 cfm (142 L/min)	6 cfm (170 L/min)
Actual flow rate set point (L/min)	114	144	173
Average measured value, ± standard deviation (L/min)	114 ± 0.5	144 ± 0.3	173 ± 0.4
Flow rate measurement target in SOPO [13]	±3%		

The second test was conducted at elevated temperature to investigate the stabilities of temperature and flow rates in the test loop at the heater outlet temperature around 540 °C (operating temperature for the discharging process for the prototype experiments). Figures 10-21 and 10-22 show the temperature and flow rate recordings, respectively, during the test experiment. The heater was heated up from room temperature to the target set point (505 °C). After the heater temperature stabilized around the set point, the heater was held at the set point for one hour to simulate the air flow condition in the test loop for the prototype experiments.

According to the temperature measurements, the temperatures in the test loop were stable during the one-hour holding time, as displayed in Figure 10-21. The heater outlet temperature (TC_Heater outlet) was stabilized around 542 °C while the air temperature after the heater (above the furnace) (TC_Above furnace) was kept around 268 °C in the loop. There was about 275 °C difference between the heater outlet and the location above the furnace. The large temperature difference was caused by the effect of the ventilation hood as well as the heat loss to the surroundings. For the actual prototype experiments, the piping and the insulation were wrapped around the piping to minimize the heat loss. Thus, as discussed later, the air temperature difference between the heater outlet and the furnace (prototype inlet) would be significantly reduced in the loop. The key point here is that the temperatures at various locations are very stable.

The flow rate in the loop was also quite stable during the hold time, as shown in Figure 10-22. When the heater was heating up from room temperature to the elevated temperature, the flow rate decreased during the transient process due to the increase of the resistance in the heater at high temperatures. When the heater temperature was cooling, the flow rate increased. Nevertheless, the flow rate was quite stable when the heater was maintained at its set temperature. Based on these initial tests, both temperature and flow rate are stable in the test loop at a specific heater setting temperature. This is quite important in conducting well-controlled heat transfer tests on the prototypes.

Table 10-3 shows the average measured values and standard deviations of the air flow rate and temperatures in the test loop during the steady state process. The TC measurements were within ±2.0 °C, except for the TC above the furnace due to the effect of the ventilation hood. Based on the preliminary experimental results, the air flow rate and temperatures were stable in the test loop at the 540 °C heater outlet temperature (simulating the discharging process for the prototype). Thus, the measurement devices are capable of providing accuracy within the expected measurement range, as claimed in the SOPO [13].

| Figure 10-21. TC measurements. | Figure 10-22. Air flow rate recording. |
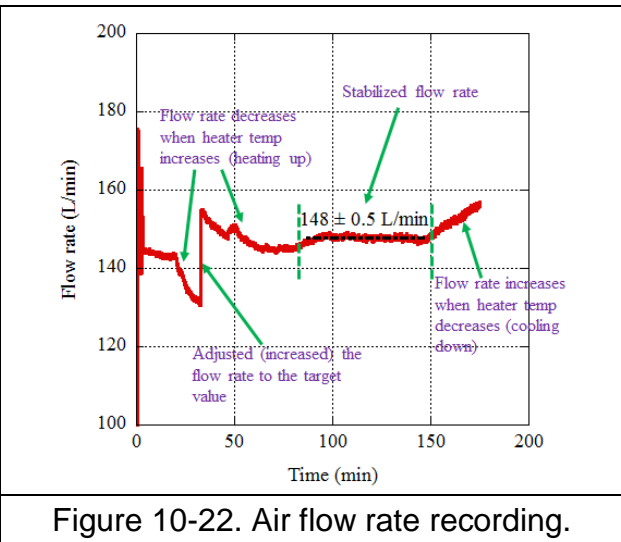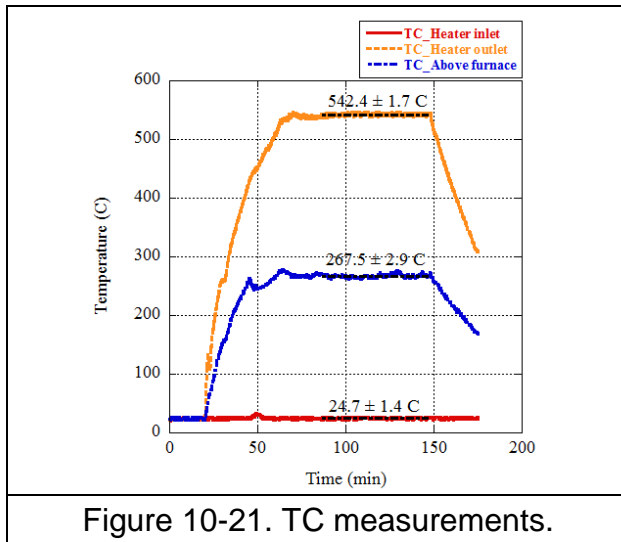
Table 10-3. Temperature and air flow rate measurements at elevated temperature.

	Average measured value ± standard deviation	Targets of experiment measurement variables control in SOPO [13]
TC_Heater inlet (˚C)	24.7 ± 1.4	±2.0 ˚C
TC_Heater outlet (˚C)	542.4 ± 1.7	±2.0 ˚C
TC_Above furnace (˚C)	267.5 ± 2.9	±2.0 ˚C
Air flow rate (L/min)	148 ± 0.5	±3%

The lab-scale prototype heat transfer test loop mainly consists of an air pump to continuously supply air flow, a heater to bring the air temperature up to the desired elevated temperature level, a furnace to hold the prototype in position as well as hold it at a desired temperature during the charging/discharging process. The connection tubing between the heater exit and the furnace is shown in Figure 10-23(a). The tubing brings the high temperature air exiting from the heater to the furnace to heat up/cool down the prototype during the charging/discharging process.

Temperatures at the heater exit and the furnace inlet were tested to ensure that 1) the heater is capable of heating the air to the expected elevated temperatures; 2) the furnace inlet temperatures can be maintained at certain level to melt/solidify the PCM inside the prototype; and 3) a correlation can be developed between the heater exit temperature and the furnace inlet temperature for future heater set up for the prototype charging/discharging process.

Testing at various heater set points indicated significant heat loss and a large temperature drop between the heater exit and furnace inlet temperatures of the air. Therefore, insulation was placed at the outside of the HTF tubes to reduce the heat loss from the tubing, and aluminum ducts were placed at the outside of the insulation to fix

the insulation in place, as shown in Figure 10-23(b). With the insulation, temperature drop between the heater exit and furnace inlet was reduced to around 150 °C at the heater exit temperature of 740 °C.

| (a) Test loop before insulation | (b) Test loop after insulation |
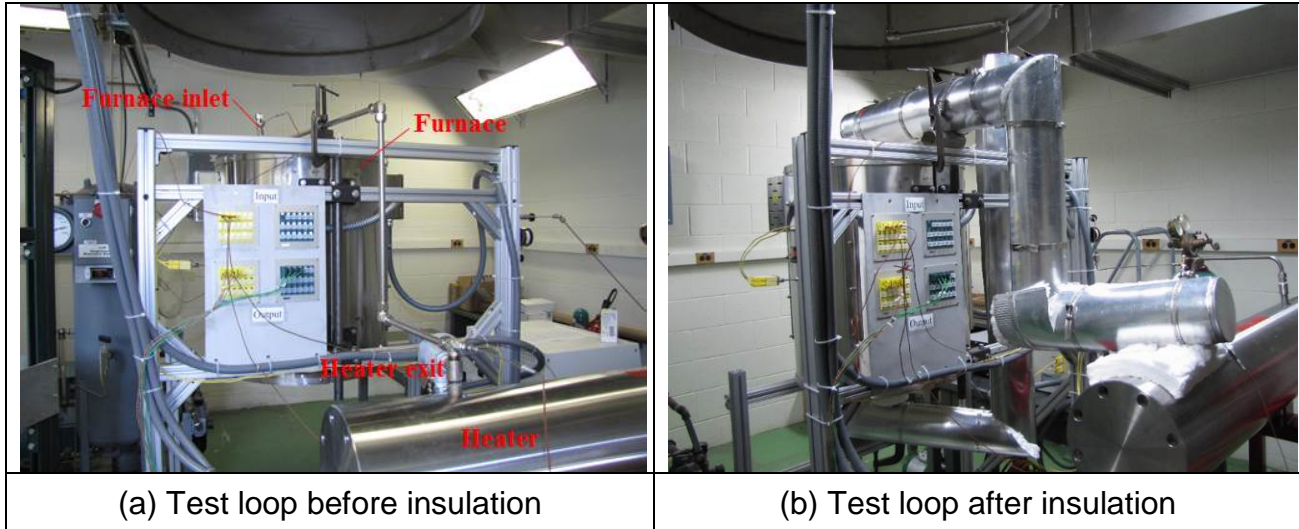
Figure 10-23. Prototype heat transfer test loop.

Although the temperature drop was reduced, the difference between heater exit and furnace inlet was still significant. To further reduce the heat loss from the HTF tubing to keep furnace inlet temperature at a high level (close to the heater exit temperature) to melt the PCM inside the prototype in the furnace, heating tapes were placed at the outside of the aluminum ducts, as displayed in Figure 10-24(a). To efficiently use the heating tapes, another layer of insulation was placed at the outside of the heating tapes to minimize their heat loss, as shown in Figure 10-24(b). The temperature difference between the heater exit and the furnace inlet was further reduced to 115 °C at the heater exit temperature of 800 °C based on this setting.

According to the heat transfer simulations, the total melting times for the amount of $MgCl_2$ (~1.4 kg) in the prototype corresponding to the air flow inlet temperatures (furnace inlet temperatures) are illustrated in Table 10-4. To obtain a reasonable melting time during the charging process, the furnace inlet temperature is expected to be above 760 °C. The over 100 °C temperature drop between heater exit and furnace inlet requires elevation of the heater exit temperature above 900 °C to achieve a furnace inlet temperature above 760 °C. Thus, additional heating tapes and insulation were placed at the heater inlet tubing, as displayed in Figure 10-25, to increase the air temperature at the heater inlet by providing a heater exit temperature above 900 °C.

| **(a)** Heating tapes installation | **(b)** Insulation installation |
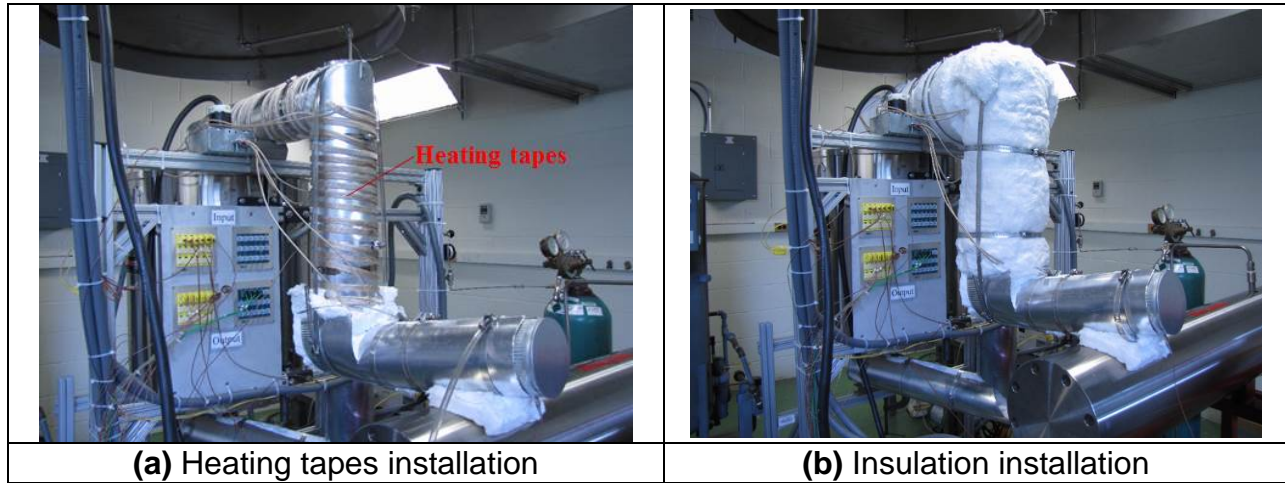
Figure 10-24. Heating tapes and insulation.

Table 10-4. Melting time versus furnace inlet temperature (numerical simulations).

Furnace inlet temp. (˚C)	Melting time (hours)
800	4
775	6.6
760	12
750	>15

| **(a)** Heater inlet setting | **(b)** Heating tape and insulation |
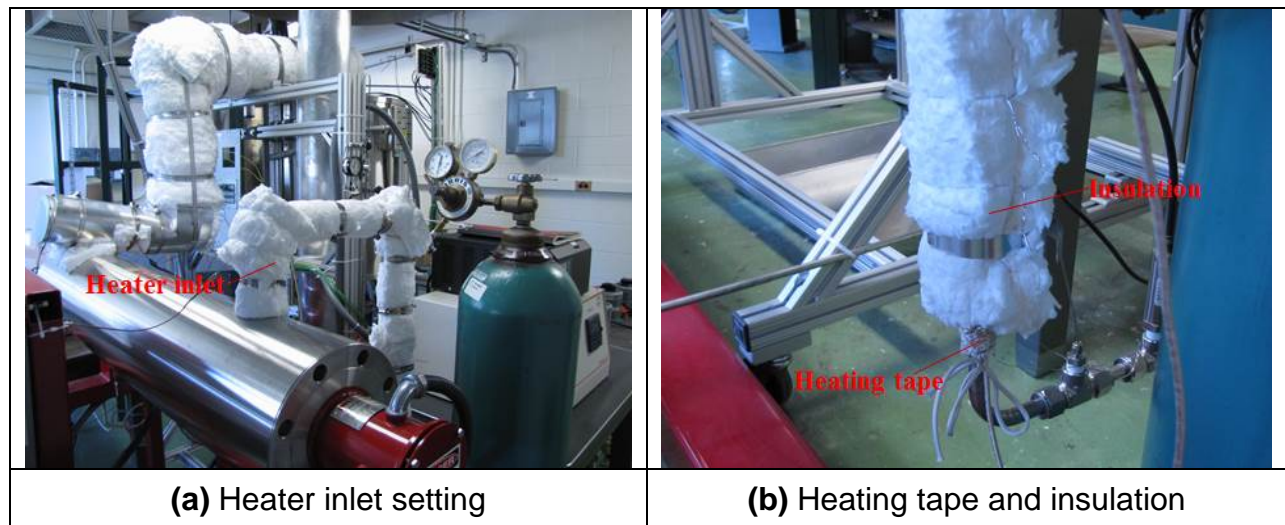
Figure 10-25. Heater inlet modifications.

The temperatures at various locations along the test loop were measured at different heater setting points. Figure 10-26 shows a typical temperature and air flow rate recording along the test loop during the charging process. Before starting the heater, the heating tapes preheated the ducts and the heater inlet tubing to (1) reduce the temperature difference between heater exit and furnace inlet and (2) provide additional heat for the heater to reduce the power requirement of the heater for high operation

temperatures, respectively. Then, the heater started to heat up to a certain temperature based on the set point. After a period of time, temperatures along the test loop (heater exit temperature, furnace inlet and outlet temperatures, etc.) reached steady state. The temperatures maintained at certain values in the test loop during the steady state process. The air flow rate was adjusted to maintain a constant rate during the entire charging process.

Various heater setting temperatures were tested. Table 10-5 illustrates the temperature measurements of the heater exit and the furnace inlet. Based on the experimental data, a correlation between heater exit temperature and furnace inlet temperature can be expressed as:

$$T_{Furnace\ inlet} = 102.71 + 0.72726 \times T_{Heater\ exit} \quad (T \text{ in } °C) \tag{10-1}$$

Furthermore, a correlation between furnace inlet temperature and heater setting point was obtained:

$$T_{Furnace\ inlet} = 102.23 + 0.76195 \times T_{Heater\ setting} \quad (T \text{ in } °C) \tag{10-2}$$

Table 10-5. Heater exit and furnace inlet temperature measurements.

Heater setting point (°C)	Heater exit temp. (°C)	Furnace inlet temp. (°C)
500	523.1	483.0
830	869.7	736.7
867	907.0	761.0
895	930.9	800.1
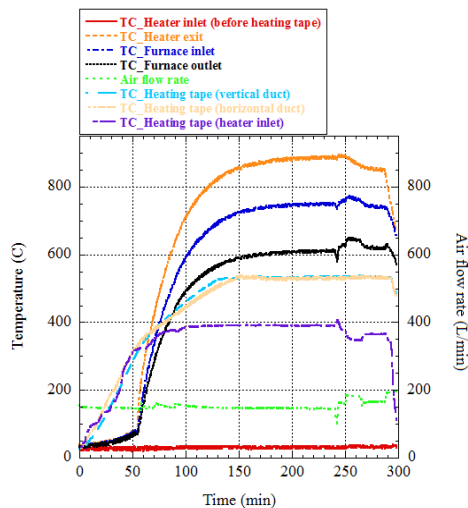
Figure 10-26. Temperature and air flow rate recordings along the test loop during charging process.

In conclusion, based on the temperature measurements in the test loop, modifications were made so that the heater would heat the air temperature above 900 °C such that the air temperature at the furnace inlet can reach 800 °C for the charging process for the prototypes to melt the PCM ($MgCl_2$). The correlations of the heater and furnace inlet temperatures developed were used as a guide for the future charging/discharging thermal cycling tests.

10.8. Furnace calibration

Prior to the charging/discharging experiments with the lab-scale prototypes, the furnace was calibrated with the Type K TCs to investigate the actual temperature distribution in the furnace at elevated temperatures. The furnace has two holes at the bottom and the top for the center HTF tube to go through it. First, the furnace was calibrated from 600 °C to 800 °C without insulation for the holes. Then, it was calibrated again with insulation for the holes. The results are shown in Figure 10-27. In the case of using insulation, the measured temperature at the center of the furnace was 15 °C higher than the controller set temperature, while it was 40–70 °C lower than the setting temperature without the insulation of the holes due to significant heat loss.

A temperature gradient was expected along the vertical axis of the furnace. To ensure the entire height of the prototype is maintained at the same temperature, we profiled the temperatures in the furnace. The temperature distribution in the axial direction of the furnace was investigated at elevated temperatures with fire-bricks used for supporting the prototypes to be placed at the center of the furnace (Figure 10-28). The bottom surface of the prototype will be located at -3 in. from the center of the furnace, and the top surface of the prototype will be located at +3 in. from the center of the furnace. The initial diameter of the firebricks was 10 in., and it was reduced to get a uniform temperature distribution in the furnace. The temperature differences between the center position and +3 in. position were less than 1 °C for all cases. The temperature differences between the center position and -3 in. position decreased with decreasing size of the firebricks. The difference was 4°C for 3-tiered firebricks (8-, 6-, and 5-in. diameter) while it was 9 °C for 10-in. diameter firebricks.

Figure 10-29 shows the temperature distributions in the axial direction of the furnace with 3-tiered firebricks at 600 °C, 700 °C, and 800 °C. The temperature distributions were very uniform for the region above the center of the furnace. There was 3-5 °C difference between the center position and -3-in. position because the firebricks absorbed some portion of the heat from the furnace.

Lastly, the temperatures of the outside insulation of the prototype and inside insulation of the prototype with firebricks at elevated temperatures were investigated to calibrate the temperatures of the outside insulation of the prototype during the charging/discharging experiments. The furnace setting temperature would be maintained at ~695 °C during the charging procedure and at ~735 °C during the discharging procedure. The measured temperatures are displayed in Figure 10-30. At the furnace setting temperature of 695 °C, the inside and outside insulation

temperatures were 701.1 ˚C and 717.3 ˚C, respectively. At the furnace setting temperature of 735 ˚C, the inside and outside insulation temperatures were 744.0 ˚C and 759.2 ˚C, respectively. There was 22 ˚C-24 ˚C difference between the furnace setting temperature and the outside insulation temperature. The relation between the furnace setting temperature and the outside insulation temperature can be used as a guide for the charging/discharging thermal cycling tests and an input for the numerical simulations.
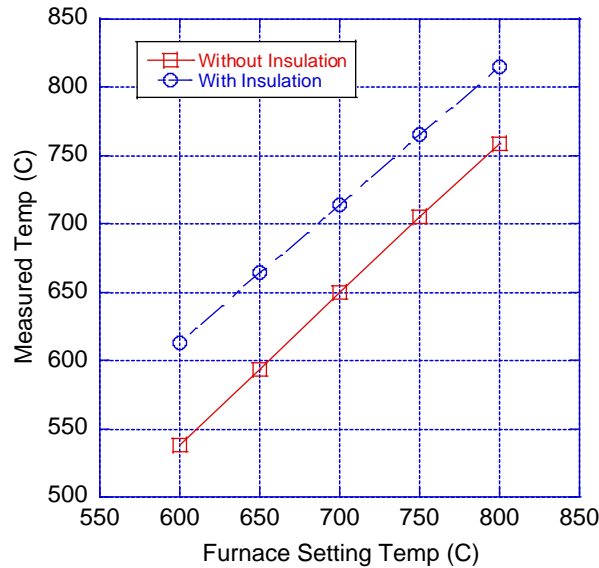
Figure 10-27. The furnace calibration with/without insulation for the holes.

| Figure 10-28. Temperature distributions in axial direction of the furnace with firebricks. | Figure 10-29. Temperature distributions in axial direction of the furnace with 3-tiered firebricks at 600 ˚C, 700 ˚C, and 800 ˚C. |
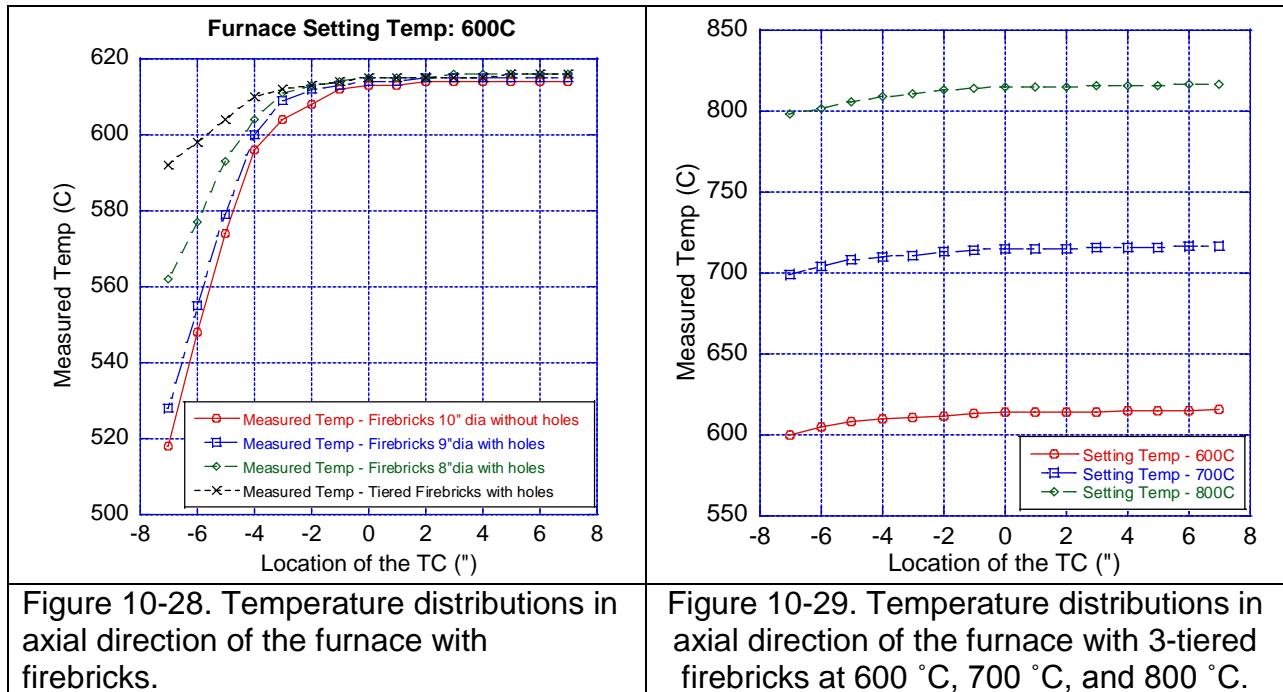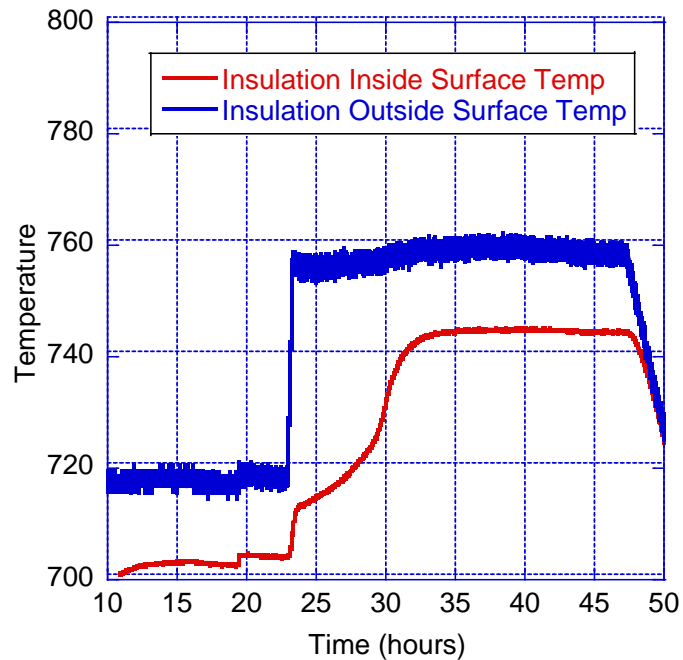
Figure 10-30. Measured temperature of inside and outside insulation of a prototype at the furnace setting temperature of 695 °C and 735 °C

10.9. Fabrication of LHTES prototypes

Prototypes were made using a sealed Incoloy 800H container filled with ~1.6 kg of graphite foam (GF)-MgCl₂. A standard half-inch tube goes through the center of the prototype container working as the HTF tube. After the fabrication of the prototype, prototypes were assembled onto the test loop for charging/discharging experiments. The objectives and the specifications for each of test series are summarized in Table 10-6. For reasons discussed later, only prototypes in series 1 were fabricated and tested.

10.9.1. Fabrication of the 1st series LHTES prototypes

For the first series of prototypes (see Table 10-6), the BNi-4 brazing process was used for bonding the graphite foam and Incoloy-800H base plate and HTF pipe. For the 1-1 prototype only, the interface of the container wall and graphite foam was not brazed to investigate the effect of the brazing on the corrosion behavior. Uncoated graphite foams were used for the first series of the prototypes to investigate whether SiC coating can be eliminated.

Figure 10-31 shows a photograph of the first series of prototypes after machining. Each prototype was inspected thoroughly after machining to verify it met the control values as per SOPO [13]. Any scratches/damage on the inside surfaces of the container tube, HTF tubes, or top and bottom plates were documented.

Table 10-6. Specifications for the lab-scale LHTES prototype experiments.

		1				2			3			4	
		1-1	1-2	1-3	1-4	2-1	2-2	2-3	3-1	3-2	3-3	4-1	4-2
Brazing	GF & HTF Tube	X	X	X	X	X	X	X					
	GF & Container Pipe		X	X	X	X	X	X					
	GF & Bottom Plate	X	X	X	X	X	X	X	X	X	X	X	X
Ni-Plating									X	X	X		
SiC Coating						X	X	X	X	X	X	X	X
Kfoam		X	X	X		X		X	X		X	X	
Graftech Foam					X		X			X			X
Goals		1. Confirm the simulation model. 2. Scale prototype to the real LHTES system in the CSP plan. 3. Investigate if the SiC coating can be removed. 4. Investigate the feasibility of the LHTES system for the CSP plant.				1. Confirm the simulation model. 2. Scale prototype to the real LHTES system in the CSP plant. 3. Investigate the feasibility of the LHTES system for the CSP plant.			1. Investigate interaction of PCM on Ni plated Incoloy. 2. Investigate how the gap affects the heat transfer process when the brazing process is removed. 3. Determine if brazing process can be eliminated.			1. Investigate corrosion of MgCl$_2$ to Incoloy pipes to see whether the Mg metal additive can prevent the corrosion or not.	
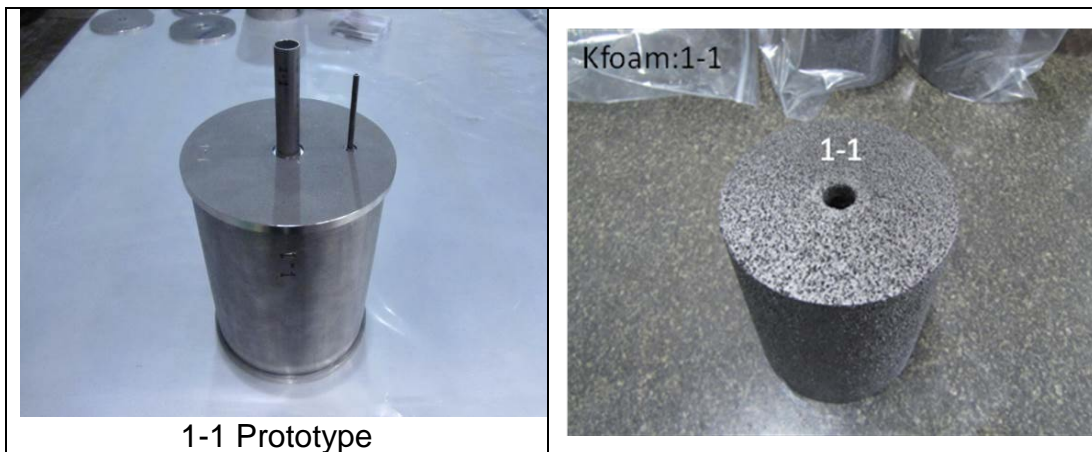
Figure 10-31. Parts for the first series prototypes after the machining process.

Graphite foams for the first series of prototypes were machined into a cylindrical shape with 0.5-in. center hole to fit each of the container pipes and HTF tubes. Clearances between the graphite foam and the HTF tube, as well as the graphite foam and the container pipe, should be 0.01 in. to achieve 0.01-in. thickness of BNi-4 layer. The dimensions of the graphite foams were measured using a caliper with 0.005-in. resolution. The dimensions of the graphite foams for the first series of prototypes after machining satisfy the ± 0.05 in. design requirement, as per SOPO [13].

After the machining, the bottom joining parts (bottom plate/container pipe and the bottom plate/the HTF tube) were welded by using the gas-tungsten arc welding (GTAW) technique. Inconel-617 alloy was used as the welding filler metal. All parts were ultrasonically cleaned prior to welding.

The first series of prototypes after the welding process are shown in Figure 10-32. Each of the prototypes was inspected thoroughly after the welding process. For the 1-1 prototype, the joining section between the HTF tube and the bottom plate was overheated. Although the 1-1 prototype has an overheated region, it passed the leakage test. Other prototypes of the first series (1-2, 1-3, 1-4) showed no damage in the welded zone, and they all passed the leakage test.

GTA Welding for the Bottom Plate and the Container Pipe	GTA Welding for the Bottom Plate and the HTF Tube
1-1 prototype	1-1 prototype
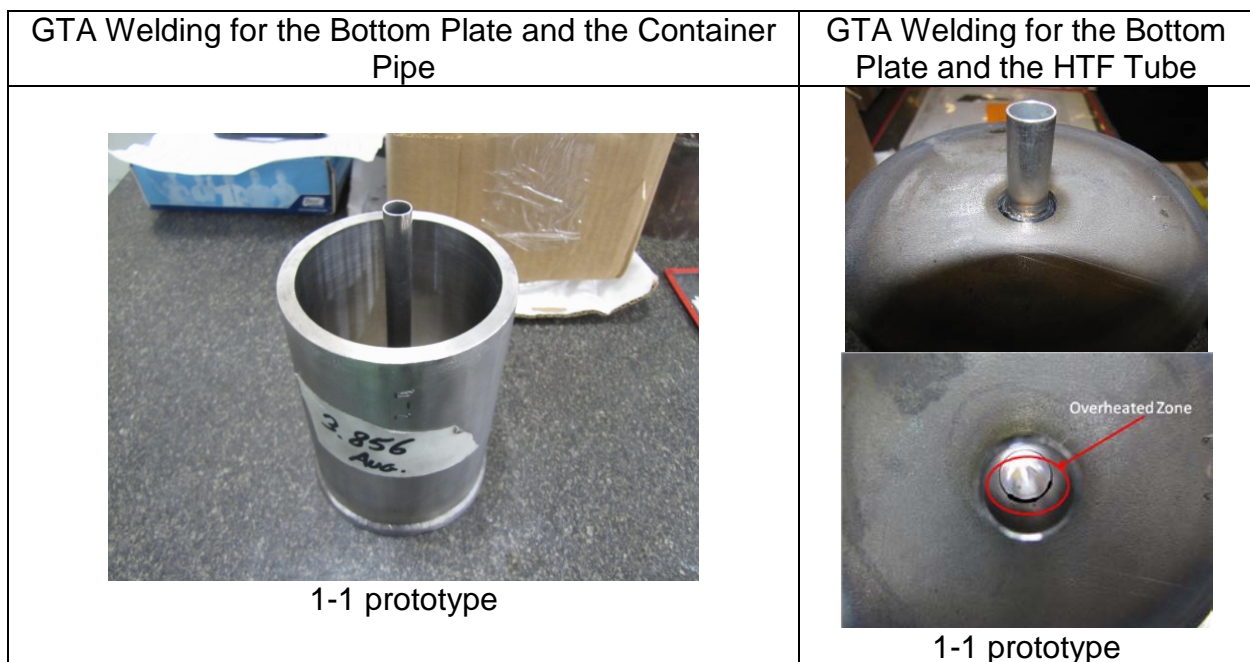
Figure 10-32. The first series prototypes after the bottom joining section welding.

After the bottom welding, the prototypes were brazed in a vacuum furnace. Prior to brazing, the surfaces of the Incoloy-800H parts were cleaned with 1200 grade SiC paper to remove any surface oxides, and subsequently, washed in a warm bath of Citranox solution 2%, then rinsed with deionized water. After cleaning and drying in the oven, brazing paste (BNi-4) was applied on both the graphite foam surfaces and the welded Incoloy-800H container surfaces. For the 1-1 prototype, the brazed regions were the graphite foam/HTF tube and the graphite foam/bottom plate. For the 1-2, 1-3, 1-4 prototypes, the brazed regions were the graphite foam/HTF tube, the graphite foam/bottom plate, and the graphite foam/container pipe. The amount of paste required was calculated from the previous brazing experiments, and the brazing paste was prepared separately for each of the prototypes. The brazing conditions are summarized in Table 10-7. The prototypes (1-4) from the first series of prototypes after the brazing process are shown in Figure 10-33. Each of the prototypes was inspected thoroughly after the brazing. The weights of these prototypes before and after the brazing were measured by using a Mettler Toledo scale with a resolution of 1 g and a capacity of

20 kg. Based on the measured weights of the first series prototypes after the brazing process, the applied braze amounts satisfy the resulting braze thickness >250μm as per SOPO [13].

Table 10-7. Brazing conditions for the LHTES prototype.

Brazing Conditions	
Brazing Temperature	1080 ˚C–1090 ˚C
Brazing Time	2 minutes
Brazing Pressure	1.0×10^{-5} Torr–1.1×10^{-5} Torr
Heating Rate/Cooling Rate	10 ˚C/min for Heating 10 ˚C/min for Cooling
Load on the Top to Keep Foam in Position	500 g

Figure 10-33. The first series prototype (1-4) after the vacuum brazing process.

After the brazing process, the prototypes were infiltrated with $MgCl_2$. A vacuum-assisted melt infiltration process was used to infiltrate $MgCl_2$ into the graphite foams of the prototypes. The prototypes were encased in a specially designed mold for the casting. Figure 10-34(a) shows the mold right after infiltration. Once the mold was disassembled, the infiltrated prototype was recovered (Figure 10-34(b)). Notice that the prototype has been bagged with desiccants to prevent/minimize any moisture pickup. The outside surfaces of the prototypes were cleaned by sand paper and ethyl alcohol. Then, the $MgCl_2$ and carbon composites that filled the 1-in. empty space above the $MgCl_2$-graphite foam composite in the prototype were removed by drill and sand paper (Figure 10-35). After the cleaning procedure of the prototypes, the infiltration rate was evaluated by measuring the weight of the prototypes. The calculated infiltration rate of the prototypes was about 90% by solid density and ~120% by liquid density. Similar values have been reported in the literature for paraffin wax PCM infiltrated in foam [39].

Figure 10-34. Prototype after the PCM infiltration.
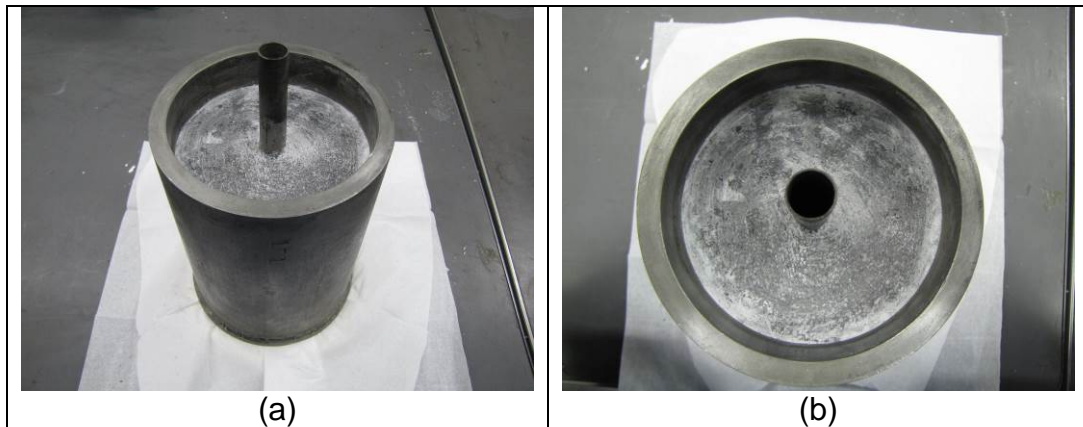
Figure 10-35. Prototype after the cleaning procedure.

Prototype 1-2 was selected for the first charging/discharging experiment. Four type-S TCs were installed in the prototype 1-2, as described in Figure 10-36(a). TC1 is located on the 2.25-in. diameter circle, 1-in. depth, and Z-direction of the graphite foam. TC2 is located on the 1.25-in. diameter circle and 2.5-in. depth with 90° angle from the TC1. TC3 is located on the 1.25-in. diameter circle and 4-in. depth with 90° angle from the TC2. TC4 is located on the 3.25-in. diameter circle and 2.5-in. depth with 90° angle from the TC3. After the first prototype 1-2, six type-S TCs were installed in the prototypes 1-1, 1-3, 1-4 as described in Figure 10-36(b). The holes for the thermocouples were drilled using a #51 drill bit with a transparent TC guide. The locations of the installed thermocouples satisfy the SOPO [13] requirements. Figure 10-37 shows the prototypes after the installation of type-S thermocouples.

Meanwhile, the feedthroughs for the thermocouples to penetrate the top plate without leakage were installed on the top plates by using the sealant material DEACON 8875 with the curing process that was described in the previous section (Figure 10-38). Then, the thermocouple wires were passed through the feedthroughs, and the top plate was placed on the top of the prototypes. A spool was used to hold the thermocouple wires during the top welding procedure, as shown in Figure 10-39.
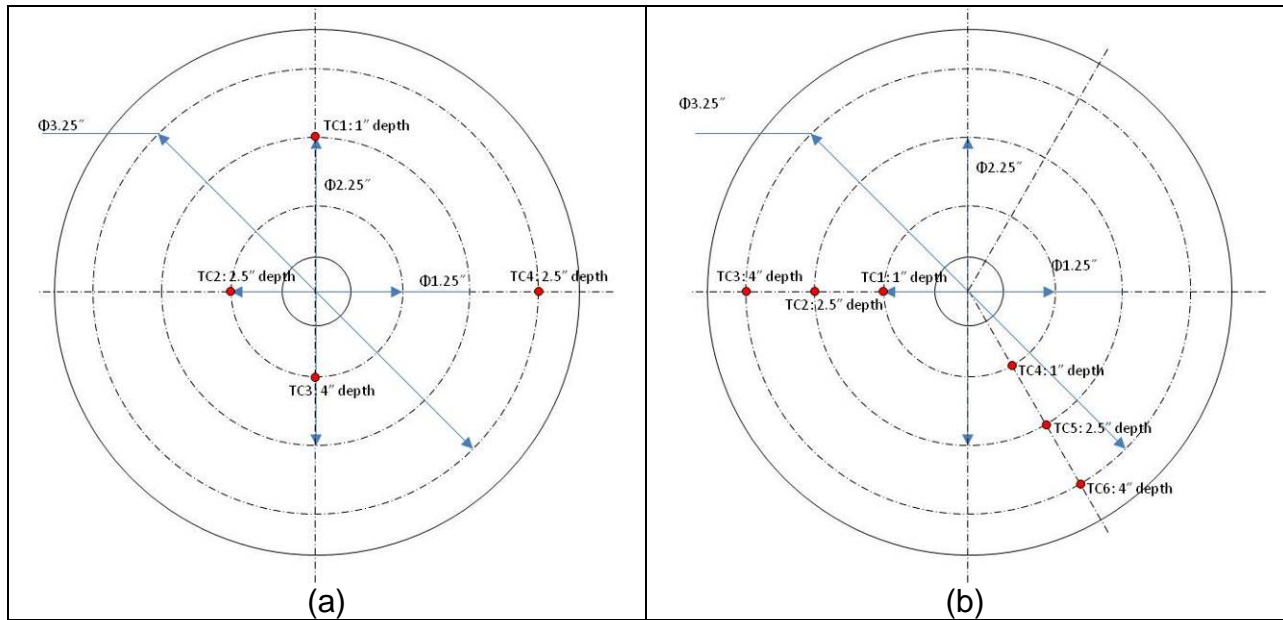
Figure 10-36. Thermocouple arrangement in prototype: (a) 1-2 and (b) 1-1, 1-3, and 1-4.
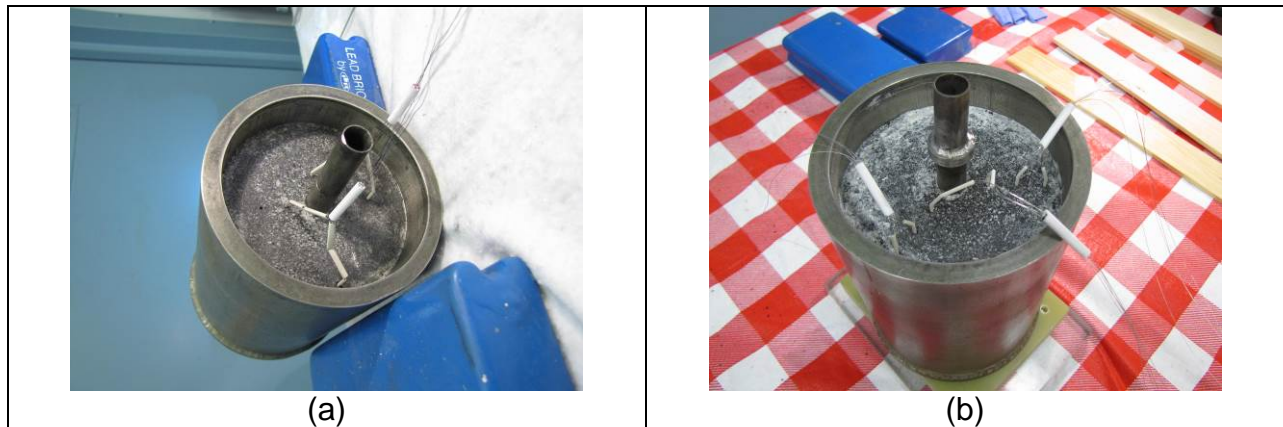
Figure 10-37. Prototypes after installation of thermocouples: (a) 1-2 and (b) 1-3.

Figure 10-38. Top plates for prototypes after feedthroughs installed: (a) 1-2 and (b) 1-3.

Figure 10-39. Prototypes after installation of top plate and TCs: (a) 1-2 and (b) 1-3.

After the installation of the thermocouples and the top plate on the prototypes, they were welded by the GTAW technique. The top welding regions were the prototype container/top plate, the center HTF tube/top plate, and the vacuum-argon line tube/top plate.

For the prototype 1-2, the first cover welding try was unsuccessful. Only the prototype container/top plate region was leak tight, and other regions were not. A crack was found on the inside surface of the center HTF tube. The vacuum-argon line tube was broken, and some of Ni-plating materials and welding filler metals plugged the hole (Figure 10-40). Some oxides on the surface of Incoloy parts after the infiltration may have affected the welding. The plugged hole was machined off to remove the Ni plating that contains phosphorus, which is not conducive to the welding process. To rectify this issue, the spot was plug-welded with filler metals. A new hole for the vacuum-argon line was drilled beside the original hole. Then, a new tube without Ni plating was welded to the new hole by using an adapter to reduce the thermal load on it (Figure 10-41(a)). A tube with 7/16-in. OD was placed inside of the center HTF tube with 0.44-in. ID, and the two tubes were welded together to repair the cracks on the center HTF tube (Figure 10-41(b)). After the repairing process, prototype 1-2 passed the leakage test and was ready for the first charging/discharging experiment (Figure 10-42). Prior to installation of the prototype to the test loop, insulation was placed on the prototype 1-2, as shown in Figure 10-43.

Figure 10-40. Prototype 1-2 after the first top welding trial.

Figure 10-41. Repair of prototype 1-2: (a) vacuum Ar line tube and (b) center HTF tube.

Figure 10-42. Prototype 1-2 after top welding completed.	Figure 10-43. Prototype 1-2 after placing insulation.

For prototypes 1-1, 1-3, and 1-4, two adapters were used to avoid the issues that occurred in prototype 1-2. One is for the center tube, and the other is for the vacuum/argon line tube. In addition, the filler metal Inconel-617 was used to weld the adapters and the tubes. After the top welding with adapters and filler metals, the prototypes 1-1, 1-3, and 1-4 passed the leakage test and were ready to go for the

charging/discharging experiment (Figure 10-44). Prior to installation of the prototype to the test loop, the insulation material was placed on the prototypes, as shown in Figure 10-43.
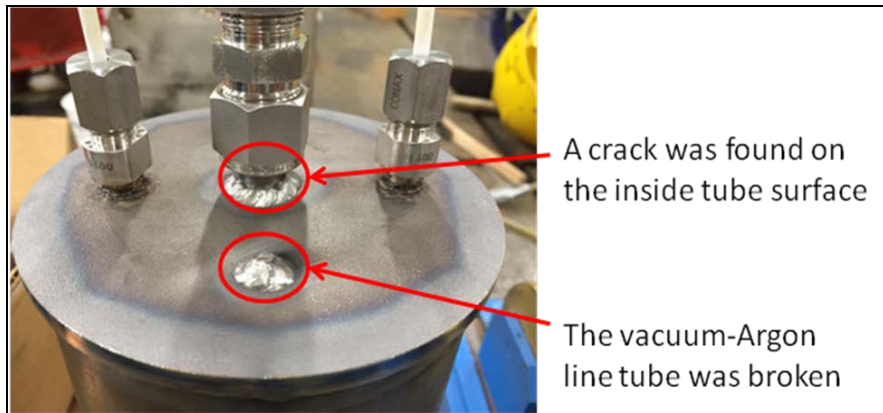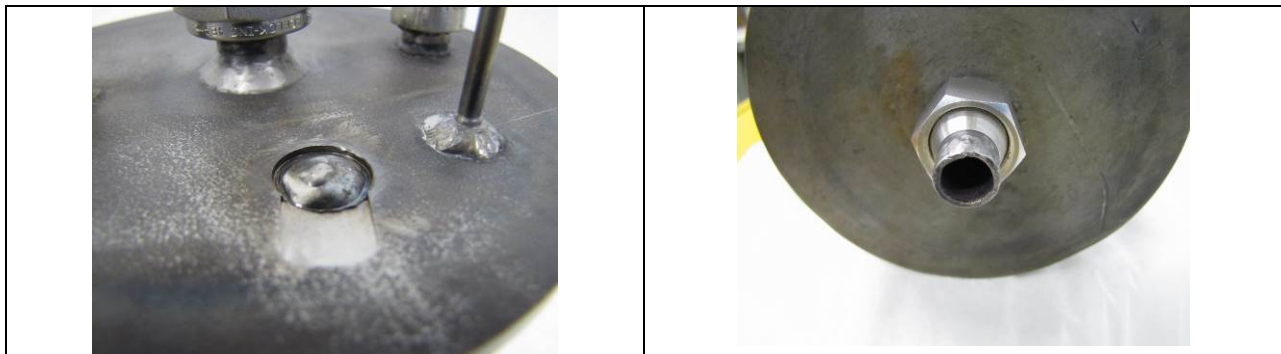

Figure 10-44. Prototype 1-3 after top welding completed.

10.9.2. Fabrication of the 2nd, 3rd, and 4th series LHTES prototypes
For the 2nd series prototypes, the BNi-4 brazing process was used for bonding the graphite foam and Incoloy-800H base plate, as well as container pipe and center HTF tube. The PDC SiC-coated graphite foams will be used for prototypes 2-1 and 2-2 to investigate if the SiC coating can protect the graphite foam from $MgCl_2$.

For the 3rd series prototypes, electroless Ni plating was used for protecting the Incoloy-800H plates, container pipe, and center HTF tube from the corrosion of $MgCl_2$. The center HTF tube and the graphite foam will not be brazed to investigate how any gap at the interface affects the heat transfer. Only the base plate and the graphite foam will be brazed to hold the graphite foam in the position. The PDC SiC-coated graphite foam will be used for the prototype 3-1 to investigate if the SiC coating can protect the graphite foam from the $MgCl_2$.

For the 4th series prototypes, no brazing or electroless Ni plating will be used for protecting the Incoloy-800H plates, container pipe, and center HTF tube from the corrosion of $MgCl_2$. Magnesium metal will be added in the $MgCl_2$ salt to prevent the corrosion of Incoloy parts. Only the base plate and the graphite foam will be brazed to hold the graphite foam in position.

Each prototype was inspected thoroughly after machining to verify they met the control values as per SOPO [13]. Any scratches/damages on the inside surfaces of the container tube, HTF tubes, top and bottom plates were documented.

After the machining of the graphite foams for the 2nd, 3rd, 4th series, prototypes 2-1, 2-2, and 3-1 graphite foams were coated by PDC-SiC. The weight change of the graphite foams before and after the coating process was recorded. Based on the weight change measurements, the weight of coating per unit surface area was calculated. The coating coverage of the foams satisfied the requirement of >0.02 g/m^2 as per SOPO [13].

Meanwhile, the bottom joining parts (the bottom plate/container pipe and the bottom plate/HTF tube) were welded by the GTAW technique. Inconel 617 alloy was used as welding filler metal. All parts were ultrasonically cleaned prior to welding. Each of the prototypes was inspected thoroughly after the welding process. For the prototype 3-1, the joint between the HTF tube and the bottom plate was overheated. Although prototype 3-1 has an overheated region, it passed the helium leakage test. All other prototypes also passed the leakage test.

Since the industrial infiltration company moved their lab so they could not conduct further infiltrations within the timeline of the project, the fabrication procedure for the 2nd, 3rd, and 4th series prototypes was stopped, and hence no results are reported for these prototypes.

10.10. Moisture removing and argon back filling of the prototypes

Prior to the charging/discharging experiments for the prototypes, the moisture absorbed in the $MgCl_2$ during the fabrication process was removed by heating and evacuation. The procedure of the moisture removing and back filling of argon gas in the prototype is as follows:

1) Evacuate the prototype using a vacuum pump to 1 psi.
2) Heat the prototype up to 400 ˚C with 2 ˚C/min ramp rate.
3) Hold the prototype at 400 ˚C for 24 hours and evacuate the prototype when the inside pressure increases.
4) Heat the prototype up to 600 ˚C with 2 ˚C/min ramp rate.
5) Hold the prototype at 600 ˚C for 24 hours and evacuate the prototype when the inside pressure increases.
6) Cool the prototype to room temperature with 1 ˚C/min ramp rate.
7) Back fill the prototype with argon gas at room temperature.
8) Evacuate the sample to 1 psi at room temperature.
9) Repeat steps 7 and 8 to further remove the impurity in the small prototype sample.

Figure 10-45 shows the pressure and temperature change of prototype 1-2 during the moisture removal. The pressure increased sharply after 250 °C, which was observed in a previous pressure monitoring experiment using small prototype samples. Because the amount of the $MgCl_2$ in the prototype is much larger than that of the small prototype sample, the prototype was evacuated for 24 hours at 400 °C. Then, the pressure was again increased sharply after 500 °C, which was observed in the previous pressure monitoring experiment using small prototype samples. Due to the large amount of the $MgCl_2$, the prototype was evacuated for 24 hours at 600 °C. After the heating and the evacuation process, the prototype was cooled to room temperature. The pressure inside

prototype 1-2 was maintained at 2.5 psi. This indicated that the vacuum-tight sealing survived the entire fabrication process and the moisture removal step.

Similarly, the moisture removal and argon back filling process were applied for prototypes 1-1, 1-3, 1-4, and their vacuum tight sealing survived throughout the fabrication and the moisture removal.
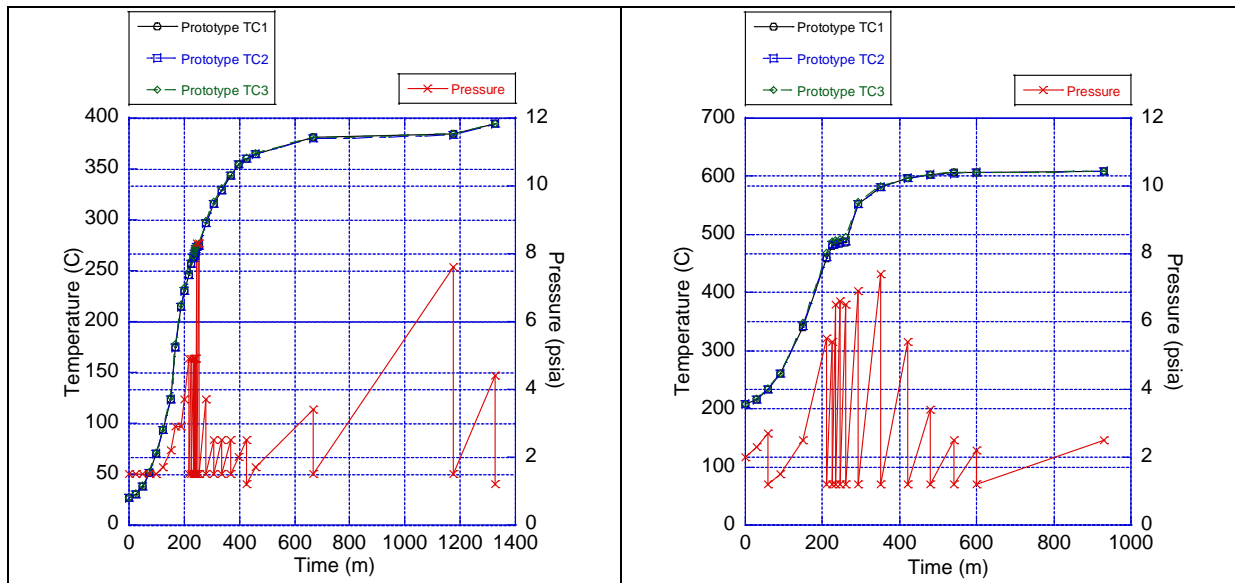

Figure 10-45. Pressure and temperature change during the moisture removal.

10.11. Preliminary conduction heat transfer test of the prototype 1-2

A preliminary heating/cooling test was conducted at low temperatures (below the melting point of the PCM) for prototype 1-2 to (1) investigate the temperature profiles in the prototype during the heating and cooling processes at low temperatures to verify the conduction thermal model and (2) compare the experimental measurement data to the simulation results to verify the numerical simulation model for charging/discharging thermal cycling tests at elevated temperatures. The test procedure was as follows.

Figure 10-46(a) shows the installation of the prototype in the furnace. The model simulating the prototype geometry in the furnace is displayed in Figure 10-46(b). There is insulation placed at the outside of the prototype and the HTF tubing to reduce the heat loss. A thermocouple was placed at the furnace inlet to measure the air inlet temperatures during the test. The furnace temperatures were recorded from the furnace thermocouple measurements.

The furnace was first heated up to 100 °C and held at that temperature to keep the prototype initial temperature at that level. Then, the heater was turned on to 100 °C to keep the air flow inside the center tubing of the prototype at that temperature, thereby maintaining the prototype initial temperature at 100 °C before the heating/cooling process. After the prototype temperature equilibrated at 100 °C, the heater setting point was increased to 522 °C to obtain a furnace inlet temperature at 500 °C according to the correlation developed in Equation (10-2) to heat up the prototype. After three hours of

heating, the heater setting temperature was reduced to 200 ˚C for the cooling of the prototype.

Figure 10-47 shows the experimental measurement data recorded by the thermocouples. The pink solid curve indicates the furnace inlet temperature during the heating/cooling test. First, the furnace inlet temperature was increased from 100 ˚C to 500 ˚C and held at 500˚C for the heating process. After three hours, the furnace inlet temperature was decreased from 500˚C to around 200°C for the cooling process. The yellow curve indicates the furnace temperature recordings during the experiment. The furnace temperatures were used for the convection heat transfer boundary condition around the prototype in the numerical simulations. The three dash lines (red, blue, and green) in Figure 10-47 are the thermocouple measurements in the prototype.

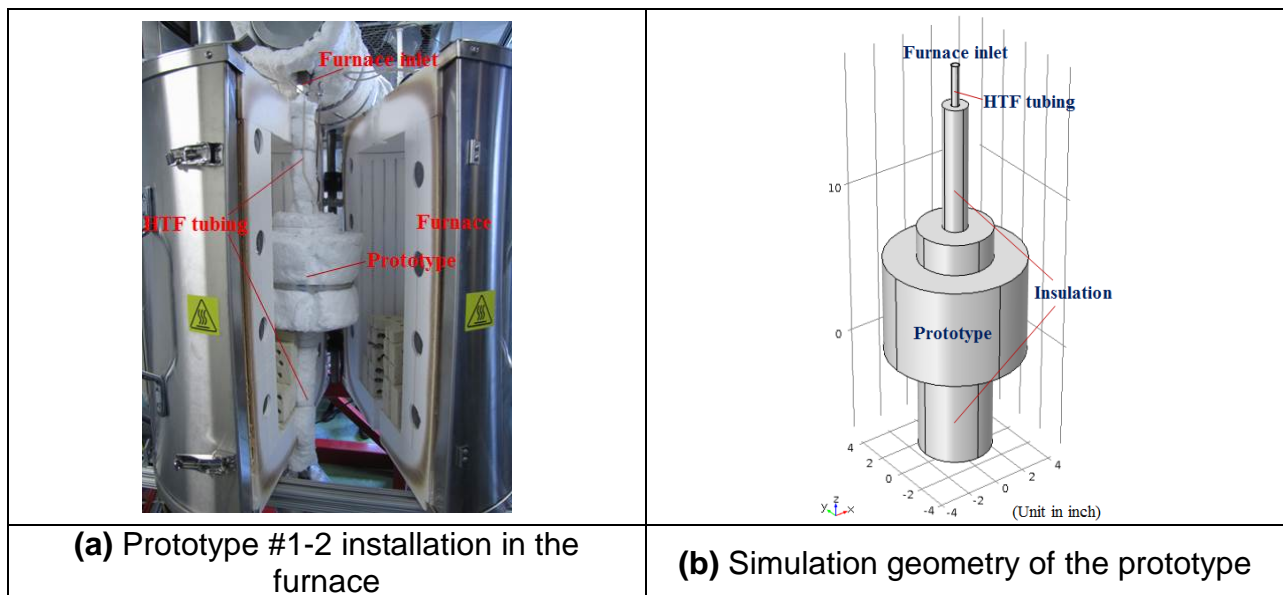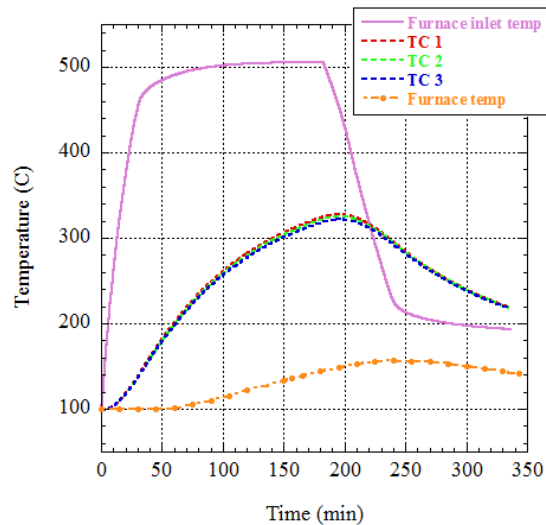| (a) Prototype #1-2 installation in the furnace | (b) Simulation geometry of the prototype |

Figure 10-46. Prototype geometry.

Figure 10-47. Temperature recordings during the heating-cooling test.

The prototype temperatures were first increased from the initial temperature 100 °C to around 325 °C, then, cooled toward 200 °C. The temperatures from the three TCs in the prototype were close to each other, as indicated in Figure 10-47 because of the low heat transfer coefficient of air flow (low Biot number).

Curves were fitted to the experimental data of furnace inlet temperatures. These fitting curves were put in the simulation model to indicate the air temperature changes at the furnace inlet. The prototype temperature profiles obtained from the simulation are displayed in Figure 10-48. The solid lines represent the simulation results of the prototype temperatures, while the dashed lines indicate the experimental measurements. Comparison of the simulation results to the experimental data showed that the predictions are quite close to the TC measurements in the prototype, with a difference less than 9%. For the heating process, the difference between the simulation results and the experimental data was within 5%. For the cooling process, the difference was less than 9%. The bigger difference during the cooling process was probably caused by the immediate cooling of the prototype after the heating process (the initial prototype temperature was not at equilibrium before the cooling process). Nevertheless, the difference between measurements and experiments was within the anticipated ±10% as stated in the SOPO [13]. In the actual charging/discharging tests, the initial prototype temperatures were stabilized before charging and discharging processes begin.

Based on the conduction heat transfer test, the temperature profiles in the prototype from the TC measurements during the heating/cooling process matched the prediction. The test loop is thus capable of carrying out the charging/discharging thermal cycling tests for the prototypes. Also, the simulation model is applicable to the heat transfer predictions of the prototypes.
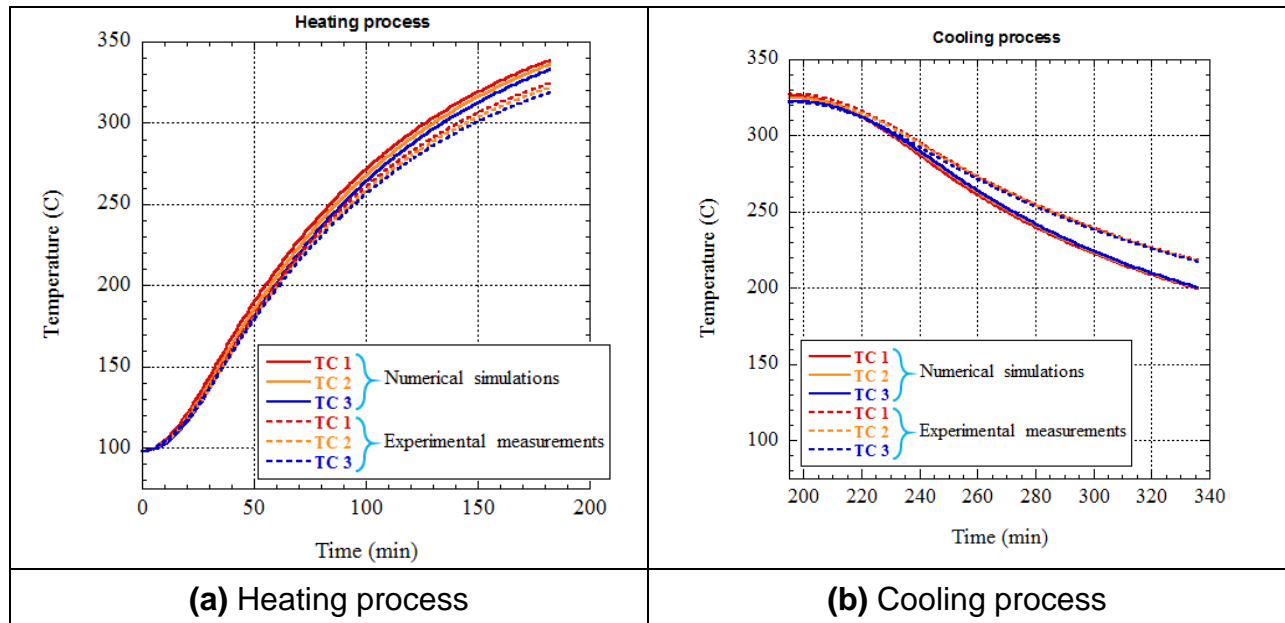

(a) Heating process   **(b)** Cooling process

Figure 10-48. Comparison of the experimental measurements and simulation results for heating-cooling test.

11. Charging/Discharging Tests and Analysis for Prototypes 1-2, 1-4, and 1-1

Charging and discharging experiments for prototypes 1-2, 1-4, and 1-1 were conducted in the experimental test facility as discussed in previous sections.

11.1. Configuration of prototypes 1-2, 1-4 and, 1-1

The main configurations of prototypes 1-2, 1-4, and 1-1 are quite similar. As shown in Figure 11-1, the prototypes were fabricated with the $MgCl_2$-infiltrated graphite foam within a cylinder container of a welded top cap and a welded bottom cap. A center HTF tubing runs through the top cap, the $MgCl_2$/graphite foam composite, and the bottom cap. This tubing, in turn, is connected to the rest of the test facility. The tubing brings the high-temperature air exiting from the heater to the furnace to heat up/cool down the prototype during the charging/discharging process. Thermocouples were preinstalled for measuring temperatures at certain locations of the $MgCl_2$/graphite foam composite (Figure 11-2). For all the prototypes, the graphite foam was brazed to the container walls and the heat transfer tubing. For prototypes 1-2 and 1-1, Koppers foam (open porosity of ~84%) was used, and for prototype 1-4, Graftech foam (open porosity 90%) was used.
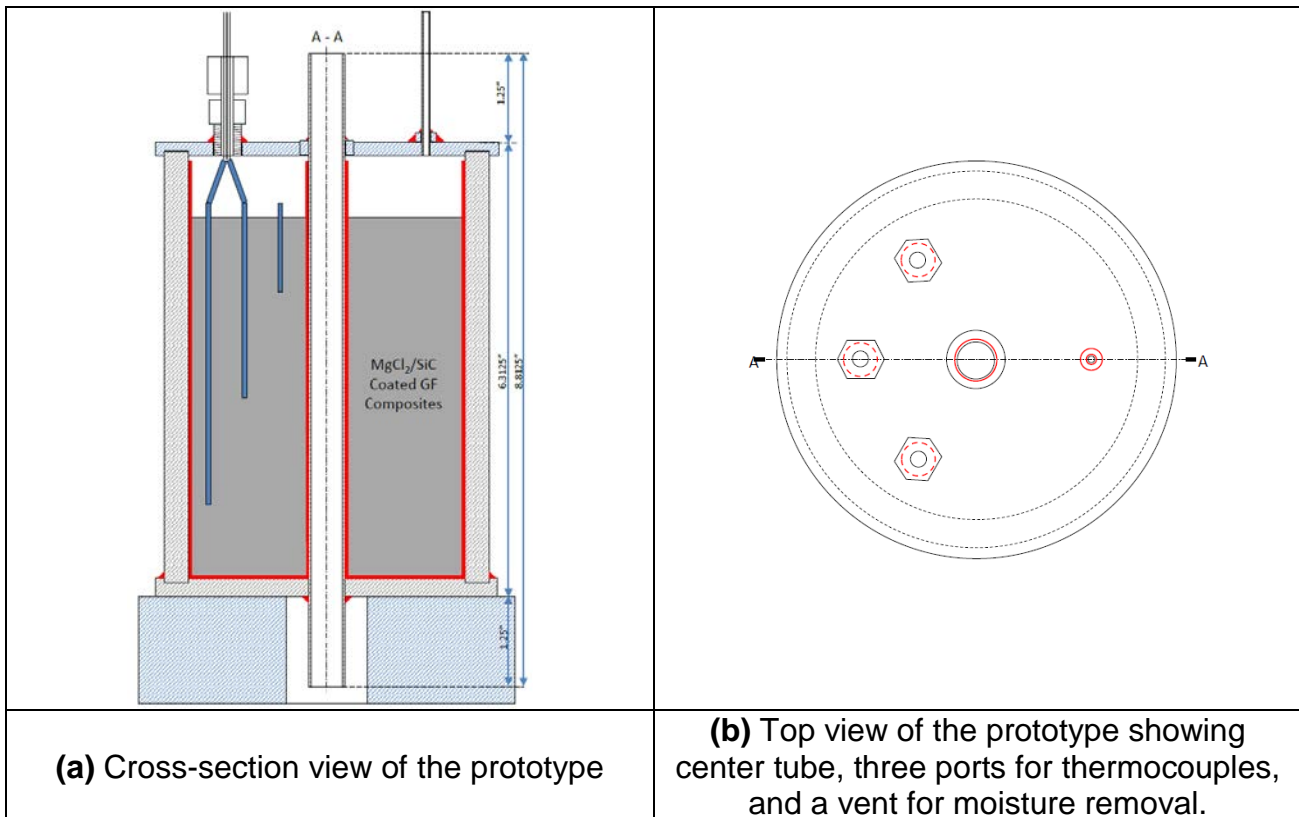

(a) Cross-section view of the prototype	**(b)** Top view of the prototype showing center tube, three ports for thermocouples, and a vent for moisture removal.

Figure 11-1. Configuration of the prototypes.

11.2. Installation of thermocouples in prototypes 1-2, 1-4, and 1-1

Thermocouples were installed in prototypes 1-2, 1-4, and 1-1 for measuring temperatures at certain locations of the graphite/foam composite. Four, six, and six thermocouples were initially installed in prototypes 1-2, 1-4, and 1-1, respectively. Thermocouples were installed at various elevations (i.e., 1-, 2.5-, and 4-in. depth) and radii in the prototype to measure the temperature profiles of the graphite foam-$MgCl_2$ during the heating/cooling process. Figure 11-2 show the locations of these thermocouples, as well as inside and outside views of the installed thermocouples.

11.3. Prototype loading into furnace

The following preparations were conducted before the prototypes were loaded into the furnace:

1. Attach extension tubing to the top and the bottom of the prototype center tubing.
2. Attach extension tubing to the vacuum port of the prototype.
3. Insulate the prototype.
4. Check the thermocouples of the prototype.
5. Make additional two-hole ceramic sheaths for thermocouple insulation.
6. Install addition ceramic sheaths onto each thermocouple.
7. Recheck the thermocouples of the prototype.
8. Mark the thermocouple number and polarity on the last ceramic sheath for each thermocouple.

The pictures in Figure 11-3 show a prototype ready to be loaded into the furnace and after it is loaded.
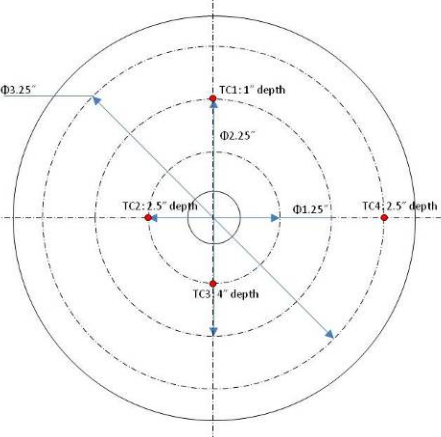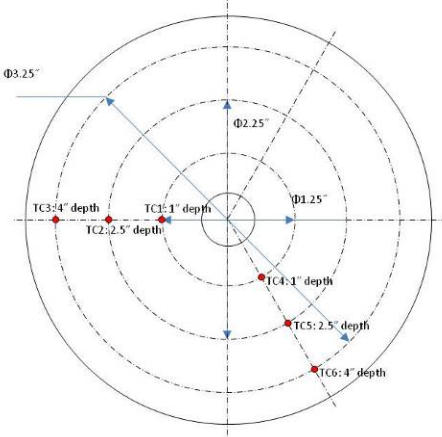
The following preparations were conducted after the prototypes were loaded into the furnace:

1. Connect the top and the bottom of the prototype center tubing to the air heat transfer tubing.
2. Connect the vacuum port of the prototype to the vacuum pump line.
3. Pump down the prototype vacuum for leak check.
4. Close the furnace and insulate the system.
5. Connect the prototype thermocouple wires to the thermocouple panel.
6. Check the thermocouple readings on the computer.

11.4. Thermocouples for heat loss/gain calculation

To account for the prototype heat loss to the furnace during the charging process and the prototype heat gain from the furnace during the discharging process, two thermocouples were installed onto the prototype for temperature measurements: one

outside the prototype container and the other outside the prototype insulation. The green lines in Figure 11-4 show the installation of these two thermocouples.

Prototype 1-2	Prototypes 1-4 and 1-1
Thermocouple locations	Thermocouple locations
Inside view of the installed thermocouples	Inside view of the installed thermocouples
Outside view of the installed thermocouples	Outside view of the installed thermocouples

Figure 11-2. Location of the thermocouples installed in prototypes 1-2, 1-4, and 1-1.
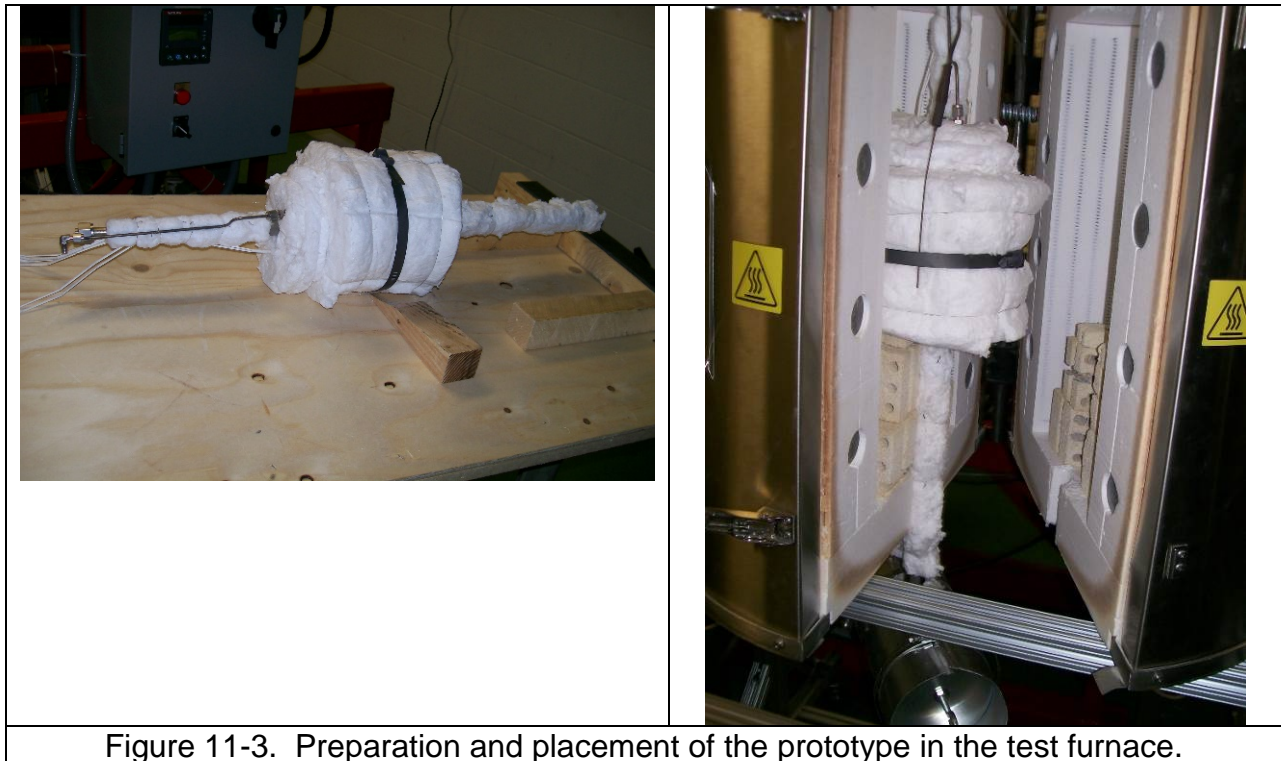
Figure 11-3. Preparation and placement of the prototype in the test furnace.
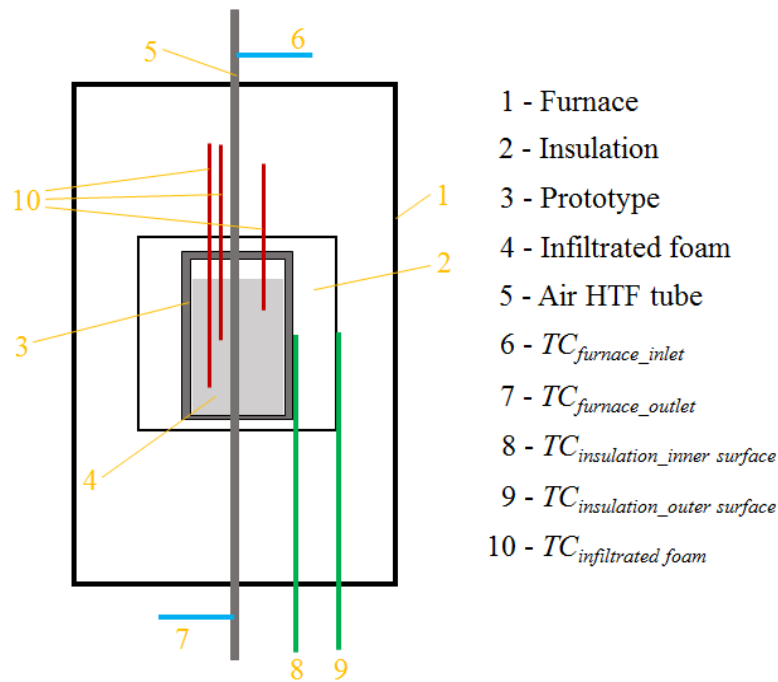
Figure 11-4. Additional thermocouples installed to measure heat loss/gain.

11.5. Prototype test procedure

The experimental testing of a prototype included two major procedures: moisture removal and charging/discharging.

11.5.1 Moisture removal

After the prototype was installed in the furnace, the moisture removal procedure was conducted according to Figure 11-5 through the following steps:

1. Pump down the prototype vacuum and monitor the vacuum level change during a 24-h period for checking any potential leakage.
2. Heat the prototype to 400 °C, keep the prototype at 400 °C for 20 h, and pump down the prototype vacuum periodically to remove moisture.
3. Heat the prototype to 600 °C, keep the prototype at 600 °C for 24 h, and pump down the prototype vacuum periodically to remove moisture.

After the moisture removal procedure, the prototype was pressurized to approximately 10 psig, and then the pressure was decreased to approximately -28 in. Hg for three times to create an argon environment in the prototype.
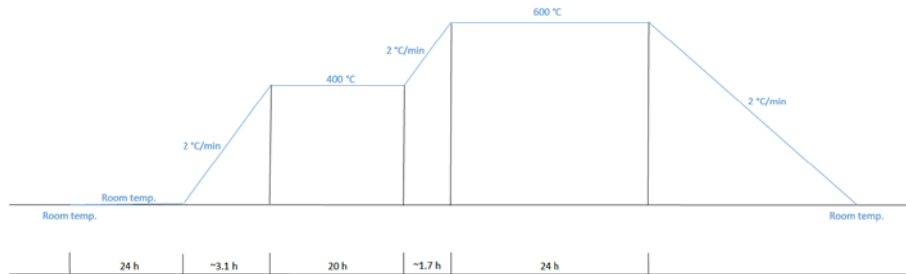
Figure 11-5. Furnace setting for moisture removal from the prototype.

11.5.2 Charging and discharging

Charging and discharging were generally conducted in one cycle, as shown in Figure 11-6 through the following steps:

1. Preheat the furnace to 695, 685, or 680 °C.
2. Switch the heating tapes for HT tubing, turn on the air pump, and set up the heater controller to obtain an air inlet temperature of approximately 700 °C.
3. Wait for approximately 2 h for the prototype to reach an equilibrium state.
4. Start the charging procedure by increasing the heater controller setting to obtain an air inlet temperature of approximately 800 °C.
5. After the charging, increase the furnace temperature to 735 °C and reduce the heater controller setting to obtain an air inlet temperature of about 750 °C.
6. Wait for approximately 2 h for the prototype to reach an equilibrium state.
7. Start the discharging procedure by decreasing the heater controller setting to obtain an air inlet temperature of approximately 500 °C.
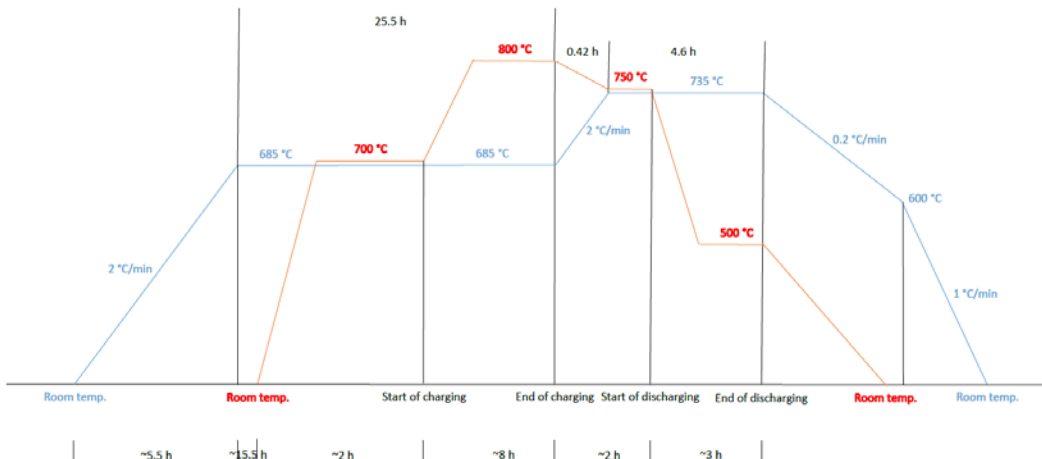
Figure 11-6. Furnace temperature settings during the charging/discharging tests.

11.6. Simulation conditions

Koppers graphite foam (GF) was used in Prototypes 1-1 and 1-2 while Graftech graphite foam was used in Prototype 1-4. Table 11-1 displays the properties of infiltrated foams used in the simulation models for the three prototypes. The open porosity is 84% for Koppers foam and 90% for Graftech foam. The properties of the foam composites listed in Table 11-1 are estimated from the experimental measurements and/or literature data. Figure 11-7 shows the typical 3D simulation results during charging/discharging process as a function of time.

Table 11-1. Properties of infiltrated foams.

	Prototype 1-1	Prototype 1-2	Prototype 1-4
Graphite foam	Koppers	Koppers	Graftech
GF open porosity (%)	84	84	90
Infiltration rate of liquid $MgCl_2$ (ϕ_{liquid})	1.26	1.19	1.20
Infiltration rate of solid $MgCl_2$ (ϕ_{solid})	0.91	0.86	0.87
Mass percentage of $MgCl_2$ for the infiltrated foam (%)	83.1	82.4	88.9
PCM melting point ($^{\circ}$C) (DSC measurement)	718	718	718
PCM solidification point ($^{\circ}$C) (DSC measurement)	706	706	706
Melting/solidification range ($^{\circ}$C)	8	8	8
Latent heat of fusion (kJ/kg)	377.3	374.0	403.6
Density (kg/m^3)	2137	2050	2035
Specific heat (J/kg K) at 700 $^{\circ}$C)	1068	1074	1018
Thermal conductivity (W/m K) (k_z at 700 $^{\circ}$C)	23.5	23.5	21.4
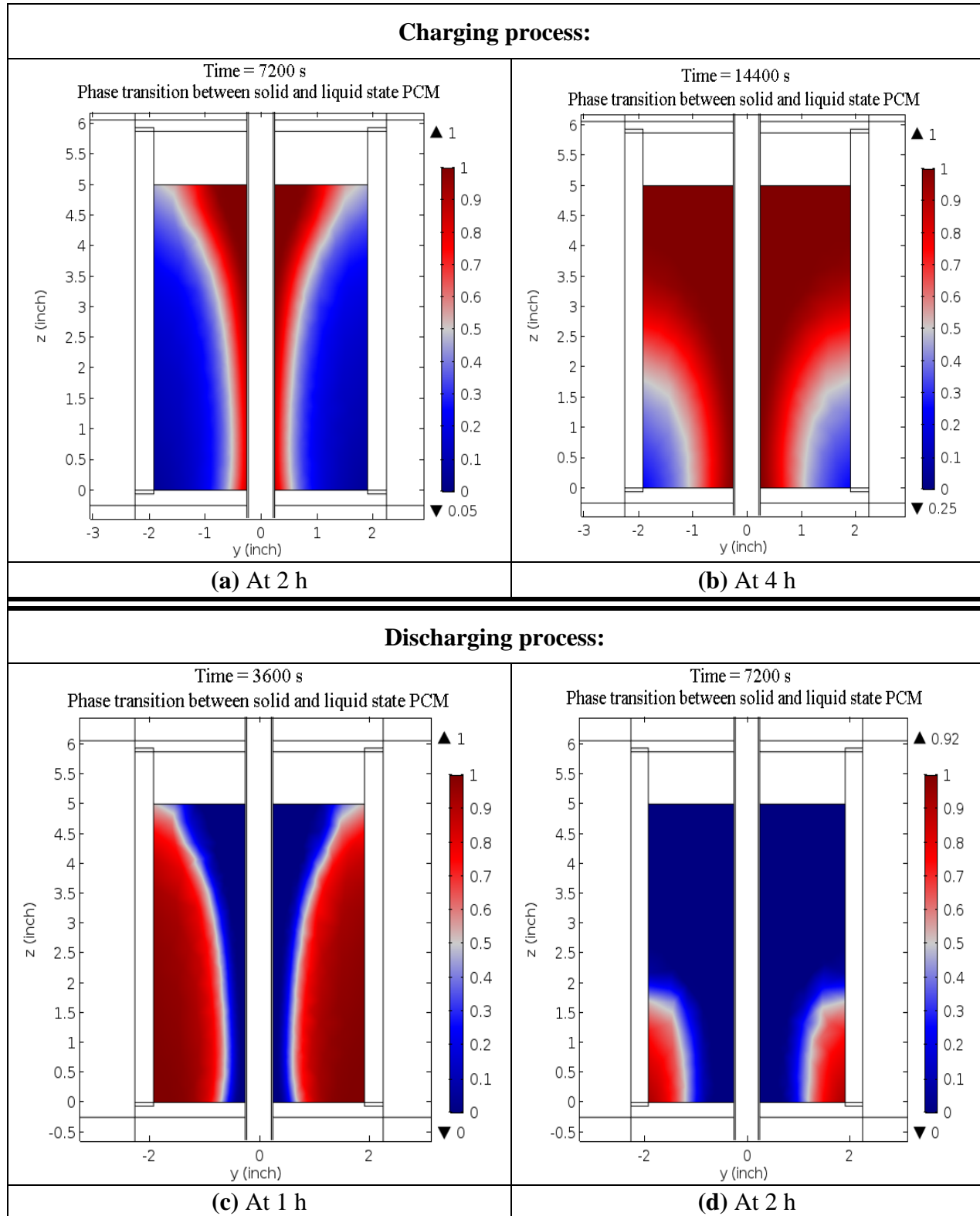
Figure 11-7. Results from 3D thermal modeling of phase transitions in the prototype during charging/discharging. HTF flows from top to bottom.

11.7. Experimental and simulation results of the charging/discharging tests

11.7.1. Prototype 1-2

Table 11-2 shows the various conditions during the three charging/discharging experiments. Figures 11-8 to 11-13 show the temperature profiles at various thermocouples at various locations during charging and discharging.

Table 11-2 Test conditions for prototype 1-2.

Charging Process	Test 1	Test 2	Test 3
Furnace set temp. ($^{\circ}$C)	695	695	685
Prototype initial temp. ($^{\circ}$C)	~697	~698	~693
Air flow rate (L/min)	177.0	179.7	184.6
Furnace inlet temp. ($^{\circ}$C)	~800	~800	~800
Latent heat of fusion (kJ/kg)	374	374	374
Furnace emissivity	0.3	0.3	0.3

Discharging Process	Test 1	Test 2	Test 3
Furnace set temp. (°C)	735	735	735
Prototype initial temp. (°C)	~744	~742	~738
Air flow rate (L/min)	190.0	191.4	199.2
Furnace inlet temp. ($^{\circ}$C)	~500	~500	~500
Latent heat of fusion (kJ/kg)	374	374	374
Furnace emissivity	0.3	0.3	0.3

Figure 11-8. Experimental data and simulations from Test 1 charging: (a) consolidated data, (b) thermocouple 1, (c) thermocouple 2, and (d) thermocouple 3.

Figure 11-9. Experimental data and simulations from Test 1 discharging: (a) consolidated data, (b) thermocouple 1, (c) thermocouple 2, and (d) thermocouple 3.
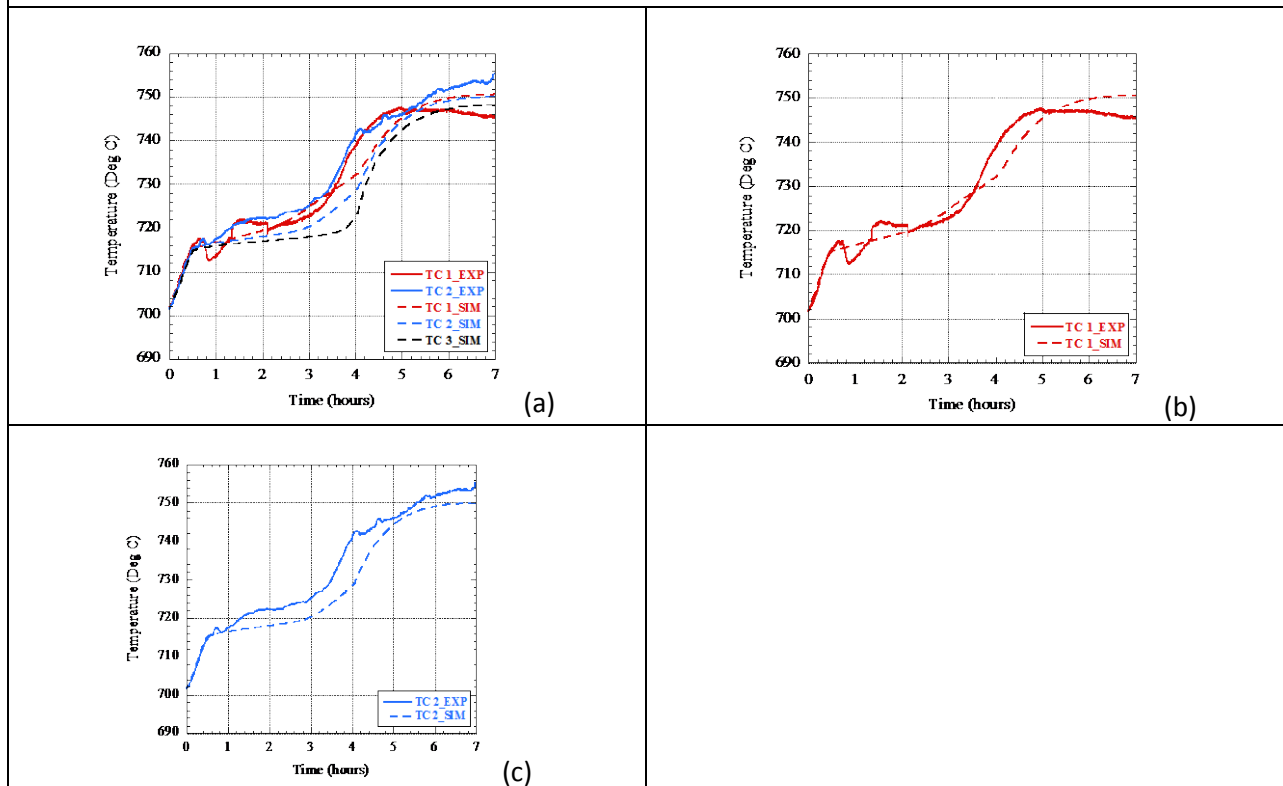
Figure 11-10. Experimental data and simulations from Test 2 charging: (a) consolidated data, (b) thermocouple 1, and (c) thermocouple 2.
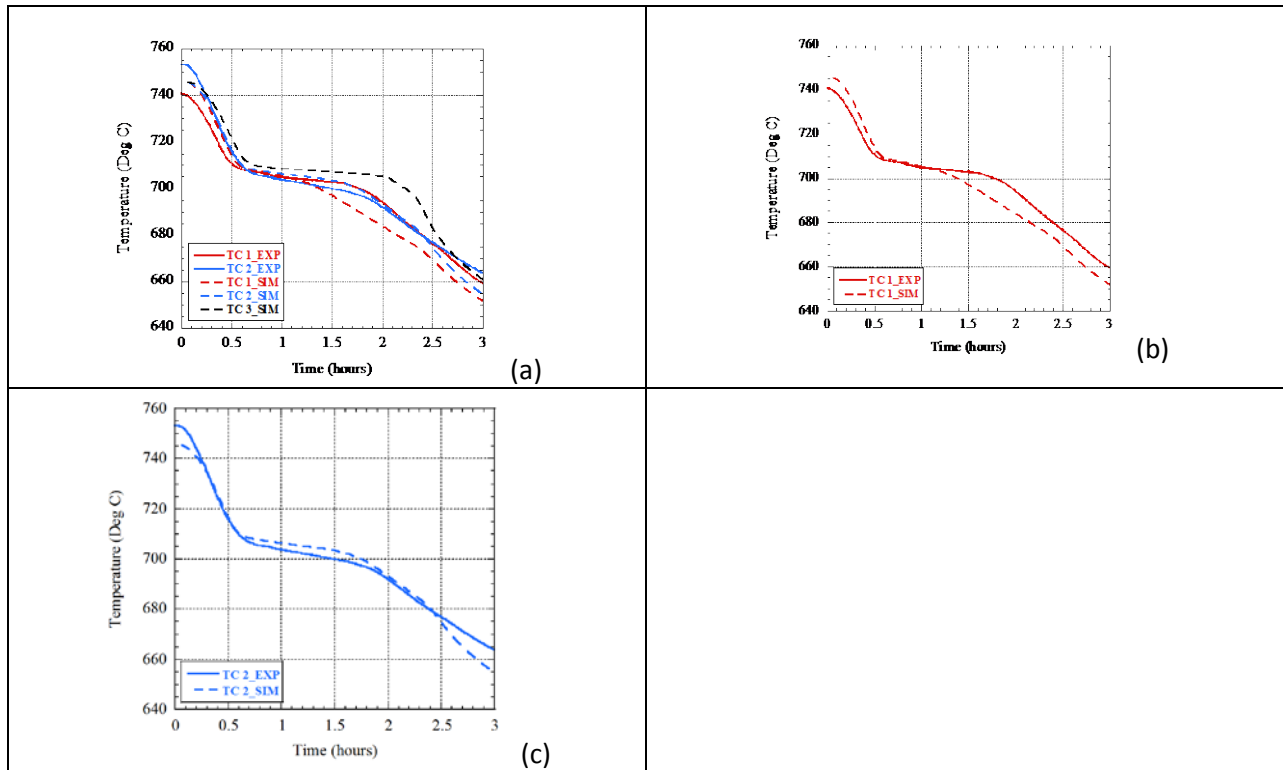
Figure 11-11. Experimental data and simulations from Test 2 discharging: (a) consolidated data, (b) thermocouple 1, and (c) thermocouple 2.
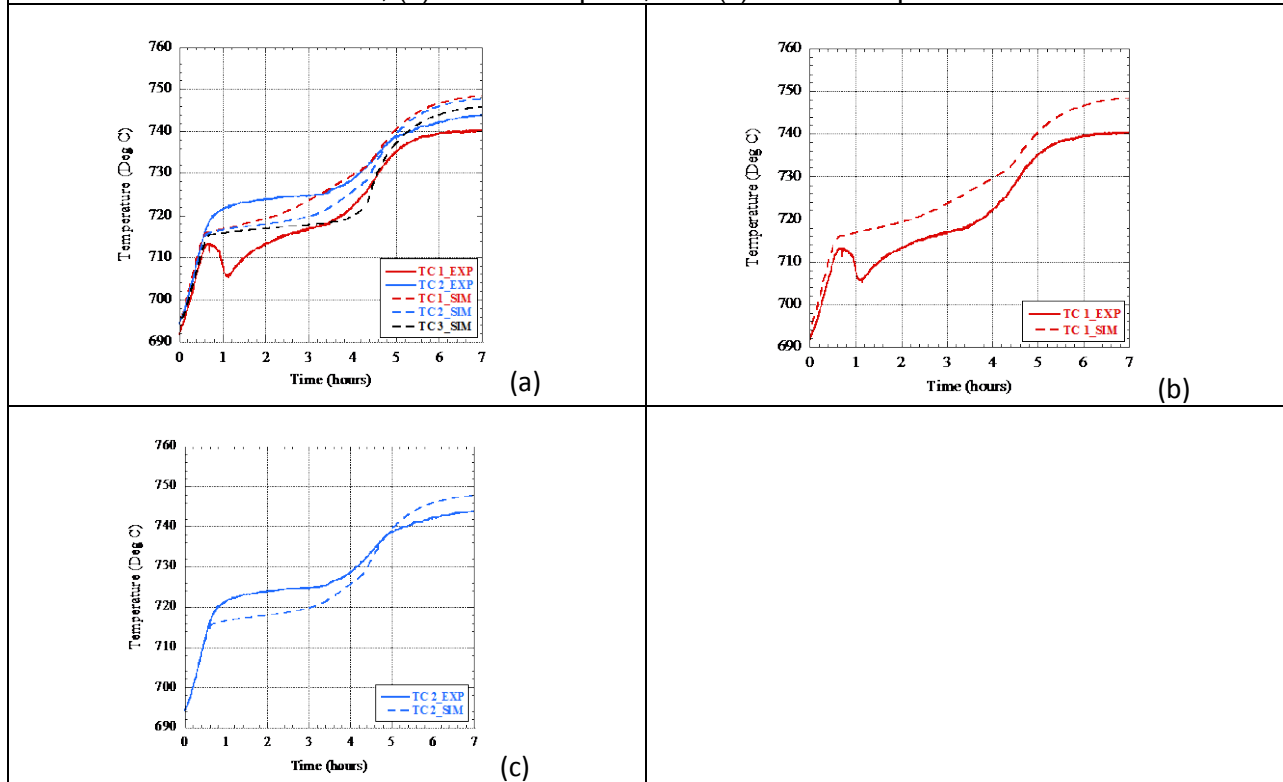
Figure 11-12. Experimental data and simulations from Test 3 charging: (a) consolidated data, (b) thermocouple 1, and (c) thermocouple 2.
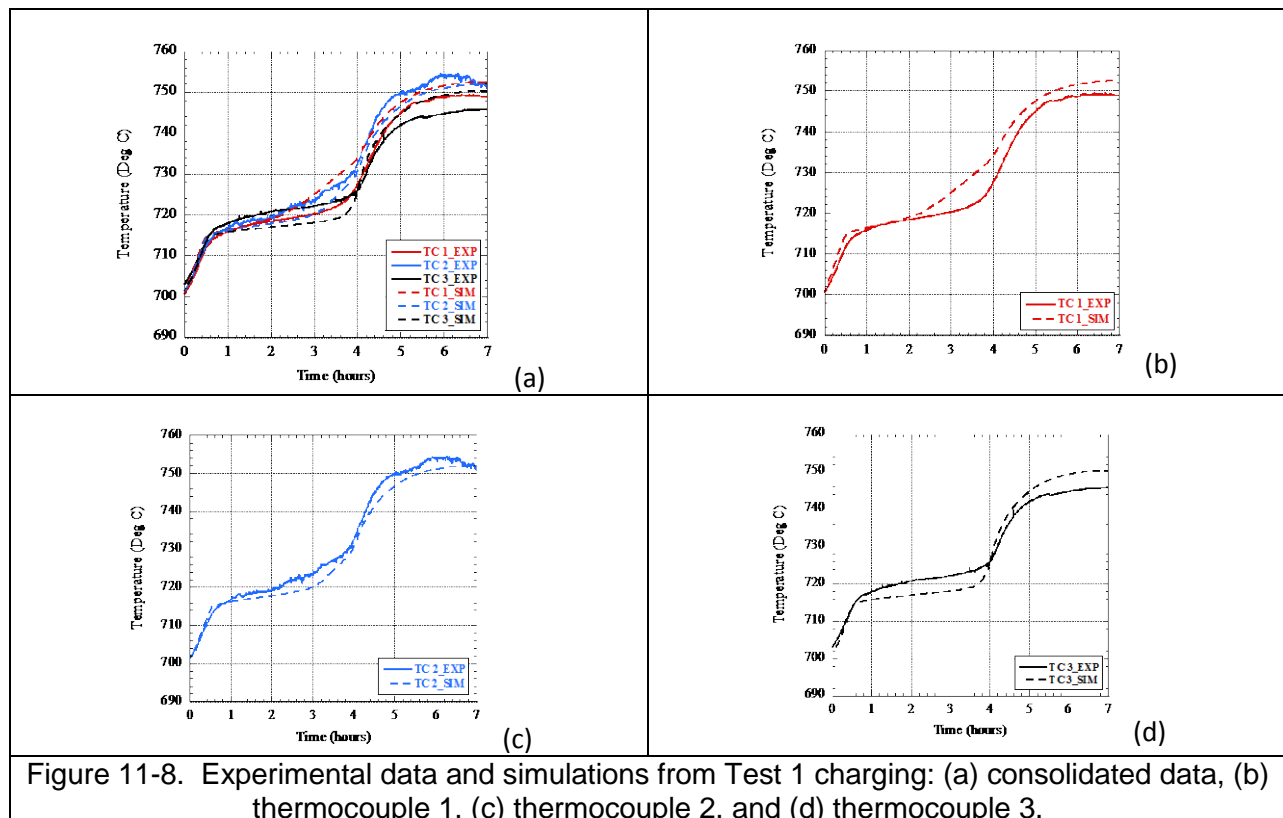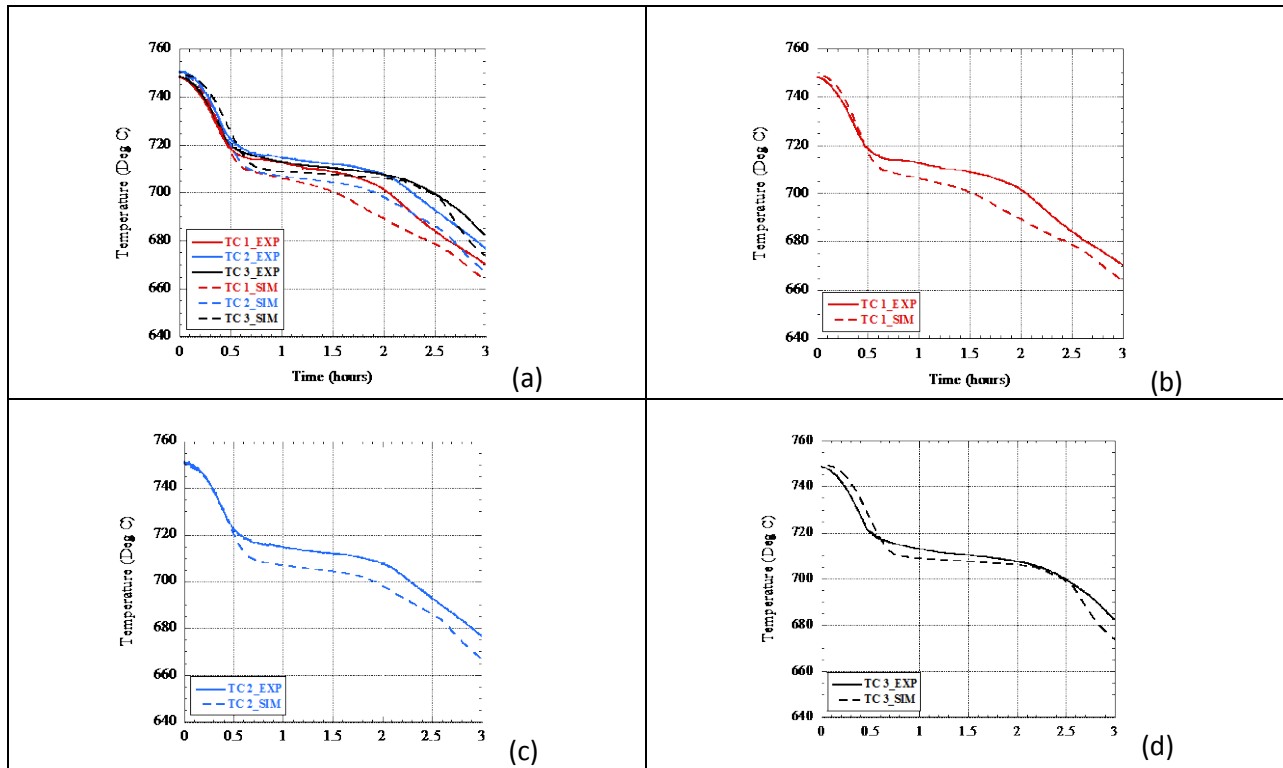
Figure 11-13. Experimental data and simulations from Test 3 discharging: (a) consolidated data, (b) thermocouple 1, and (c) thermocouple 2.
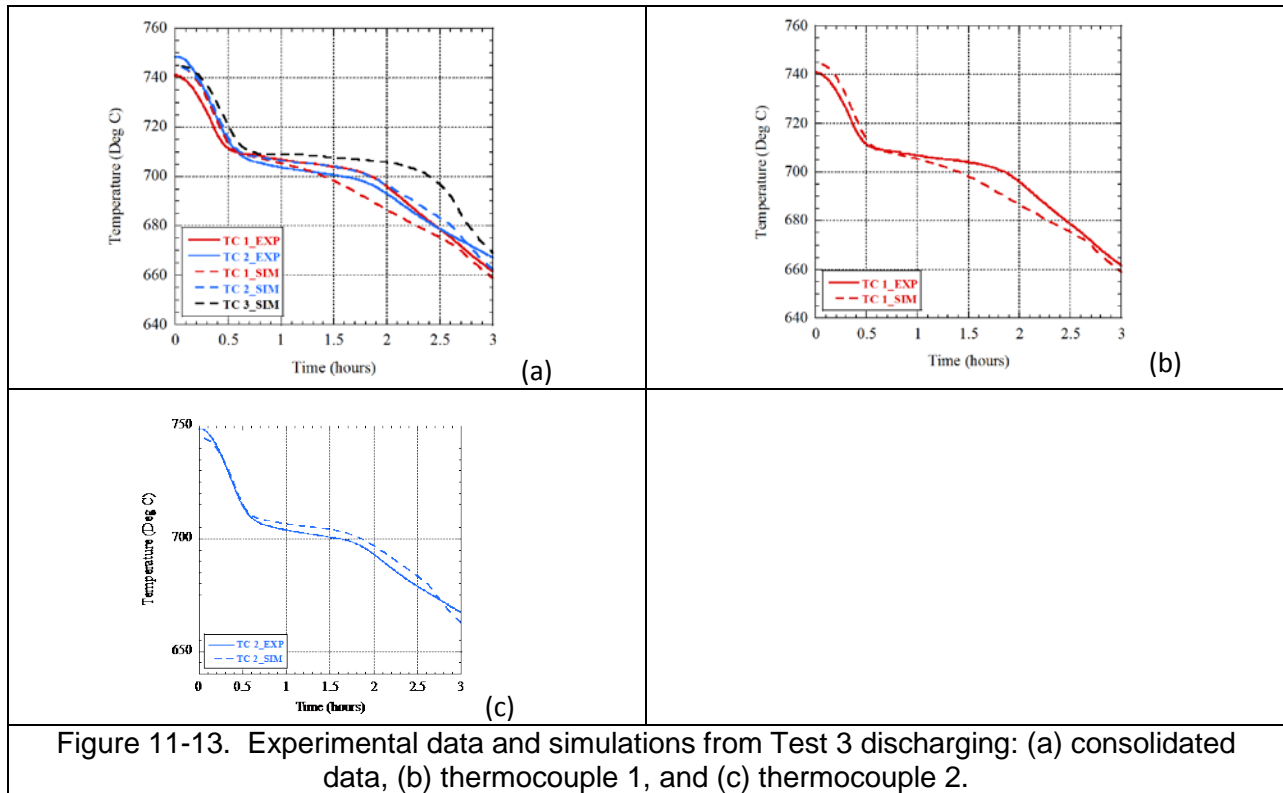
Based on the comparison results (Table 11-3), the temperature measurement data match the simulation results very well: the difference is less than 2.0%, except for thermocouple 1 during Test 1 discharging and Test 3 discharging. Most of the data of the time difference between the experiments and simulations are larger, but still within the 15% difference as stated in the SOPO [13]. Moreover, the actual times are less than the prediction from simulation, which implies the actual thermal performance of the LHTES is better than that based on predictions from modeling for the charging/discharging conditions.

Table 11-3. Comparison of experimental data and simulations for prototype 1-2.

Charging Process	Test 1			Test 2			Test 3		
	TC 1	TC 2	TC 3	TC 1	TC 2	TC 3	TC 1	TC 2	TC 3
Maximum temperature difference (˚C)	7.0	4.0	4.5	6.5	12.0	---	8.0	6.0	---
Percentage of the max. temp. diff. compared to the charging operating temperature (%)	1.0	0.6	0.6	0.9	1.7	---	1.1	0.8	---
Time difference at 730 ˚C (h)	-0.5	0.1	-0.1	0.2	0.6	---	-0.5	0.3	---
Percentage of the time diff. at 730 ˚C compared to the total charging time (%)	-7.1	1.4	-1.4	2.9	8.6	---	-6.2	3.8	---

Discharging Process	Test 1			Test 2			Test 3		
	TC 1	TC 2	TC 3	TC 1	TC 2	TC 3	TC 1	TC 2	TC 3
Maximum temperature difference (°C)	12.0	10.0	9.0	10.0	10.0	---	10.0	5.0	---
Percentage of the max. temp. diff. compared to the discharging operating temperature (%)	1.7	1.4	1.3	1.4	1.4	---	1.4	0.7	---
Time difference at 700 °C (h)	-0.5	-0.4	-0.03	-0.4	0.3	---	-0.5	0.2	---
Percentage of the time diff. at 700 °C compared to the total discharging time (%)	-16.7	-13.3	-1.0	-13.3	10.0	---	-15.3	8.0	---

11.7.2. Prototype 1-4

For this prototype we were able to conduct two tests only because the heater control thermocouple stopped working. Table 11-4 lists the test conditions for prototype 1-4. The data from the two tests are presented in Figures 11-14 to 11-17. In this case, we had 3-4 working thermocouples.

Table 11-4. Test conditions for prototype 1-4.

Charging Process	Test 1	Test 2
Furnace temp. (°C)	698.9	699.0
Prototype initial temp. (°C)	~687	~685
Air flow rate (L/min)	186.4	186.3
Furnace inlet temp. (°C)	~800	~800
Latent heat of fusion (kJ/kg)	403.6	403.6
Furnace emissivity	0.3	0.3

Discharging Process	Test 1	Test 2
Furnace temp. (°C)	747.2	747.1
Prototype initial temp. (°C)	~742	~742
Air flow rate (L/min)	202.9	202.1
Furnace inlet temp. (°C)	~500	~500
Latent heat of fusion (kJ/kg)	403.6	403.6
Furnace emissivity	0.3	0.3

Comparison between experimental measurements and simulation results – consolidated data	
TC 1 comparison	TC 2 comparison
TC 5 comparison	TC 6 comparison

Figure 11-14. Experimental and simulation data for prototype 1-4, Test 1 charging.

Comparison between experimental measurements and simulation results – consolidated data

TC 1 comparison	**TC 2 comparison**
TC 5 comparison	**TC 6 comparison**
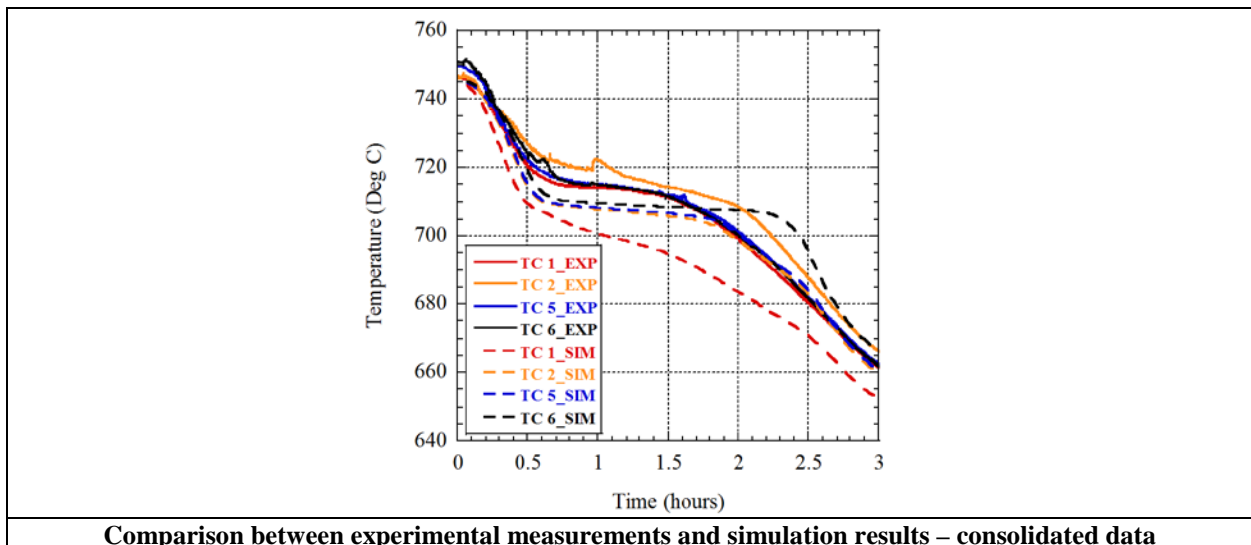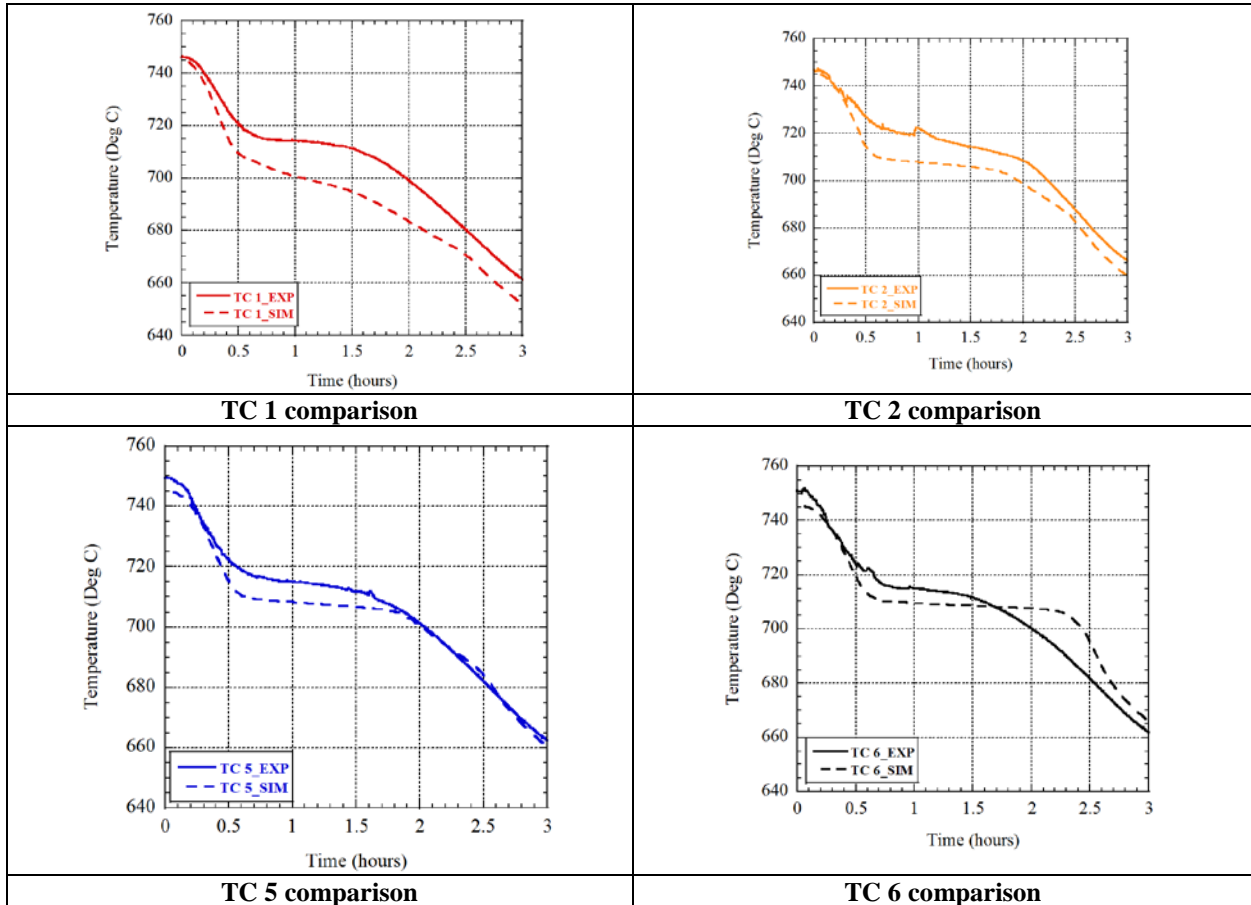
Figure 11-15. Experimental and simulation data for prototype 1-4, Test 1 discharging.

Comparison between experimental measurements and simulation results – consolidated data	**TC 1 comparison**

| TC 2 comparison | TC 5 comparison |
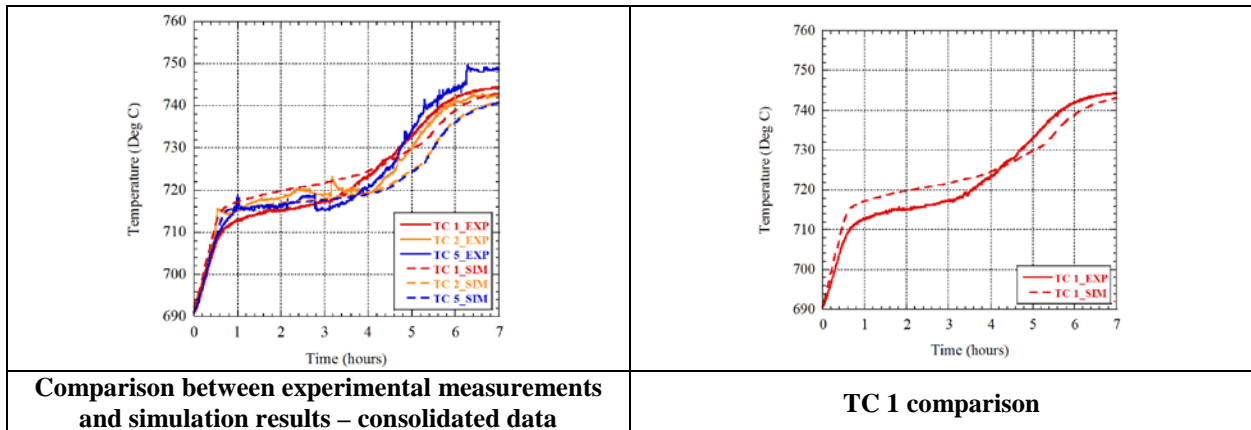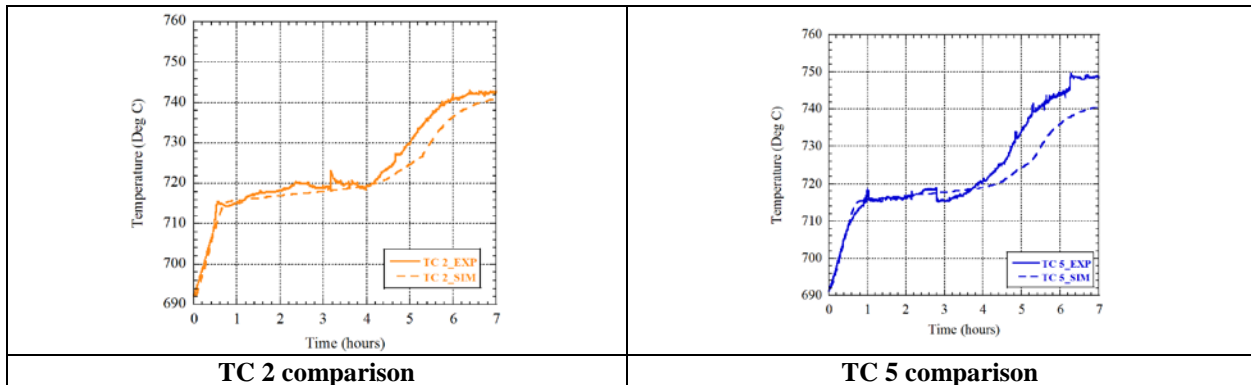
Figure11-16. Experimental and simulation data for prototype 1-4, Test 2 charging.

| Comparison between experimental measurements and simulation results – consolidated data | TC 1 comparison |
| TC 2 comparison | TC 5 comparison |
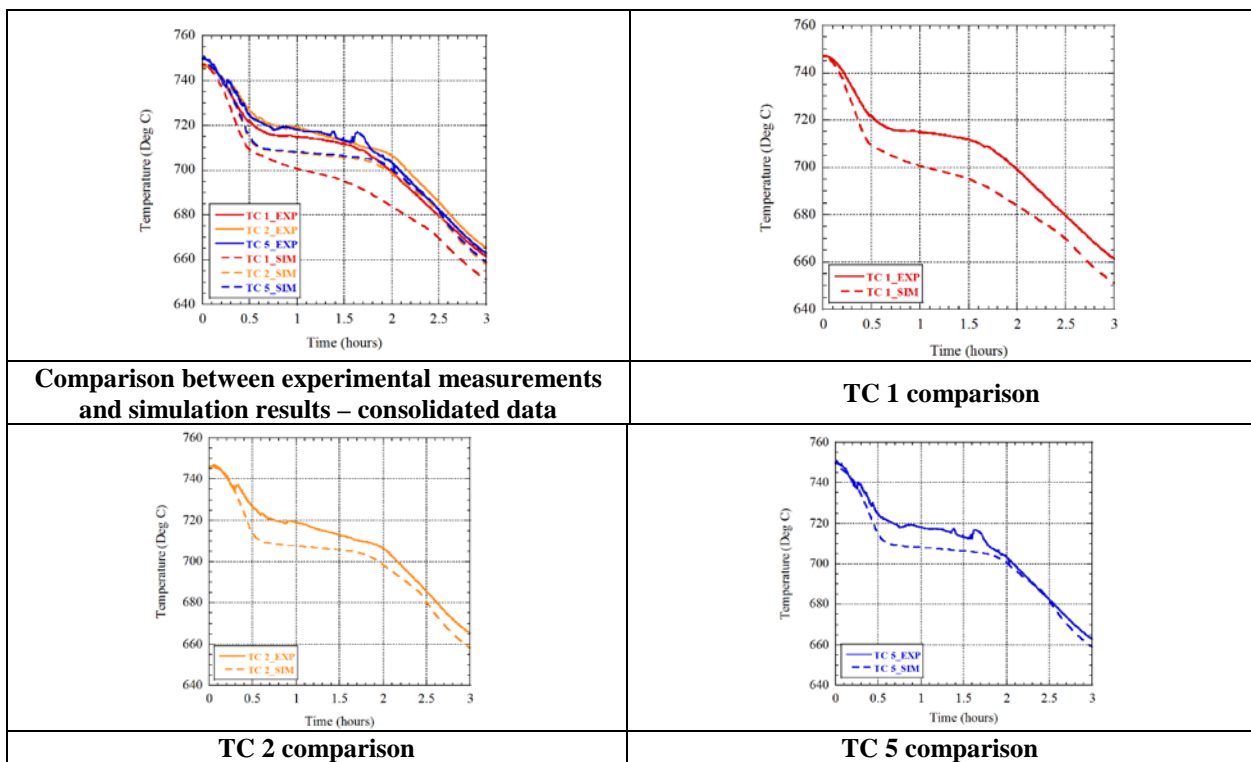
Figure 11-17. Experimental and simulation data for prototype 1-4, Test 2 discharging.

Based on the comparison results (Table 11-5), the temperature measurement data match the simulation results quite well, with the difference being less than 2.5%. Most of the data on the time difference between experiments and simulations are within 15% difference, except for thermocouple 1 in the discharge case. Note that TC1 is located near the surface, close to the head space inside the prototype.

Table 11-5. Comparison of experimental data and simulations for prototype 1-4.

Charging Process	Test 1				Test 2		
	TC 1	TC 2	TC 5	TC 6	TC 1	TC 2	TC 5
Maximum temperature difference (˚C)	4.0	8.0	8.0	11.0	6.0	7.0	10.0
Percentage of the max. temp. diff. compared to the charging operating temperature (%)	0.6	1.1	1.1	1.5	0.8	1.0	1.4
Time difference at 730 ˚C (h)	0.4	0.9	0.9	0.6	0.4	0.5	0.8
Percentage of the time diff. at 730 ˚C compared to the total charging time (%)	5.0	11.2	11.2	7.5	5.0	6.2	10.0

Discharging Process	Test 1				Test 2		
	TC 1	TC 2	TC 5	TC 6	TC 1	TC 2	TC 5
Maximum temperature difference (˚C)	17.0	12.0	8.0	15.0	17.0	15.0	10.0
Percentage of the max. temp. diff. compared to the discharging operating temperature (%)	2.4	1.7	1.1	2.1	2.4	2.1	1.4
Time difference at 700 ˚C (h)	1.0	0.3	0.0	0.4	1.0	0.3	0.1
Percentage of the time diff. at 700 ˚C compared to the total discharging time (%)	33.3	10.0	0.0	13.3	33.3	10.0	3.3

11.7.3. Prototype 1-1

Table 11-6 shows the various conditions during the three charging/discharging experiments for prototype 1-1. Experimental data are presented in Figures 11-18 to 11-23.

Table 11-6. Test conditions for prototype 1-1.

Charging Process	Test 1	Test 2	Test 3
Furnace temp. (˚C)	698.4	698.3	697.7
Phase change temp. (˚C)	718	718	718
Melting/solidification range (˚C)	8	8	8
Air flow rate (L/min)	162.5	165.4	161.0
Furnace inlet temp. (˚C)	~800	~800	~800
Latent heat of fusion (kJ/kg)	377.3	377.3	377.3

Discharging Process	Test 1	Test 2	Test 3
Furnace temp. (˚C)	752.9	752.6	751.9
Phase change temp. (˚C)	706	706	706
Melting/solidification range (˚C)	8	8	8
Air flow rate (L/min)	185.7	182.4	176.5
Furnace inlet temp. (˚C)	~500	~500	~500
Latent heat of fusion (kJ/kg)	377.3	377.3	377.3

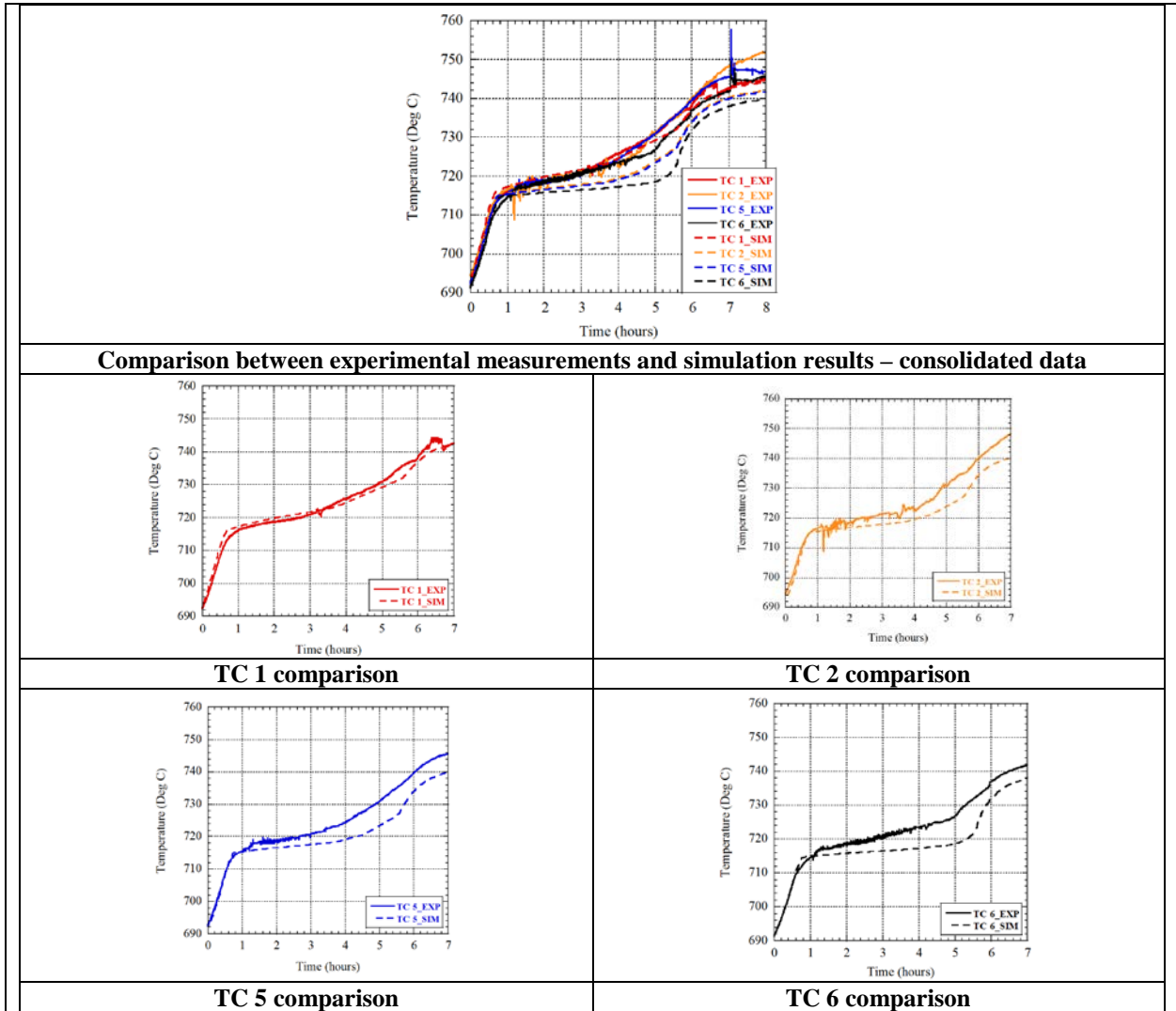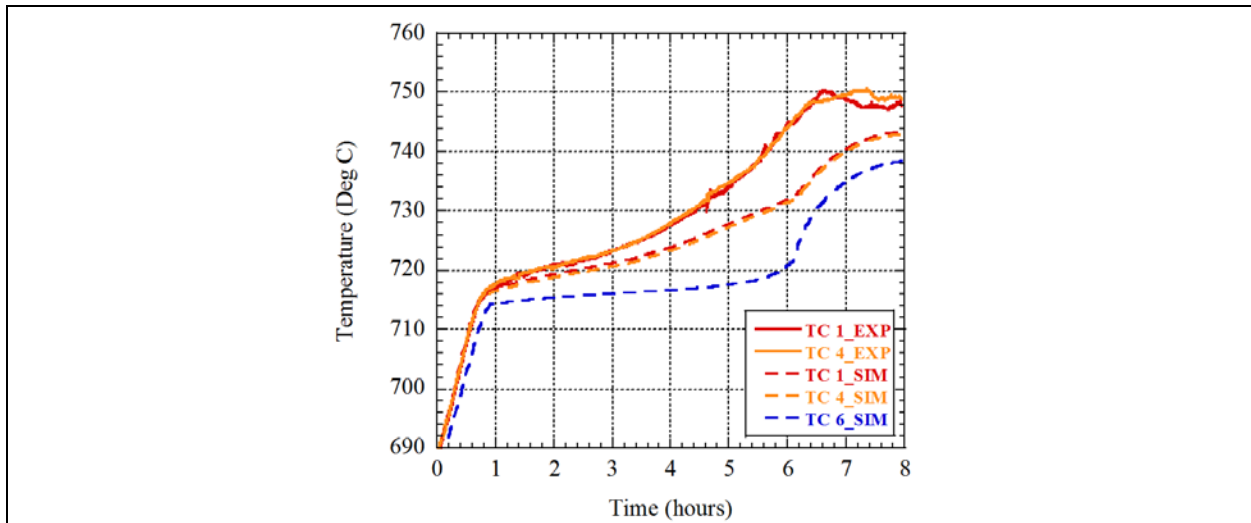|	
Comparison between experimental measurements and simulation results – consolidated data	
TC 1 comparison	TC 4 comparison

Figure 11-18. Experimental and simulation data for prototype 1-1, Test 1 charging.

Comparison between experimental measurements and simulation results – consolidated data	TC 1 comparison

| TC 4 comparison | TC 6 comparison |

Figure 11-19. Experimental and simulation data for prototype 1-1, Test 1 discharging.

| Comparison between experimental measurements and simulation results – consolidated data | TC 1 comparison |
| TC 4 comparison | TC 6 comparison |
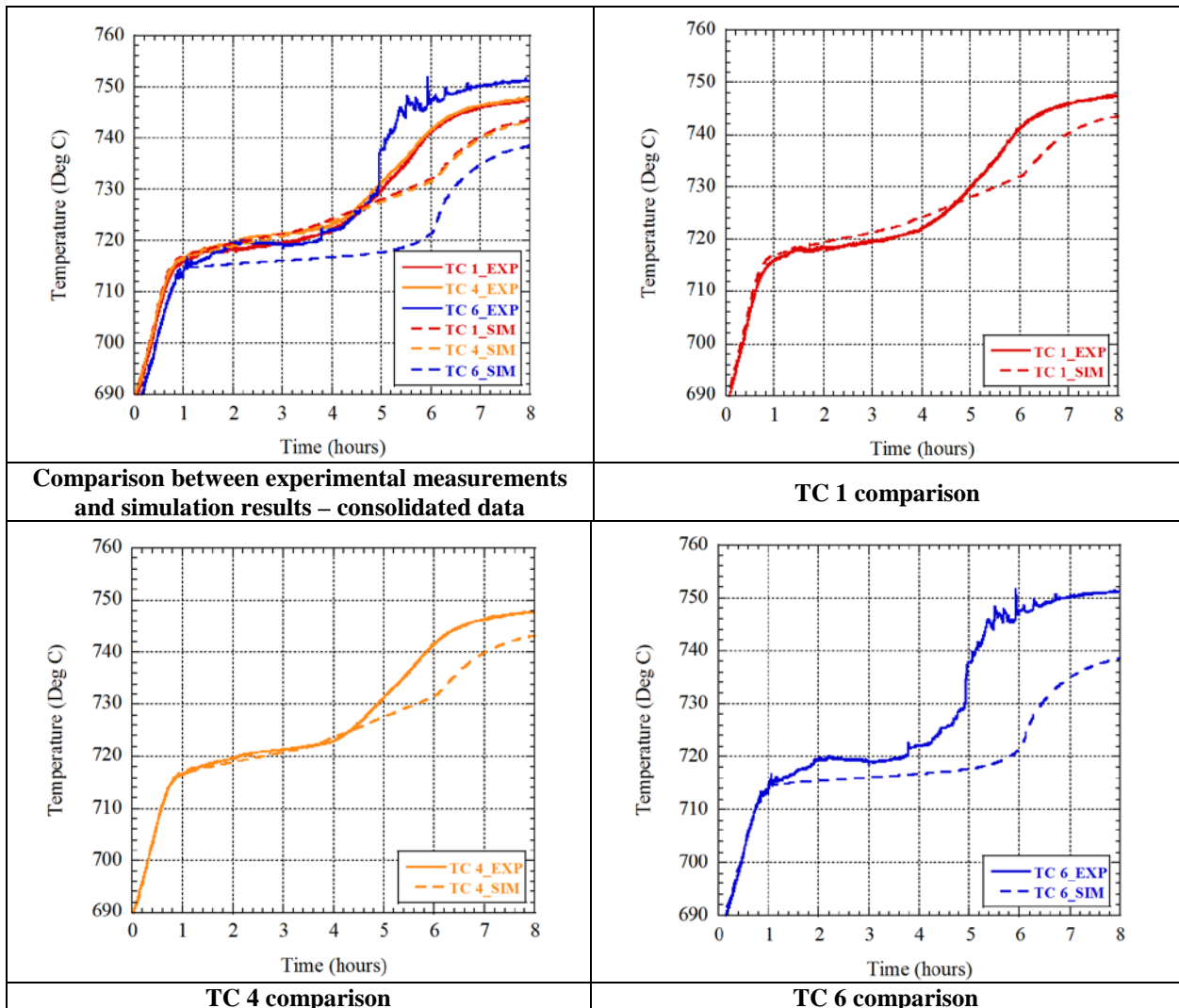
Figure 11-20. Experimental and simulation data for prototype 1-1, Test 2 charging.
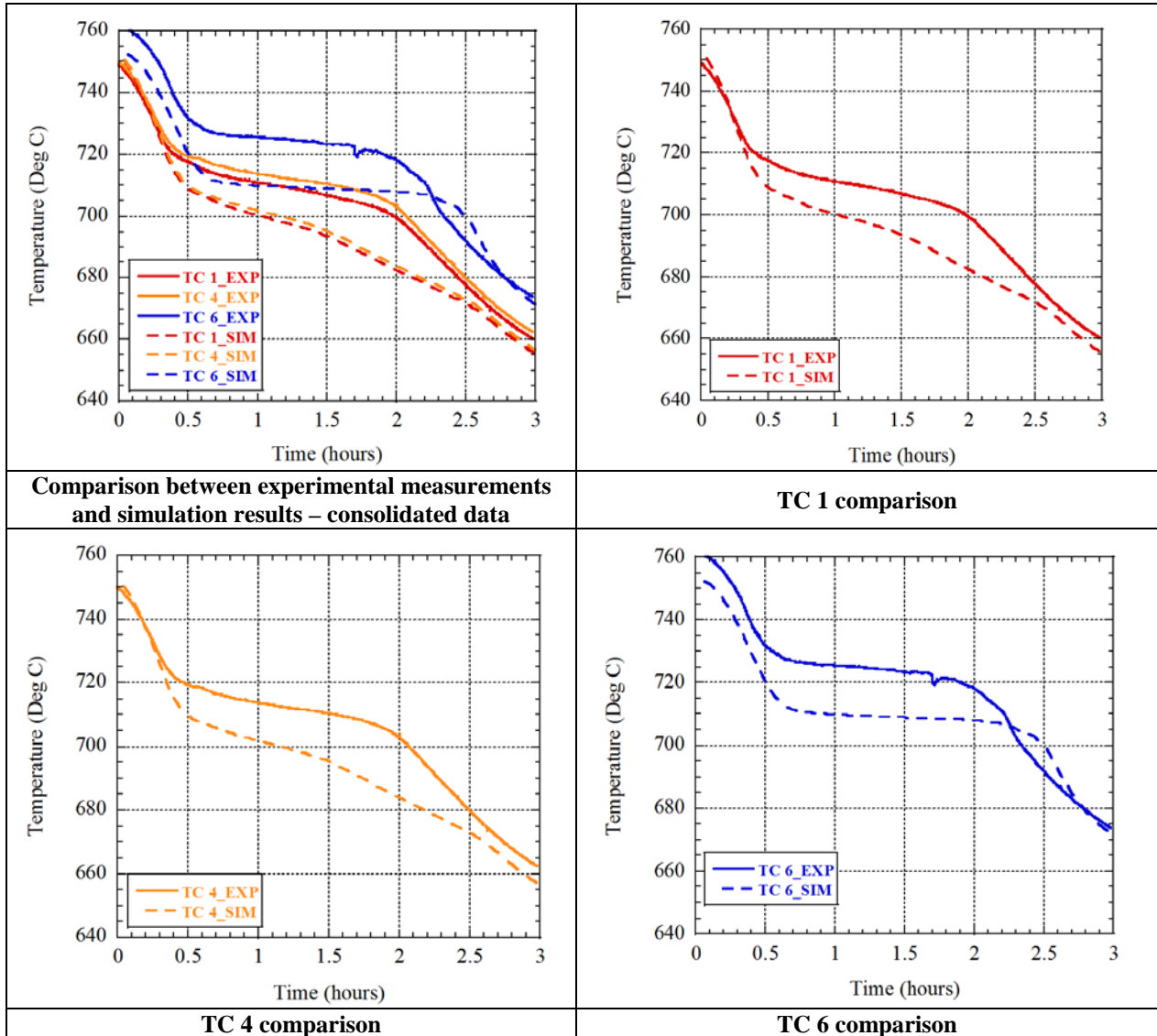
Figure 11-21. Experimental and simulation data for prototype 1-1, Test 2 discharging.
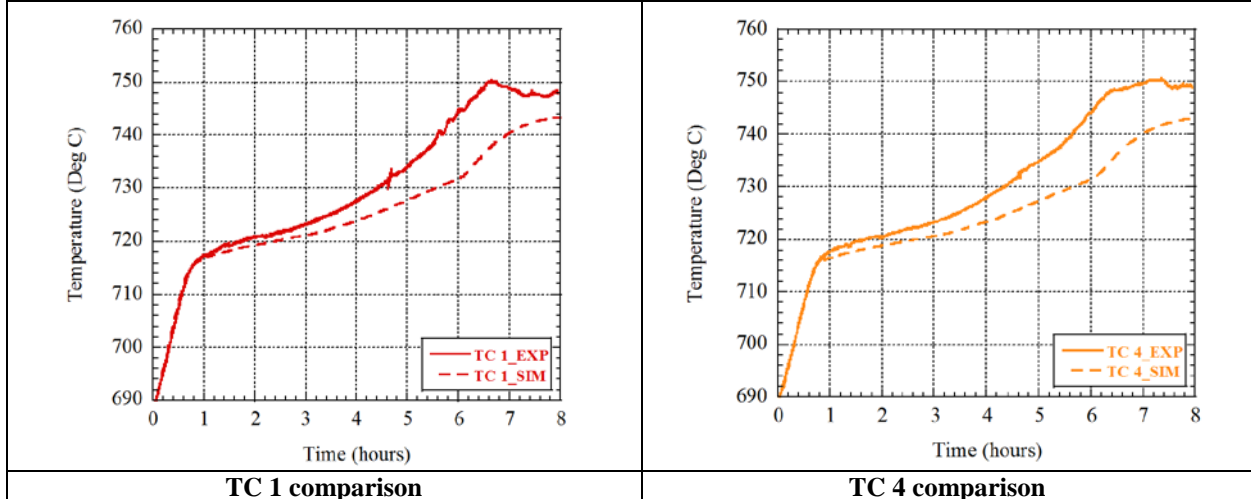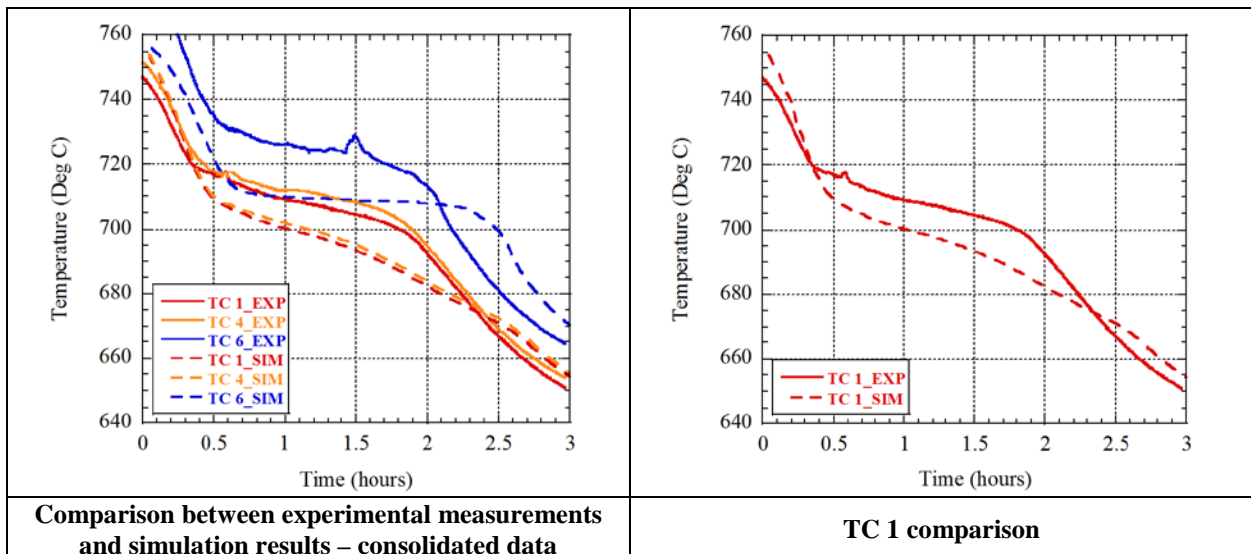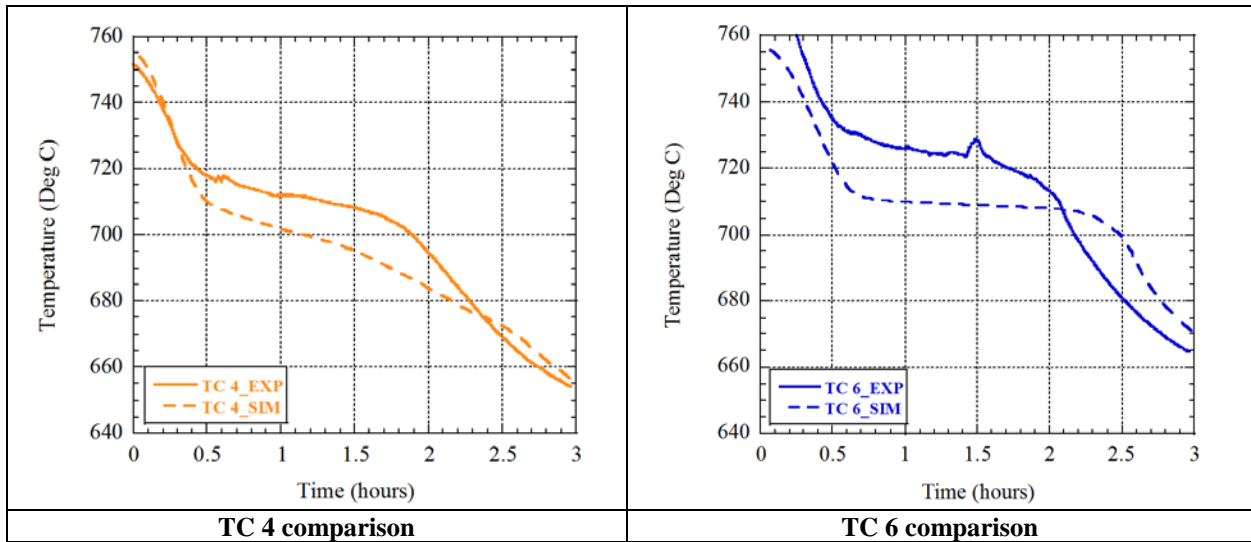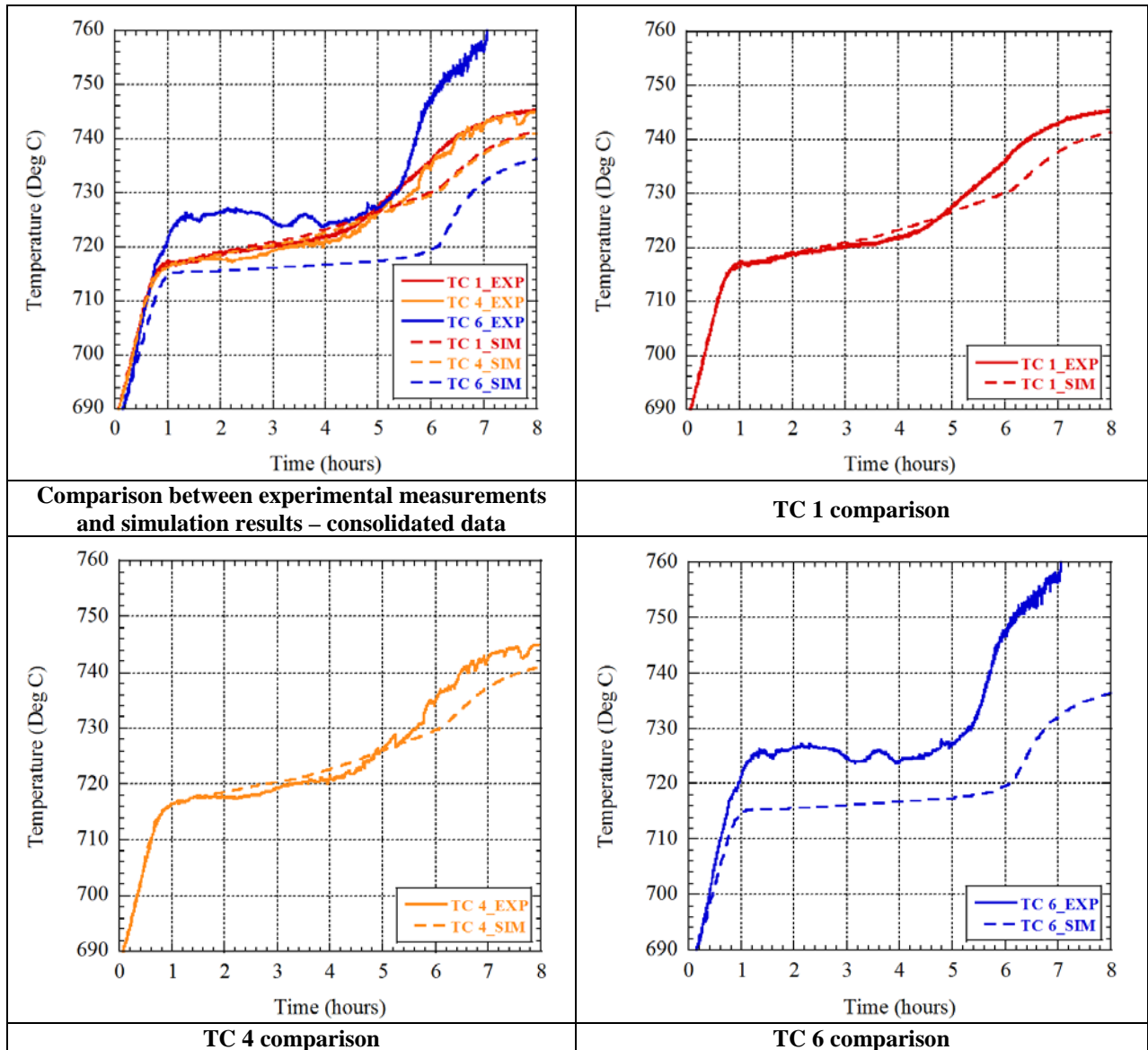
Figure 11-22. Experimental and simulation data for prototype 1-1, Test 3 charging.
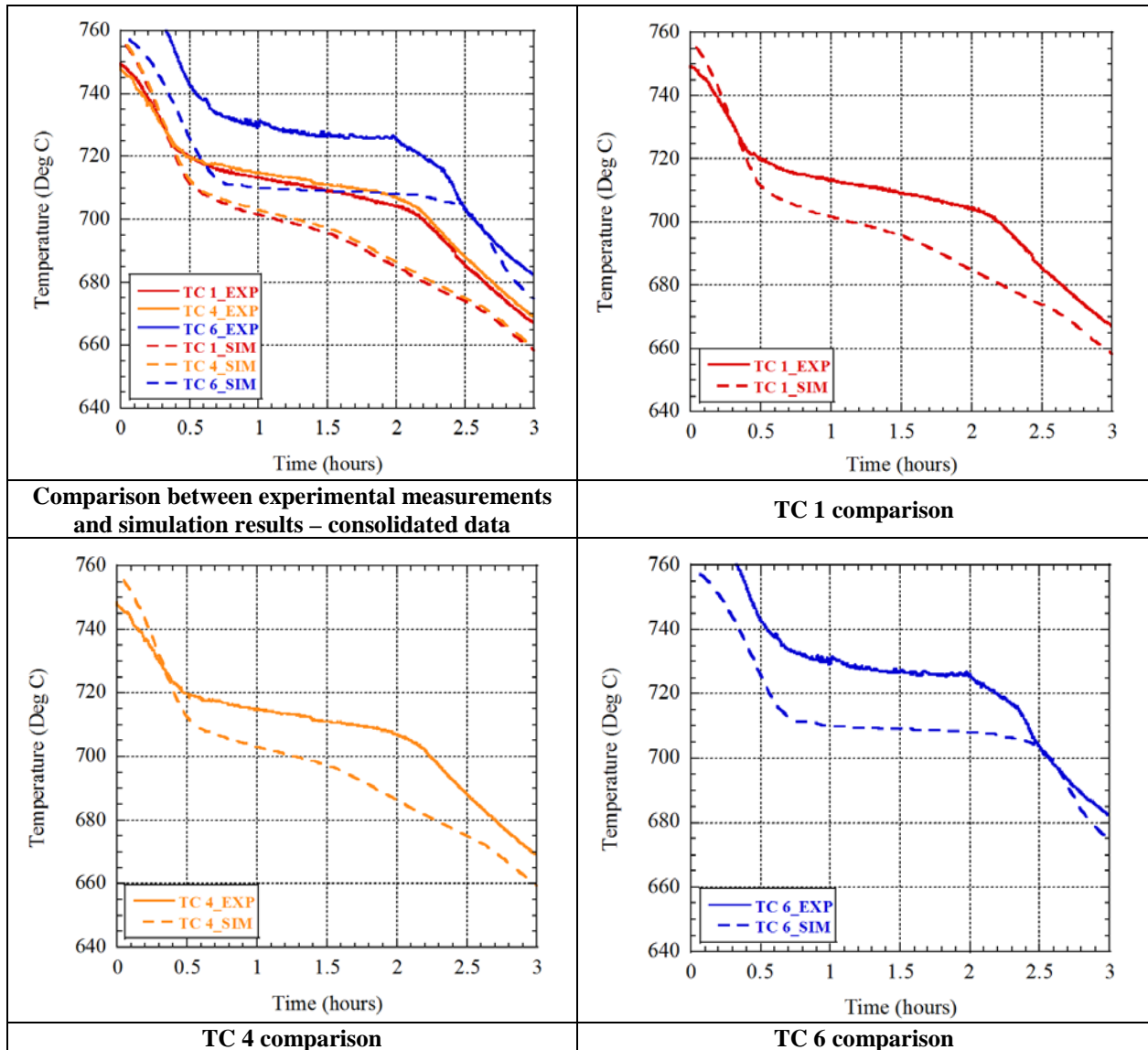
Figure 11-23. Experimental and simulation data for prototype 1-1, Test 3 discharging.

Based on the comparison (Table 11-7) results between the experimental measurements and the numerical simulations for thermocouples TC 1, TC 4, and TC 6, the temperature measurement data match with the simulation results quite well, with the difference being less than 4.0%. Thermocouple TC6 did not work during the first charging run. For the charging process, most of the data of time difference between the experiments and simulations are within the 15% difference, which meets the experiment target as stated in the SOPO [13]. However, for the discharging process, the time difference data for TC 1 and TC 4 exceed 15%. Based on the discharge curves, these large differences may be because the solidification temperature used in the simulations (706 °C) is much different from the actual solidification temperature.

Table 11-7. Comparison of experimental data and simulations for prototype 1-1.

Charging Process	Test 1			Test 2			Test 3		
	TC 1	TC 4	TC 6	TC 1	TC 4	TC 6	TC 1	TC 4	TC 6
Maximum temperature difference (˚C)	12	12	---	9	10	27	6	6	26
Percentage of the max. temp. diff. compared to the charging operating temperature (%)	1.7	1.7	---	1.3	1.4	3.8	0.8	0.8	3.6
Time difference at 730 ˚C (h)	1.2	1.2	---	0.6	0.8	1.4	0.7	0.4	1.4
Percentage of the time diff. at 730 ˚C compared to the total charging time (%)	15.0	15.0	---	7.5	10.0	17.5	8.8	5.0	17.5

Discharging Process	Test 1			Test 2			Test 3		
	TC 1	TC 4	TC 6	TC 1	TC 4	TC 6	TC 1	TC 4	TC 6
Maximum temperature difference (˚C)	12	15	20	17	20	15	20	23	20
Percentage of the max. temp. diff. compared to the discharging operating temperature (%)	1.7	2.1	2.8	2.4	2.8	2.1	2.8	3.3	2.8
Time difference at 700 ˚C (h)	0.8	0.7	0.3	1.0	0.9	0.15	1.05	0.95	0.0
Percentage of the time diff at 700 ˚C compared to the total discharging time (%)	26.7	23.3	10.0	33.3	30.0	5.0	35.0	31.7	0.0

11.8. Exergy efficiency calculation for the prototype

The round trip exergy efficiency was calculated from the expression:

$$\varepsilon = \frac{\text{Exergy retrieved during discharging}}{\text{Exergy supplied during charging}} = \frac{Ex_{dis}}{Ex_{char}}$$

The exergy supplied during charge is determined from the expression:

$$Ex_{char} = \left\{ \dot{m}_{air} c_{pair} (T_{air,in} - T_{air,out}) \left(1 - \frac{T_0}{T_{\text{infiltrated foam}}} \right) - \dot{Q}_{loss} \left(1 - \frac{T_0}{T_{\text{infiltrated foam}}} \right) \right\} t$$

In the above equation, $\dot{m}_{air}$ is the air mass flow rate, c_{pair} is the specific heat of the air, $T_{air,in}$ is the air flow temperature at the prototype inlet, $T_{air,out}$ is the air flow temperature at the prototype outlet, T_0 is the environment temperature (K), $T_{\text{infiltrated foam}}$ is the graphite foam-MgCl$_2$ combination temperature, and t is the time. Also,

$$\dot{Q}_{loss} = \dot{Q}_{\text{incoloy container}} + \dot{Q}_{\text{insulation}} + \dot{Q}_{\text{loss to surrounding}}$$
$$= M_{\text{incoloy container}} c_{pincoloy} \Delta T / t + M_{\text{insulation}} c_{pinsulation} \Delta T / t + 2\pi L k_{\text{insulation}} (T_{inner} - T_{outer}) / \ln(r_{outer} / r_{inner})$$

where $\dot{Q}_{\text{incoloy container}}$ is the mass of the Incoloy container holding the storage medium (graphite foam-MgCl$_2$), $c_{pincoloy}$ is the specific heat of Incoloy 800H material, $\Delta T = T_{final} - T_{initial}$, $M_{\text{insulation}}$ is the mass of the outside insulation material, $c_{pinsulation}$ is the specific heat of the insulation, $k_{\text{insulation}}$ is the thermal conductivity of insulation material, L is the height of the prototype, T_{inner} is the measured insulation inner surface temperature, T_{outer} is the measured insulation outer surface temperature, r_{inner} is the radius of the insulation inner surface, and r_{outer} is the radius of the insulation outer surface.

The exergy supplied during charge is determined from the expression:

$$Ex_{dis} = \left\{ \dot{m}_{air} c_{pair} (T_{air,out} - T_{air,in}) \left(1 - \frac{T_0}{T_{\text{infiltrated foam}}} \right) - \dot{Q}_{\text{gain}} \left(1 - \frac{T_0}{T_{\text{infiltrated foam}}} \right) \right\} t$$

In the above equation,

$$\dot{Q}_{gain} = \dot{Q}_{\text{incoloy container}} + \dot{Q}_{\text{insulation}} + \dot{Q}_{\text{gain from surrounding}}$$
$$= M_{\text{incoloy container}} c_{pincoloy} \Delta T / t + M_{\text{insulation}} c_{pinsulation} \Delta T / t + 2\pi L k_{\text{insulation}} (T_{outer} - T_{inner}) / \ln(r_{outer} / r_{inner})$$

where $\Delta T = T_{initial} - T_{final}$

Using the above equations and experimental data, exergy and energetic efficiencies were determined using the test data for each of prototypes 1-1, 1-2, and 1-4 (Table 11-8). The results indicate the efficiencies are quite high for the prototypes, which used different types of graphite foams. It should be noted that the heat loss and gain are included in the above efficiency calculations.

Table 11-8. Summary of measured efficiencies.

	Round trip exergy efficiency (%)	Energetic efficiency (%)
Prototype 1-1	98.9	99.5
Prototype 1-2	95	96
Prototype 1-4	94.5	95

11.9. T-test analysis of temperature measurements (prototypes 1-1 and 1-4)

The t-test analysis was conducted for temperature measurements of TC 1 of prototypes 1-1 and 1-4. While TC 1 was installed in the same location for prototypes 1-1 and 1-4, there were several differences of the prototype structures and the testing conditions, including mainly: (a) foam materials (Koppers foam for prototype 1-1 and Graftech foam for prototype 1-4), (b) center air tubing arrangements (with an inner tubing for prototype 1-1 and without any inner tubing for prototype 1-4), and (c) furnace temperature settings for the charging process (680°C for prototype 1-1 and 685°C for prototype 1-4). T-test values were calculated at all data sampling times for both the charging and the discharging process; their comparisons to the critical values are presented together with the temperatures in Figures 11-24 and 11-25.
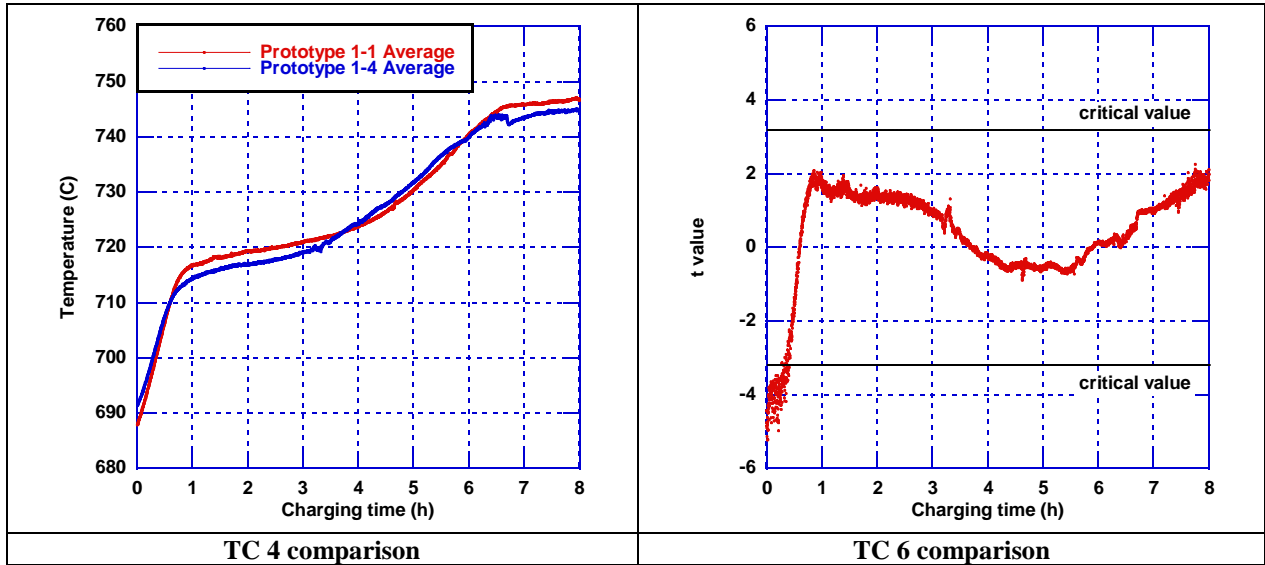
| TC 4 comparison | TC 6 comparison |
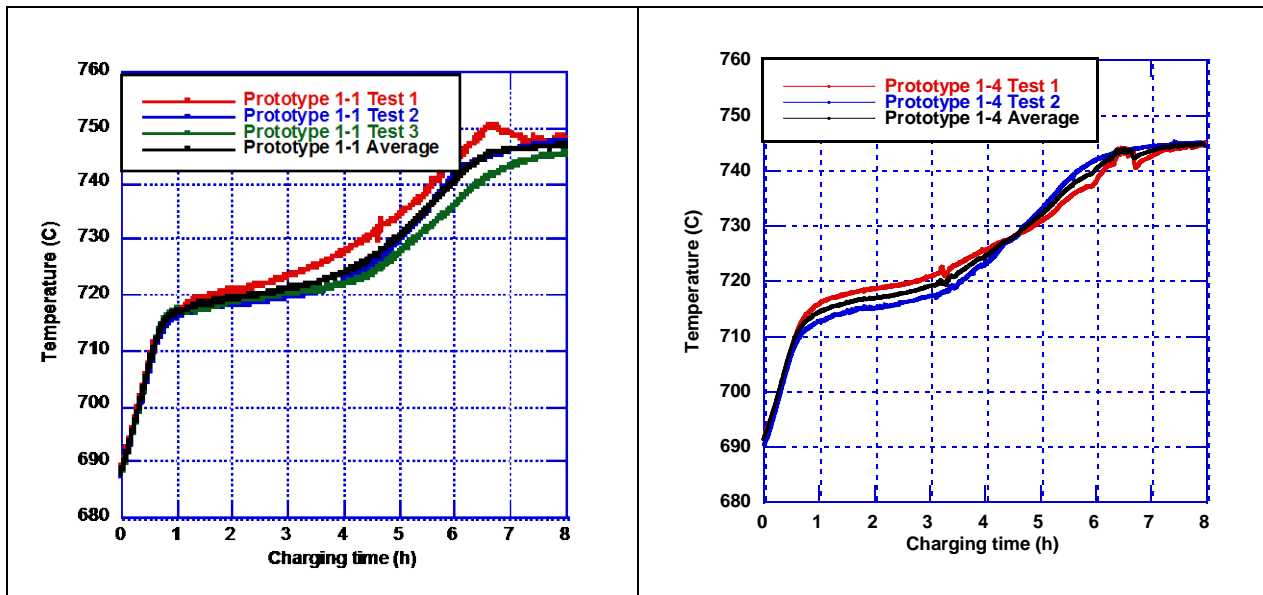
Figure 11-24. T-test of prototypes 1-1 and 1-4, TC 1 charging.
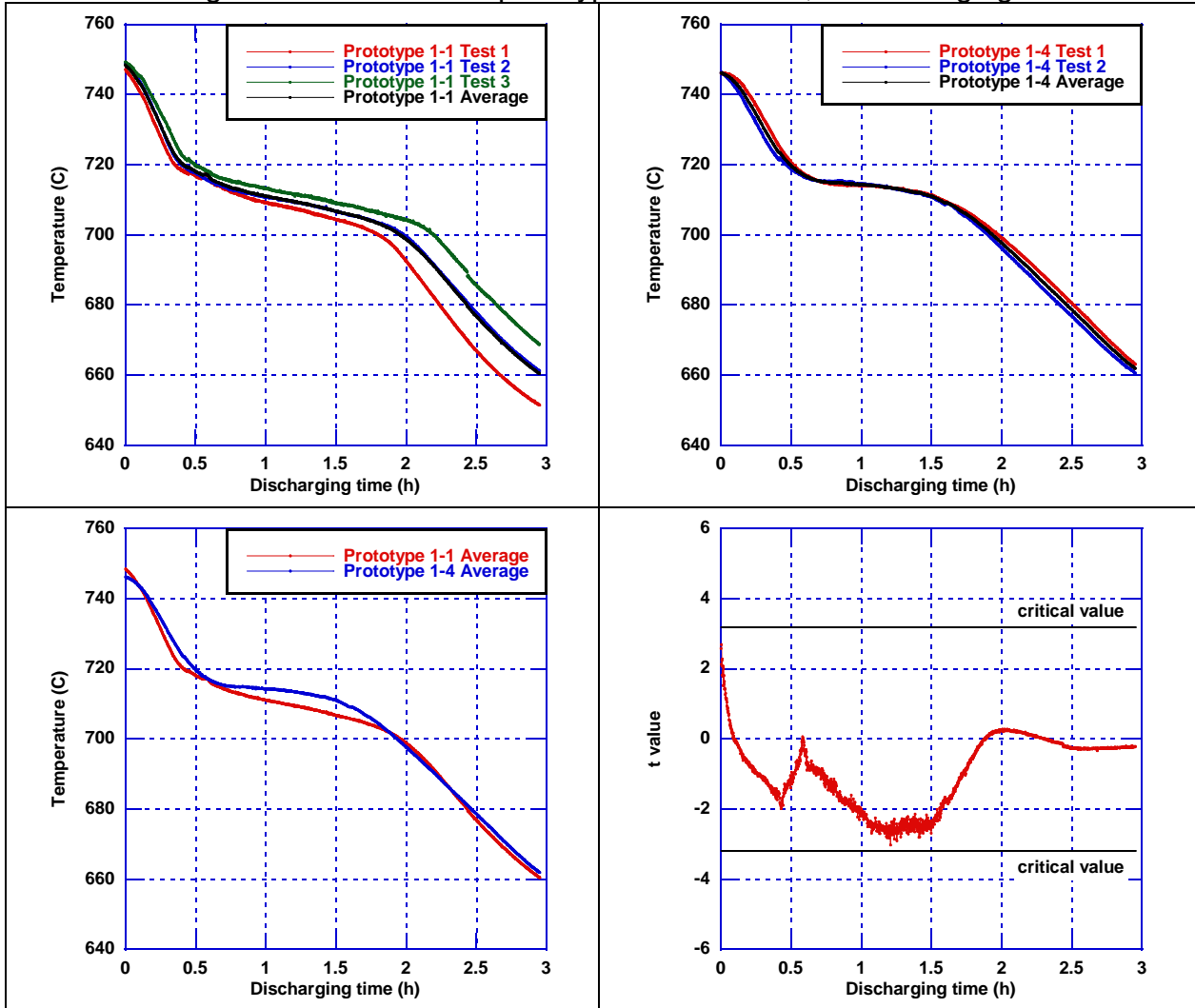

Figure 11-25. T-test of prototypes 1-1 and 1-4, TC 1 discharging.

Several features can be seen from Figures 11-24 and 11-25. First, while there are some differences in the temperature measurements, all charging and discharging curves follow similar trends. Moreover, the temperature measurement differences are generally small. Second, all t-test values for the discharging process are within the critical values, indicating that two prototypes have similar thermal performance. Third, the t-test values are beyond the critical values in the beginning part of the charging process, which is caused by the initial temperature differences due to the different furnace temperature settings for the charging process. For the rest of the charging process, t-test values are within the critical values. The t-test analysis is in agreement with the temperature comparisons. Based on the above results, the thermal performance of two prototypes can be considered similar. Therefore, (a) the foam type is not critical in that it has a high enough thermal conductivity for effectively conducting heat during charging and discharging and (b) the wall thickness of the center HTF tubing is also not critical in that its thermal resistance is not a dominant factor for heat transfer between the charging/discharging fluid and the foam-PCM combination.

11.10. Long-term exposure study

After the charging/discharging experiments, prototype 1-2 was placed in a furnace at 750°C for 250 hours to evaluate the effects of long-term exposure on the prototype. After the exposure, the prototype was removed from the furnace. Clearly, during the test, some of the salt leaked out from the vent used for moisture removal. This vent was not leak tight. In future testing we will weld the vent hole prior to testing.

The prototype was longitudinally sliced and the cut surfaces are shown in Figures 11-26 and 11-27. Figure 11-26 shows a higher magnification photo of the bottom section of the prototype. Clearly, the salt is nicely filled and contained within the pores in the bottom section of the prototype, and no degradation of the graphite foam is visible, which is desired. If the salt is mostly contained in the foam pores, its contact with alloy parts will be minimized. Further, the braze delamination can be seen at the bottom. It is not clear whether this occurred during slicing or existed before.

Figure 11-27 shows a high magnification photo of the side-wall section. Clearly, braze between the Incoloy container wall and foam as well as the center HTF pipe and foam is intact, and no degradation is visible. In future, a detailed microstructural analysis will be conducted to determine the corrosion effects, if any, of the PCM salt on the braze and/or the Incoloy.

In summary, a limited long-term exposure study shows no observable attack of PCM on the metal components. The PCM appears to be contained within the pores. A more detailed study is required to investigate PCM characteristics during melting and solidification processes as well as their effects on metal components.

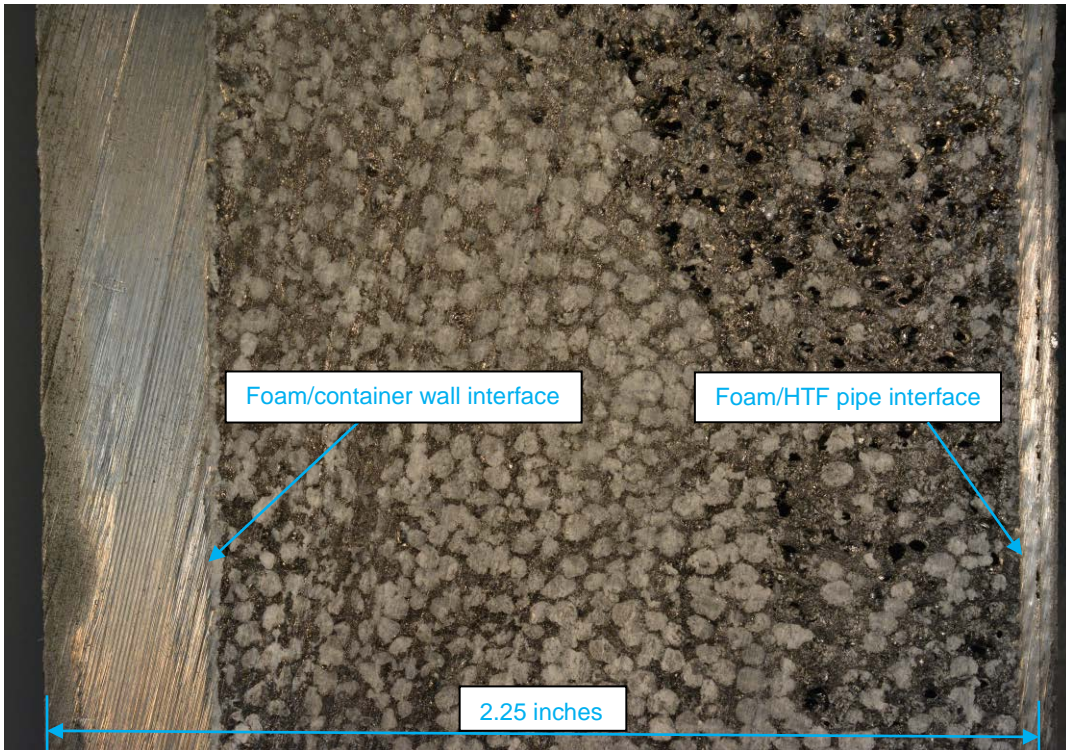Figure 11-26. Bottom section of prototype 1-2 after 750°C/250 h exposure.

Figure 11-27. Side wall section of prototype 1-2 after 750°C/250 h exposure.

12. Challenges and Solutions

During the testing of the prototypes, several challenges/issues were encountered. These challenges and their potential solutions for future work are listed below.

Heater Issue

During the testing of prototype 1-2, the heater broke down. The heater had to be sent back to the manufacture for repair. It was found that the heating element did not have appropriate support, and a short circuiting occurred between the heating element and the heater body. This repair resulted in significant loss of time. Heater selection needs to meet the rating and performance ranges as required by the test needs.

Thermocouple Reading

Some of the thermocouples in prototypes 1-2, 1-4, and 1-1 did not have stable readings during the charging/discharging procedure. A possible reason is that the melted $MgCl_2$ caused electrical short circuiting of these thermocouples. This could potentially occur if the tip of the thermocouple comes into contact with the graphite foam. One possible solution could be that the thermocouple tip should be smaller than the foam pore size to minimize the contact.

Another issue with the thermocouples was that several of them did not work or stopped working during tests. We think this is due to damage caused during insertion of the thermocouple wires in feedthrough(s). Several of the thermocouples were later found to be broken at the feedthrough. In future, insertion of thermocouples will be more carefully controlled.

Thermocouples located at the heater outlet were problematic and would break down after 2-3 runs. This problem was overcome by using a ceramic-sheathed thermocouple for better thermal protection.

Sealing Issue

Prototypes 1-4 and 1-1 were found to have leakage between the feedthrough bodies and the prototype top cap during the leak check procedure. Leak-sealing welding had to be conducted to fix the problem. Figure 12-1 shows one of the feedthrough bodies being leak-sealing welded by using an adaptor. Other two feedthrough bodies were welded in the same way. This problem also resulted in delays. However, now we have a procedure to mitigate the leakage from the thermocouple feedthroughs.

Damage to the HTF Pipe

During welding of the HTF pipe to the prototype cover, the HTF pipe would get damaged since the wall thickness was small. This damage was apparent on one prototype when leak tests were performed right after assembly, but was not detected in others. During testing of one of the prototypes, the leak developed and the PCM salt escaped into the HTF pipes. This required dismantling and replacement of a large section of the HTF piping. To avoid this problem in the future the approach will be to use thick-walled HTF pipes.
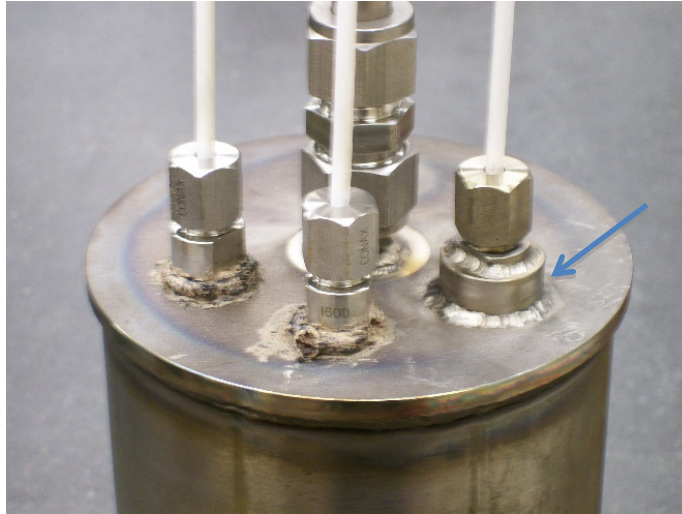
Figure 12-1. One of the feedthroughs welded using an adaptor to prevent leakage.

13. Summary

1. A high temperature system based on a phase-change material in combination with high thermal-conductive graphite foam was investigated.

2. Thermal modeling and simulations using analytical and commercial software demonstrated that the proposed latent heat-based thermal energy storage system can potentially meet the Sunshot Initiative's targets of rapid charging/discharging cycles with high efficiencies.

3. Parametric study was conducted to establish the effects of various system variables, such as the effective thermal conductivity of the PCM/foam composite, the HTF velocity, the HTF pipe diameter, the HTF pipe wall thickness, and the type of PCM used.

4. The pressure-assisted vacuum infiltration approach was used to infiltrate the graphite foams, with varying porosities, by $MgCl_2$ PCM to almost full capacity. Composite samples were evaluated for thermal cycling and heat flow. The observed behavior was consistent with predictions based on material properties, thus confirming the PCM fillage in the foam.

5. A laboratory-scale prototype was designed to demonstrate the LHTES system concept. Thermal modeling was conducted to define the experimental test parameters for the charging/discharging tests.

6. Based on the information generated for prototype modeling, a test loop was designed and built to evaluate the performance of the prototypes. Numerous tests were conducted to establish the variability/stability of the test loop such as the air-flow rates, heater temperature control, heat losses from the piping, and effect of additional heat using heating tapes to supplement heat losses.

7. Various system integration approaches were developed to join graphite foam to metal alloys such as Incoloy 800H, weld Incoloy tubing to the prototype body, and connect the heat transfer pipes to various sensors and pump. To minimize corrosion in the braze, chrome-free braze was demonstrated to join graphite foam to Incoloy 800H. Mechanical and thermal evaluations were conducted to determine the efficacy of the joints. For welding of Incoloy 800H to Incoloy 800H, Inconel 617 weld material was used.

8. To prevent graphite foam from any oxidation and/or enhance its mechanical integrity, thin (few microns) coatings were applied. Two approaches were used: chemical vapor reaction and polymer derived. Both coatings showed similar performances in minimizing oxidation as well as improving the mechanical properties. However, the ease of applying polymer derived SiC coating makes it an attractive option for large-scale applications.

9. Three prototypes were tested during the course of the project. These prototypes were quite similar in their construction; however, key distinctions were in foam porosity and brazing/no brazing of the foam to the prototype body.

10. Several charging/discharging tests were conducted on each of the prototypes and compared with the simulation models. For the most part, the simulation results and experimental data agree well. However, during the discharge process, the agreements are not always as good. The thermocouples that do not have good agreement are all located near the top of the PCM/foam. Potentially there could be surface effects from the head space within the prototype. This effect is more prominent during discharge because the temperature difference between the HTF and prototype is >100°C as compared to the charging process. To understand this, more experiments are planned.

11. Exergy and energetic efficiencies were estimated by including the heat loss/gain during charging/discharging. The estimated values are >95% for all three prototypes.

12. One of the prototypes underwent long term (250 h) exposure at 750°C. After the test, the prototype was sliced and analyzed. No visible degradation of Incoloy 800H or the uncoated graphite was observed. However, there was a region where the PCM was depleted. This was probably caused during the long-term exposure since the vent was not hermetically sealed.

13. Based on the data gathered from the prototype tests, the thermal properties of the PCM/graphite foam composite, and the 3D simulations of prototypes and scaled-up LHTES systems, the developed technology is a viable one.

Acknowledgements

References

1. C. Oh, et al., "Development of a Supercritical Carbon Dioxide Brayton Cycle: Improving PBR Efficiency and Testing Material Compatibility," Project Number: 02-190 Nuclear Energy Research Initiative, Idaho National Lab, INEEL/EXT-04-02437 (2006).
2. V. Dostal, M. J. Driscoll, and P. Hejzlar, "A Supercritical Carbon Dioxide Cycle for Next Generation Nuclear Reactors," MIT-ANP-TR-100 (March 10, 2004).
3. J. C. Gomez, "High-Temperature Phase Change Materials (PCM) Candidates for Thermal Energy Storage (TES) Applications," NREL /TP-5500-51446 (2011).
4. N. C. Gallego and J. W. Klett, "Carbon Foams for Thermal Management," Carbon 41: 1461-66 (2003).
5. A. Bradu and K. Alam, "3-Dimensional Modeling of Graphite Foam Heat Sink," Ceramic Engineering and Science Proceedings – Developments in Strategic Materials and Computational Design II, CESP Volume 31, Issue 10, eds, W.M Kriven, A.L. Gyekenyesi and J. Wang (2011).
6. P.G. Stansberry, E. Pancost, Y. Xiong, and J. Norley, "Graphite Foam Performance in Heat Exchanger Applications," *Proceedings of the SAMPE Fall Technical Conference*, Wichita, Kansas, October 19-22, 2009.
7. K. Lafdi, O. Mesalhy, and A. Elgafy, "Graphite Foams Infiltrated with Phase Change Materials as Alternative Materials for Space and Terrestrial Thermal Energy Storage Applications," Carbon, 46: 159–168 (2008).
8. Mesalhy, K. Lafdi, A. Elgafy, "Carbon Foam Matrices Saturated with PCM for Thermal Protection Purposes," Carbon 44: 2080-2088 (2006).
9. Y. Zhong, Q. Guo, S. Li, J. Shi, and L. Liu, "Heat Transfer Enhancement of Paraffin Wax Using Graphite Foam for Thermal Energy Storage," Sol. Energy Mater. Sol. Cells 94: 1011-1014 (2010).
10. R. Warzoha, O. Sanusi, B. McManus, and A.S. Fleischer, "Evaluation of Methods to Fully Saturate Carbon Foam with Paraffin Wax Phase Change Material for Energy Storage," Thermal and Thermomechanical Phenomena in Electronic Systems (ITherm), 13th IEEE Intersociety Conference, pp. 834-839 (2012).
11. S. Pincemin, X. Py, , R. Olives, , M. Christ, , O. Oettinger, "Elaboration of Conductive Thermal Storage Composites Made of Phase Change Materials and Graphite for Solar Plant," J. Sol. Energy Eng. 130: 011005 (2008).
12. W.Jianfeng et al., "Molten Salts/Ceramic-Foam Matrix Composites by Melt Infiltration Method as Energy Storage Material," J. Wuhan Univ. Tech.-Mater. Sci. Ed. (August 2009).
13. D. Singh, "High Efficiency Thermal Energy Storage System for CSP," Argonne National Laboratory, DOE EERE SunShot Initiative (2014).
14. T. F. Chen et al., "Volume and Grain Boundary Diffusion of Chromium in Ni-Base and Ni-Cr-Fe Alloys," Materials Trans. 44(1): 40-46 (2003).
15. A. Leger et al., "Capillarity in Pressure Infiltration: Improvements in Characterization of High-Temperature Systems," J. Mat Sci. 47: 8419-30 (2012).
16. P. Baumli and G. Kaptay, "Wettability of Carbon Surfaces by Pure Molten Alkali Chlorides and Their Penetration into a Porous Graphite Substrate," Mat. Sci. & Engg. A 495: 192-196 (2008).
17. J. Song et al., "Mo_2C Intermediate Layers for Wetting and Infiltration of Graphite Foams by Liquid Copper," Carbon 49(10): 3165-70 (2011).
18. Y. Zhang and A. Faghri, "Semi-analytical Solution of Thermal Energy Storage System with Conjugate Laminar Forced Convection," Int. J. Heat Mass Trans. 39: 717-724 (1996).
19. F. Samara, D. Groulx, and P.H. Biwole, "Natural Convection Driven Melting of Phase Change Material: Comparison of Two Methods," Excerpt from the Proceedings of the COMSOL Conference, Boston (2012).
20. N. Bianco, O. Manca, S. Nardini, and S. Tamburrino, "Transient Heat Conduction in Semi-infinite Solids Irradiated by a Moving Heat Source," Excerpt from the Proceedings of the COMSOL Users Conference, Grenoble (2007).
21. J. Michalski and E. Gutierrez-Miravete, "An Analysis of Heat Conduction with Phase Change during the Solidification of Copper," Excerpt from the Proceedings of the COMSOL Conference, Boston (2009).
22. Properties of graphite foam with temperature provided by OAI.

23. S. Jegadheeswaran, S.D. Pohekar, and T. Kousksou, "Exergy Based Performance Evaluation of Latent Heat Thermal Storage System: A Review," Renewable and Sustainable Energy Reviews 14: 2580-2595 (2010).
24. H. Shabgard, C.W. Robak, T.L. Bergman, and A. Faghri, "Heat Transfer and Exergy Analysis of Cascaded Latent Heat Storage with Gravity-Assisted Heat Pipes for Concentrating Solar Power Applications," Solar Energy 86: 816-830 (2002).
25. Y. Li, Y. He, Z. Wang, C. Xu, and W. Wang, "Exergy Analysis of Two Phase Change Materials Storage System for Solar Thermal Power with Finite-Time Thermodynamics," Renewable Energy 39: 447-454 (2012).
26. T. Watanabe and A. Kanzawa, "Second Law Optimization of a Latent Heat Storage System with PCMs Having Different Melting Points," Heat Recovery Systems & CHP 15(7): 641-653 (1995).
27. Advanced Research Projects Agency - Energy (ARPA-E), U.S. Department of Energy, "High Energy Advanced Thermal Storage (HEATS)," Funding Opportunity Announcement (FOA).
28. K. Fujii, J. Nakano, and M. Shindo, "Improvement of the Oxidation Resistance of a Graphite Material by Compositionally Gradient SiC/C Layer," J. Nucl. Mater. 203: 10-16 (1993).
29. F. J. Buchanan and J. A. Little, "Oxidation Protection of Carbon-Carbon Composites Using Chemical Vapour Deposition and Glaze Technology," Corrosion Sci. 35: 1243-1250 (1993).
30. H. T. Tsou and W. Kowbel, "A Hybrid PACVD SiC/CVD Multilayer Coating for Oxidation Protection of Composites," Carbon 33: 1279-1288 (1995).
31. J. R. Strife and J. E. Sheehan, "Ceramic Coatings for Carbon-Carbon Composites," Ceram. Bull. 67: 369-374 (1988).
32. R. Voytovych, V. Bougiouri, N.R. Calderon, J. Narciso, and N. Eustathopoulos, "Reactive Infiltration of Porous Graphite by Ni-Si Alloys," Acta Mater., 56: 2237-2246 (2008).
33. C. Rado, S. Kalogeropoulou, and N. Eustathopoulos, "Wetting and Bonding of Ni-Si Alloys on Silicon Carbide and Carbon," Acta Mater., 47: 461-473 (1999).
34. V. Bougiouri, R. Voytovych, O. Dezellus, and N. Eustathopoulos, "Wetting and Reactivity in Ni–Si/C System: Experiments Versus Model Predictions," J. Mater. Sci. 42(6): 2016-2023 (2007).
35. N. Eustathopoulos, M.G. Nicholas, and B. Drevet, *Wettability at High Temperatures*, Pergamon, Oxford, UK (1999).
36. M. Singh, C. Smith, A. Gyekenyesi, and R. Asthana, "Integration of High-Conductivity Graphite Foam to Metallic Systems Using Ag-Cu-Ti and Ag-Cu-Pd Braze Alloys," Intern. J. Appl. Ceram. Technol. 10(5): 790-800 (2013).
37. M. Singh, R. Asthana, A. Gyekenyesi, and C. Smith, "Bonding and Integration of Titanium to Graphitic Foams for Thermal Management Applications," Intern. J. Appl. Ceram. Technol. 9(4): 657-665 (2012).
38. M. Lucio et al. "On the Thermal Properties of a Two-Layer System," Physica Status Solidi 150(2): 695-704 (1995).
39. R. Warzoha et al. "Development of Methods to Fully Saturate Carbon Foam with Paraffin Wax Phase Change Material for Energy Storage," J. Solar Energy Eng. 135(2): 021006 (2013).